Imperial College
London

The Properties and Consequences of Mobile Ionic Defects in Metal Halide Perovskites

---

PhD thesis by Mr. William Richard Fisher

A thesis submitted in partial fulfilment
for the degree of Doctor of Philosophy

Supervisors: Piers R.F Barnes and Jenny Nelson

Department of Physics, Imperial College
London, UK, April 2022

Statement of Originality

The work presented in this thesis was carried undertaken between October 2017 and April 2022 in the Department of Physics at Imperial College London under the supervision of Dr. Piers R.F. Barnes and Professor Jenny Nelson. I declare that the results presented are the product of my own work, except where specific reference is made to the contribution of others.

William Fisher

April 2022

Abstract

Metal halide perovskites are a class of semiconductors that are solution processable and have received much research attention over the last decade for the application of photovoltaics and other electronic devices. They differ from conventional semiconductors since in addition to free electrons and holes (electronic charge carriers) they also contain mobile ionic defects (ionic charge carriers) whose concentration can exceed the electronic charge carriers. Efficiency and other performance metrics have improved greatly yet the devices suffer from instability that hinders their wider application in industry. Further understanding of the mechanisms underlying their characteristics is still needed for the eventual commercial success of these material. Using drift-diffusion simulations, as well as time and frequency resolved optoelectronic measurements, I examine the implications of these ionic charge carriers for the fundamental properties of, interpretation of measurements of, and the stability to humidity of, metal halide perovskite electronic devices.

Using drift-diffusion simulations, the mobile ionic charge is found to modify the device's energetic profile during the attainment of thermodynamic equilibrium, doping the perovskite layer. This doping mechanism is shown to be controllable through the choice of materials and through the application of a long timescale pre-biasing voltage. The existence of this 'interfacial doping' mechanism is confirmed experimentally using a pulsed-voltage technique.

I show that the relative densities of the ionic and electronic charges in the perovskite define which of the species control the device's electronic properties, this understanding is critical when characterising the material's properties. To highlight this, I asses the validity of the commonly applied Mott-Gurney law used to find the electronic mobility from current-voltage measurements of single carrier perovskite devices (space-charge-limited current measurements, SCLC). The electronic charge density needs to be approximately five times higher than the ion density for the law to apply. I show that, even using an experimental protocol that limits ionic redistribution during the measurement, determining the electronic mobility from SCLC measurements is difficult or impossible.

Both water, and ionic transport are considered to play important roles in the degradation of metal halide perovskites, understanding their interaction may help to develop strategies to improve stability. Using electrochemical impedance spectroscopy interpreted with an equivalent circuit model I show that the activation energy for ionic charge migration decreases as environmental humidity increases. This observation is consistent with previous ab-initio calculations which calculate that the existence of the monohydrate phase decreases the ion transport activation energy. Using these findings, I suggest the process by which perovskites interact with water and forms new phases on the way to degradation. Finally, I show that the addition of Cs to the perovskite stops this decrease in ion migration activation energy. These findings have significant implications and provide valuable additions to the understanding of the degradation of different metal halide perovskites with exposure to water.

Acknowledgments

Completing a PhD has been a great experience, I have learned a lot and I have been challenged on many levels; the disruption of the COVID-19 pandemic really changed the dynamics of my studies. Nevertheless, I am proud of the work I have to show for my efforts. My experience would not have been the same without the people who supported me through the journey, and I would like to use the following pages(s) to thank some very important people:

To my primary supervisor Piers Barnes, thank you for being so welcoming and friendly from the very start of my time at Imperial College. Thank you for your brilliant guidance and tuition in the art of scientific research. Thank you for your unwavering scientific curiosity, for your willingness to dedicate so much time to discussing the minutiae and to finding interesting tangents to get lost in. Thank you for being so helpful in re-directing and adapting my research throughout the pandemic, without your help I would not have finished my degree. Thank you for all the parties, the lunches, and the skiing you have involved me in - I can't imagine there are many PhD students and supervisors who can slide down mountains quite like us! Thank you for being such genuine person and for seeing the potential in me.

To Jenny Nelson, thank you for being a brilliant scientist and such an inspiration to me and to everyone else in the research group. Everyone I have ever spoken to holds you in the very highest regard and as a role model. Thank you for replying to my email back in 2017 and inviting me to an interview. Thank you for all your help and guidance, particularly early on in my studies.

To Phil Calado, thank you for your patience, kindness and for always being true to yourself. Thank you for your thorough scientific insights and great company in the Barnes group. Without your fantastic simulation software, Driftfusion, my work would not have been possible.

To Mohammed Azzouzi, thank you for your willingness to share your ideas and to have discussions, you truly have a brilliant scientific mind. Thank you for your help and guidance in the laboratories and thank you for being a great friend throughout my PhD.

To Flurin Eisner, thank you for sharing your time in the labs, I really enjoyed the work we did with the TSCPC setup. Thank you for the many laughs we have shared over the years.

To Davide Moia and Xingyuan Shi, thank you for all your help in the early days, for showing me your work, helping me with electronics and providing brilliant scientific insight throughout our shared time in the group.

To Jason Röhr, thank you for being such a great collaborator and a bottomless pit of SCLC knowledge. I have really appreciated your insight and feedback. Thank you for being such a cool desk-neighbour when I first arrived and for sending me home when I turned up to the office with a cold!

To Alexander Giovannitti, thank you for sharing your brilliant materials and great insight into the world of conjugated polymers. It is a shame that I couldn't get any of our great ideas to a conclusion, but I learned so much along the way.

To Jun Yan ("Prof"), thank you for being so kind, welcoming, and friendly throughout my time at Imperial. Thank you for introducing me to so many delicious Chinese foods and teaching me about your amazing culture.

To Anna Szumska, thank you for being a great friend and for organising so many socials (the dinners and the walks in particular) for the group. Your role as "group mum" will not be forgotten.

To Tom, Li, Lin, Tian, and Pabitra. Thank you for your brilliant introduction to perovskite solar cell synthesis and all your help. Thank you for your scientific insights and amazing devices.

To Joel and Onkar, thank you for our collaboration, your great feedback, and absolutely brilliant devices.

Thank you to everyone else in the Barnes and Nelson groups and the H1101 office past and present including Noushin, Sam, Nick, Brian, Sachetan, Hang, Paloma, Jiaxin, Dan, Tahiyat, Jack, Drew, Beth, and Alise. Thanks for sharing your scientific observations, great company and for creating such a friendly working environment.

Thank you to the people of the Plastic Electronics CDT cohort 9, I have really enjoyed spending time with you all whether it be whilst learning, having lunch, socialising or at the winter school.

To my sponsors at EPSRC, for providing me with the funding.

A personal thanks to my closest friends and family:

Most importantly to Hania Thompson, thank you for your love and unquestioning support through the hardest times of my studies and the pandemic. Thank you for all the amazing times we have shared together and for being my companion in life.

To my parents and brother, Kai, Catherine, and Ollie. Thank you for being there when the world descended into temporary chaos and for allowing me to live with you for the last two years. Thank you for your unconditional support, love, and unfaltering confidence in me throughout my studies. Thank you, mum, for your so very thorough proof reedinf…

To the Thompson clan, thank your welcoming me into your family, for the amazing trips to Scotland and for hosting me in your lovely home. The times I have spent with your family have been a fantastic break from the work for this thesis.

To the Birmingham Physics gang, thank you for your support and friendship, particularly with the quizzes through the pandemic. It has meant a huge amount to me.

And last, but certainly not least, to David Joseph. Thank you for your friendship throughout our PhDs at Imperial. Our gym sessions, Friday swimming, Athletics, pub visits and chats about everything and anything going on in the world have been of great value. Sharing the experience of a PhD from beginning to end has really helped to drive me onwards and to keep me focussed.

Table of Contents

List of Figures

List of Tables

Physical Constants, Abbreviations and Symbols

q	Elementary charge (C)
k_B	Boltzmann constant (eV K^{-1} or J K^{-1})
$\boldsymbol{\epsilon_0}$	Vacuum permittivity (F/m)
MHP	metal halide perovskite
$MAPbI_3$	Methylammonium lead iodide
$FAPbI_3$	Formamidinium lead iodide
$CsPbI_3$	Caesium lead iodide
MA	Methylammonium lead
FA	Formamidinium
LED	Light Emitting Diode
PV	Photovoltaic
SCLC	Space-Charge-Limited Current
MG	Mott Gurney
DOS	Density of States
T	Temperature (K or $°C$)
t	Time (s)
V	Voltage (V)
$V_{pre\text{-}bias}$	Pre-bias voltage (V)
I, J	Current, current density (A, A cm^{-2})
JV	Current density *vs* voltage curve
n	Electron density (cm^{-3})
p	Hole density (cm^{-3})
a	Anion density (cm^{-3})
c	Cation density (cm^{-3})
n_t	Trap density (cm^{-3})
A	Area (cm^{-2})
E_c	Conduction band edge energy (eV)
E_v	Valance band edge energy (eV)
E_g	Bandgap (eV)

E_F	Fermi energy (eV)
E_{fn}	Quasi fermi energy for electrons (eV)
E_{fp}	Quasi fermi energy for holes (eV)
E_{vac}	Vacuum energy (eV)
IP	Ionization Potential (eV)
EA	Electron Affinity (eV)
N_c	Conduction band DOS
N_v	Valence and DOS
E	Electric field (V cm^{-1})
$\boldsymbol{\epsilon_r}$	Relative permittivity
L	Thickness (cm)
V_{bi}	Built-in potential (eV)
V_{tfl}	Trap-filled limit voltage (V)
EIS	Electrochemical Impedance Spectroscopy
$\boldsymbol{\phi}$	Workfunction (eV)
$\boldsymbol{\phi_{inj}}$	Energy barrier to injection (eV)
$\boldsymbol{\phi_{sc}}$	Workfunction of a semiconduction (eV)
$\boldsymbol{\phi_{offset}}$	Workfunction offset (eV)
$\boldsymbol{\phi_m}$	Workfunction of a metal (eV)
$\boldsymbol{\mu}$	Mobility (subscript denotes the species) (cm^2 s^{-1} V^{-1})
D	Diffusion coefficient (cm^2 s^{-1})
P	Power (W)
V_{oc}	Open-circuit voltage (V)
I_{sc}, J_{sc}	Short-circuit current (A), Short-circuit current density (A cm^{-2})
FF	Fill-Factor
PCE	Power Conversion Efficiency
g	Gradient of a log-log relationship
i	Imaginary number
R	Resistance (Ω cm^2)
C	Capacitance (F cm^{-2})

L	Inductance (L)
$\boldsymbol{\omega}$	Angular frequency (Hz)
Q	Total charge (C)
Z	Impedance ($\Omega\ cm^{-2}$)
$\boldsymbol{\sigma}$	Conductivity (S cm^{-1})
G	Conductance (S)
E_a	Activation Energy (eV)
ASA	Advanced Semiconductor Analysis

Chapter 1 - Introduction

1.1 Motivation

The Intergovernmental Panel on Climate Change (IPCC) working group contribution of 2021 “presenting the physical science basis for climate change” (1) presents unequivocal evidence that anthropogenic climate change is already affecting many weather extremes around the world. They show that all climate models (except for modelling scenarios of net negative CO_2 emission by 2060) predict global warming of $\geq 1.8°C$ above pre-industrial levels will be reached during the 21st century unless drastic reduction of greenhouse gas emissions occurs (which is unlikely to happen). This increase in global temperature would be extremely likely to cause increasing rates of extreme heat, extreme draught and extreme flooding which would incur widespread food shortages and create millions of climate refugees in the coming centuries. In the worst-case scenarios, positive feedback loops would cause even more extreme changes in climate (such as an almost total loss of Greenland’s icesheet) which would likely lead to a drastic change in humankind’s way of life on Earth.

For the futures of an inevitable increase in energy demands (which is likely to be evermore electricity focused) (2) and the desperate need for the reduction of greenhouse gas emissions to coexist, humankind must both reduce the energy cost of electronics and, in parallel, greatly increase the fraction of our energy systems that is renewable and/or low carbon. In terms of electricity production, the trend is in the right direction with some parts of the world meeting targets to keep warming below $2°C$. As of 2020, the share of electricity production from renewable sources in the European Union was $22.089\ \%$ - double the share in 2005 (3). The figures for the European continent are encouraging (although, debatably the energy share transformation is still too slow) where renewable generation capacity increased by 261 GW (10.3%) in 2020 of which solar (mainly photovoltaic - PV) lead the way, with an increase of 127 GW (a 22% increase on 2019’s production) (4). Solar PV also has huge potential in developing countries nearer to the equator where solar irradiance is higher and, therefore, any technologies that decrease the cost of PV installation whilst maintaining efficiency would be a great asset in the fight against the climate disaster. Metal halide perovskites have emerged as a frontrunner in the race to satisfy this need; this material class is processed from solution at low temperatures and therefore could require less energy to manufacture and less upfront capital investment on an industrial scale than the currently ubiquitous silicon solar panels.

1.2 Lead-Halide perovskites for solar energy and other electronic devices

In 2018, Snaith (5) wrote that metal halide perovskites (MHPs) were first reported as the active layer in PV cells (solar cells) in 2012 and since then have presented as a promising new solution-processable PV technology with some potential in other optoelectronic applications (such as LEDs and phototransistors). The benefits of getting MHPs to the wider market in PV and other electronics over conventional PV/electronics materials are lower materials and manufacturing costs and independence from rare elements without any significant loses in power conversion efficiency (PCE). There is also a great opportunity for MHP PV to reach the market in tandem configurations because of their bandgap tunability, where a layer of MHP is added to a silicon solar cell in order to boost the cell's efficiency. At the time of writing, Oxford PV (a UK-based perovskite company) are aiming to produce commercially available perovskite-silicon solar cells and have achieved a PCE of 28% (6).

The largest hurdle to overcome before the commercialisation of MHP devices can be realised is their poor stability in the presence of water vapour, light and oxygen (7). There have been great improvements in the stability of devices to these environmental conditions, but further understanding of the degradation pathways/mechanisms and further improvements in device stability are still needed.

The key focus of this thesis is to understand some of the properties and consequences of the high density of mobile ionic defects found in MHPs. These mobile ions complicate the analysis of many measurement and modelling techniques that are used in the research processes aimed at understanding and improving device performance. There are also suggestions that these ions are involved in some degradation pathways (8) that hinder the commercialisation of MHPs. Therefore, further understanding of the consequences of the mobile ionic charge is of great value to improving the viability of this material class in commercial PV and other optoelectronics applications.

1.3 Scope and Outline

In this thesis I present experimental and simulation studies of the ionic and electronic conducting nature of MHPs and how they change under different electrical and environmental conditions.

I begin with – Background and summarise the basic physics of semiconductor interfaces relevant to the systems and devices that are investigated in this thesis. Where appropriate, resources for further reading material are provided to readers who wish to delve deeper. I also give a brief introduction to the material of interest in this thesis: metal halide perovskites (MHPs). This chapter is intended to give the reader some general context to the profuse literature surrounding MHPs, more detail relevant to each chapter is given in their respective introductions.

– Methods describes the general technical detail (including resources for further reading) of the simulations and experimental methods used in this thesis. More specific measurement and simulation parameters are given in each chapter where necessary.

In – The Interfacial Doping Effect in Perovskite Devices I investigate the consequences of high densities of mobile ionic charge when basic parameters describing device structure are varied. With the aid of the Driftfusion simulation tool, I describe a new interplay between ionic and electronic charge carriers in mixed-conducting devices during the attainment of thermodynamic equilibrium and I investigate the effect of the ionic charge carriers on the electronic charge density in several MHP device configurations. Further to this, I then investigate the consequences of pre-conditioning a device with a long timescale voltage. This is done in the context of the discussion of the equilibrium process from earlier in the chapter and contextualised using the language of semiconductor doping. Finally, I present experimental results demonstrating this doping effect and suggest the uses of this new understanding.

- SCLC Measurements of Metal Halide Perovskite Devices investigates the validity of applying conventional space-charge-limited current (SCLC) type analysis of semiconductors to MHPs to two JV curve measurement techniques: voltage sweeping and voltage pulsing. The Driftfusion simulation package is used to investigate the effect of certain device parameters on the validity of the application of the Mott-Gurney (MG) law. A discussion of the reasons for the observed behaviour reveals correlations to the processes discussed in Chapter 4 and I present device/material constraints on the application of these SCLC measurement techniques. Further to this, some experimental evidence demonstrating the limitations of the application of the MG law to MHPs is presented.

In – The Effects of Environmental Humidity on the Ionic Conductivity of Metal Halide Perovskites I investigate the effects of environmental humidity on MHP solar cells and the effect of modifying the cation content of the perovskite. I present experimental results displaying the changes to device characteristics when in equilibrium with environments of different humidities. I then analyse these results using equivalent circuit modelling and extract parameter values that quantify the observed changes in the experiments. These values, in combination with previous calculations from the literature, are used to analyse the mechanism by which water interacts with MHPs and thus, insight into MHP stability and the effects of cation mixing on it in humid environments is gained.

In Chapter 7 I summarise the conclusions of this work and provide discussion of the significance of this work in the context of the currently published literature and the future developments of perovskite devices.

1.4 Publications realised from this work

The publication process for each of the chapters of this work is underway, part of the work Chapter 5 has been released on arXiv:

Fisher WR, Calado P, Röhr JA, Smith JA, Shi X, Game O, et al. The Validity Window of Space Charge-Limited Current Measurements of Metal Halide Perovskite Devices. arXiv [Internet]. 2022 Apr 1; Available from: http://arxiv.org/abs/2204.00459

The rest of the work has not been released publicly.

Chapter 2 – Background

2.1 Introduction

One of the underlying themes of this thesis is the critical importance of junctions and interfaces between layers of materials in semiconductor devices. Understanding how the relative energy levels of the materials and the associated charge distributions in the interfacial region affect the performance and function of semiconductor devices is crucial. In this chapter, a summary of the relevant theory for interfaces between traditional semiconductors and other materials is given. The reader is referred to J. Nelson (9) and S.M Sze and Kwok K. Ng (10) for more detailed presentations of the device Physics that is summarised in this chapter. An introduction to the material of interest in this work, metal-halide perovskites (MHPs), is then provided, focusing on the qualities of MHPs that are important to the work of this thesis.

Whilst having properties favourable to their application in many optoelectronic devices, MHPs are known to contain high densities of mobile ionic defects which migrate in response to electric fields and in turn, significantly alter the internal energetic landscape in the MHP layer (11). This mixed-conductor behaviour complicates the application of the analysis and thinking that is often applied to traditional semiconducting devices, and it requires either significant modifications or even a complete overhaul of experimental techniques and device modelling methods to accurately characterise/understand the devices made with MHPs. It is also thought that these mobile ionic defects contribute to certain degradation pathways in MHPs, so understanding the consequences of the existence of this mobile ionic charge is not only important for correctly modelling the Physics of devices made with MHPs but also for combatting some of the issues with degradation. A review of some of the relevant literature regarding these mobile ionic defects and their effects on measurements, modelling and stability is given in this chapter to provide context for the rest of this thesis.

2.2 Semiconductor energetics and interfaces

2.2.1 Doping

In order to make semiconductor devices with the most useful properties, some sort of manipulation of the semiconductor’s “natural” state is often carried out. A very common approach is to alter the densities of electronic carriers in a semiconductor by doping it. Traditionally, in semiconductor classes other than MHPs (silicon or III-V semiconducting materials, for example) the goal is to increase or decrease the electron or hole concentration in the device which is often achieved by adding a small concentration of an extrinsic element/compound that is heterovalent with the surrounding semiconductor (for example, boron being added to silicon) and thus adding an extra hole or electron to the compound. As a result, the Fermi energy (also referred to as Fermi level) moves, which is depicted in Figure 2.1 along with the nomenclature for semiconductor energy levels and a representation of adding impurities to semiconductors for doping.

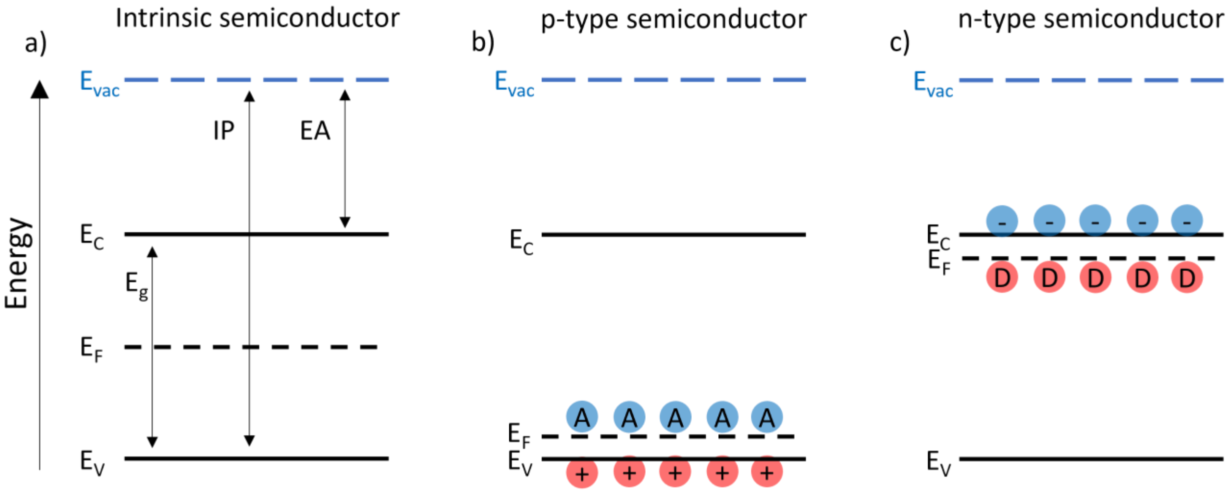

Figure 2.1 Energy levels of un-doped and doped semiconductors. a) An un-doped intrinsic semiconductor where E_c and E_v are the conduction and valance band edge energies respectively, E_F is the Fermi energy, E_{vac} is the vacuum energy, E_g is the bandgap, IP is the ionization potential and EA is the electron affinity. b) A p-type semiconductor where acceptor impurities (depicted by the blue circles with *A* in them) have been added which add holes to the valance band. This moves the Fermi level closer to the valance band. c) A n-type semiconductor where donor impurities (depicted by red circles with *D* in them) have been added, which add electrons to the conduction band. This moves the Fermi level closer to the conduction band. The donor and acceptor impurities are uniformly distributed throughout their respective semiconducting layer.

When the doping concentrations in a semiconductor are smaller than the density of states (DOS) in the conduction/valance bands and the semiconductor Fermi level is more than several thermal energies away from either band edge, the semiconductor is in considered non-degenerate and the Fermi-Dirac integral can be successfully approximated by Boltzmann statistics. The charge carrier densities are then described by:

$$n = N_c e^{-\frac{E_C - E_F}{k_B T}} \text{ and } p = N_v e^{-\frac{E_F - E_V}{k_B T}}$$

Equation 1

where n and p are electron and hole densities respectively, N_c and N_v are the DOS of the conduction and valence bands respectively and k_BT is the thermal energy (the Boltzmann constant multiplied by the temperature). All other symbols have their previously defined meaning. When doping concentrations approach the DOS of the conduction/valence band and the Fermi level is $< k_B T$ from the conduction/valence band edge, Boltzmann statistics no-longer apply, and some other method must be used for solving/approximating the Fermi-Dirac integral.

Not only does process this allow for the density of either charge carrier to be tuned for certain applications but it allows for very precise energetic offsets between materials to be engineered and it allows for the creation of an internal electric field.

2.2.2 *p-n* junction

In the following, I only consider the ideal case where no surface states are formed, and I only discuss cases of an assumed "abrupt junction". Discussion of other impurity distributions near the interface is not within the scope of this thesis. A *p-n* junction is formed when two regions of semiconducting material of differing doping levels are brought together to form a junction. This is often achieved in a homojunction (where the two regions consist of the same semiconductor with different dopant impurities). The Physics of a *p-n* junction are of great importance in solid-state electronic devices and allows for the creation of many different types of diodes due to their current-selective nature under bias, under illumination, or both. When a p-type and n-type region of a semiconductor (Figure 2.1a and Figure 2.1b respectively) form a junction and are electronically connected such that they reach thermodynamic equilibrium with each other, a band profile as demonstrated in Figure 2.2a is formed.

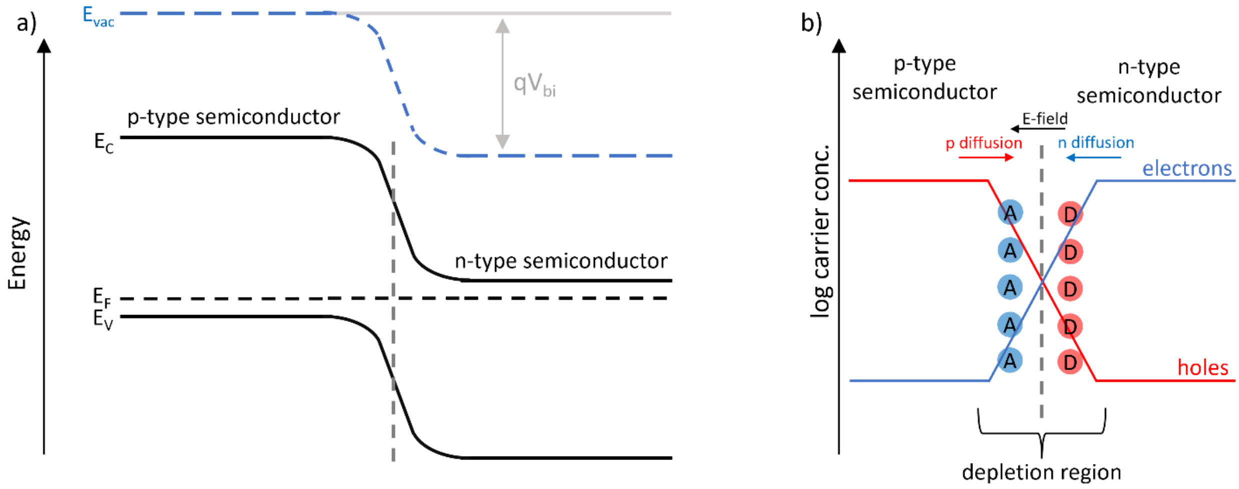

Figure 2.2 Diagrams of a semiconductor p-n junction. a) The band profile of a p-n junction in equilibrium, where V_{bi} is the built-in potential as a result of the band bending during the Fermi-level alignment. b) A cartoon representing the change in charge carrier distribution across the junction and the depletion region. Arrows showing the direction of diffusion current are given. The diffusion is opposed by the electric field at equilibrium, the direction of which is shown by the black arrow.

Once the interface between the two regions is formed, the Fermi levels must align. This process is driven by a difference in free energy of the charge carriers in either region; charge carriers in one region can lower their free energy by moving to the other region. As a result, charge carriers diffuse across the interface leaving behind the fixed (and charged) impurity states on either side. The resulting electric field opposes further charge diffusion across the interface and as a result a region of electronic charge depletion near the interface is formed; this is shown in Figure 2.2b. If an external voltage is applied to the junction, the width of the depletion region will change, either greatly increasing or decreasing the junction's resistance (depending on the sign of the applied field relative to the direction of the field in the depletion region) and thus the amount of current flowing through the whole device. This bias-dependent current selectivity is the operational principle of a diode and underpins many very important electronic devices used throughout the world, every day.

2.2.3 *p-i-n* junction

The junction structure most relevant to MHP solar cells is the *p-i-n* junction, where an intrinsic or undoped semiconductor (the perovskite) is "sandwiched" between a p-type and a n-type semiconductor. The same total V_{bi} is formed across this junction composition as in a *p-n* junction, but the electric field now forms not only across the depletion regions in the p-type and n-type layers, but also across the whole intrinsic region.

2.2.4 Metal-semiconductor junction

2.2.4.1 Schottky Barrier

In much the same way as in the formation of a *p-n* junction (see section 2.2.2), once a metal and a semiconductor form electrical contact, the Fermi-levels must align (due to a difference in charge carrier free energy between the metal and semiconductor). The Fermi-level in the semiconductor will change much faster than in the metal due to the semiconductor having a much lower density of valence electrons. As such, the Fermi-level in the semiconductor will move much more than in a comparable situation in a *p-n* junction. As the Fermi-levels align, charge moves across the metal-semiconductor interface and E_{vac} changes across the interface (since the workfunctions do not change). Once equilibrium is established, a region of increased charge density forms at the interface and a local electric field is formed.

As an example, I will present the formation of a Schottky barrier with an n-type semiconductor in contact with a metal of larger workfunction ($\phi_m > \phi_{sc}$) which is shown in Figure 2.3. In this case, during the formation of thermodynamic equilibrium, electrons exit the n-type semiconductor to the metal leaving behind uncompensated donor atoms which form the space-charge region in the semiconductor. In reality, the density of holes also increases in the semiconductor near the interface, but their density will be much lower than the donor density in this region, therefore they are omitted from the diagram. This means that there is a depletion region in the semiconductor side of the junction where the electronic charge density is lower than in the bulk. The whole region, including the side of the metal is referred to as a space-charge region.

Once equilibrium is achieved, E_c and E_v in the semiconductor bulk are now lower than at the interface. The gradient of this change in energy levels represents the electric field. This field exists almost entirely in the space-charge region. The size of the change in E_c and E_v (which is mirrored by the change in E_{vac}) represents a change in the electrostatic potential. These changes in E_c, E_v, *and* E_{vac} are shared between the metal and the semiconductor depending on the size of their relative dielectric permittivities. Semiconductors store charge much more effectively than metals (their relative dielectric permittivities - ϵ_r - are much higher) and so all the change in electrostatic potential happens in the semiconductor. Therefore, the space-charge region is much thicker in the semiconductor than in the metal, where the space-charge region is of negligible width. This is shown in Figure 2.3 by the existence of band bending in only the semiconductor region.

In the space-charge region of the semiconductor, the majority carrier is of a lower density than in the bulk of the semiconductor, and the electric field is such that the majority charge carrying species drifts away from the interface. This interface, therefore, presents a high resistance to the majority carrier and a low resistance to the minority carrier. In other words, an energy barrier to majority carriers has formed at the interface: a Schottky barrier.

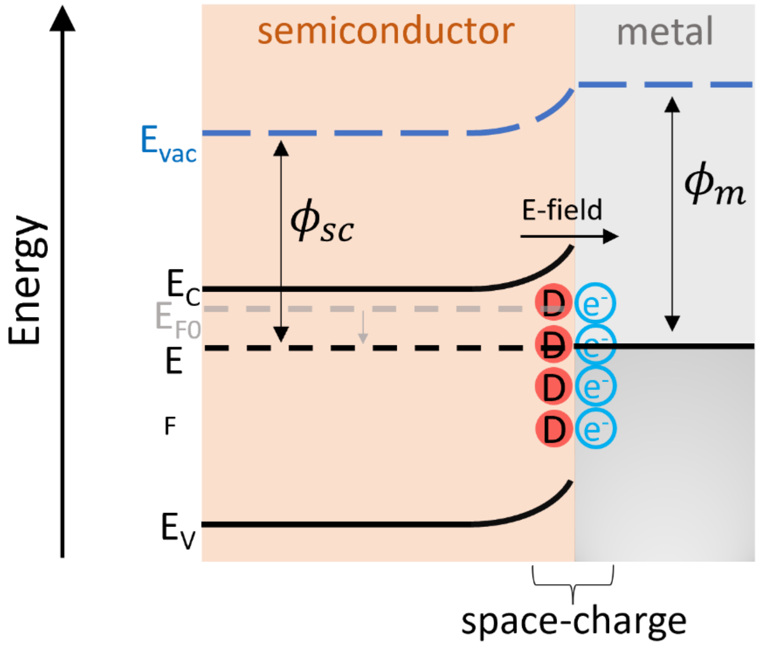

Figure 2.3 A cartoon showing the formation of a Schottky barrier: the interface between a doped semiconductor and a metal, where $\phi_m > \phi_{sc}$. The red circles containing *D* represent donor atoms that are contributing to the interfacial space-charge region. The asymmetry in the width of the space-charge regions in the metal and the semiconductor is not shown here for the sake of clarity. The small accumulation of holes in the semiconductor side is also omitted, since the donor impurities will be of higher density.

2.2.4.2 Intrinsic semiconductor-metal junction

In this example, an intrinsic semiconductor in contact with a metal is examined, where the metal's workfunction (ϕ_m) is less than the semiconductor's workfunction (ϕ_{sc}) (shown in

Figure 2.4), electrons move into the semiconductor and holes to the metal. This example is very different to that of the p-n junction in section 2.2.2 and the Schottky barrier in section 2.2.4.1 because there are no fixed, charged donor/acceptor species to form a depletion region. Instead, there is a space-charge region of only electrons/holes near the interface. Since the population of electrons and holes is equal in the intrinsic semiconductor before contact is made with the metal, the change in density of both species in the space-charge region make somewhat significant contributions to the electric field profile. In this configuration with an intrinsic semiconductor in contact with a metal there is never a case where the majority charge carrier density is lower in density in the space-charge region than in the bulk, the fact that there is a majority carrier is induced by the contact energetics and is electrons in this example. Once the Fermi levels are aligned, the electric field direction causes the majority carrier to drift towards the interface. As such, this interface presents a low resistance to the majority carrier and high resistance for the minority carrier – the opposite of a Schottky barrier.

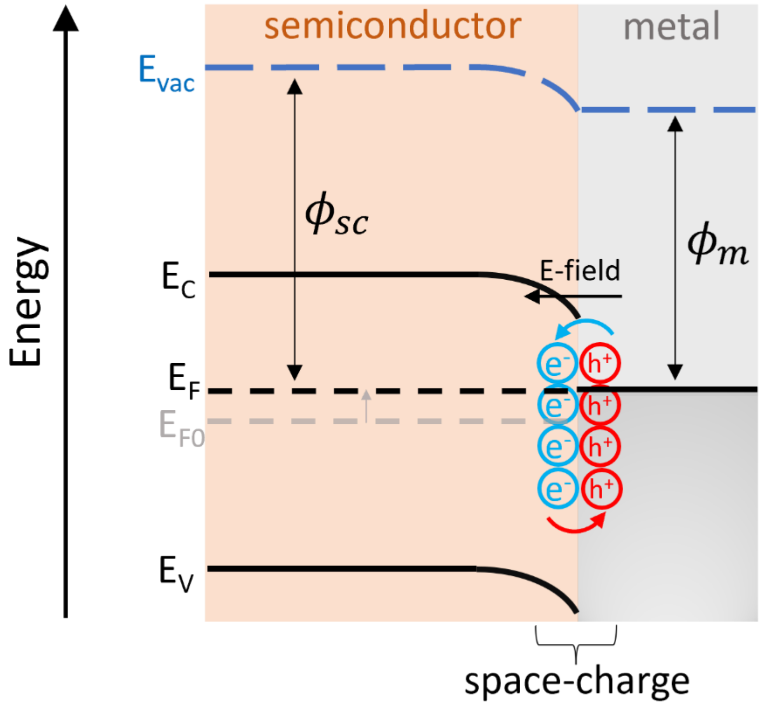

Figure 2.4 A cartoon showing an interface between an intrinsic semiconductor and a metal in equilibrium. In this example $\phi_{sc} > \phi_m$ and thus before equilibrium, the semiconductor's Fermi level (E_{F0} and represented by the grey dashed line) is below the metal's Fermi level. The space-charge region is formed by electrons moving into the semiconductor and holes leaving it, a process depicted by the coloured arrows, which moves the semiconductor's fermi level up (grey arrow). The width of the space-charge region would, in reality, be asymmetric across the junction due to the difference in dielectric constant between the metal and the semiconductor. This is not represented here for the sake of clarity.

2.2.4.3 On the formation of space-charge in a metal-semiconductor-metal sandwich

In this section, I provide a derivation for the exponential distribution of charge carriers at the metal-semiconductor interface. The device in question would be formed exactly by the combination of two interfaces identical to the junction represented in Figure 2.4 and I will use Boltzmann statistics as in the discussion of Equation 1. Most of the information in this section is extracted from a combination of Sze and Ng, Mott and Gurney, and Geppert (10,12,13).

At equilibrium, the drift current exactly cancels out the diffusive current as discussed in sections 2.2.2 to 2.2.4.2:

$$qn\mu E = qD\frac{dn}{dx}$$

Equation 2

where q is the elementary unit charge, n is the electron density, μ is the electron mobility, E is the electric field, D is the diffusion constant, and x is the one-dimensional position across the semiconductor (of thickness L) with $x = -\frac{L}{2}$ at one interface and $x = \frac{L}{2}$ at the other. In this case, the Einstein relation is used for the diffusion coefficient ($D = \mu k_B T$) and so Equation 2 becomes:

$$\int \frac{1}{n}\, dn = \frac{1}{k_B\, T} \int E\, dx$$

Equation 3

noting that the line integral of the electric field, E, is the electric potential, V. Using the boundary condition at $x = \frac{L}{2}$, $V = \phi_m - EA$ (the potential barrier at the semiconductor-metal interface) and $n = n_{L/2}$, where ϕ_m is the metal contact workfunction, EA is the electron affinity of the semiconductor and $n_{L/2}$ is the density of electrons at the interface, the electron charge distribution is then described by,

$$n = n_{L/2} e^{\frac{(\phi_m - EA) - V}{k_B T}}$$

Equation 4

Equation 4 shows that the charge distribution of electrons is exponentially dependent on the difference between the energy barrier at the interface and the electric potential. This is a key insight in the understanding of charge carrier accumulation/depletion at the interface of an intrinsic semiconductor and a metal.

2.2.4.4 Ohmic contacts

An Ohmic contact is simply a case where there is very little/no resistance to the transport of a majority carrier across an interface. More specifically, I will use the definition of an Ohmic contact where there is no injection barrier, $\phi_{\text{inj}} = 0\ eV$ (14) where ϕ_{inj} is the difference between ϕ_m and the nearest band-edge at the interface when ϕ_m lies within the bandgap. The contact is still considered Ohmic if ϕ_m lies outside the bandgap.

2.3 Solar cells

Semiconductors that have efficient charge transport characteristics (slow recombination characteristics) and contain a bandgap ($E_v - E_c$) of energy that is equal to the photons of the visible spectrum (more specifically that match the photon wavelengths emitted by the sun) can theoretically be used to create a solar cell that is of use on Earth. Once a photon of the right energy is absorbed, an electron is excited to the conduction band leaving a hole in the valence band and thus creating an electron-hole pair, which are often weakly bound. In order to prevent the electrons and holes recombining at the "wrong" interface (current selectivity) an electric field is used. In most conventional solar cell structures, this is achieved with a *p-n* junction (see section 2.2.2) that sets up an electric field that carries out this charge selectivity. Once the charges are extracted from the semiconductor, they flow to the electrical contacts and then through an external circuit that may have some load to drive. If no charge is allowed to exit the device (for example, if a very high resistance electrical load is connected in series) then a voltage will build up across the cell until some new equilibrium is reached.

In order to characterise a solar cell's performance, the current-voltage (IV) curve under illumination is often used. Figure 2.5 shows an example of an IV curve of a solar cell under illumination. As voltage is applied to the solar cell, if the electric field associated with the applied voltage opposes the direction of generated current, then there will be a point at which the current reduces to zero. The cell is said to be at "open-circuit" in these conditions and the voltage at which this happens is the open-circuit voltage (V_{oc}). If there is no voltage applied to the cell and there is no load-resistance in the external circuit, the cell is said to be at "short-circuit". The current in this condition is the short circuit current (I_{sc}). The power from the solar cell along this illuminated IV curve can be calculated by using $P = IV$. There will be a point on the IV curve at which the power is maximum (P_{max}), referred to as the maximum power point. Researchers then define another parameter that represents the "squareness" of the IV curve: the fill-factor (FF),

$$FF = \frac{P_{max}}{V_{oc} I_{sc}}$$

Equation 5

The power conversion efficiency (PCE) of the solar cell is the ratio of power in from illumination (P_{ill}) to the power out,

$$PCE = \frac{FF(V_{oc}I_{sc})}{P_{ill}}$$

Equation 6

The IV curve of a solar cell under illumination can, therefore, be used to determine all these parameters. The characteristics of the curve's shape at open circuit in the dark and under illumination are highly related to recombination in the cell. In Figure 2.5 the gradient of the IV curves is shown to be related to the recombination resistance by the green lines and text. This is useful to note in the discussions of equivalent circuit modelling in section 3.4.2 and Chapter 6; recombination dominates the cell's characteristics at open circuit.

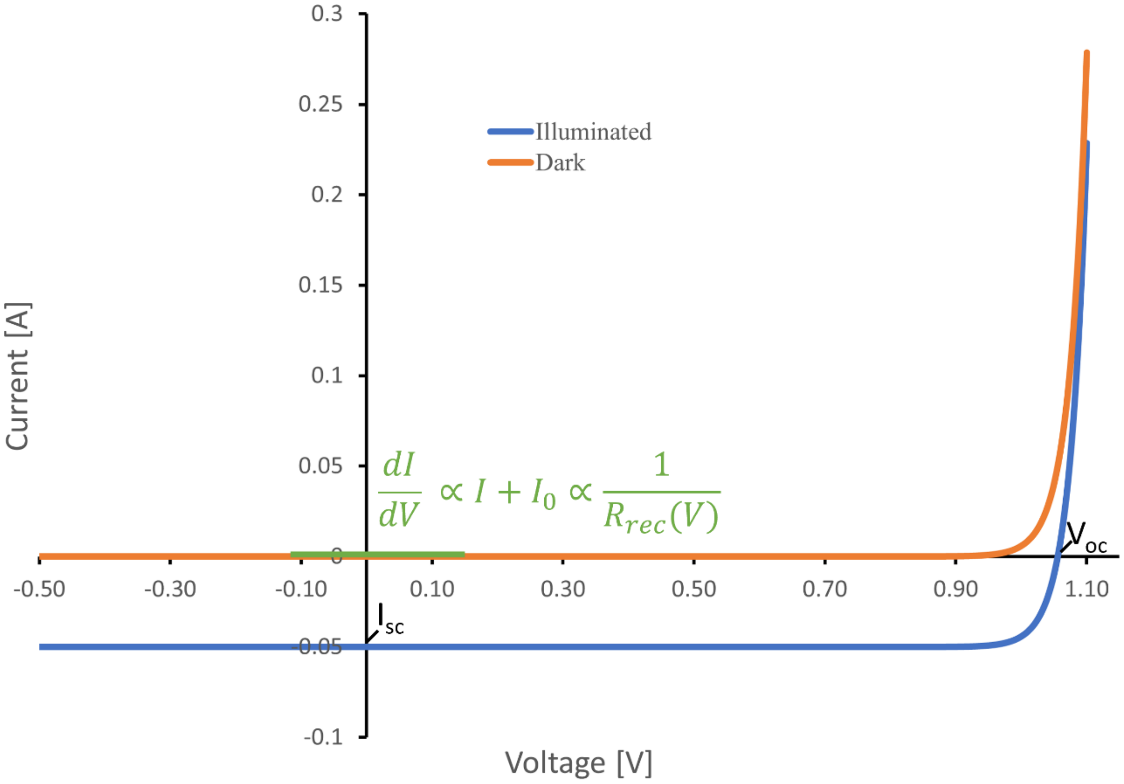

Figure 2.5 An example of a solar cell IV curve under illumination and in the dark. V_{oc} and I_{sc} (open circuit voltage and short circuit current respectively) of the illuminated curve are labelled on the graph for clarity. The relationship between the gradient of the IV curve and the cell's recombination (recombination resistance here) at open circuit in the dark is shown by the green line where I_0 is the saturation current density.

2.4 Metal halide perovskites

2.4.1 Chemical Structure

The term “perovskite” originates from the discovery of naturally occurring mineral calcium titanate ($CaTiO_3$). It became a generalized term for compounds of the same ionic crystal structure as $CaTiO_3$ after Victor Goldschmidt described it in 1926 whilst working on crystal tolerance factors (15). The way this generalized perovskite structure is referred to is ABX_3 where *A* represents a cation of oxidation state +1, *B* represents a cation of oxidation state +2 and *X* represents an anion of oxidation state -1. An example of the crystal structure in the cubic phase is given in Figure 2.6. The metal halide perovskite (MHP) is the specific classification of perovskite material that is of interest in this work. MHPs became of great interest to the scientific community after their use as a light absorbing material in solar cells was documented, specifically for the compound methylammonium lead iodide ($CH_3NH_3PbI_3$ or $MAPbI_3$) (16,17). As research has progressed, some partial/total substitution of the elements in the ABX_3 structure has been carried out to improve structural and optoelectronic properties, hence the use of the slightly more generic term MHP.

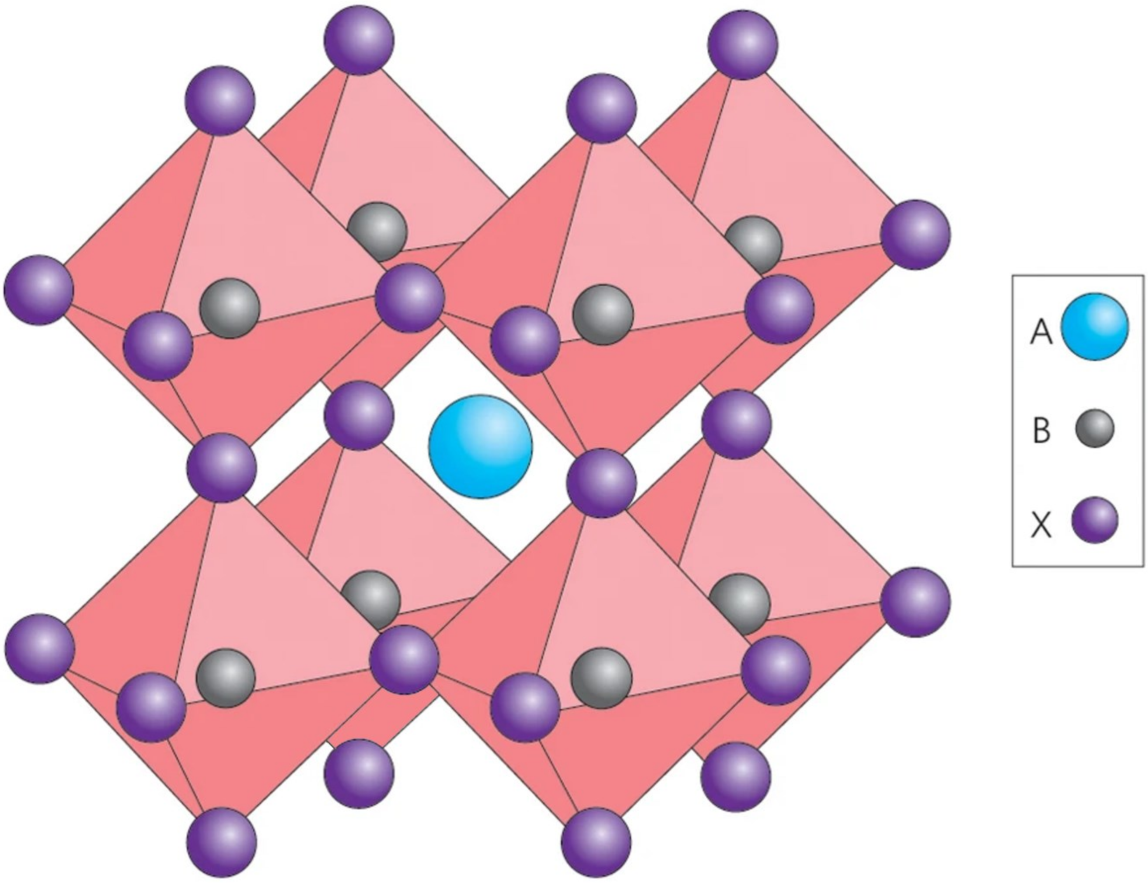

Figure 2.6 The ABX_3 perovskite crystal structure in the cubic phase. The atoms are bonded to one-another ionically. In the case of $MAPbI_3$, the *A* site is MA^+, the *B* site is Pb^{2+} and the *X* site is I^-. Reproduced and modified from ref.(18) with appropriate permission.

The Goldschmidt tolerance factor is a good way of analysing the stability and distortion in a perovskite crystal structure. The Goldschmidt tolerance factor is defined as:

$$t = \frac{r_A + r_X}{\sqrt{2}(r_B + r_X)}$$

Equation 7

where r_A, r_B and r_X are the ionic radii of the cations in the *A* and *B* positions and the anion in the *X* position respectively. For MHPs, a stable perovskite structure is formed when $0.8 < t < 1$ and outside this region some non-perovskite structures form, one of the main causes of lattice instability/distortion is the *A* site cation not “fitting” in the BX_3 framework (which is shown in Figure 2.6). Changing the cation in the *A* site, or even mixing them, is one way of optimizing the tolerance factor and stabilizing the desired phase. When Equation 7 is analysed it can be seen that if the *A* site radius, r_A, is reduced/increased, *t* decreases/increases (19,20).

2.4.2 Solar cell structure

The application of MHPs to solar energy production was the finding that initiated the drastic increase in research we have seen in the community over the last ten years. Presently, the most efficient MHP solar cells effectively treat the perovskite layer as an intrinsic semiconductor, meaning the electron and hole densities in the layer are roughly equal at equilibrium ($n_0 = p_0$). To avoid very high recombination at the interface with the electrodes and to encourage charge separation, the perovskite is then sandwiched by one n-type and one p-type semiconductor as is shown in Figure 2.7. These layers act as selective contacts to the relevant charge carrier for that electrode. One can assemble the layers of a perovskite solar cell from bottom to top in two orders: *p-i-n* and *n-i-p* (Figure 2.7a and Figure 2.7b respectively). There is still debate in the community about which structure is preferable with different research groups preferring different structures.

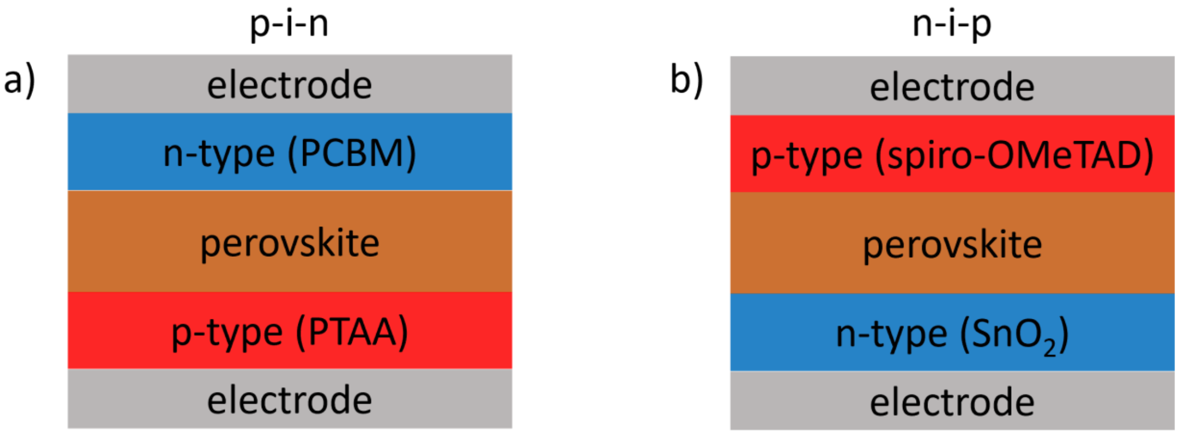

Figure 2.7 The layered structure of most MHP solar cells. a) a *p-i-n* structure with examples of commonly used materials for the p-type and n-type layers, namely poly[bis(4-phenyl)(2,4,6-trimethylphenyl)amine] (PTAA) and [6,6]-Phenyl-C61-butyric acid methyl ester (PCBM). b) a *n-i-p* structure with examples of commonly used materials for the n-type and p-type layers, namely tin oxide (SnO_2) and 2,2’7,7’-Tetrakis[N,N-di (4-methoxyphenyl)amino]-9,9'-spirobifluorene (spiro-OMeTAD).

2.4.3 Defects, traps, and mobile ions

MHPs are generally thought to have a high defect tolerance. (21,22) Early work from Yin *et al.*(23) studied the relative formation energies of point defects under different growth conditions and found that the donor type of the defects is tuneable by changing the ratios of precursor concentrations, allowing for both p-type and n-type MHPs to be made by controlling the relative amounts of point defects in the active layer, without using the doping method discussed in section 2.2.1. Yin *et al.*(23) also reported that the defects of low formation energy (high density) form very shallow defects and are essentially electronically inactive (24,25) and that the deep defect states have very high formation energies (low density). Other such studies using DFT focused, *ab-initio* have shown similar findings (11,26–28) and this suggests that MHPs have a high intrinsic concentration of defect sites, the majority of which are likely to have only a very small contribution to charge trapping and recombination. The very high formation energy of deep defect states explains, in part, the low non-radiative recombination rates seen in MHP solar cells when compared with other low temperature, solution processable technologies such as OPV and dye-sensitised solar cells.(29) Techniques used to reduce non-radiative recombination include the control of perovskite crystallization, defect passivation and interface engineering. (30) There is much debate in the scientific community as to the mechanism of the contribution of grain boundaries to defect mediated recombination of polycrystalline MHPs (31–35), although the overall consensus is that more grain boundaries leads to more recombination. The density of defects may be reduced under illumination (36) and in MHPs with a mix of halides (in the *X* site) when compared to $MAPbI_3$ in the dark, although the different halide phases seem to segregate under illumination (the Hoke effect) (37,38).

This leaves a rather complicated picture of trap states and defects in relation to recombination in MHPs due to: (i) their variety of origin in different specific perovskite structures, (ii) their variety in distribution in energy and density and (iii) the fact that defects themselves can be modified by environmental conditions and synthesis recipe (36,39).

Even though some of the defect states in MHPs are thought to be essentially inactive in terms of recombination, some of these defect states are known to be mobile (11) with the iodine vacancy in $MAPbI_3$ having the lowest activation energy to migration. These mobile defects have low formation energies and are thought to be Schottky-type defects shown in the following reaction using Kröger – Vink notation as suggested by Walsh *et al.* (26):

$$nil \rightarrow V'_{MA} + V''_{Pb} + 3V^{\cdot}_{I} + MAPbI_3$$

Equation 8

where *nil* is a defect free $MAPbI_3$ crystal lattice, V'_{MA} is a methylammonium vacancy with a -1 charge, V''_{Pb} is a lead vacancy with a -2 charge and $V_I^{\cdot}$ is an iodine vacancy with a +1 charge. This reaction is charge neutral and does not require compensation by electronic carriers, so the formation of these defects does not cause any doping effect. There is often a disparity in the quoted density of these mobile ionic defects (often referred to simply as mobile ions): It is quoted as high as $10^{18} - 10^{19}\ cm^{-3}$ in some theoretical models and experimental results (11,26,40–45) but in some other studies as low as $10^{16} - 10^{17} cm^{-3}$ (46–48) and sometimes even lower ($\approx 10^{13}\ cm^{-3}$) (49). In almost all cases, this is higher than the expected equilibrium charge carrier densities which have been measured in the dark as below $10^{15}\ cm^{-3}$.(50) The diffusion coefficient for iodide vacancies was also estimated by Eames *et al.*(11) and was found to be $10^{-12} cm^2 s^{-1}$, assuming Boltzmann-like barrier hopping, but has been measured as high as $10^{-7} cm^2 s^{-1}$ (51). The reported diffusion coefficient for electrons/holes in $MAPbI_3$ is $\sim 1\ cm^2 s^{-1}$ (52) and the reported mobility is $\sim 1\ cm^2 V^{-1} s^{-1}$ (53), although there is a large range around these values it is generally agreed that the electronic charge carriers are many orders of magnitude more mobile than the ionic charge.

This feature of a high density of mobile ionically charge defects that are very slow moving in comparison to electronic charge, has some important implications on device characterisation and potentially implications on device stability. This thesis focusses on some of these implications.

2.4.3.1 Measurement artefacts introduced by mobile ionic charge

Any measurement that requires a voltage to be applied to a device is compromised by the high density of mobile ionic charge in the MHP and as such, appropriate measures either in analysis or experimental technique need to be taken in order to account for the field-screening and band bending they cause. Here, an overview of two measurement techniques that are relevant to the scope of this thesis and the effects of mobile ionic charge on them are given.

Measuring the current density – voltage (JV) curve of a solar cell under an illumination intensity equivalent to 1 sun (where 1 sun is the equivalent to standard illumination at AM1.5, or 1 kW/m^2) is the established method for determining the PCE of a solar cell. There are several key performance metrics that can be extracted from this measurement including: power conversion efficiency (PCE), short-circuit current density (J_{sc}), open-circuit voltage (V_{oc}) and fill-factor (FF). The details of these metrics and their implications for solar-cell performance are beyond the scope of this thesis.

Early in the research history of MHP solar cells, there was much discussion of how the measurement protocol for obtaining the JV curve effected hysteresis and the aforementioned performance metrics. The key protocols for influencing JV hysteresis are device preconditioning (pre-bias voltage), scan speed and start/end voltage (54–56). The appearance of JV hysteresis in the literature was a key driving-force in determining the existence of the mobile ionic charge discussed in section 2.4.30 and has been found as the cause of JV hysteresis (44,57–59). More specifically, the ionic charge accumulates at the interfaces (46), screening the applied voltage and reducing the internal field. The accumulation of ions at the interfaces has also been attributed to some factors that are detrimental to solar cell performance such as phase segregation and chemical reactions (37,60–62), although there is no community-wide consensus on the overall contribution of these mobile ionic defects to overall solar cell performance.

JV curves are not only used to determine the performance of solar cells but can also be used to extract other information about devices/materials. SCLC measurements, which involve measuring a JV curve for a two terminal device and analysing it with a specific set of equations, can be used to extract a mobility for the majority charge carrier (63) and potentially to estimate the trap density (64). Recently, short pulses of voltage interrupted by a long re-equilibration time have been used to try to determine an “ion-free” JV curve in order to maintain the validity of the SCLC measurements and their associated analysis (49,65). This measurement technique could be used for other applications in the attempt to avoid ionic contributions to the measurement, this measurement technique, and its application for measuring SCLC is the focus of Chapter 5 and more specifically in section 5.2.

Measurement of MHP devices using electrochemical impedance spectroscopy (EIS) revealed curiously large capacitive ($> 10^{-3}\ Fcm^{-2}$) and inductive ($> 1\ Hcm^{-2}$) features which were explained by Moia *et al.* (66) as electronic recombination at the interfaces of perovskite solar cells, modulated (gated) by ionic charge. These features appear at specific frequencies where this modulation causes an effective capacitance or inductance.

2.4.4 Stability

The largest aspect of MHP devices that prevents their viability in real-world applications and commercialization is the stability of the perovskite to conditions in the environment, specifically the long timescale exposure to water (via atmospheric humidity), oxygen, heat, and light (specifically ultraviolet). The degradation processes include the halide vacancy-mediated formation of a superoxide in the presence of light and oxygen (8), photoinduced degradation under vacuum to lead iodide and to lead salts under air (67), photoinduced phase segregation of mixed halide perovskites (68) and many processes involving water which are discussed later. There have even been calculations showing some intrinsic thermodynamic instability of MHPs. (69) These stability issues affect all devices made with a MHP active layer, however, the solar-cell community are the most focused on studying and improving device stability. Significant progress has been made in improving unencapsulated cell stability (maintaining 80% of their original performance) to >5000 hours by using a hydrophobic top transport layer in a triple-cation device (70) and encapsulated/coated films have been shown to have stable performance for >1000 hours with no obvious decline in performance (71) and 6 months under illumination or 1 month under high humidity (72). These performance metrics are impressive but still fall short of the expected 20+ year lifetimes of commercially available Si solar panels. There is still some way to go. A comprehensive review of perovskite solar cell stability can be found in Wang *et al*. (7) and Rao *et al.*(73).

Mixing the cationic composition of MHPs has been shown to greatly improve device stability in inert environments and under atmospheric conditions. Adding Cs to $FAPbI_3$ has been shown to reduce its Goldschmidt tolerance factor (Equation 7)reducing the likelihood of an unwanted phase change (74,75) and improves the thermal stability of the bromide(76). Adding Cs to $MAPbI_3$ has been shown on multiple occasions to improve stability (77–79) and its inclusion in small amounts in mixed cation and mixed halide perovskites has been found to be important (80). The practical benefits of these structural modifications to the MHP lattice are evidently well understood but insights into the mechanism by which these benefits occur are not well studied with very little published work at the time of writing.

2.4.5 Modelling MHP devices

2.4.5.1 Drift-diffusion simulations

Semiconductor devices are complicated systems with many physical processes occurring simultaneously and, as such, using analytical models with analytical solutions to describe these devices can only be done for a limited set of circumstances. The power of a drift-diffusion model is that the drift and diffusion equations describe the charge carrier densities very accurately, throughout the modelled materials at the macroscopic level. Naturally, their accuracy deteriorates as quantum effects become significant. The drift-diffusion equations can also encompass a wide range of semiconducting materials and device architectures so long as the input parameters and boundary conditions are reasonably well/accurately defined.

Typically, the electron and hole densities are modelled as discrete energy levels. More complicated DOS profiles can be included where necessary but often at the cost of computational time and resources. Then, the transport model of the drift and diffusion are used to describe the motion of charge carriers in response to a carrier density gradient and an electric field. It is often sufficient to model devices in one spatial dimension (unless the material being modelled is significantly inhomogeneous and anisotropic), thus all calculations occur on a well-defined 1D spatial grid. Once the drift-diffusion equations are established, continuity equations that describe the spatial and temporal variation of carrier densities at each point are included to create a set of coupled partial differential equations. Drift-diffusion models for MHP devices are certainly non-trivial to create due to the necessity of the addition of the mobile ionic charge I introduced in section 2.4.3. For the rest of this section, a brief review of the literature of drift-diffusion device simulation of MHPs is given to provide some context and for the introduction of the simulation package used in this work and to provide the reader with some alternative options.

Van Reenen *et al.* (81) published what I have found to be the first simulations using a coupled drift-diffusion model that included, additionally, a mobile ionic species. After further investigation it was found that the ionic charge densities at the interfaces of MHP devices were likely very high (>10^{18} cm^{-3}) and the 4nm grain size used in their work was probably too coarse. Richardson *et al.*(42) then incorporated and expanded on some of their previous work (82) to aid in the numerical calculations of high electric field gradients at the interfaces. JV hysteresis effects were able to be modelled but there were still issues implementing interfacial recombination accurately. The same group updated the model with interfacial recombination included (83) but only in one interface (which was claimed to be a more significant contribution than the other interface). There were still issues with reproducing experimental results, however, arising largely from the fact that these simulations that included ionic charge (often at very high densities) were of single layer devices and did not include ETLs and HTLs formally. Calado *et al.*(41) incorporated mobile ionic charge into a *p-i-n* model in which p-type and n-type regions represented the transport layers, where interfacial recombination was approximated by including high rates of recombination throughout these layers. Neukom *et al.* (84) published results from a comprehensive model using the package SETFOS and a MATLAB based ionic carrier solver combined, verified with a diverse set of reproduced experimental results. Courtier *et al.*(85) and Jacobs *et al.*(86) have published fully coupled, three-layer device models including mobile ionic charge with boundary conditions such that interfacial recombination can be included. The former is freely available and the later uses COMSOL Multiphyics® and MATLAB Livelink™ and both have demonstrated the capability to simulate (and enable the investigation of) a variety of different experimental conditions giving great insight into the underlying physical processes dictating the behaviours of such MHP devices. There are other simulation tools available, including *gpvdm* by Roderick MacKenzie (87) which is a comprehensive open-source simulation tool, written in C, and allows for a variety of semiconducting devices to be simulated including perovskite devices with mobile ionic charge and the ability to set arbitrary trap distributions in the bulk layer (a feature that is often missing in the aforementioned, currently available software).

The simulation software used in this work for perovskite device simulation in this work is Driftfusion (written by a member of my research group, Dr Philip Calado) which is an open-source code for simulating ordered semiconductor devices with mixed ionic-electronic conducting materials in one-dimension (88). This software enables users to model devices with multiple, distinct, material layers using up to four charge carrier species: electrons and holes and up to two ionic species. It is open source but is written in MATLAB so is not entirely freely available. An interesting recent development in this software, which is included in Calado *et al.* (88), is moving from the use of the Boltzmann approximation of the

Fermi-Dirac integral to Blakemore's approximation (89). The Fermi-Dirac integral of order ½ is given by:

$$F_{\frac{1}{2}}(\eta) = \int_0^{\infty} \frac{\xi^{\frac{1}{2}}}{1+\exp{(\xi-\eta)}} d\eta$$

Equation 9

Where the following substitutions have been made:

$$\text{For electrons } \xi = \frac{E - E_C}{k_B T} \text{ and } \eta = \frac{E_{fn} - E_C}{k_B T}$$

$$\text{Or for holes } \xi = \frac{E_v - E}{k_B T} \text{ and } \eta = \frac{E_v - E_{fp}}{k_B T}$$

where E represents the original energy variable for the integral before the substitutions, E_{fn} and E_{fp} are the electron and hole quasi-Fermi energy levels respectively and the other variables have their previously defined meaning. η is therefore the number of k_BT's away from the band edge the quasi-Fermi levels are. Equation 9 has no analytical solution(s) and so we make the approximations. The Boltzmann approximation is well known; for values of $\eta \leq -2$,

$$F_{\frac{1}{2}}(\eta) \approx \exp(\eta).$$

Equation 10

During simulations of devices with high doping concentrations or Ohmic contacts this approximation is no longer accurate since $\eta \geq -2$. In order to widen the range of utility of Driftfusion, the Blakemore approximation is used:

$$F_{\frac{1}{2}}(\eta) \approx \frac{1}{\exp(-\eta) + \gamma}$$

Equation 11

where γ is adjusted depending on the system being approximated – it is a parameter controlling how close to the Boltzmann regime the system is. Generally, for classical 3D semiconductors (and in this work) $\gamma = 0.27$, which was empirically determined by fitting Equation 11 to the numerical calculations of the Fermi-Dirac integral, is used as suggested by Farrell *et al.* (90), yielding good approximations of the Fermi-Dirac integral for $\eta \leq 1.3$. This change to the distribution function also alters the diffusion constant. The gradient of charged particle density with respect to the local potential is the driving-force for diffusion making the diffusion coefficient,

$$D = \frac{\mu k_B T}{q} \frac{F_{\frac{1}{2}}(\eta)}{F'_{\frac{1}{2}}(\eta)}$$

Equation 12

where $F'_{\frac{1}{2}}(\eta)$ is the first derivative of the distribution function with respect to η. All other symbols have their previous meaning. This allows for semiconductors with high levels of doping and Ohmic contacts to be accurately simulated in Driftfusion.

2.4.5.2 Equivalent Circuit Modelling

Modelling with equivalent circuits has its origins in attempts to analyse the electrochemical impedance spectroscopy (EIS) of electrochemical systems, although fitting such data with equivalent circuits is valid for any system being measured in this way. A description of EIS measurements relevant to this thesis is given in section 3.3.4. In essence, EIS allows for the determination of the frequency dependent complex impedance ($Z(\omega)$) of a device/system by taking the ratio of the applied oscillating voltage ($V(\omega)$) and the resulting oscillating current through the system ($I(\omega)$). This is mathematically identical to the way in which a traditional electrical circuit responds to an oscillating voltage and as such, very good approximations of experimentally determined EIS can be made by creating (mathematically) an equivalent circuit and subjecting it to the same oscillations. These circuits could then be used to model other electrical behaviours of the same material system, assuming that the model is well chosen.

EIS and the modelling of it with equivalent circuits is a vast topic on its own. The details of the strict mathematical treatment of this topic, the history of the measurement technique and the choice of many different equivalent circuits is beyond the scope of this thesis. I refer the reader to work by Lasia (91), Kanoun (92), and Macdonald (93,94) for a comprehensive theoretical and experimental review of EIS and equivalent circuit modelling. A very brief summary of the principles of this technique, taken from a combination of the above sources, is given below.

The equations (linear and differential) describing the characteristics of the main passive, linear circuit elements, namely resistance (Ohm's law, $V = IR$), capacitance ($V(t) = \frac{1}{C}\int_0^t I(t)\,dt$) and inductance ($V(t) = L\,\frac{dI}{dt}$), can be solved (either directly or via Laplace transformation) to find the relationship between the voltage applied to the element and the current flowing through it. The result reveals the characteristic impedance of each circuit element: $Z = R$, $Z = \frac{1}{i\omega C}$ and $Z = i\omega L$ for a resistor, capacitor, and inductor respectively where *i* is the imaginary number. If an entire circuit is created, the impedances of each element can then be summed by using Kirchhoff's laws to find the mathematical expression for the whole circuit. The component values in this mathematical expression (*R*, *C* and *L* for example) can be changed (often by some minimization algorithm) to make the impedance expression as close to the obtained experimental EIS data as possible. This set of theory and the analysis process is only relevant to the EIS of material systems when the circuit elements in the equivalent circuit are chosen to represent actual physical processes happening in the material system during the measurement. When this is the case, the values of the circuit elements that reproduce the experimentally determined EIS carry physical significance.

Due to the physical processes underlying their behaviour in a standard electrical circuit, resistors and capacitors represent physical processes of the modelled material system in an equivalent circuit. Examples of the link between the circuit element and a physical process are: (i) resistance represents some limited charge transport and is related to the mobility of a charge passing through a region of the material. (ii) capacitance represents charge separation in either space or chemical potential. If the capacitance is voltage dependent, then a differential capacitance can be use ($C = \frac{dQ}{dV}$). (iii) an inductance represents a resistance to a change in current that may occur if the measured system has a high conductivity and/or a measurement series resistor with very low resistance.

Combinations of resistors and capacitors in parallel and in series can be used to model more complete physical processes. A good example is the combination of resistors and capacitors in series and parallel to represent the dispersion and absorption of dielectrics with a generalized relaxation time (95). If other, well defined circuit elements such as the Warburg element (96) (in its many forms) are used, rather sophisticated systems including mass-transport, adsorption and absorption and corrosion can be modelled.

For the analysis of solar cells, if the system is described by long carrier lifetimes, charge transport and recombination processes can be characterised by EIS and equivalent circuit modelling. In solar cells where these processes are too fast to detect, other device features can be analysed such as doping profiles and doping densities, even the dielectric constant can be characterised. I refer the reader to work by Elizabeth Von Hauff (97) for a more detailed analysis of the EIS of solar cells. In MHP solar cells, this set of analysis is further complicated by their mixed-conductor nature. The high density of slow-moving ionic charge discussed in section 2.4.3 induces a strong frequency dependent impedance in the low frequency regime and further contributes to some very large capacitive and inductive behaviour in the impedance spectra (98–100). These features have previously made the determination of a physically meaningful equivalent circuit quite challenging (101–104) with the inclusion of inductors into equivalent circuits without an obvious physical origin (105,106).

In this thesis, I base my EIS measurement technique and analysis on previous work from our research group by Moia *et al.*(66) where the MHP solar cell interfaces are represented by bipolar transistors that control recombination and injection rates. The transistors are gated by the ionic charge distribution, which represents the trans-carrier amplification that is the cause of many curious features in perovskite EIS data. This circuit can model the inductive and giant capacitance features previously observed in MHP impedance spectroscopy and can reproduce JV hysteresis.

Chapter 3 – Methods

3.1 Declaration of contributions

J.A. Smith[1,2] and O. Game[2] performed the device fabrication method described in section 3.2.1.

C.T. Lin[3] and T.J. Macdonald[4,5] performed the device fabrication method described in section 3.2.2.

B.C. O'Regan[6] designed, coded, and built the original TRACER setup described in 3.3.1.

P. Calado[7] designed and coded the VJL procedure in Igor Pro. He also coded the simulation software, Driftfusion.

X. Xi[7] and D. Moia[8] aided in the design of the unity gain buffer amplifier circuit (Figure 3.1) for the TRACER system.

[1]Department of Physics, Clarendon Laboratory, University of Oxford, Oxford, OX1 3PU, UK

[2]Department of Physics and Astronomy, University of Sheffield, Sheffield, S3 7RH, UK

[3]Department of Materials and Centre for Processable Electronics, Imperial College, London, W12 0BZ UK

[4]School of Engineering and Materials Science and Materials Research Institute, Queen Mary University of London, London, E1 4NS UK

[5]Department of Chemistry and Centre for Processable Electronics, Imperial College, London, W12 0BZ UK

[6]Sunlight Scientific, 1190 Oxford Street, Berkeley, CA, 94707 USA

[7]Department of Physics and Centre for Processable Electronics, Imperial College London, South Kensington Campus, London, SW7 2AZ, UK

[8]Max Planck Institute for Solid State Research, Stuttgart, Germany

3.2 Materials and sample preparation

3.2.1 Single carrier devices investigated in Chapter 4 and Chapter 5

All materials were purchased from Sigma Aldrich unless otherwise stated and used as received. Indium tin oxide (ITO) substrates were etched using Zn and 4 M hydrogen chloride (HCl) and cleaned by sonication in dilute Hellmanex with boiling deionised (DI) water for 15 minutes, rinsed with boiling DI water, sonicated in DI water, rinsed with acetone, and sonicated in isopropyl alcohol (IPA). Substrates were dried with N_2 and UV ozone cleaned for 15 minutes. All fabrication was in a N_2 glovebox with continuous purging. Poly(N,N'-bis-4-butylphenyl-N,N'-bisphenyl)benzidine (PolyTPD - Ossila) solution (1.5 mg ml^{-1} in dichlorobenzene) was spin-coated at 6000 rpm for 30 s (acceleration 2000 rpm s^{-1}) followed by annealing at 100 °C for 10 minutes. Next poly({9,9-bis[3'-({N,N-dimethyl}-N-ethylammonium)propyl]-2,7-fluorene}-alt-2,7-{9,9-di-n-octylfluorene}) (PFN-P2, 1-Material, 0.5 mg ml^{-1} in methanol) was coated at 5000 rpm for 20 s (dynamic dispense). Acetonitrile:methylamine $MAPbI_3$ solution was prepared following the procedure by Noel *et al.*(107), with methylamine gas flowed through a 0.5 M solution with a 1:1 molar ratio of methylammonium iodide (MAI, Greatcell) and lead iodide (PbI_2, TCI) until dissolved. Films were spin-coated at 2000 rpm and annealed at 100 °C for 15 minutes. PTAA solution (10 mg ml^{-1} in toluene) was prepared with additives (per ml) of 4 µl of tBP (4-*tert*-butylpyridine) and 7.5 µl of lithium bis(trifluoromethanesulfonyl)imide (LiTFSI, from a 170 mg ml^{-1} stock solution in acetonitrile) and stirred overnight. The poly[bis(4-phenyl)(2,4,6-trimethylphenyl)amine (PTAA) was then spin-coated at 4000 rpm (dynamic dispense). Devices were completed by thermally evaporating 80 nm of Au (CooksonGold) at 0.1 -1.2 Å s^{-1}. Finally, silicon dioxide (SiO_2, K J Lesker) encapsulation was deposited by e-beam evaporation at 1 Å s^{-1} with a base pressure of 3×10^{-6} mbar. A 150 nm layer was deposited in two 75 nm steps to minimise substrate heating. The active area for each pixel of each device was $0.12\mathrm{cm}^2$.

3.2.2 Solar cells investigated in Chapter 6

The perovskite solar cells were made with a structure of ITO/PTAA/PFN-Br/perovskite/PCBM/BCP/Cr/Au where PCBM is [6,6]-phenyl-C61-butyric acid methyl ester and BCP is Bathocuproine. The perovskites investigated in this study include $MAPbI_3$, $Cs_{0.05}MA_{0.95}PbI_3$ and $FA_{0.05}MA_{0.95}PbI_3$. The ITO glass substrates were cleaned with soap, DI water, acetone and IPA in sequence and then transferred into a UV ozone machine and treated for 10 minutes. The PTAA solution (2 mg/ml in toluene) and PFN-Br solution (0.05 mg/ml in methanol) sequentially are spin-coated on the ITO substrates at 5000 rpm for 20 seconds. After the substrates are dried, the 1.5M perovskite solutions ($MAPbI_3$, $Cs_{0.05}MA_{0.95}PbI_3$ and $FA_{0.05}MA_{0.95}PbI_3$) in DMF: DMSO (dimethylformamide: dimethyl sulfoxide) mixed solvent (ratio 8.9:1.1) are spin-coated on substrates at 4000 rpm for 30 second, and the diethyl ether (0.4 ml) is dripped on the substrate at 10 seconds of the spin-coating process. The films were then annealed at 100°C for 90 minutes. After the substrates cooled down to room temperature, the PCBM (30 mg/ml in chlorobenzene, CB) and BCP (0.5 mg/ml in IPA) are coated on the substrates in sequence. Finally, the 3 nm Cr and 100 nm Au are thermally evaporated on the substrates to finish the devices. The active area for each pixel of each device was $0.045\ \mathrm{cm}^2$.

3.3 Experimental methods

3.3.1 TRACER measurement system

The TRACER (transient and charge extraction robot) is a measurement system allowing for customizable optoelectronic measurements to be performed on devices (108). The system is programmed using the Igor Pro structured programming language, which allows for automated data collection, graphing and analysis. The TRACER system has many capabilities involving illumination from a system of LEDs, which is of great utility but is not the focus of this thesis since all the measurements were performed in the dark. The cell voltage and switch control are supplied by a National Instruments USB-6251 DAQ card with a slew rate of $20\ Vms^{-1}$ which allows for switching times $< 1\ \mu s$ for voltage ranges used in this thesis. Low capacitance metal-oxide-semiconductor field-effect-transistors (MOSFETs) are part of the switching circuit which allows the device to be changed from open circuit, short circuit, and disconnected voltage environments.

3.3.2 JV curves

The JV curves measured using a sweep that are presented in Chapter 4 and Chapter 5 were measured using the TRACER system described in section 3.3.1 using the VJL (voltage current-density light control) procedure. None of the measured JV curves in these two chapters are illuminated.

To supply the required current for the devices investigated in the SCLC measurements of Chapter 5, a unity gain follower amplifier circuit was made and inserted into the TRACER system between the DAQ (data acquisition) card and the measured device. Design considerations included operational amplifier capabilities, ensuring unity gain, relatively good signal to noise ratio, high enough bandwidth, and the capability to drive a capacitive load. Capacitive loads induce a frequency dependent response of the output of operational amplifiers and without correct compensation, one can find oscillations in the feedback loop. All solar cells have a certain capacitance to them so the circuit would need to be able to cope with a range of capacitive loads that can change between solar cells. The circuit is represented in Figure 3.1.

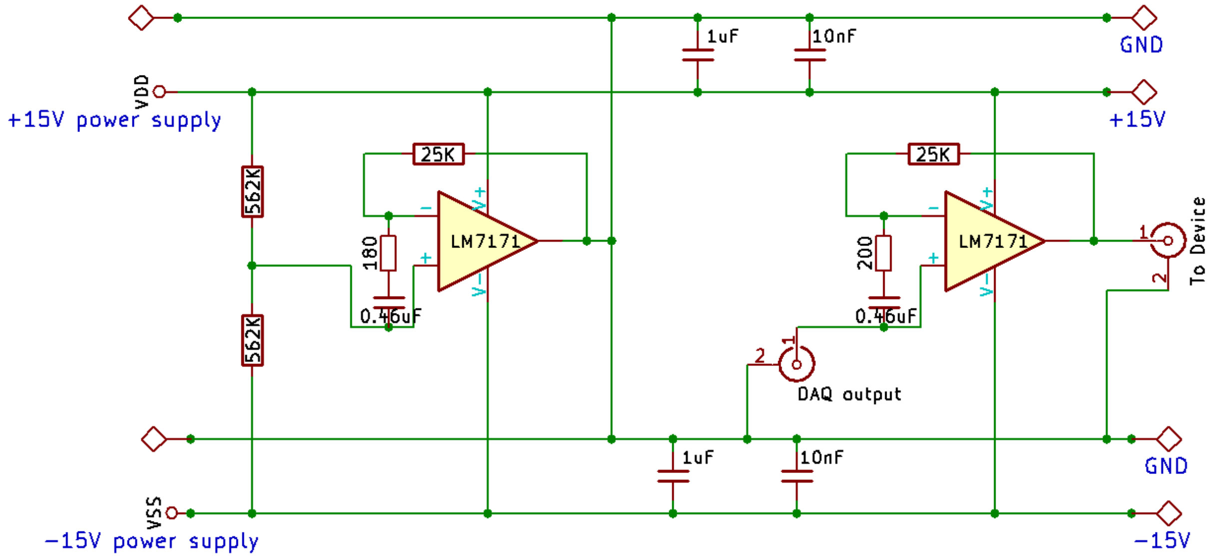

Figure 3.1 A circuit diagram for the unity gain buffer amplifier circuit used to increase the maximum current capability of the TRACER measurement system during the measurement of JV curves. The circuit elements were chosen to improve the performance of the system under a capacitive load.

The operational amplifier LM7171 was chosen as it is a very high speed, high output current, voltage feedback amplifier which is also unity gain stable. The $25\ k\Omega$, $200\ \Omega$ and $180\ \Omega$ resistors and $0.46\ \mu F$ capacitors were all included for the main purpose of stabilizing the operational amplifiers to capacitive loads whilst ensuring a high enough bandwidth.

The JV curves presented in Chapter 6 were measured using an Ivium CompactStat potentiostat on the CV scan measurement protocol. The specific scan parameters are given in the captions of each set of results that are presented. Any illumination of the solar cells in Chapter 6 is provided by a ring of white LED rings whose intensities are roughly calibrated to a solar simulator, but the efficiencies and fill-factors of the solar cells are not calculated due to the lack of known illumination intensity.

3.3.3 Pulsed voltage technique

For the JV results in Chapter 4 and Chapter 5 obtained using the so-called puled voltage method, the measurements were made with the TRACER system described in section 3.3.1.

A bespoke measurement protocol was written in Igor Pro, utilizing the VJL procedure already in place and the voltage buffer circuit described in section 3.3.2. The device being measured is set to a certain equilibrium state by applying a pre-bias voltage, $V_{pre\text{-}bias}$, for a long time (10s of minutes). Subsequently, a very short voltage pulse is applied, during which the current is measured, before returning to $V_{pre\text{-}bias}$. This process is repeated for a series of voltage pulses and is depicted in Figure 3.2a. The pulse duration (t_{pulse}) was set to 500 μs and the pre-bias time (t_{bias}) to 600 s. To extract the current density due to each voltage pulse, a linear fit was performed in MATLAB to the current density transient for $50\ \mu s < t_{pulse} <\ 250\ \mu s$ and, by extrapolation, a value for the instantaneous current density at $t_{pulse}\ = 0\ s$ was found. This process is demonstrated for four different voltage pulses in Figure 3.2b The series of probe voltages and the associated current densities are then plotted to create a JV curve.

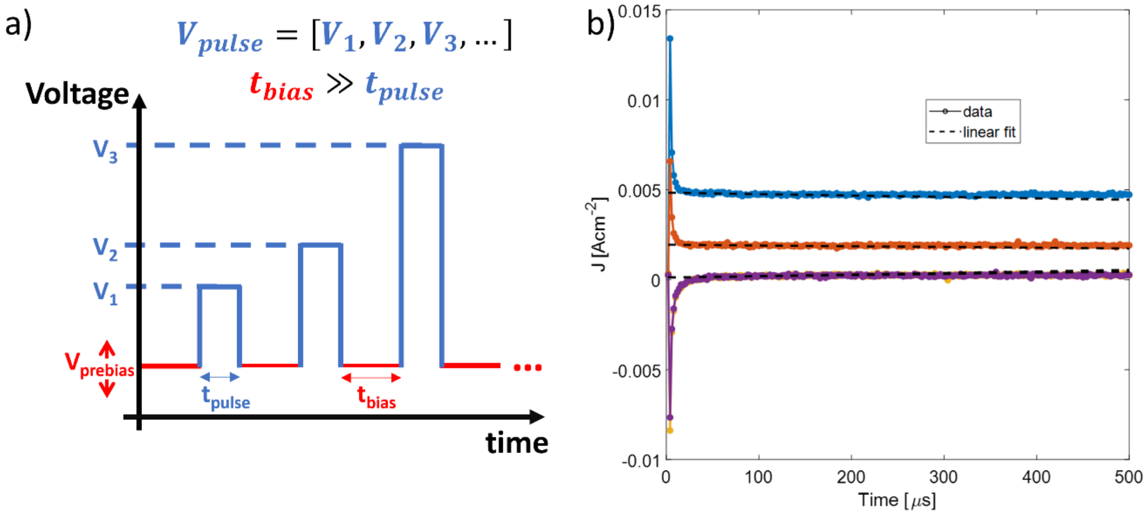

Figure 3.2 The pulsed-voltage measurement procedure, detailing the successive application of voltage and the method for finding the current density. a) A cartoon representing the measurement protocol the pulsed voltage technique of determining the JV of a device. b) An example of current transients at four separate probe voltages (two negative and two positive). The dotted lines represent the linear fits to the data at times immediately after the capacitive response. The instantaneous current density (excluding the capacitive component) is then inferred from the linear fit at t = 0 s. This is then plotted against V_{pulse} from a).

3.3.4 Electrochemical impedance spectroscopy

Impedance measurements presented in Chapter 6 were performed using an Ivium CompactStat. All impedance measurements were performed with a sinusoidal voltage perturbation of amplitude 20 mV to a solar cell held at 0 V DC. The frequency of this perturbation was varied successively from 1 Hz to either 500 kHz or 1 MHz, an averaging setting in the Ivium software was used that takes the average of 30 impedance measurements at each frequency. The impedance spectroscopy measurement was performed after a stabilization at 0 V of 600 s using the chronoamperometry technique, ensuring the signal was stable before each impedance scan.

3.4 Device modelling

3.4.1 Drift-diffusion simulations

Device simulations are carried out using the open-source simulation code Driftfusion. This code allows for the simulation of semiconductors with electronic and ionic conduction and is introduced in 2.4.5.1. Details of the code, reasoning for the choices made in its construction and its capabilities can be found in Calado *et al.*(88). Here, a brief summary of some of the functions and simulation techniques used in this thesis is given.

3.4.1.1 Finding the device's equilibrium condition

This process is outlined in Calado *et al.*(88) but is included here for clarity. The device starts with a set of initial conditions and runs through several steps to find the equilibrium solutions. The equilibrium solutions take the form of the potential energy profile and the charge carrier densities as a function of position given no flow of energy or mass in or out of the defined system. For the devices simulated in this work without any semiconducting layers in addition to the perovskite layer, a linearly varying electrostatic potential, exponentially varying electronic carrier densities and a uniform density of anions and cations over the layer thickness are used for the initial conditions. These conditions ensure the boundary conditions are satisfied.

For the entire device (multi-layered) simulations the initial conditions are different in that the electronic carrier densities are set to the equilibrium densities of the individual layers (defined by the set fermi level/doping density). This ensures the boundary conditions are satisfied. The equilibrium solution process is the same as for single layer devices.

If an equilibrium condition needs to be found after a pre-bias voltage, the function jumptoV() in Driftfusion is used to find the device's new equilibrium solution under the applied bias.

3.4.1.2 Simulating JV sweeps

Driftfusion has a built-in function for simulating JV sweeps called doJV(). This allows for the forward and reverse sweeps of a JV to be simulated with the scan rate, start and end voltages, illumination intensity and the initial condition of the device all being definable parameters in the simulation function. This function is used throughout this thesis to simulate the JV response of a device to a smoothly varying applied voltage.

3.4.1.3 Simulating pulsed voltage JV curves

In order to simulate the pulsed voltage method described in Chapter 4, Chapter 5 and section 3.3.3, the function jumptoV() is used to simulate a pre-bias voltage, which jumps to a new applied voltage and stabilises the cell at the new voltage for a user-defined time period or until the cell has reached a new equilibrium. This stabilized solution is then used as the initial condition of the device in a JV sweep using doJV() with the ion mobility set to zero.

3.4.1.4 Calculation of conductance per unit area

The conductivity of a semiconducting material is given by $\sigma = q\left(\mu_n n + \mu_p p\right)$. In Driftfusion, the solution produces *n* and *p* as functions of position (on a nonlinear grid-mesh) *x*. The conductivity is therefore calculated as a series of elements at each point in the grid which need to be added in series to obtain the total conductivity. To obtain the total conductivity as a function of *x*, it needs integrating over the whole device thickness. Conductivity is then converted to conductance per unit area as above such that:

$$\frac{G}{A} = \frac{1}{\int_0^L \frac{1}{q\left(\mu_n n(x) + \mu_p p(x)\right)} dx}$$

Equation 13

I show in figure E.3 that the result of this calculation is exactly equivalent to finding the gradient of a simulation of the JV curve close to 0 V when the charge trap density is much lower then the electronic charge density.

In a multi-layered device the conductance per unit area of the whole device is calculated using the same method only while additionally summing the contribution of each transport layer in series using the defined mobility for each layer.

3.4.2 Equivalent circuit modelling

As described in section 2.4.5.2, the equivalent circuit used in this work is based on the work of Moia *et al.* (66), using the approximation circuit given for the 0 V in the dark conditions, where recombination dominates the electrical characteristics of the solar cell (and the ideality factor is set to 1 under these 0 V conditions). This circuit is then further updated to the circuit presented in Figure 3.3 and Figure 6.2c, where the geometric capacitance has been broken down into the geometric contribution from the bulk perovskite of the solar cell and the partial contribution of the ionic capacitances.

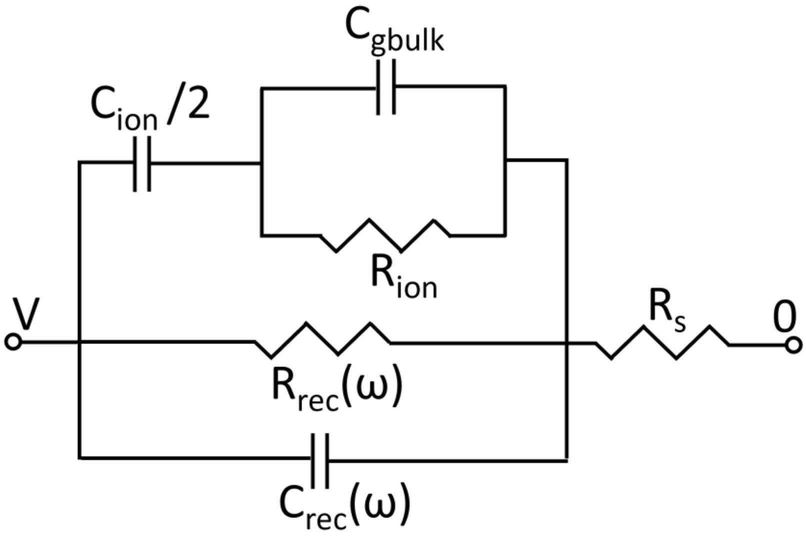

Figure 3.3 The equivalent circuit used to model the MHP solar cell dark, 0 V EIS data presented in Chapter 6. The top circuit branch represents the purely ionic components to the total impedance of the device, the lower branches represent the electronic impedances that are coupled to the ionic branch. R_{ion} is the ionic resistance, C_{ion} is the capacitance of each interface due to ion accumulation (here the interfaces are treated as identical and summed into one component), C_{gbulk} is the MHP bulk contribution to the device's geometric capacitance, $R_{rec}(\omega)$ and $C_{rec}(\omega)$ are the recombination resistance and capacitance respectively and R_s is the series resistance.

This equivalent circuit is fit to the experimental data by writing a mathematical representation of the device impedance in MATLAB – the impedance of the equivalent circuit in Figure 3.3. This model is then tested by calculating the impedance with a set of initial input parameters (estimates) at every experimentally used frequency and finding the sum of the difference between each data-point and this initial estimates. As suggested in Moia *et al.*(66), the estimates are extracted from the impedance data itself, $C_{ion}/2$ is estimated from the low frequency end of the capacitance *vs* frequency plot and C_g from the high frequency end, R_{ion} is then estimated by finding the frequency of maximum imaginary impedance in the ionic semi-circle of the Nyquist plot and using the approximation $\omega_{ionic} \approx \frac{1}{R_{ion}Cion}$. A minimization function is then used to vary each input parameter such that the difference between the model and the experimental data in minimized. The values of the parameters at this final solution are determined as representative of the physical system. The equation for the impedance of the equivalent circuit in Figure 3.3 is:

$$Z = R_s + \left(\frac{1}{Z_{rec}} + \frac{1}{\left(\frac{1}{\left(i\omega C_{gbulk} + \frac{1}{R_{ion}} \right)} + \frac{2}{i\omega C_{ion}} \right)} \right)^{-1}$$

Equation 14

Where $$Z_{rec} = \left(\frac{1}{R_{rec}} + i\omega C_{rec} \right)^{-1},$$

$$C_{rec}(\omega) = \left(\frac{C_{ion}R_{ion}}{4 + \omega^2 R_{ion}^2 \left(2C_{gbulk} + C_{ion}\right)^2} \right) \frac{qJ_{rec}}{k_B T}$$

$$R_{rec}(\omega) = \left(\frac{4 + \omega^2 R_{ion}^2 \left(2C_{gbulk} + C_{ion}\right)^2}{2 + \omega^2 R_{ion}^2 \left(2C_{gbulk} + C_{ion}\right)\left(C_{gbulk} + C_{ion}\right)} \right) \frac{k_B T}{qJ_{rec}}$$

and $$\frac{1}{C_g} = \frac{1}{C_{gbulk}} + \frac{2}{Cion}$$

The derivation of Equation 14 and the derivation of C_{rec} and R_{rec} using the method set out by Moia *et al.* (66) are given in Chapter 8Appendix H. J_{rec} is the size of the recombination current (assumed to be the main contribution to current flowing through the device during EIS in the dark at 0 V). With the set of equations, the built-in MATLAB minimization function fmincon() is used to vary the input parameters $C_{ion}, C_g, R_{ion}, R_s$ and J_{rec}, then calculate C_{gbulk} and fit the data to Equation 14. The fit tolerances need to be set very fine, otherwise incorrect solutions that appear as mathematical local minima will be found rather than the true solution.

Chapter 4 – The Interfacial Doping Effect in Perovskite Devices

4.1 Declaration of contributions

Joel A. Smith[1,2] and Onkar Game[2] performed the device fabrication for the device measured in this chapter, the method is described in section 3.2.1.

Philip Calado[3] wrote the simulation package Driftfusion and aided in the interpretation of the data.

Piers Barnes[3] aided in the design of the study and the interpretation of the data.

[1]Department of Physics, Clarendon Laboratory, University of Oxford, Oxford, OX1 3PU, UK

[2]Department of Physics and Astronomy, University of Sheffield, Sheffield, S3 7RH, UK

[3]Department of Physics and Centre for Processable Electronics, Imperial College London, South Kensington Campus, London, SW7 2AZ, UK

4.2 Abstract

Controlling the conductivity of semiconductors is of central importance for the design of electronic devices and is typically achieved by incorporating static ionising dopants into the semiconductor lattice to tune the concentration of electronic charge carriers. Here I demonstrate a new approach to control the conductivity of semiconductors containing mobile ionic defects (such as metal halide perovskites) through choice of interfacial contact materials and voltage pre-biasing. Using drift-diffusion simulations and conductivity measurements I show that the contact workfunctions, the semiconductor layer thickness, and voltage pre-biassing, control the equilibrium (and operational) distribution of mobile ionic charge in the perovskite. Accumulation or depletion of ions at the interfaces that screen potential differences result in a corresponding depletion or accumulation of ions in the bulk of the semiconductor. The change in ionic charge distribution is compensated accordingly by electronic carriers leading to orders of magnitude variation in the bulk semiconductor, and whole device, conductivity analogous to what can be achieved by traditional semiconductor doping. This effect can be viewed as related, but distinct from, the changes in interfacial resistance caused by mobile ions leading to hysteresis also seen in perovskite devices. Our observations help to explain the wide variation in conductivities

measured in undoped perovskite materials and indicate a new set of characteristics that can be considered in the applications of MHP devices.

4.3 Methods

4.3.1 Conductance vs conductivity

To demonstrate the effect interfacial doping in this chapter, we have calculated either the conductivity (σ [$\mathrm{Scm^{-1}}$]) or the conductance per unit area (*G/A* [$\mathrm{Scm^{-2}}$]) of the device. The calculation of σ instead of *G/A* occurs when the device thickness is being varied, since σ is a property of the material and

$$\sigma = \frac{GL}{A}$$

Equation 15

where *L* is the thickness of the device, the gradient of a $\sigma\ vs\ L$ graph is meaningful. In devices where *L* is fixed, *G/A* is calculated because this is equivalent to the gradient of the low voltage region of a current density *vs* voltage (JV) curve:

$$\frac{G}{A} = \frac{J}{V}$$

Equation 16

The conversion of *G/A* to σ is simply to multiply by L.

4.3.2 Simulation

Driftfusion in used to simulate devices in their equilibrium condition or after a pre-bias voltage as described in section 3.4.1.1. In cases where a pre-bias voltage has been applied the contribution of injected electronic charge from the applied voltage in removed. This is achieved by using the pre-bias solutions as the initial condition for a JV scan starting from the pre-bias voltage and ending at 0 V with the ionic charge mobility set to zero. The conductance of each solution is then calculated using the method described in section 3.4.1.4. In this way, all the calculated conductance per unit area values are a representation of the change in device conductance due to the change in ion distribution in response to an applied voltage and all values are directly comparable.

The parameter search investigations are carried out by a series of loops in a MATLAB script in which the equilibrium calculations and other analyses are carried out successively. These are then plotted using the surface plot function available in MATLAB

4.3.3 Experimental determination of the change in device conductance due to $V_{pre\text{-}bias}$

The JV curve of the measured device was determined using the pulsed voltage technique (section 3.3.3) but changing the value of $V_{pre-bias}$for each curve. The range of voltage pulses used was $-0.5\ V \rightarrow 0.5\ V$. The region of each curve close to 0 V was then fitted to a straight line using the MATLAB fitting function fit(). The gradient of this straight line is the conductance per unit area.

4.3.4 Estimation of errors in the experimentally determined conductance values

During the procedure of determining the conductance of a device using the pulsed voltage technique (section 3.3.3), MATLAB's built in fitting functions fit() and fmincon() were used to fit linear functions to extract values from data. Neither function allows for uncertainties to be input or for errors on determined parameters to be produced. Instead, fitting quality metrics can be produced and confidence intervals for parameters can be produced. This does not easily lend itself to propagating uncertainties through the fitting procedure (given the low tolerances set) and so, an approach of best judgement combined with calculations is used instead.

The error in the calculation of the y-intercept of the linear fit of the current density and voltage transients (the values of current density and voltage at t=0) was, therefore, estimated. The linear fit had fitting function and step tolerances set at 10^{-10} and the spread of current density and voltage points around the linear fit was $J_{spread} \approx 5 \times 10^{-5}\ Acm^{-2}$ and $V_{spread} \approx 7 \times 10^{-4}\ V$ respectively. The error on the calculated J(t=0) and V(t=0) points was, therefore, estimated as $\pm 2 \times 10^{-6} Acm^{-2}$ and $\pm 5 \times 10^{-4} V$ respectively. Applying these values to each point in the JV, a 'worst case linear fit' was performed by taking points at the extremes of the error bars and the difference to the actual fit was calculated. This was done via the resistance values determined i.e. $R_{error} = |R_{fit} - R_{worst-case}|$. This technique was used on all JV curves at each $V_{pre\text{-}bias}$ and averaged to find one error that applies to all resistances determined using this method. This error was then rounded up to $\pm 1500\ \Omega cm^{-2}$. This was likely to be a large overestimate of the error.

Finally, since $\frac{\sigma G}{G} = \frac{\sigma R}{R}$ the error in the calculated conductance is $\sigma G = \frac{\sigma R}{R^2}$.

4.4 Introduction

Due to their apparent defect tolerance, tuneable bandgap, high absorption coefficient and high charge carrier mobility, metal halide perovskites are a semiconducting material class of considerable interest for applications including solar cells(17,109), photodetectors(110), light emitting diodes(111), and memristors(112). Measurements and characterization of these metal halide perovskite devices are confounded by features introduced by the presence of high concentrations of mobile ionic defects within the crystal lattice such as JV curve hysteresis (54), complicating the analysis of impedance spectroscopy (66) and reducing the amount of charge extraction at device interfaces (113) among others. These complications are caused by the ionic charges redistributing and significantly impacting the internal electric field profile of the perovskite, altering the optoelectronic properties. The relative densities of the ionic and electronic charge have also been found to be important when characterising the properties of the electronic charge in these materials (114,115). Given the wide variety of compositions and the array of devices possible, there is great interest in improving the understanding of the factors controlling the electronic charge densities in these devices, which is clearly influenced by the mobile ionic defects under certain conditions.

A very common approach to alter the densities of electronic carriers in a semiconducting material is to dope it. The meaning of the term “doping” is broad and applies to many separate processes but in general it implies that an additive (something that strays from the usual, stoichiometric material composition) changes the electronic properties of the material, either by altering the charge carrier densities, improving the charge transport properties, or altering the defect structure in some way. Traditional forms of doping in semiconductors and their uses are discussed in sections 2.2.1 and 2.2.2. Strictly, the traditional extrinsic impurity type of doping has not been observed in metal halide perovskites, rather the changes in Femi level with respect to the band-edges have been induced by altering the ratio of the reactants in the formation of the perovskite (116–118) or by reducing the density of intrinsic iodine vacancies with atmospheric iodine, varying the partial pressure.(119,120) This form of doping is claimed to act via the modification of defect densities, altering the "charge balance" in the perovskite. Analogously, variation in uncompensated oxygen defect densities is considered to be a primary mechanism for changing the electronic conductivity of metal oxides such as TiO_2(121). Forming a homogeneous *p-n* junction, however, is problematic because a high density of mobile ionic charge would screen the field produced by the doped layers(122). Many other forms of "doping" have been reported in perovskites, where some extrinsic cationic species is introduced into the crystal lattice including Na^+, K^+, Al^{3+}, Co^{2+}, Mg^{2+}, Sr^{2+} and Ca^{2+}. The addition of these extrinsic defects generally improves the perovskites crystallinity and grain size and, therefore, reduce trap state/defect density (Al^{3+}, Na^+, K^+, Ca^{2+}) (123–126). Whereas others can alter the device energetics (Co^{2+})(127) and move the Fermi level relative to the band edges by interacting with the material's defects (Mg^{2+}, Sr^{2+})(128).

In systems with both ionic and electronic charge present, other types of doping processes can occur. Electrochemical doping (129–131) is usually a process by which a system of a certain type of conductive polymer and a suitable electrolyte are in contact, each with their own electrode. The polymer can oxidise (p-type dope) or reduce (n-type dope) when a potential is applied across the electrodes and an ion simultaneously moves from the electrolyte into the polymer to balance the charges. For example, if an electron is removed from polymer via the contacting electrode a negative ion from the electrolyte will move into the polymer to balance the change in charge, leaving the polymer with a deficit in electrons (p-type doping) and has, therefore, been oxidised. Although some of the processes discussed in this chapter are conceptually similar, this process of ionic charge leaving/entering a perovskite device in order to compensate for electronic charge is yet to be demonstrated explicitly. Another example of ionic doping is heterogeneous doping (132,133) which is a doping effect with its origin at interfaces of certain materials; a "higher dimensional defect" (an interfacial state or a dislocation, for example) leads to a variation in defect concentrations which, in turn, lead to a variation in the concentration of other charged species in the material. An example of this doping type has been demonstrated in perovskites by Kim *et al.*(134) where an excess of positive ionic charge at the interfaces with Al_2O_3 and TiO_2, possibly due to cation adsorption from the perovskite to the metal-oxide, leads to a local depletion of holes and other positive defects (such as iodide vacancies, $V_i^{'}$). This effect could occur at interfaces with other materials, specifically other metal oxides and cause the same changes in the relevant electronic charge density in the interfacial region.

In this chapter, I demonstrate that the accumulation or depletion of ionic charge at perovskite device interfaces form in response to a space-charge potential or built-in potential, altering the energetic landscape of the entire perovskite layer and thus, changing the electronic charge densities in the perovskite (compared to an ion-free device) and the conductivity. I show that this effect can be controlled by modifying the work functions of contact materials or by applying bias voltages, to vary the background concentration of ions in the bulk of the perovskite layer, and consequently to modify the density and distribution of the electronic charge carrier which has the same sign as the dominant ionic species. In other words, the state of ionic accumulation at the interfaces effectively changes the doping state of the bulk of the perovskite material, and thus its conductivity. I refer to this process as interfacial doping.

To study this effect, I use drift-diffusion simulations (using our modelling package, Driftfusion (88)) to analyse the effect of several device and material properties on the conductive state of the equilibrium solution of the metal halide perovskites in the dark, both with and without an applied voltage. Since the doping state of a device has significant effects on the current density *vs* voltage (JV) characteristics of a device, particularly in the low voltage regime, I attempt to verify the findings through measurements of the JV curves in the low voltage regime, thus replicating the findings of the simulations. To overcome the problems related to dynamic equilibration of mobile ionic charge during a slow JV scan and the capacitive contributions to current during a fast JV scan, I have developed a pulsed-voltage technique to measure JV curves similar to that used by Duijnstee *et al.*(65,135) The technique allows the state of the device to be preconditioned with a set background bias voltage, and the JV characteristics of the device in this state to be determined without significantly perturbing the device from that state. These findings reveal a new dimension to be exploited in device design and in applications in which the ionic charge can be manipulated to control the conductivity.

Before presenting the results of our calculations and measurements I begin by describing the physical processes that result in the interfacial doping the effect for a semiconductor layer with and without mobile ionic charge carriers. The final thermodynamic equilibrium conditions and electronic carrier densities in the semiconductor depend on whether charged mobile ionic defects compensated by oppositely charged static defects are present.

In section 2.2.4.2, the equilibration of an intrinsic semiconductor-metal junction without ions is described in more detail, here I provide a summary for the sake of clarity. Consider the thermodynamic equilibration of an intrinsic semiconductor layer sandwiched between two metal electrodes where the Fermi-level (E_F) is exactly in the middle of the band-gap (Figure 4.1a). Most metal halide perovskites are thought to be prepared close to an intrinsic state, but I have also calculated results including intentional static ionic dopants. In this device the

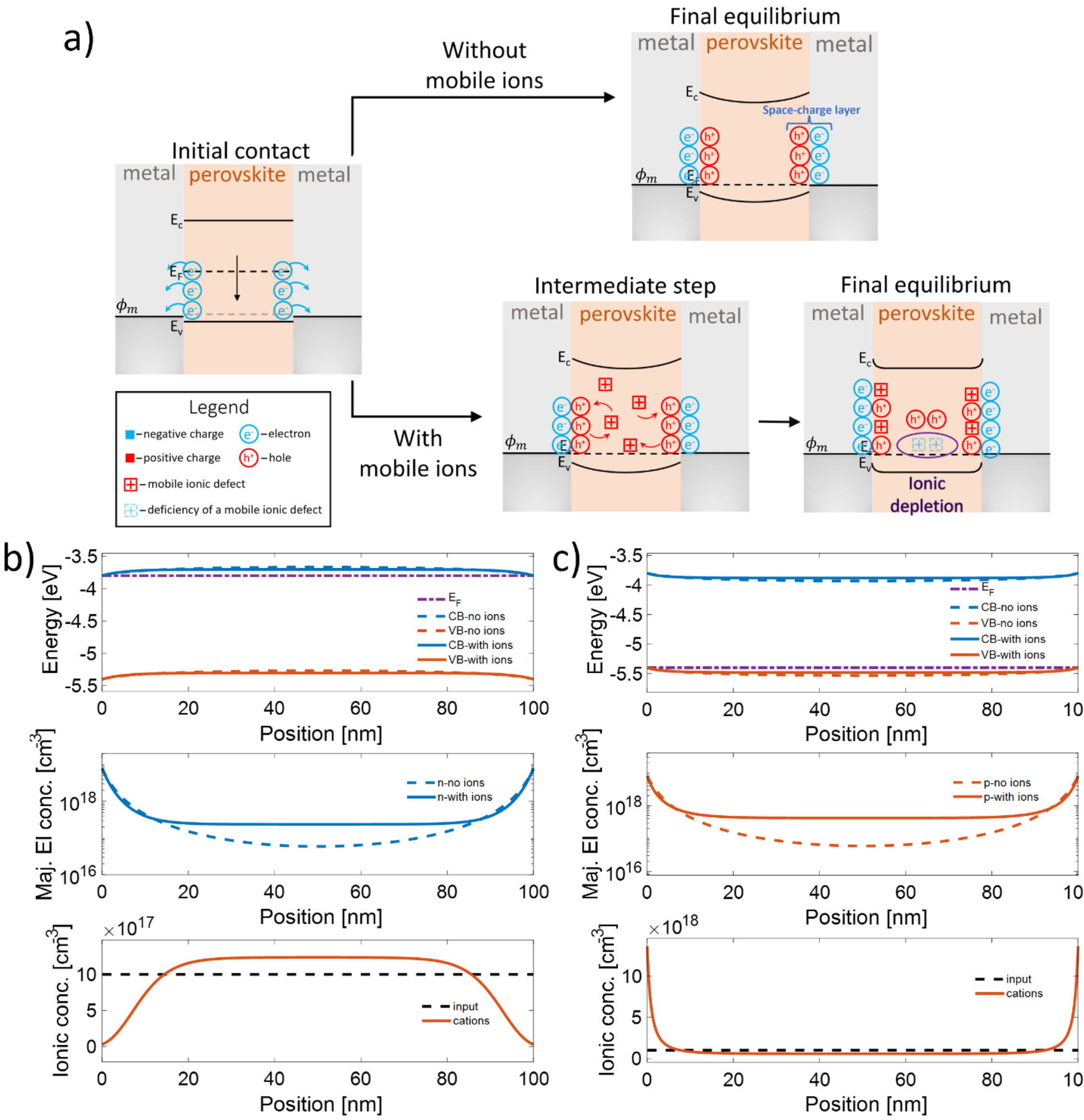

workfunction of the metal contacts have a Fermi energy close to the valence band energy of the semiconductor.

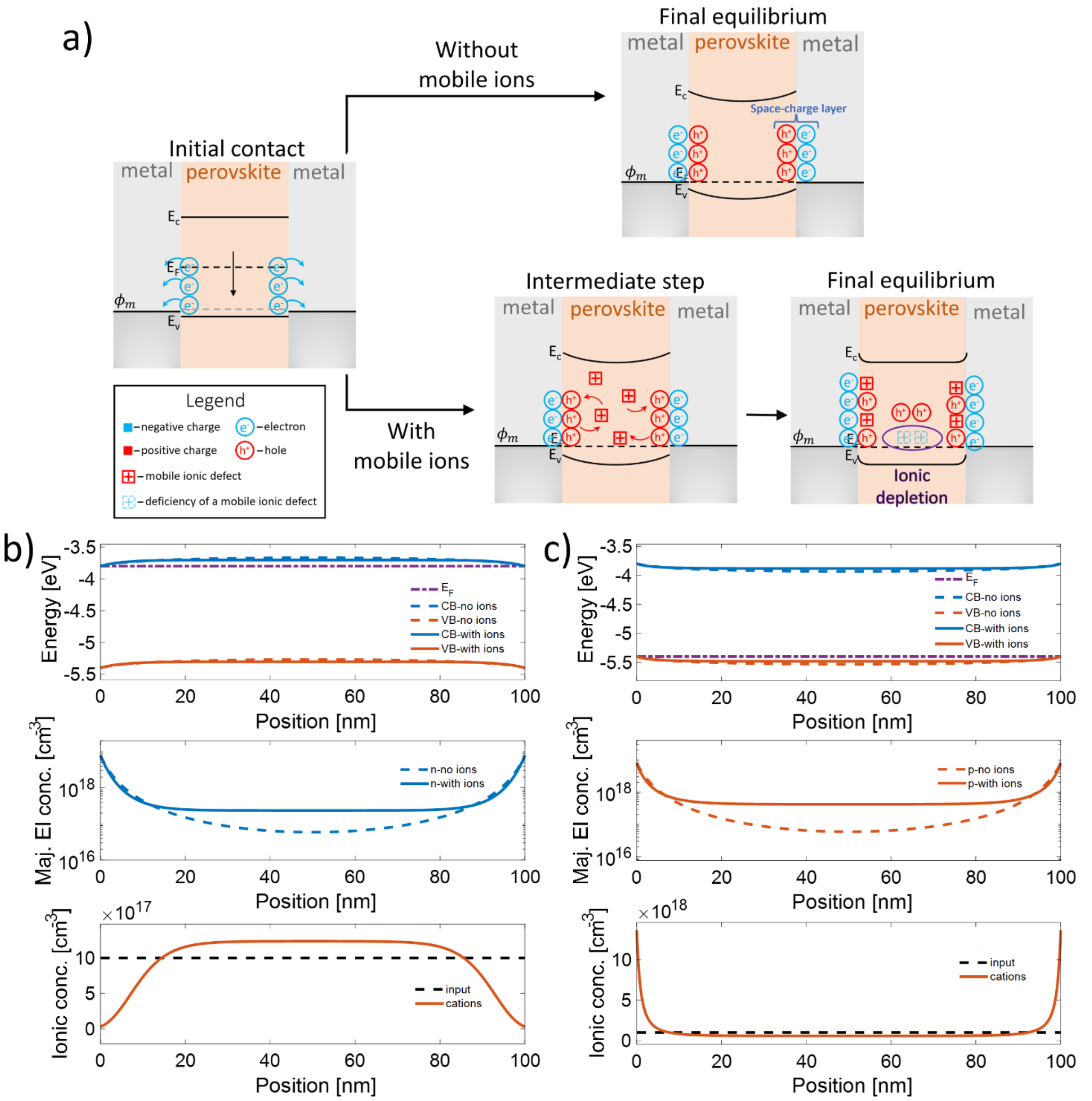

Figure 4.1 A cartoon and simulations to explain the mechanism of the interfacial doping effect. (a) A cartoon detailing the motion/distribution of charged species in devices with/without ionic charge where E_C and E_V are the conduction and valance band edges respectively, E_F is the semiconductor's fermi-level and ϕ_m is the workfunction of the metal. (b) The equilibrium condition of an electron device with $\phi_{offset} = 0\ eV$ (see Equation 17 for definition) with and without one positively charged ionic species with density $10^{18}\ cm^{-3}$. The energy level diagram, majority charge carrier density and ion density are shown in the

subplots respectively. (c) The equivalent of (b) for the equilibrium condition of a hole device with $\phi_{offset} = 0\ eV$ and one positively charged ionic species with density $10^{18}\ cm^{-3}$.

Once the metals contact the perovskite the electrons, holes, and mobile ionic charge must redistribute in the system to align the Fermi levels to attain thermodynamic equilibrium. At a conventional semiconductor-metal interface a region of electronic charge accumulates (the semiconductor's space-charge charge layer), this may also include a surface dipole or charge trapped in surface states. The interface of semiconductors with metals is discussed in section 2.2.4, a summary is provided here for clarity. This process is displayed in the top branch of Figure 4.1a and results in a layer depleted of electrons with holes accumulated by the interfaces where the space-charge extends throughout the layer. In this example the electrons have left the device during the equilibration of the Fermi levels, leaving behind a hole space-charge layer in the semiconductor at the interface with the contacts. The electrostatic potential distribution and the electric field distribution in the semiconductor are then defined by this space-charge. If a semiconducting material is a mixed conductor (with both ionic and electronic carriers) where the ionic charge carriers are confined to the semiconductor layer, then ionic charge responds to the change in internal electric field during equilibration at a rate that depends on the relative mobilities of the electronic and ionic charge. In MHPs, the ionic charge has a mobility that is many orders of magnitude smaller than the electronic charge, but the density of ionic carriers may be comparable or greater than the electronic charge. Thus, the ions will redistribute slowly after the initial redistribution and interfacial transfer of electronic charge responding to the space-charge field, drifting to or from the interfaces depending on their sign displacing electronic charge until a new equilibrium is reached. If the density of mobile ions is large its redistribution will ultimately dominate the electrostatics of the device drastically altering the curvature and magnitude of the electrostatic potential relative to the no mobile ion case. This process is depicted in the bottom branch of Figure 4.1a where one positively charged mobile ionic species is considered (compensated by a uniformly distributed static negative ionic species which is not shown). This is an entirely different process to the *p-n* junction and Schottky barrier formation described in sections 2.2.2 and 2.2.4.1 respectively because the defects in this example are mobile and there is no charge carrier depletion in the space-charge region. The physical processes and driving forces are all shared.

4.5 Results and discussion

Figure 4.1b and Figure 4.1c show simulated energy level diagrams as a function of position *x* for the equilibrium conditions described above (see simulation details in section 3.4.1 and Table A.1 for key simulation parameters) for two metal-halide perovskite devices with different contacts. In each case, the simulations were repeated with and without one positive mobile ionic charged species with a density of $10^{18}\ cm^{-3}$. The devices have symmetrical contacts with no workfunction offset, $\phi_{offset} = 0\ eV$:

$$\phi_{offset} = |E_{BE} - \phi_m|$$

Equation 17

where E_{BE} is either the conduction band edge energy, E_c (Figure 4.1b) or the valence band edge energy, E_v (Figure 4.1c) of the semiconductor and ϕ_m is the workfunction of the metallic contact. When $\phi_{offset} = 0\ eV$ the contact is deemed Ohmic (as described in section 2.2.4.4) since there is no injection barrier between the contact and the energy band of the perovskite. In cases where the device has contact asymmetry, the contacts will be addressed individually (eg. $LHS\ \phi_{offset}$ and $RHS\ \phi_{offset}$). If there is no reference to individual contact energetics, the device has symmetrical contact energetics. The energy levels, electronic and ionic charge densities are displayed in each of the sub-panels respectively.

The results of these simulations are consistent with the process described by Figure 4.1a: The ionic species is shown to accumulate/deplete in the interfacial region (Figure 4.1b and Figure 4.1c bottom sub-plot) in a similar way to electronic charge and the space-charge regions are thinner since there is more charge in the space-charge regions when ions are present. I note that in devices where the ionic charge depletes at the interface (Figure 4.1b, bottom sub-plot), due to the space-charge region being oppositely charged to the ionic species, the space charge layer is wider than the case where the ionic charge has the same charge as the space-charge region (Figure 4.1c, bottom sub-plot). The reason is that the ionic charge can accumulate to much higher concentrations than it can be depleted (limited by zero remaining carriers). The second subplots in Figure 4.1b and Figure 4.1c show the charge densities in the cases for semiconductors with and without ionic charge. In both cases the distribution of electronic charge changes as a result of the change in electrostatic potential following Poisson’s equation and the amount of electronic charge in the device also changes. In the bulk of the device the majority charge carrier density increases, due to the presence of ions, by more than one order of magnitude and the minority carrier reduces in density also by more than one order of magnitude. The opposite happens in the space-charge region, but to a lesser extent. This increase in electronic charge density in the bulk is due to the decreased space-charge layer width and the decrease in electrostatic potential in the bulk, creating an energetic environment that allows more charge to be in the device at equilibrium. This is displayed in Figure 4.2 where the electrostatic potential and electric field distributions of simulated devices at their equilibrium state are shown. These results are for hole devices (Figure 4.2a and Figure 4.2b) and electron devices (Figure 4.2c and Figure 4.2d) with Ohmic contacts and no or $10^{18}\ cm^{-3}$ positive mobile ionic charge. I observe a decrease in the width of the interfacial space-charge region due to the addition of ionic charge (from 10.8 nm to 3.9 nm), this decrease is lower when the ionic charge and majority charge carrier have opposite signs (10.8 nm to 4.9 nm). Additionally, the ionic charge flattens the profile of the electrostatic potential and significantly lowers its magnitude in the bulk. This effect is also observed in the electric field profile where the bulk contains no electric field in the presence of ions. The net effect of these changes is an increase in conductivity of the device, and this is what I refer to as the interfacial doping effect. I now present investigations into the parameters that vary the magnitude of the interfacial doping effect.

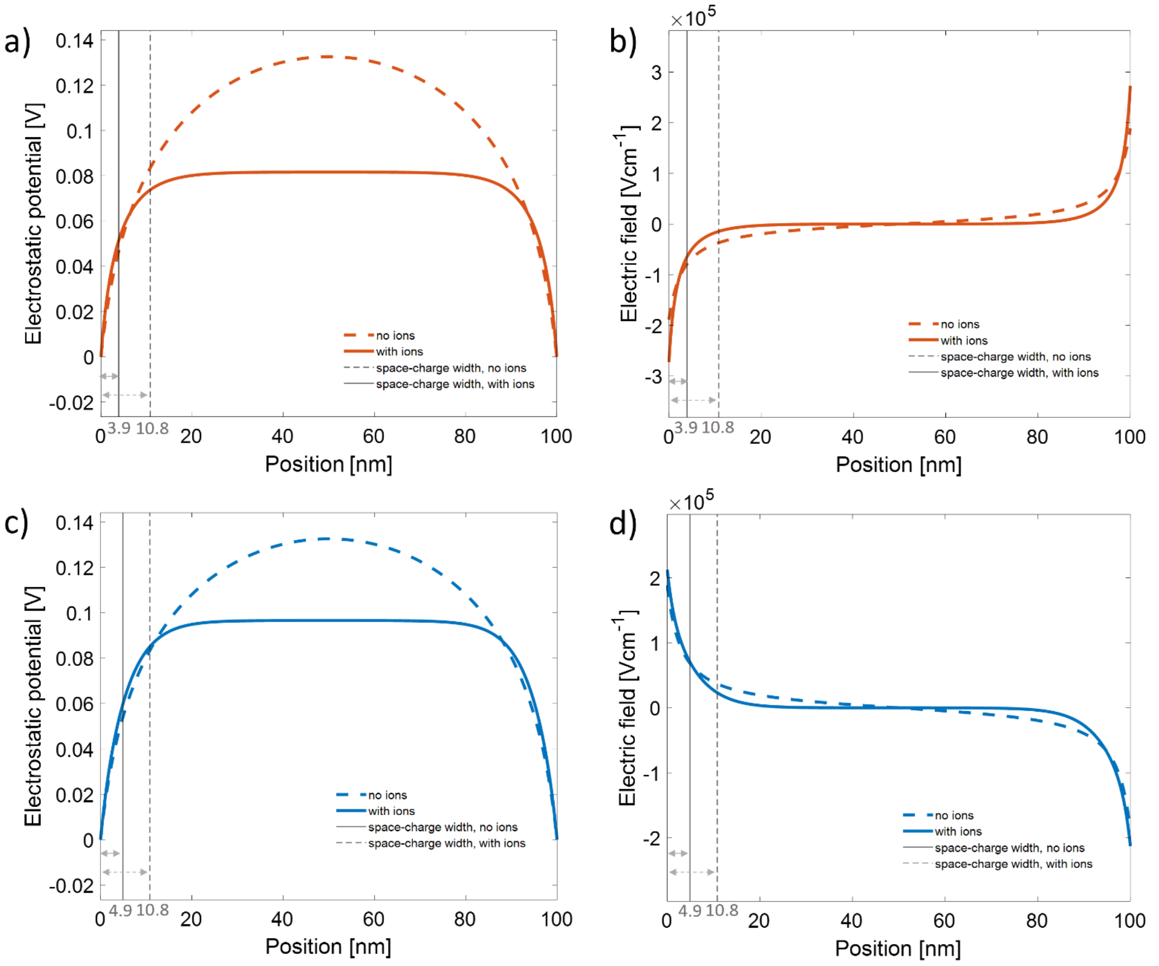

Figure 4.2 Calculated distributions of electrostatic potential and electric field from simulated equilibrium (at 0 V).(a) The electrostatic potential distribution of a hole device with 10^{18} cm^{-3} positive ions and without ions. The widths of the space-charge layers in these devices are displayed by the grey lines and numbers. The space-charge layer width is calculated as the position at which the electrostatic potential reaches $V_{max} \times (1 - 1/e)$, where V_{max} is the highest value of the electrostatic potential for that device. (b) The electric field for the devices in (a) with the space-charge widths calculated in (a) displayed for clarity. (c) The electrostatic potential distribution of an electron device with 10^{18} cm^{-3} positive ions and without ions. The widths of the space-charge layers in these devices are displayed by the grey lines and numbers and are calculated in the same way as in (a). (d) The electric field calculations for the devices in (c).

Using simulation input parameters matching physical values from the literature for methylammonium lead iodide as a test case for mixed conductor semiconductors, I investigate the effect of three key parameters on the conductance/conductivity of these devices: mobile ion density, film thickness and ϕ_{offset} for symmetrical contacts. Figure 4.3a, Figure 4.3b and Figure 4.3c show colour maps of the calculated conductance per unit area

(G/A) or average conductivity (σ, for cases where the thickness varies) of the film from simulation results for devices in their equilibrium condition. Reasoning for differentiating between G/A and σ is given in the section 3.4.1.4.

Figure 4.3a and Figure 4.3b show G/A calculated for devices of 400 nm thickness with varying ion density and ϕ_{offset}. Figure 4.3a shows the expected dependence of G/A on ϕ_{offset} following the inverse exponential relationship on energy of the electronic carriers' statistical distribution function (see discussion of the Blakemore approximation, Equation 11Equation 9, in the introduction to Driftfusion in section 2.4.5.1). When the range to values of ϕ_{offset} near to the band edges of the perovskite ($\phi_{offset} \leq 0.2\ eV$ and $\phi_{offset} \geq 1.4\ eV$) is closely inspected (see Figure 4.3b where the y-axis is restricted to values of $\phi_{offset} \geq 1.2\ eV$), I find that G/A increases by orders of magnitude with ion density increasing; the interfacial doping effect is present. When $\phi_{offset} = 0\ eV$ the change in G/A for this device is an increase by as much as two orders of magnitude. The ion density has little or no effect on G/A for devices with contacts approximately in the middle of the bandgap ($\phi_{offset} \approx 0.8\ eV$ in this case). This is because very little electronic charge redistributes from its initial uniform distribution during Fermi level alignment; the contact workfunctions (ϕ_m) are close to the semiconductor's intrinsic Fermi level. This causes the fields due to electronic charge redistribution (the process in the top branch of Figure 4.1a) to be very weak and, as such, the ionic charge does not redistribute very much in response. The space-charge layers in devices with contact energetics close to the middle of the perovskite bandgap have very low electronic charge density and the ionic charge makes up very little of it.

Figure 4.3c shows σ calculated for devices of varying thickness and ion density. I chose to set $\phi_{offset} = 0\ eV$ to maximize the interfacial doping effect in these examples. I observe that, for very thin devices, where the thickness of the perovskite is comparable to or less than the size to two space charge layer widths (thickness $\leq 10^{-6}\ cm$), the ion density has little effect on the conductivity because the whole device is taken up by the space-charge layers and there is very little enhancement of electronic charge density in the bulk of the device (*vs* low ion density cases). As the device thickness increase, the magnitude of the interfacial doping effect increases (even though the overall conductivity decreases). This is because the interfacial doping effect increases the conductivity of a device by enhancing the majority charge carrier density in the bulk (by altering the energetics and width of the space-charge regions) and so, when the bulk of the semiconductor makes up a proportionally larger amount of the total thickness, the effect is more distinct. The general decrease in σ with thickness is expected: the space-charge layers at the interface have a decaying majority charge carrier density as the distance from the interface increases. If the space-charge layer makes up proportionally less of the thickness of the device, most of the device will be made of the low charge density bulk region where the effects of interfacial doping are strongest.

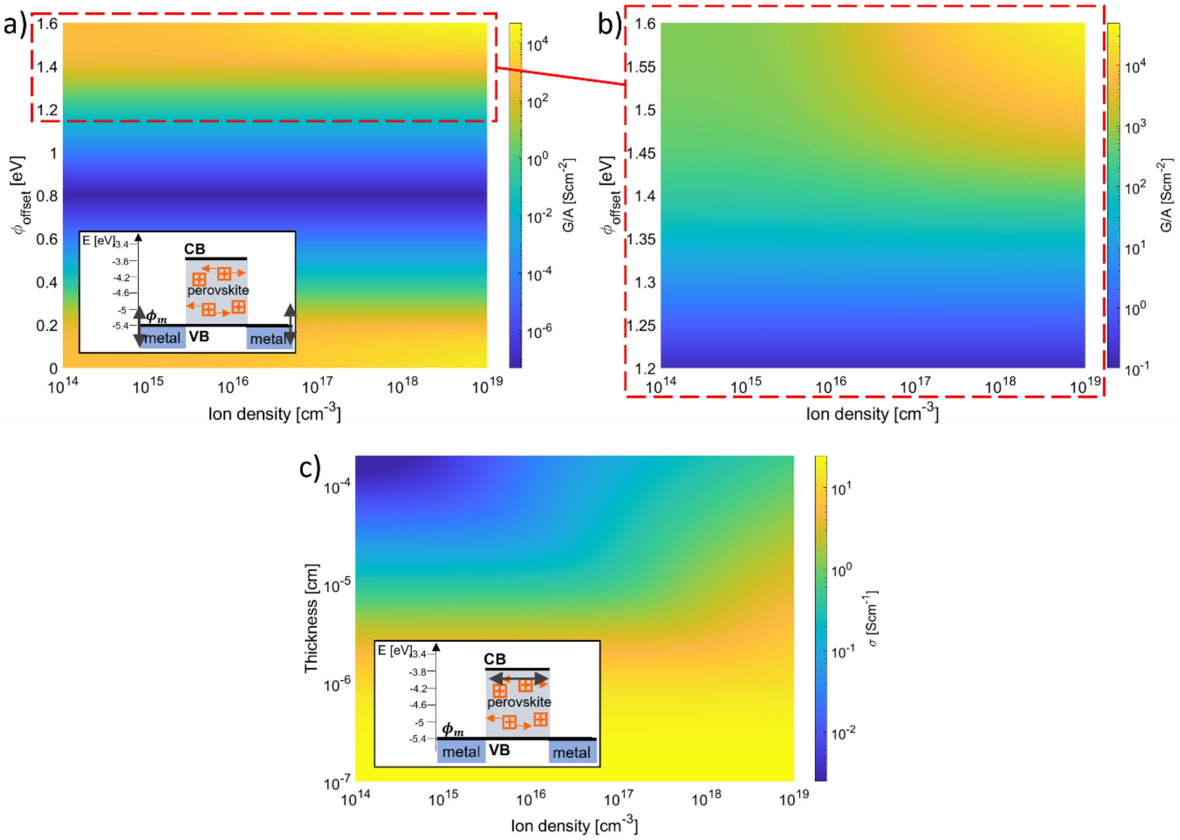

Figure 4.3 Simulations of the equilibrium condition for symmetrical metal-perovskite-metal devices ($V_{bi} = 0\ eV$). (a) A colour map depicting the variation of conductance per unit area as the density of mobile ionic cations and the contact ϕ_{offset} vary. The extent of the variation in ϕ_{offset} is equal to the bandgap of the simulated perovskite. The inset depicts the parameter variation performed. (b) A ‘zoom in’ on the region of interest from panel (a) which is demonstrated by the red boxes. The colour scale has been updated and thus, the variation in G/A due to ion density is made clearer. (c) A colour map depicting the change in σ of a device with $\phi_{offset} = 0\ eV$ as the perovskite layer thickness and the density of cations changes.

Equivalent results for electron devices with positively charged ions and for a device with two oppositely charged ionic species are shown in Figure E.1 and Figure E.2 respectively. The interfacial doping effect has the same dependence on thickness and ϕ_{offset} as the hole device, but the values of conductivity (and so, the magnitudes of the interfacial doping effect) are lower for the electron device and marginally higher for the device with two ionic species. For devices with opposite charges of the charge carrying species and ions (such as the electron device simulated in the Figure E.1), there are depletion regions at the interface which tend to be wider than the accumulation regions in the hole devices described earlier. This is the same effect that is displayed in Figure 4.1b and Figure 4.1c. As was further stated in the discussion of Figure 4.1, this is because depletion has a physical limit of no charge density ($0\ cm^{-3}$) and accumulation is not limited in this way. This, in effect, reduces the magnitude of the interfacial doping effect slightly in devices with oppositely charged ions and majority carriers when compared to devices where they have the same sign. Devices with two oppositely charged ionic species see a slight enhancement of the interfacial doping effect due to the greater density of ions in the space-charge region (both ionic species each have the same set density as the ionic charge in devices with one ionic species).

The results from Figure 4.3 show that σ and G/A of metal halide perovskite devices can be tuned by altering the ion density and contact energetics: parameters which manipulate the equilibrium distribution of ionic charge. It is well known that in mixed ionic-electronic conductors (such as metal-halide perovskites) the ionic charge redistributes in response to an applied field and screens it. I will now show the effect of manipulating the ionic distribution by applying a long-lasting voltage to the device, which I call a pre-bias voltage ($V_{pre\text{-}bias}$). To decouple the effects of charge entering the device due to the applied bias and the modification of σ due to the redistributed ionic charge, I perform the simulations in the following manner: after the equilibrium state of the device has been found, a voltage is applied to the device and the device's new equilibrium is calculated. Following this, the ionic charge is frozen (ionic mobility is set to zero) in that new distribution and the applied voltage is returned to 0 V. In effect this finds the new equilibrium of electronic charge carriers in the electrostatic landscape of the ionic charge screening $V_{pre\text{-}bias}$. G/A and σ are then calculated for the device in this state where the ionic charge is screening an applied field, but the device is at short circuit. This simulation is physically equivalent to applying a

$V_{pre\text{-}bias}$ for a long time (many 10s of minutes) and then measuring the JV characteristics starting from 0 V immediately. The slope of this JV response close to 0 V is the G/A calculated in the simulations for a trap-free device (see Figure E.3 that shows the slope of the JV curve is equal to the calculated equilibrium G/A).

Figure 4.4a contains a cartoon depicting the change to the energetic landscape, the electronic and the ionic charge carrier distribution due to a voltage applied to a symmetrical perovskite device where the majority electronic carriers are electrons, and the mobile ionic defects are positively charged. Much like the examples presented in Figure 4.1, the positive ionic charge is created in charge neutral pairs, but their static negatively charged counterparts (which have a uniform distribution throughout the perovskite layer) are omitted for the sake of not overcrowding the image. The left-hand diagram of Figure 4.4a shows the device at equilibrium with ionic depletion at the interfaces and accumulation in the bulk. Electrons are the majority charge carrier in the space charge regions. The right-hand diagram of Figure 4.4a shows the same device after a voltage has been applied and the device has then reached its new equilibrium. I note that the ionic charge has drifted towards the left-hand interface in response to the applied field, screening the electric field in the perovskite bulk (which can be seen by the flat region of E_c and E_v). This diagram also shows that the electrons have also redistributed in response to the new internal electric field distribution. These diagrams are far too "coarse-grain" to show the detail of the new electron distribution, but the representation of charge redistribution is broadly correct. Greater detail of this process and the charge distributions are given in Figure 4.5 and discussed later.

Figure 4.4b, Figure 4.4c, Figure 4.4d and Figure 4.4e show the change in G/A and σ with the application of $V_{pre\text{-}bias}$ (as described earlier) for devices with different densities of ionic charge. Figure 4.4b shows the simulation results for a device with thickness = 400 nm and contacts that are the same as those in the device depicted by the diagrams in Figure 4.4a (the contact metal workfunctions are equal to the electron affinity of the perovskite) and thus, the majority electronic charge (electrons) has the opposite sign to the ionic charge. The application of $V_{pre\text{-}bias}$ decreases the conductance and to the highest degree (four orders of magnitude) when the ion density is high. As such, one of these devices could be switched from a highly conductive state to a very low conductive state by changing the bias history by, for example, applying 1 V for many minutes. One could then probe the conductivity by measuring the JV characteristics at a low voltage over a very short timescale ($\sim ms$). Due to a *V*

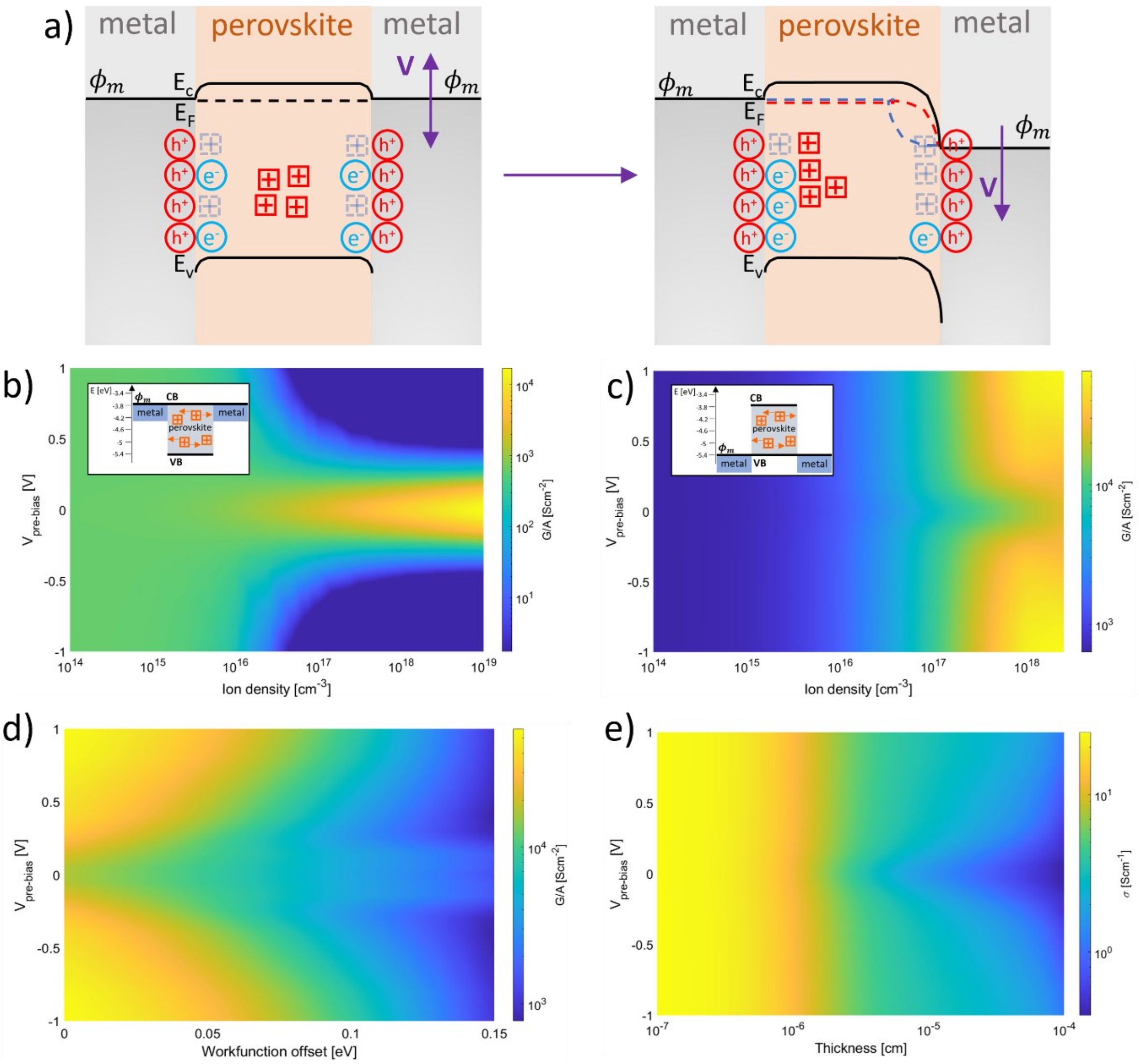

Figure 4.4 Results from simulations of the 0V condition for symmetrical metal-perovskite-metal devices after the device has reached equilibrium at a pre-bias voltage. This implies the mechanism for and the results of changes in G/A and σ. (a) Is a diagram showing the change in band-edge energies and charge carrier (electronic and ionic) distribution in an electron device due to an applied voltage ($V_{pre\text{-}bias}$). (b) a colour map depicting the variation of G/A as the density of mobile ionic cations vary with $V_{pre\text{-}bias}$ in an electron device with $\phi_{offset} = 0\ eV$. (c) a replica of (b) where the contacts define the device as a hole device, here the majority electronic charge carrier is of the same sign as the mobile ionic charge. (d) a colour map depicting the variation of G/A as ϕ_{offset} varies with $V_{pre\text{-}bias}$ in a symmetrical device

with ion density = 10^{18} cm^{-3}. (c) a colour map depicting the variation of σ as device thickness varies with *V_{pre-bias}* in a symmetrical hole device with ion density = 10^{18} cm^{-3}.

Figure 4.4c, Figure 4.4d and Figure 4.4e are results for simulations of devices where the majority charge carrier (holes) has the same sign as the ionic charge: the contact metal workfunctions are equal to the ionization potential of the perovskite. Figure 4.4c is analogous to Figure 4.4b with the same set of parameters being varied but the application of $V_{pre\text{-}bias}$ has the opposite effect on G/A; it increases. The difference in magnitude of the high and low conductive states is lower in Figure 4.4c than in Figure 4.4b (one order of magnitude *vs* four orders of magnitude), I suggest that this is because of the difference in space-charge width between the accumulation and depletion regions (see Figure 4.5 and the discussion of it for further detail). Figure 4.4d shows that this effect on a hole device with 10^{18} cm^{-3} ions, is dependent on the contact energetics since at $\phi = 0.15\ eV$, the application of $V_{pre\text{-}bias}$ reduces the conductance. There is even some interesting behaviour at $\sim 0.1\ eV$ where small $V_{pre\text{-}bias}$ ($V_{pre-bias} \approx 0.1\ V$) decreases the conductance, yet large $V_{pre\text{-}bias}$ ($V_{pre-bias} > 0.25\ V$) increases the conductance. Since ϕ_{offset} is related to the majority carrier density, this suggests that the interplay between the ion density and the electron density at the interface is complicated; in some cases where the densities of both ions and the majority charge carrier are low ($\phi_{offset} \geq 0.1\ eV$) applying $V_{pre\text{-}bias}$ can lower conductance, in other cases where the relative densities are higher, it can enhance conductance.

Figure 4.4e investigates the $V_{pre\text{-}bias}$ dependent changes in σ for devices with $\phi_{offset} = 0\ eV$ and 10^{18} cm^{-3} ions as the thickness increases, revealing the same $V_{pre\text{-}bias}$ dependence shown in Figure 4.4c and Figure 4.4d at thickness = 400 nm, showing self-consistency in the simulation results. In very thin devices (thickness $< 5 \times 10^{-6}\ cm$) there is no change in σ with $V_{pre\text{-}bias}$ due to the same reasons as mentioned in the discussion of the results in Figure 4.3c: the device is made up of entirely space-charge and the ion distribution makes very little difference. For thick devices (thickness $\approx 10^{-4}\ cm$) the enhancement of σ is larger than that observed for devices of intermediate thickness (thickness $\approx 10^{-5}\ cm$). This matches the trend from Figure 4.3b which showed the increase in the interfacial doping effect for very thick devices (see Figure 4.5 and the discussion of it for further detail). These results show that small changes in these key parameters can change the magnitude and direction of the interfacial doping effect when applying *V_{pre-bias}* and so, since controlling each of these parameters precisely could prove difficult real devices, I suggest measuring and/or simulating each device set to confirm the achieved interfacial doping effect.

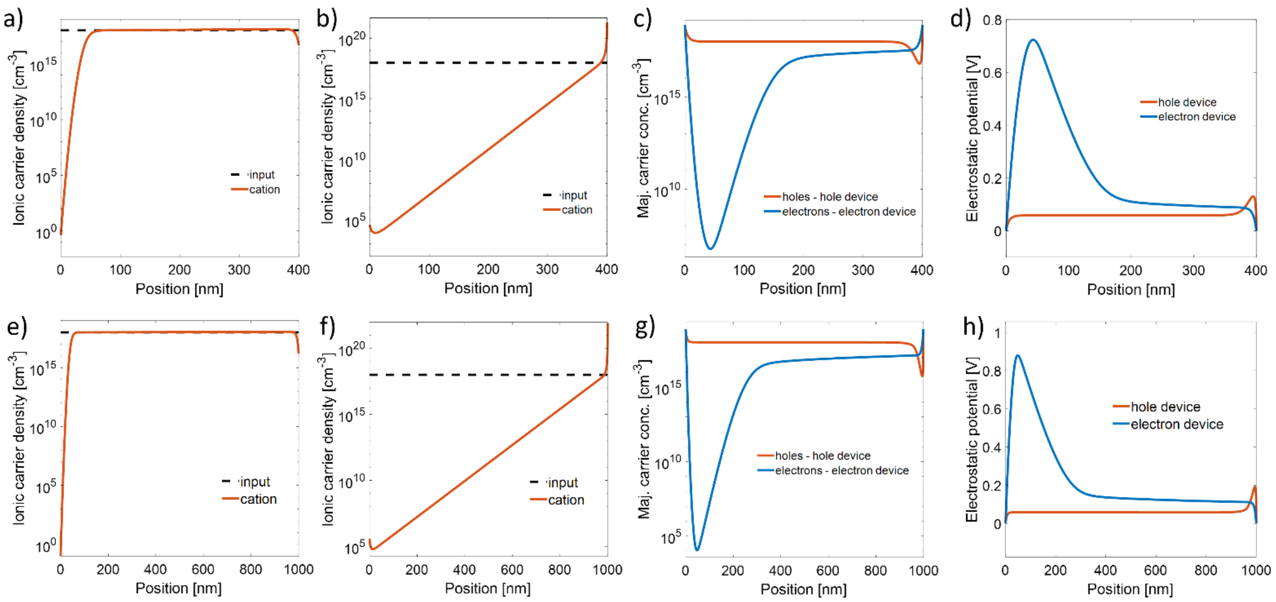

Figure 4.5 The simulated distributions of ion density, majority carrier density and electrostatic potential for devices with positive mobile ionic charged species of concentration $10^{18} cm^{-3}$. All devices had $V_{pre-bias} = 1\ V$ applied and equilibrium at this voltage was reached, then the ionic mobility was set $= 0\ cm^2V^{-1}s^{-1}$ and the device was allowed to reach a new equilibrium at 0 V, these figures are of a device in this final 0 V equilibrium. (a-d) Are devices of thickness 400 nm. (a) The ion distribution of an electron device. (b) The ion distribution of a hole device. (c) The distributions of the majority electronic carriers in the hole and electron devices. (d) The electrostatic potential distribution in the hole and electron devices. (e-h) are all devices of 1000nm thickness. (e) The ion distribution of an electron device. (f) The ion distribution of a hole device. (g) The distributions of the majority electronic carriers in the hole and electron devices. (h) The electrostatic potential distribution in the hole and electron devices.

I now present further evidence for the mechanism of the interfacial doping effect under bias for some example cases from Figure 4.4. Figure 4.5a shows the ion distribution after the application of $V_{pre-bias} = 1\ V$ for the electron devices investigated in Figure 4.4b (with ion density = 10^{18} cm^{-3}) and show the ionic charge having redistributed in response to $V_{pre\text{-}bias}$ from its initial distribution. The ionic charge has drifted towards the right-hand interface in response to the applied voltage. The new distribution still maintains features of its initial equilibrium distribution (Figure 4.1c) with depletion in space-charge regions at the interfaces, although these are now asymmetric, and the left-hand depletion region being much thicker than the right-hand depletion region. Figure 4.5b shows the ion distribution of the hole device from Figure 4.4c after $V_{pre-bias} = 1\ V$ and, as with the device in Figure 4.4b and Figure 4.5a, the ionic charge has drifted towards the right-hand interface, but the regions of ionic accumulation at the interfaces are thinner than the depletion layers in the electron device. These differences in ion distribution after $V_{pre\text{-}bias}$ are causing the changes in calculated G/A. The majority charge carrier distributions with the devices at 0 V but with the ionic charge frozen in their $V_{pre-bias} = 1\ V$ distributions are shown in Figure 4.5c, with a large decrease in electron density in the electron device occurring in the large ionic depletion region. This decrease in majority charge carrier density does not occur in the hole device to the same extent, the depletion is very small and on the opposite interface. I suggest that this difference in charge carrier distribution between the hole and electron devices is due to the difference in accumulation and depletion in the interfacial space-charge regions. To demonstrate this point further, the electrostatic potentials of the electron and hole devices with the ionic charge frozen in their $V_{pre-bias} = 1\ V$ distribution but with the device at 0 V are plotted in Figure 4.5d. The electrostatic potential of the electron device reaches a maximum of $\sim 0.38\ V$, which is significantly higher than the values of the device at equilibrium at 0 V, shown in Figure 4.2c, where the maximum electrostatic potential is $\sim 0.1\ V$. This maximum occurs in the same region of the device as the very large ionic depletion region of the left-hand interface. I conclude that this configuration, with a very thick space-charge layer at one of the interfaces, creates and energetic landscape which causes less electronic charge to exist in the perovskite layer when compared to the 0 V case. The opposite is true for the hole device, where the electrostatic potential in the bulk is slightly lower in magnitude ($\sim 0.06\ V$) than the 0 V case ($\sim 0.08\ V$), shown in Figure 4.2a, which creates an energetic environment that increases the electronic carrier density in the device.

The ion distributions for electron and hole devices of thickness = 1000 nm are shown in Figure 4.5e and Figure 4.5f with majority carrier densities and electrostatic potential distributions shown in Figure 4.5g and Figure 4.5h respectively. The changes in ion distribution, majority carrier density and electrostatic potential when compared to thinner devices (Figure 4.5a, Figure 4.5b, Figure 4.5c and Figure 4.5d) explain the trend in σ due to thickness in Figure 4.4e; the electrostatic potential in the interfacial regions is higher (generally) but more of the bulk contains regions of lower electrostatic potential. This region of low electrostatic potential in the bulk outweighs the changes in the interfacial region, since it fractionally makes up more of the device thickness, increasing the overall interfacial doping effect. These simulation results show how the redistribution of ionic charge due to an applied voltage aids to minimize the electrostatic potential throughout the semiconductor layer, which in turn modifies the charge carrier density in the layer and modifies the conductivity. I note that the process is the same for a device at equilibrium, but the driving force is the space-charge field rather than then applied voltage.

The results displayed in Figure 4.3, Figure 4.4 and Figure 4.5 reveal the importance of symmetrical contact energetics, ion density and applied voltage as factors in defining the conductivity of perovskite devices. Fabricating a device with symmetrical contacts may pose a challenge and, in most cases, the contacts will be asymmetrical to a certain degree. In semiconductor device that are free of high density mobile ionic defects, asymmetric contacts will lead to a built-in potential (V_{bi}) forming during the equilibration process. In the presence of mobile ionic defects, the V_{bi} will be screened out by the ions redistributing in a similar manner to when a voltage is applied. The ions will accumulate at the interface(s) during this process, potentially causing an interfacial doping effect as I have observed in the results shown in Figure 4.4. I now provide an investigation into asymmetric contacts on the interfacial doping effect.

Figure 4.6a and Figure 4.6b show two examples of asymmetric contacts. Figure 4.6a presents devices where one contact is Ohmic ($LHS\ \phi_{offset} = 0\ eV$) and the other contact workfunction is varied. In this case, the interfacial doping effect is present for all values of $RHS\ \phi_{offset}$ but the effect is only significant when the contacts are close to symmetrical ($RHS\ \phi_{offset} < 0.4eV$). In Figure 4.6b, where one contact is fixed in the middle of the perovskite bandgap, the interfacial doping effect occurs only for $RHS\ \phi_{offset} \leq 0.6\ eV$. I note that this case is for a device with positive ions and the region of most interfacial doping is when the contacts cause the device to have holes as the majority charge carrier in the device, when the sign of the ionic carrier and majority carrier is the same. In Figure E.4 I show that if the compensating negative ionic species is made mobile in the perovskite layer (and has equal properties to the positive ions) then the region of high interfacial doping is reflected in the y-axis about $RHS\ \phi_{offset} = 0.8\ eV$; the negative ions can carry out the same doping effect as the positive ions do in figure 4b. When comparing the absolute values of G/A in Figure 4.6a and Figure 4.6b, I see that contact energetics drastically effect G/A, regardless of the ion concentration (as shown in Figure 4.3a.) These results, interestingly, show that the majority of device architectures are in some way effected by the interfacial doping effect and a high density of these ionic defects could prove to be a useful feature of perovskite materials as they allow for the enhancement of electronic charge density in the perovskite layer, allowing for a controllable state of conductance by applying $V_{pre\text{-}bias}$ to them.

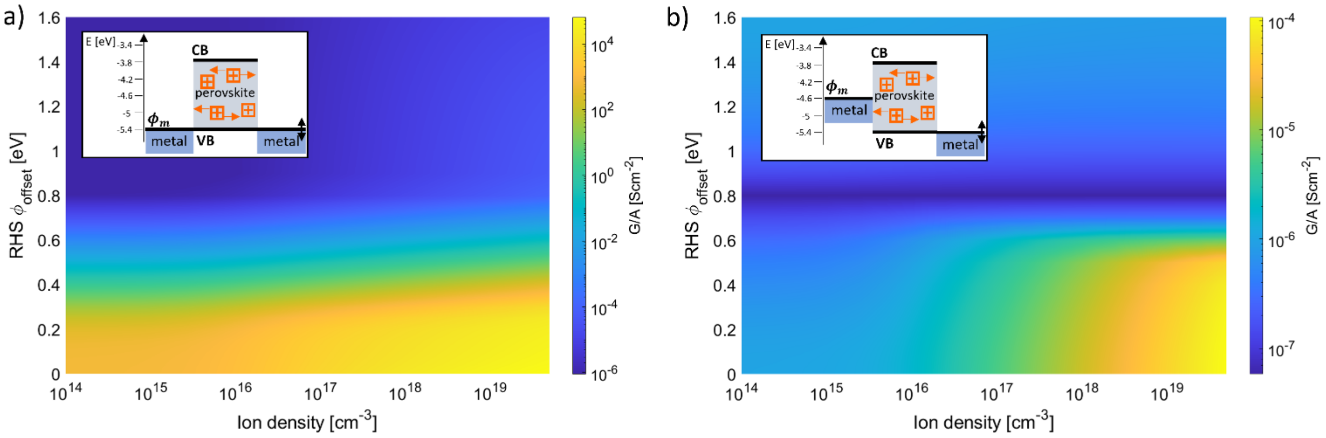

Figure 4.6 Simulations of the equilibrium condition for asymmetrical metal-perovskite-metal device. This shows the influence of built-in potential on the conductance per unit area of devices with mobile ionic charge. (a) a colour map depicting the variation of conductance per unit area as the density of mobile ionic cations vary as the workfunction of the right-hand contact (ϕ_{RHS}) varies and as the left hand workfunction offset remains fixed at $\phi_{offset} = 0\ eV$. (b) a colour map depicting the variation of conductance per unit area as the density of mobile ionic cations vary and as the workfunction of the right-hand contact (ϕ_{RHS}) varies as the left hand workfunction offset remains fixed at $\phi_{offset} = 0.8\ eV$.

Considering the recently reported methods for doping metal-halide perovskites mentioned in the section 4.4, I provide an investigation into the effects of simultaneous traditional static doping (acceptor or donor type) and interfacial doping from mobile ionic charge. The results are presented in Figure 4.7 with both dopant density and resulting fermi-level energy displayed as variables. These results show that the interfacial doping effect is significant when the ion density is much greater than the dopant density and, therefore, the majority charge carrier density. This is due to two reasons: i) when the doping density is very high and $\phi_m \approx E_F$ before equilibrium, less electronic charge moves during the attainment of thermodynamic equilibrium *vs* the $\phi_m - E_F \gg 0\ eV$ case, this leads to narrower space-charge regions with less variation in charge-carrier density. This causes the electric fields in the space-charge region to be smaller and, as such, the ionic charge redistributes less than when $\phi_m - E_F \gg 0\ eV$ before equilibrium and the interfacial doping effect is lower. ii) When the ionic charge has redistributed to the interfacial region, the relative density of the ionic charge and the electronic charge defines which species controls the space-charge layer width and the electrostatic potential distribution in the device. If the electronic charge density is much greater than the ion density, the ion density has little effect on the device's energetic landscape. These findings confirm the results from Figure 4.3a and Figure 4.3b which show that the relative positions of E_F and ϕ_m before equilibrium are important for determining the magnitude of the interfacial doping effect at equilibrium. These findings also show that the relative densities of the ionic charge and the electronic charge in the space-charge layers at the interfaces and in the bulk are also an important factor in the size of the interfacial doping effect.

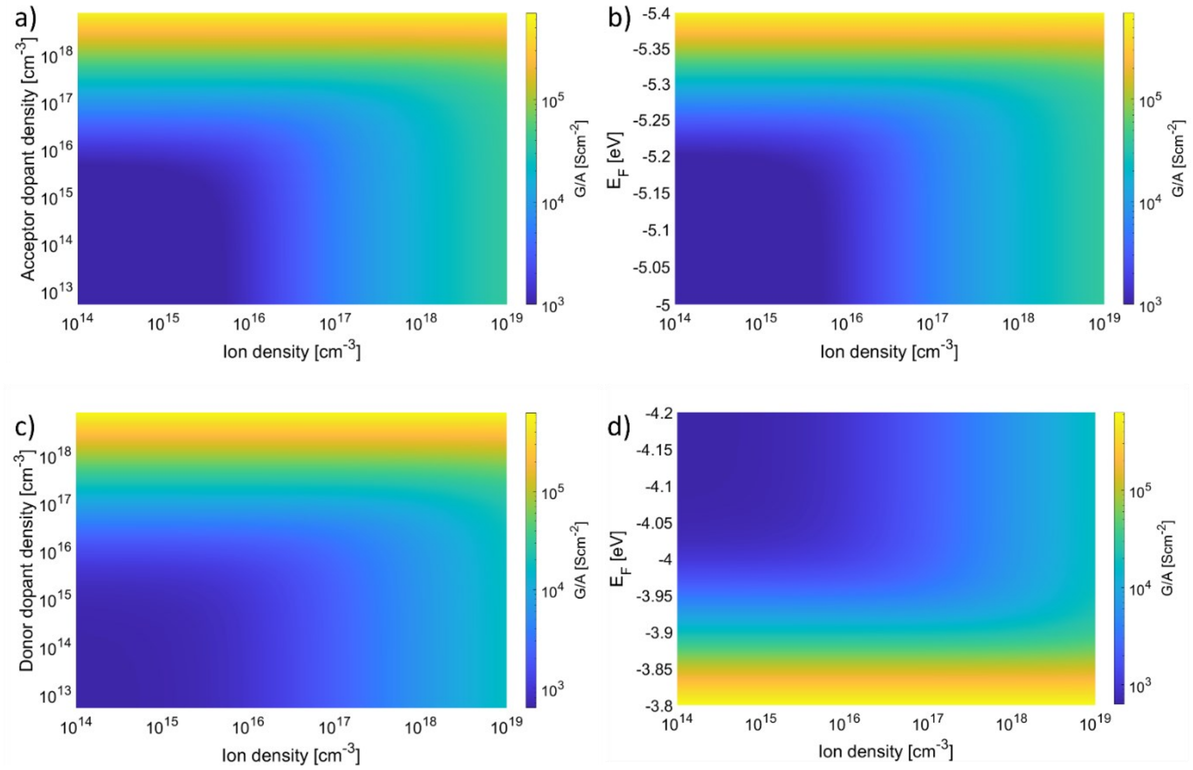

Figure 4.7 Colour maps depicting the variation in calculated G/A with ion (cation) density for 400 nm devices with increasing static dopant density. The "amount" of doping is represented in two ways: i) The density of ionized dopants in the device (which will be approximately equal to the number of extra free charge carriers), ii) The fermi-level of the semiconductor (E_F) before the device is formed and thermodynamic equilibrium is reached. a) and b) are hole devices ($\phi_m = E_C$) with mobile cationic defects (no electronic charge compensation) of varying density and with varying static acceptor-type donor densities, the results in a) and b) are identical only with the y-axis representation changed for clarity. c) and d) are for electron devices ($\phi_m = E_C$) with mobile cationic defects (no electronic charge compensation) of varying density and with varying static donor-type donor densities, the results in c) and d) are identical only with the y-axis representation changed for clarity.

I now present experiment results demonstrating the interfacial doping effect in Figure 4.8. I used a measurement technique I refer to as the "pulsed voltage" method, which allows for the JV curve to be measured without the contribution of mobile ionic charge drifting in response to the applied field, the obtained JV curves are presented in Figure E.5. The equilibrium distribution of the mobile ionic charge still effects the JV curve. The details of this procedure are given in section 4.3.3. Once the JV curve data for several $V_{pre\text{-}bias}$ values was obtained, the gradient close to 0 V (which is equivalent to G/A) was found. I note that the steeply rising portions of the JV curves in Figure E.5 are omitted from this portion of fitting since this region is likely to no-longer be Ohmic. Along with the experimental results, simulations of this device were also performed (using the same simulation method as the other simulated $V_{pre\text{-}bias}$ study from Figure 4.4), the parameters of the simulated device are given in Chapter 8Appendix B, section Chapter 8B.1. The results in Figure 4.8 do show a $V_{pre\text{-}bias}$ induced interfacial doping effect with the peak in G/A at $V_{pre-bias} = -0.1\ V$. The total enhancement of G/A is much smaller than expected in the simulations of this device: a $\sim 50\%$ increase *vs* approx. x10 increase in the simulations. I suggest that the difference between the experimental results and the simulations of this device could be due to one or both of: (i) not knowing all the input parameters for representing the device accurately and (ii) the simulations not formally including electronic charge trapping states and other interfacial states. During the application of small voltages in the JV curve (in the Ohmic regime), these trap states could fill, reducing the current density and making the equality in Figure E.3Figure E.3 invalid. During the application of $V_{pre-bias} \neq 0\ V$, and more so for larger voltages, most of these possible trap states are filled so there would be no such change for the values with pre-bias. I also note that the onset voltage for the steeply rising portion of the JV curves in Figure E.5 shows a similar trend to the changes in G/A. As G/A increases, the onset of the steeply rising current density moves to a lower voltage. This is not a trap-filled limit behaviour (136) because if it were, the high voltage $V_{pre\text{-}bias}$ curves would see similar gradients in their JV curves to these regions of greatly increasing current in the low voltage $V_{pre\text{-}bias}$ curves. Rather, I suggest that this is due to the mobile ionic charge distribution (specifically the wide ionic depletion at one interface) causing a potential barrier to be overcome for charge injection (represented in the peak of electrostatic potential in Figure 4.5d and Figure 4.5h). This potential barrier depends on the ionic depletion layer width and is, therefore, dependent on $V_{pre\text{-}bias}$. This depletion region can occur at either interface and, therefore, this effect should be symmetrical in voltage about $V_{pre-bias} = 0\ V$ if the device has no asymmetry. The onset voltage is not symmetrical, providing more evidence that this device is indeed, asymmetrical.

I also note that the increases in G/A in these results (both simulation and experiment) are lower than some previous examples in Figure 4.4. I suggest that this is due to the device architecture: the workfunctions of the contacts are difficult to know exactly due to the combination of asymmetric metallic contacts with large offsets being in combination with doped transport layers (the exact doping level is also unknown) but I am confident that the contacts are asymmetric and, additionally, would fall in the regions of Figure 4.4d where $\phi_{offset} > 0.1\ eV$, causing the G/A enhancement to be less than one order of magnitude. I also suggest that the effect of $V_{pre\text{-}bias}$ could be reduced by the existence of the polymer transport layers because some of the $V_{pre\text{-}bias}$ would drop across these layers (which have non-zero dielectric constants), reducing the amount of ionic redistribution and, therefore, altering the interfacial doping effect's dependence on $V_{pre\text{-}bias}$.

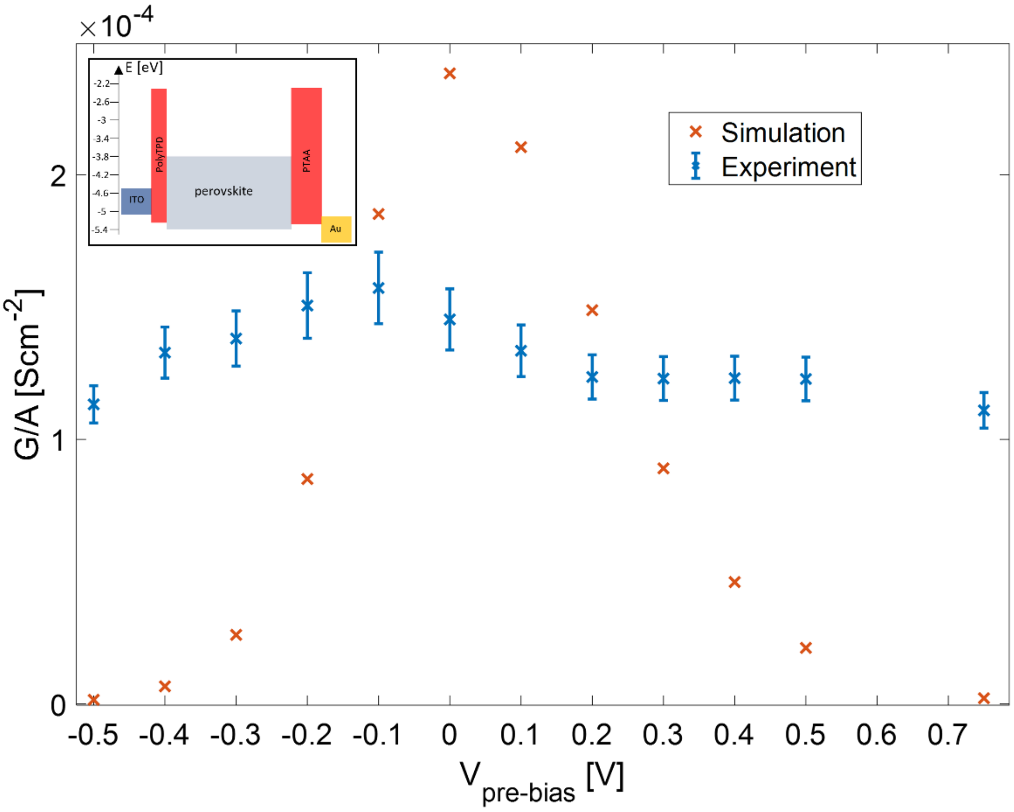

Figure 4.8 A comparison of experimental results and simulation results calculating the conductivity of a thin film device of structure shown in the inset with varying $V_{pre\text{-}bias}$. The experimentally determined pulsed voltage JV curves from which G/A is calculated are shown in Figure E.5. The error bars were estimated by combining an estimation of the error on the JV points from the pulsed-voltage technique and combining this with the variance of data points around the Ohmic fit, intentionally overestimating the error. A more detailed description of the error calculation is given in section 4.3.4. The simulation parameters for this simulated device are given in Table B.1.

4.5.1 Heterogeneous doping *vs* interfacial doping

Finally, I will include a comparison between the heterogeneous doping process described by Kim *et al.* (134) and the interfacial doping described in this chapter. Heterogenous doping occurs due to some physical/chemical interaction of the ionic charge with the contact material at the interface whereas interfacial doping is purely due to the modification of the space-charge layer width at the interface as due to some dynamic interplay between the electronic and ionic charge and the associated electric field. The magnitude of heterogenous doping decreases with device total thickness (assuming the surface area of the interface remains constant) whereas interfacial doping increases with device thickness. Heterogenous doping depends on the physical and chemical structure of the interface and its overall surface-area whereas interfacial doping purely depends on the energetics of the contact materials, the static doping state of the mixed-conducting material and the density of states for the relevant charge carriers.

4.6 Conclusion and future work

In summary, I have demonstrated a new mechanism by which mobile ionic defects in semiconducting devices can act as an effective dopant by modifying the energetic landscape of the interfaces both at equilibrium and under applied bias. Which I have referred to as "interfacial doping". By simulating metal-halide perovskite devices as a test case, I have shown that increased densities of mobile ionic defects increase the density of electronic charge carriers in the bulk of the perovskite (an increased conductance per unit area), even though the modelled defects are formed in charge neutral pairs with no initial compensation by electrons or holes. Having analysed the resulting electrostatic potential and electric field profiles of the simulated devices, I have concluded that the doping effect is caused by the ionic charge dominating the space-charge region at the interface, reducing the thickness of these regions, and thus creating an energetic environment that induces more electronic charge in the device's bulk when compared to an ion-free case. I have shown that the magnitude of the interfacial doping effect is increased by having more Ohmic contacts and by having a thicker perovskite layer. I then demonstrated that the interfacial doping effect not only occurs at equilibrium but also under applied voltage: the density of mobile ionic charges greatly effects the conductance state of a device under long-timescale applied voltage. Our simulation results suggest that perovskite devices with high densities of mobile ionic defects could have a switch of conductance per unit area of as much as three orders of magnitude after a pre-bias voltage of $\pm 1\ V$. This combination of conductance tunability at equilibrium and under applied bias presents a possible opportunity to design devices to intentionally make use of this effect by tuning the device thickness, contact energetics and operation conditions. It also has great implications for many measurement techniques used to characterise mixed-conductor devices. Finally, I confirmed the existence of this effect through measurements of a device using a pulsed voltage method, although the magnitude of the interfacial doping effect was not a large as the simulations suggested. This interfacial doping effect, that varies with device composition, could be one of the causes for the wide variety of measured and calculated conductivities of MHPs.

Further experimental investigation into the trends found by the simulation results in this chapter would demonstrate the utility of these findings. One may be able to work with small single crystal MHPs with platinum electrodes, which give great ohmic contacts for holes. If the stoichiometric ratio of the precursors was altered to “dope” the MHP statically, one could investigate the interplay between these two processes.

Chapter 5 - SCLC Measurements of Metal Halide Perovskite Devices

5.1 Declaration of contributions

Joel A. Smith[1,2] and Onkar Game[2] performed the device fabrication for the device measured in this chapter, the method is described in section 3.2.1.

Philip Calado[3] wrote the simulation package Driftfusion and aided in the interpretation of the data.

Jason Rohr[4] contributed to the interpretation of the findings, performed the simulations that use the Advanced Semiconductor Analysis (ASA) software and aided in the design of the study.

Jenny Nelson[3] aided in the design of the study and the interpretation of the results.

Piers Barnes[3] designed the study and aided in the interpretation of the data.

[1]Department of Physics, Clarendon Laboratory, University of Oxford, Oxford, OX1 3PU, UK

[2]Department of Physics and Astronomy, University of Sheffield, Sheffield, S3 7RH, UK

[3]Department of Physics and Centre for Processable Electronics, Imperial College London, South Kensington Campus, London, SW7 2AZ, UK

[4]Department of Chemical and Biomolecular Engineering, Tandon School of Engineering, New York University, Brooklyn, New York 11201, USA

5.2 The validity window for SCLC measurements

5.2.1 Abstract

SCLC measurements are commonly used to estimate charge carrier mobilities and electronic trap densities of semiconductors using the Mott-Gurney (MG) law, either in its original form or with some modifications, which relate mobility to the current density-voltage (JV) characteristics of unipolar devices. However, the interpretation of SCLC measurements has been problematic for MHPs due to mobile ionic defects, which redistribute in response to the electrostatic field in devices and screen them. To avoid this issue, a refinement to SCLC current JV measurement protocols has been recently suggested that aims to minimise ionic

charge redistribution throughout the measurement by probing the current during ~ms voltage pulses superimposed on a background bias. Here, I use drift-diffusion simulations including mobile ions to investigate the validity of the MG law and for analysing both the traditional and newly proposed JV measurement protocols. We simulated idealised perovskite devices with differing mobile ion concentrations and compared them with measurements and simulations of devices contacted with materials typically available to perovskite researchers. Our results show that the region of validity for the MG law is limited to perovskite devices with ion densities lower than the device's equilibrium charge carrier density (approximately $< 10^{17}\ \mathrm{cm}^{-3}$ for methylammonium lead iodide, $MAPbI_3$, of films of thickness ~400 nm) and contacts with injection/extraction barriers no larger than 0.1 eV. The latter limitation can be partially overcome by significantly increasing the device thickness, whereas the former limitation cannot. This greatly restricts the range of perovskite layer compositions that can be reliably analysed with the MG law and the viable choice of contact materials. Furthermore, the nature of these limitations also calls for critically reviewing the validity of other common methods, such as estimating trap densities from the apparent voltage onset to trap-free SCLC regime. Our experimental results, in combination with the constraints on the applicability of the technique, demonstrate that extracting meaningful and accurate values for metal halide perovskite material properties with SCLC is in some cases challenging, and often impossible.

5.2.2 Methods

5.2.2.1 Experiments - JV curves

For the JV sweeps, the method described in section 3.3.2 using the TRACER system was used. For the results in this chapter the measurement parameters are given in the caption and/or discussion of each result.

For JV curves obtained by the pulsed voltage method, the procedure described in section 3.3.3 was used with $V_{pre-bias} = 0\ V$.

5.2.2.2 Simulation methods

During the simulation of the JV curves of ideal devices, the methods referred to in section 3.4.1 were used. Calculating $g(V)$ for simulated JV curves was done by using MATLAB's diff() function and taking $diff(J)/diff(V)$.

The colour maps featuring throughout this chapter were created by making many sequential simulations and the relevant calculations of their results for each set of input parameters. The results were then plotted using MATLAB's surf() plotting function.

5.2.3 Introduction

Metal halide perovskite materials are of considerable interest for applications including solar cells(17,109), photodetectors(110), light-emitting diodes(111), and memristors(112). Given the wide variety of compositions possible amongst this material class, there is great interest in developing accessible methods to measure properties such as charge carrier mobility, charge carrier concentration and trap density as new perovskite variants are developed.

Superficially, one of the most common approaches to estimate these parameters is via space-charge-limited current (SCLC) measurements; analysis of current density *vs* voltage (JV) measurements of two-terminal perovskite single-carrier devices. Besides the numerous factors that complicate the analysis of SCLC measurements of non-perovskite devices, such as trap states(136,137), doping (138) and energetic disorder(139), the high density of mobile ionic charge in metal halide perovskites (11,26,40) further complicates the application of this measurement technique and the ensuing analysis. Adapting the SCLC measurement technique and/or analysis to account for these mobile ions to find electron and hole mobilities in perovskites would, therefore, be of great interest.

In principle, the JV curve of a semiconducting layer sandwiched between symmetrical and Ohmic contacts demonstrates SCLC beyond a voltage threshold, this SCLC region of the curve is known as the MG drift regime. JV curves are generally measured by stepping sequentially (sweeping) through an increasing or decreasing series of applied voltages, *V*, at some rate while recording the resulting current density between electrical contacts, *J*(*V*). SCLC analysis usually involves determining the log-log gradient of the measured JV curve as it varies with voltage, $g(V) = \mathrm{d}log(J)/\mathrm{d}log(V)$, to identify the exponent of the power-law relationship $J \propto V^g$. Voltage regions where $g(V) \approx 2$ are identified and analysed using the Mott-Gurney (MG) law (12),

$$J = \frac{9}{8}\mu\epsilon_r\epsilon_0\frac{V^2}{L^3}$$

Equation 18

to extract a charge carrier mobility, μ, assuming the thickness of the perovskite layer, L, and the relative and vacuum permittivities, ϵ_r and ϵ_0, are known. Further modifications to this analytical framework account for the effects of electrode/semiconductor energy barriers, electronic trap states and regimes other than SCLC in the JV measurement (64,136,140,141). For many devices, neglecting these contributions results in the incorrect interpretation of JV curves, namely identifying regions where $g(V) \approx 2$ as space-charge limited when they are not, and then applying the standard SCLC analysis (Equation 18) to find μ.

However, the application of the MG law and its associated analyses on MHPs is further confounded by the presence of high concentrations of mobile ionic defects within the crystal lattice. These ions redistribute in response to varying internal electric fields during measurements (11,142), changing the electrostatic profile in the device, and hence the observed JV curve. Although there are examples of SCLC-type analyses and other associated techniques being applied to metal halide devices in the literature, the presence of mobile ionic charge is likely to invalidate the interpretation and conclusions drawn from the data (143–147). Recent works (49,65,148) challenged the validity of the application of the MG law and associated analyses to perovskite devices and suggested experimental techniques to account for the effects of mobile ions. Here we will investigate and review the arguments presented in these publications.

In this chapter, we show that applying the MG law to JV measurements of mixed electronic-ionic conducting materials such as MHPs is only valid under specific measurement conditions and when the electronic charge density is significantly greater than the mobile ionic charge density in the device at equilibrium (herein, ‘equilibrium’ is defined as the condition where no (net) energy or mass flows in or out of the defined system). For the typical class of materials and devices of interest to the perovskite community it is difficult to ensure these conditions are met, hence limiting the utility of the MG law and associated techniques in this context. We demonstrate these findings by presenting simulations of JV measurements of ‘ideal’ thin-film devices (which are not necessarily always possible to make) over a large voltage range (which is experimentally impractical) and by contrasting them to experimental results from real thin-film devices and corresponding simulations of them. This is done for two SCLC measurement techniques: (i) JV sweeps performed by incrementally stepping the applied voltage with time at a fixed rate as described in section 3.3.2 and (ii) the so-called “pulsed-voltage” method where voltages are applied in very short pulses, probing the device in a quasi-fixed state as described in section 3.3.3. Noting the discrepancy between the ideal simulations and the experimental results, an analysis revealing the validity regime for the MG law is provided. The effects of increasing perovskite layer thickness on these validity limits are also investigated. The consequences of this validity regime and the mechanisms at play have important implications for any JV measurement of perovskite single-carrier devices.

5.2.4 Results and discussions

5.2.4.1 Ionic contribution to the electric field distribution

The derivation of the MG law requires two assumptions: i) that the spatial variation of the internal electric field is governed only by injected majority electronic charge (the majority charge carrier here is holes) with no contribution from other charged species, and ii) that the electronic current is dominated by drift. While the first assumption should be valid in an ideal device at reasonably high voltages, a high density of mobile ionic charge, which might be expected in metal halide perovskites, is likely to invalidate this assumption since we expect the ionic charge to dominate the electric field profile in a device. The electric field profile, E, can be determined from Gauss’ law which is related to the spatially varying distribution of charge. If the electronic charge in the perovskite is dominated by free holes of concentration, p, and the perovskite also contains a mobile cationic charge species with concentration, c, compensated for by an equally and oppositely charged, uniformly distributed static anionic species, with concentration a, then at steady state:

$$\frac{dE(x)}{dx} = \frac{q}{\epsilon_r \epsilon_0}[p(x) + c(x) - a]$$

Equation 19

Where *x* refers to the position along the one-dimensional space of the perovskite layer and *q* is the elementary charge. The corresponding steady state drift current density, *J*, through the device will be given by:

$$J = q\mu_p p(x)E(x)$$

Equation 20

where $\mu_p$is the mobility of holes. Note that while ions contribute to the overall electric field driving the drift current, there is no direct contribution from mobile ions to the conductivity, i.e., $q\mu_p p$. We assume there are no other ionic interactions with the device interfaces (such as chemical reactions). Following the approach of *Schottky and Prim* (63), which analyses a case where no ionic charge is present, Equation 19 and Equation 20 would be combined by substitution and then integrated to derive the MG law. However, this method is no longer possible because the mobile ion density cannot be removed from the resulting equations or correctly accounted for without knowing its spatial distribution.

The MG law also assumes that JV measurements are made on semiconducting layers interfaced with Ohmic electrical contacts. Ohmic contacts maximise the concentration of electronic charge in the device at equilibrium and minimise any barriers to electronic charge injection, assuming all other variables (contact area, interfacial surface/dipole states etc.) are equal. We define an ideal Ohmic contact as one with no workfunction offset

($\phi_{offset} = 0\ eV$), ϕ_{offset} is defined in section 4.5, Equation 17. The convention we use here is to discuss the smallest offset of the two according to the contact selectivity of carrier species in the unipolar devices. Variation of ϕ_{offset} impacts the charge carrier density in the device. In an out-of-thermal-equilibrium semiconductor with quasi-fermi levels $E_{Fn}$and E_{Fp} and with effective density of states N_c and N_v for electrons and holes respectively, the Blakemore approximation (89,90) gives charge carrier densities that follow Equation 11. At the device interfaces $E_c - E_{Fn}$ or $E_{Fp} - E_v$ are equal to ϕ_{offset}. The Blakemore approximation is used instead of the Boltzmann approximation in this calculation of the charge carrier density because for small ϕ_{offset} (of less than a few k_BT) Boltzmann statistics are no longer valid. The use of the Blakemore approximation is discussed in the section 2.4.5.1 and the entire approach of calculating the charge carrier density of semiconductor devices is discussed in Chapter 8Appendix F, section Chapter 8F.2 where an upper limit for charge carrier densities in perovskite devices is also estimated without such assumptions for the Blakemore distribution function. Throughout this work, one can view ϕ_{offset} as a proxy for majority charge carrier density with an inverse and exponential relationship. As we will show later in section 5.2.4.4, if the contacts to the perovskite are not perfectly Ohmic (i.e., when $\phi_{offset} > 0\ eV$) the MG law's window of validity in the presence of mobile ions is further reduced.

5.2.4.2 JV sweeps

To investigate the consequences of mobile ionic charge for the application of the MG law and its associated analyses we present drift-diffusion simulations (using our modelling package, Driftfusion (88)) of JV sweeps on thin-film metal/perovskite/metal devices. The contact energy levels were set such that holes were the majority charge carrier (see Figure F.1a-b), although the results are generalisable to electron-only devices. All device parameters and material constants for these ideal devices are presented in Table C.1. Figure 5.1 show results for the device depicted by the inset in Figure 5.1a in which the 400 nm thick perovskite layer has mobile ions but no electronic trap states and has ideal Ohmic contacts with $\phi_{offset} = 0\ eV$ between the metal contacts and the perovskite valence band. A voltage range of 0 to 500 V is applied to investigate the full range of device behaviour, albeit noting that a 500 V applied to a real-world device of this thickness would cause damage and is not realistic in practice. This range was discovered by incrementally increasing the scan range until all features of the simulated JV curves were visible.

The example simulated JV curves for forward (from 0 to 500 V) and reverse (from 500 to 0 V) voltage sweeps at different scan rates in Figure 5.1a show hysteresis caused by the mobile ionic charge. The lowest scan rate shows the least hysteresis, indicating that the ions have almost reached a quasi-static distribution for each voltage sampled independent of scan direction. At higher scan rates the ions have insufficient time to respond and thus screen the applied potential, resulting in more hysteresis. These curves also show a higher threshold voltage at which the gradient of the JV curve increases from its initial low-bias slope during the forward scan. The corresponding $g(V)$ values, as a function of forward scan voltage are shown in Figure 5.1b (in the reverse scan $g(V) \approx 1$ for the fast scans and is similar to the forward scan at low scan rates). The regions of the g(V) curves that fall within the grey band in Figure 5.1b are equivalent to $g(V) = 2 \pm 0.2$, this equates to $J \propto V^2$ where the MG law may be applied while allowing for some experimental error. We analysed these regions using the MG equation (Equation 18), to obtain the hole mobilities that would be inferred from SCLC measurements (Figure 5.1c). This range of $g(V)$ values is chosen purposefully to represent a reasonable range of gradients for which a researcher might consider applying the MG law to analyse the JV curve due to experimental errors or insufficient data points/range. For comparison, the hole mobility defined in the simulations (20 $cm^2 V^{-1} s^{-1}$) is also shown (dashed red line). It is evident that mobility values inferred from the forward scans depend strongly on the scan rate, and that applying the MG law to a slow JV scan can overestimate the mobility by more than two orders of magnitude ($\sim$2000 $cm^2 V^{-1} s^{-1}$) due to a different distribution of ionic charge corresponding to each voltage. We conclude that these gradient regions could easily be misinterpreted as falling within the MG regime and regions that lie above the grey-shaded area in Figure 5.1b, i.e. $g(V) > 2$, could be misinterpreted as being due to charge-trapping effects (143,145,147). This misinterpretation is investigated in section 5.3. At sufficiently high scan rates we approach the limit where ionic charge is unable to respond to the rapidly changing field in the device (maroon curves in Figure 5.1b and Figure 5.1c), which corresponds to ionic charge that is effectively frozen in its initial distribution during the JV scan. In this state, the extracted mobility is close to the mobility set in the simulation. This suggests that if a device could be measured with the ions effectively frozen in their equilibrium distribution, then the MG law and other associated analysis might be meaningfully applied. In the following section (section 5.2.4.3) we will investigate this hypothesis.

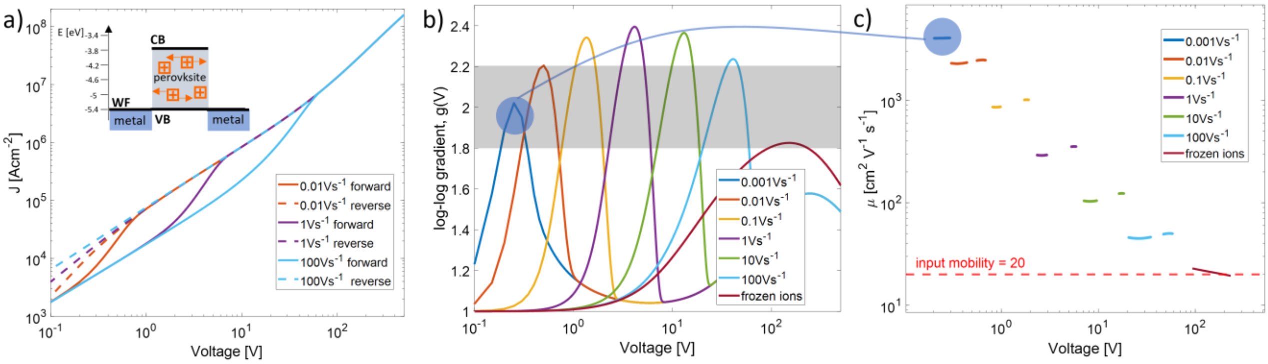

Figure 5.1 Simulated JV sweeps and their analysis. (a) Example JV sweeps at three scan rates of a device represented in the inset with one mobile ionic species. (b) Calculated *g(V)* of the JV sweeps' forward scans in panel (a) with additional scan rates presented, the grey box represents a region of $g(V) = 2 \pm 0.2$ where one may attempt to apply the MG law to calculate μ from experimental data. (c) The corresponding μ calculated using the MG law from the regions of the JV curve where $g(V) \approx 2$ in the grey box of panel (b). The simulation parameters are listed in Table C.1.

We now consider experimentally measured JV curves of perovskite hole only devices. Figure 5.2a-c display results for a thin-film device of architecture shown in the inset of Figure 5.2a, with an approximate thickness of 400 nm for the perovskite layer. The chosen materials and processing techniques are those commonly used in relevant photovoltaic research, where additional thin selective transport layers are included to make the contacts closer to Ohmic than they would otherwise be. Details of the device fabrication are presented in section 3.2.1. The maximum applied voltage was limited to 1.5 V to minimise bias-induced degradation. Figure 5.2d-f display the simulation results for a device approximately the same as the aforementioned experimental counterpart; the energetics and charge carrier densities from the simulation are shown in Figure F.1c-d. These results do not show an agreement with the experimental results in Figure 5.2a-c but do crucially contain shared features in their general behaviours and trends. Concerning these trends, the simulations show the same dependence of JV hysteresis on scan rate, they show a large peak in the *g(V)* values and also show a similar estimation of the mobility, albeit all shifted to a lower voltage range. Meanwhile, there are differences between the simulations in Figure 5.2d-f and the experimental results in Figure 5.2a-c: the simulations give a slightly larger range of current densities and estimated mobilities over the JV sweep, particularly in the lower voltage region, and the location of the *g(V)* peaks is at a lower voltage in the simulations. These differences are likely due to the omission of charge trapping and interfacial states in the simulations, which will be present in real devices, and the error on the values assigned to certain physical input parameters. The estimated mobilities are $\mu_p \approx 10^{-3}\ cm^2V^{-1}s^{-1}$ from the experiments (Figure 5.2c) and $\mu_p \approx 10^{-2}\ cm^2V^{-1}s^{-1}$ from the simulations (Figure 5.2f) in the regions of the JV curve with appropriate values of *g(V)*, we note the values are imprecise due to the large variance in *g(V)* throughout the scans. These values are orders of magnitude smaller than values of electronic carrier mobilities typically reported for $MAPbI_3$ films in the literature ($\mu \approx\ 7.5\ cm^2V^{-1}s^{-1}$ (149) or $\mu = 10 - 44\ \ cm^2V^{-1}s^{-1}$ (150)). A recent communication by Xia *et al.* addressing the mobilities of lead-halide perovskites summarises reported electronic charge carrier mobilities in the literature, where the range of carrier mobility values for metal-halide perovskites given was between $\mu = 0.7 - 600\ c\mathrm{m}^2\mathrm{V}^{-1}\mathrm{s}^{-1}$(151). Assuming the film morphology in this work is similar to those in the studies mentioned, this shows that our calculated mobilities substantially underestimate the actual mobilities. The general agreement between the full device simulations with the experiment implies that some of the non-ideal features of the experimental results (when compared to the results in Figure 5.1) are likely due to the addition of selective transport layers and possibly due to ϕ_{offset} asymmetry, since these are the main differences between the simulated devices in Figure 5.1a-c and Figure 5.2d-f.

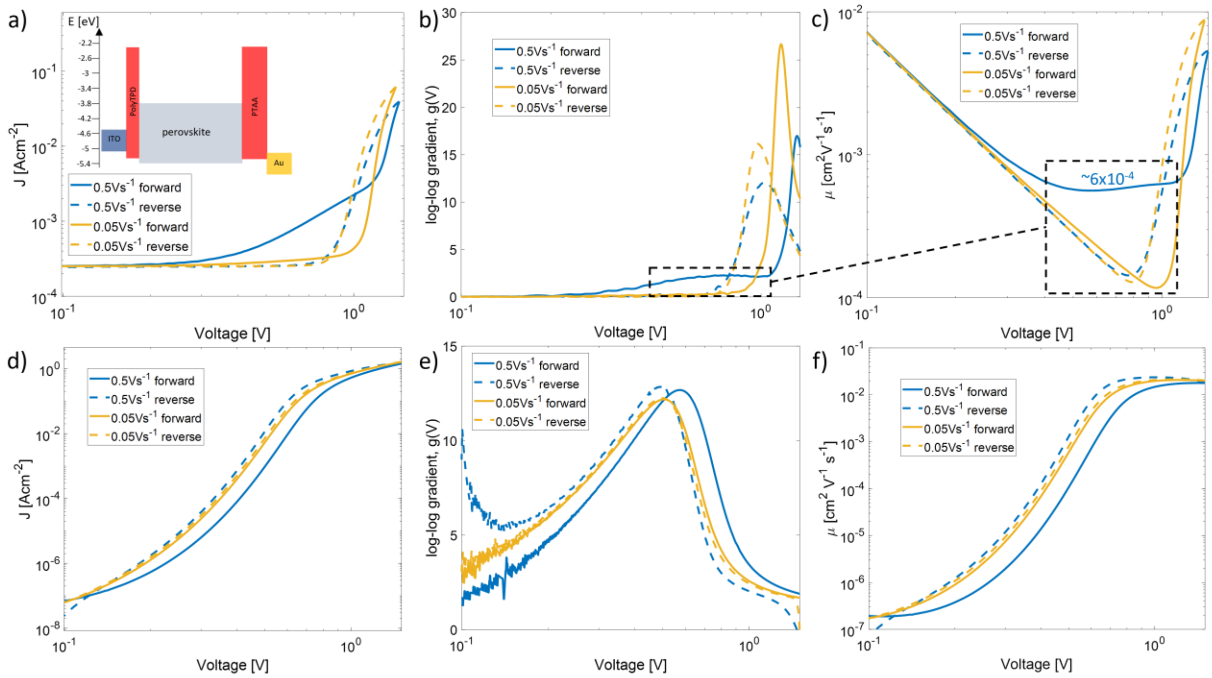

Figure 5.2 Results of JV sweeps from experiment and simulation of a thin film single carrier device. (a) JV sweep experimental results at two different scan rates of a device represented in the inset. (b) *g(V)* of the sweeps in panel (a). (c) μ calculated using the MG law and values from the sweeps in panel (a) with the region of interest highlighted by a black-dashed box. The region of interest is a guide to the eye and does not have the same meaning as the grey region in Figure 5.1b. (d-f) are the simulation results of a device representative of the device investigated in (a-c) using the same analysis techniques. The simulation parameters are listed in Table D.1.

The ionic drift during the JV scans in Figure 5.2 results in hysteresis and contributes to the substantial increases or decreases in current density at intermediate applied voltages. The changes in current due to ionic drift can be explained by the accumulation/depletion of ionic charge increasing or decreasing the electronic current flowing across the interface(s) with the direction and magnitude of this depending on the relative signs of the ionic and electronic charge carriers. This modulation of the electronic current by the accumulation/depletion of ions at the interface(s) might prevent SCLC conditions from arising within this chosen scan range. Additionally, the presence of hysteresis in these JV scans indicates the ionic charge is greatly influencing the electronic carriers' spatial distribution (and thus, the internal electric field and the electronic current density), invalidating assumptions of the MG law and contributing to $g(V) \gg 2$. It is the redistribution of ionic charge, not the injected electronic charge, that primarily determines the electric-field profile in the device.

Figure 5.3 shows the extended-range JV curves of the device measured in Figure 5.2 which display asymmetry between positive and negative applied voltages, which is influenced (partially) by the energetics of the contacts being asymmetric. The asymmetry of the JV shown in Figure 5.3a has been shown by Game *et al.* (59) to also be a function of ionic drift during the measurement, suggesting that JV sweeps of MHP devices cannot reliably indicate contact asymmetry. Figure 5.3b is measured using the pulsed voltage technique that is used in section 5.2.4.3 (the method is described in section 3.3.3) which removes the contribution from drifting ionic charge during the measurement. The results of Figure 5.3b still show asymmetry, although less than is shown in Figure 5.3a, suggesting that contact asymmetry exists in this device and does play a role in the device behaviour along with the mobile ionic charge. We, therefore, conclude that the large peak in the *g(V)* in Figure 5.2 and the underestimated mobility values are due to some combination of asymmetric contacts, the ionic drift during the scans and the additional selective charge transport layers, the exact contributions of these factors are difficult to decouple. We doubt the underestimated mobility is due to the limited scan range used in the experiments/simulations due to the significant plateau in estimated μ at voltages $> 1\ V$ in Figure 5.2f and the significant decrease in $g(V)$ at voltages $> 1\ V$ in Figure 5.2b. From Figure 5.2 it is clear that JV curves of non-ideal single carrier devices give results that should not be analysed using the MG law and, if they are analysed in this way, it is likely that a large under-estimate of the charge carrier mobility is obtained.

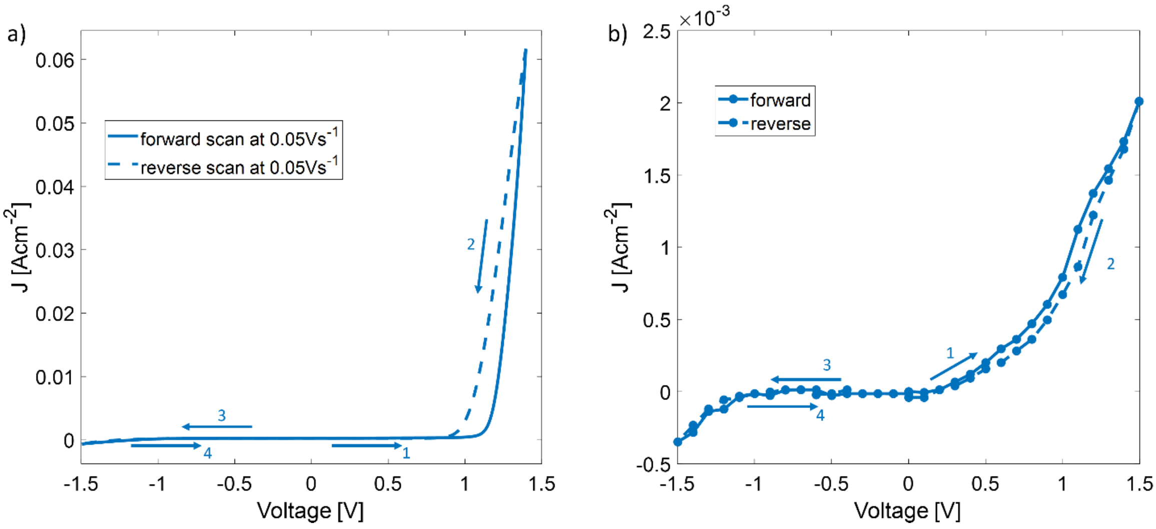

Figure 5.3 The experimentally determined JV curves in the dark from -1.5V to 1.5V of the thin-film device measured in Figure 5.2 and Figure 5.4. a) The JV sweep measured at $0.05\ Vs^{-1}$ in the order depicted by the numbered arrows starting from 0 V. b) the JV curve measured by the pulsed-voltage technique in the order depicted by the numbered arrows starting from 0V. The asymmetry in the current density magnitude in both figures between $V > 0$ and $V < 0$ suggests that the device energetics are asymmetric.

Comparing the experimental and simulation results in Figure 5.2 to the simulation of ideal devices in Figure 5.1, reveals behaviour/trends in common: the direction of hysteresis in the JV curves is the same in both, and the location of the *g(V)* maximum in the forward scan is at a higher voltage when the scan rate is higher in both. We note that there are several differences between the results in Figure 5.1 and Figure 5.2: *g(V)* reaches very high values in the measured devices which was not reproduced in the simulations of the idealised device; the voltage at which the forward scan *g(V)* peaks is less scan-rate dependent than in the simulation of the ideal device, whilst there is a significant disparity in the magnitude of the current densities between the simulations and the experiments. These differences between Figure 5.1a and Figure 5.2a (when compared over a similar voltage range) particularly the latter, can be attributed to the existence of asymmetric contacts and selective transport layers. The limitations of available materials and processing techniques can clearly be seen.

Given the strong effect from mobile ions during the JV measurements and simulations, on both in the magnitude and shape of the JV curves, and the differences in JV hysteresis at different scan rates, it is clear that more sophisticated ways of measuring SCLC in perovskites must be employed. In the following section we investigate a recently developed pulsed voltage SCLC method and the limits of its applicability. An in-depth explanation of the technique is provided in sections 3.3.3 and 5.2.2.1.

5.2.4.3 Pulsed voltage method

Recently, Duijnstee *et al.* published an approach for measuring JV curves without significantly altering the distribution of ions during the scan(65). This technique involves applying a series of short voltage pulses typically of 10s to 100s of ms, with each pulse separated by a return to a reference dc bias voltage (usually 0 V) for a long period of time (> 300 s). The short pulse durations aim to ensure that the ion distribution does not have time to deviate from the reference distribution set at each dc measurement voltage. This method is adopted in this section and referred to as the "pulsed-voltage method", the method used in this chapter is given in sections 3.3.3 and 5.2.2.1 with $V_{pre-bias} = 0\ V$.

Figure 5.4a-c display simulation results where the ionic charge is frozen in its equilibrium (i.e., no (net) energy or mass flowing in or out of the defined system) distribution during the scan (see the section 3.4.1.1 for a detailed explanation of the meaning of the equilibrium condition) but is mobile during the equilibration process. In Figure 5.4a, we only present the forward scans because the reverse scans are identical due to the lack of ion drift during the simulated JV scan. These results are significantly different to those presented in Figure 5.1, showing that the pulsed voltage method is significantly supressing the effect the ionic charge has on the JV curves. We do, however, see changes in the JV curves by varying the ion density: the magnitude of the currents observed, and *g(V)* are affected by the concentration of ionic charge. The extracted MG mobility (Figure 5.4c) is also affected, although the values obtained for this ideal device are within $\pm 50\%$ of the set mobility (i.e., 18-26 cm^2 V^{-1} s^{-1} as compared to 20 cm^2 V^{-1} s^{-1} as the numerical input). The effect of a static equilibrium ion distribution on SCLC characterisation is best demonstrated in Figure 5.4b - the devices containing higher ion densities hardly reach a $g(V) = 2 \pm 0.2$ within the voltage range investigated. These results indicate that devices with high ion densities may not be suitable for the application of the MG law, since their JV curves are significantly different to those with no ionic carriers, and they never reach the same $g(V) \approx 2$ as the case with no ionic carriers, even if the technique can produce reasonable estimates for the mobility.

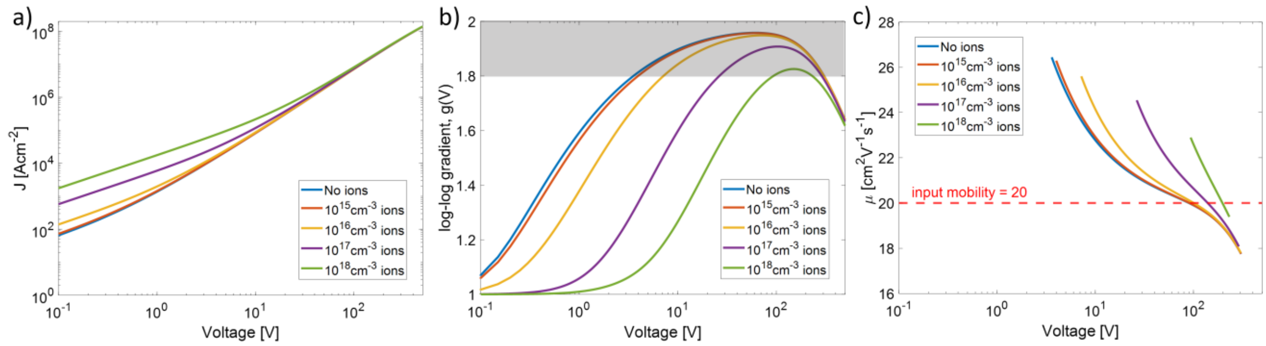

Figure 5.4 Drift-diffusion simulations of JV curves with the mobile ionic charge frozen in its equilibrium position. (a) Simulated JV curves of the same device as in Figure 5.1a with varying ion concentrations, we present only the forward scans because the reverse scans are identical due to the lack of ion motion. (b) Calculated *g(V)* of the JV curves in panel (a). (c) μ calculated using the MG law from the regions of $g(V) \approx 2$ in panel (b).

In Figure 5.4a, as the input ion density increase, the current density increases at low voltages. This is an exact representation of the interfacial doping effect displayed in Chapter 4; the increased ionic charge density is increasing the device conductivity near 0 V. Figure 5.4b shows that in the intermediate voltage regime (up to $\approx 100\ V$) the current-limiting processes are the same as in a device with no ions; however, because of the ionic charge, such space-charge limited current either occurs at different voltage onsets or is even obscured. At higher voltages ($> 100\ V$) in our simulations we observe that a combination of the charge-extraction coefficient at the electrodes (representing the interfacial resistance of a metallic electrode) and the electronic carrier saturation limit (141) starts to limit the increase in current. Both effects could occur in an experiment if these high voltages could be achieved. For the higher ion densities at very high voltages this current limitation dominates the response before any SCLC effect (fully) emerges, as the latter are obscured by other processes. This supports the proposition that the MG law and other associated analyses are not valid for perovskites with high ion densities: this is even in the absence of electronic traps, injection barriers and with ions frozen in their equilibrium state.

As described in Chapter 4, the equilibrium distribution of the ionic charge has a significant effect on the simulated JV curves. As electronic charge redistributes to align the Fermi level in the perovskite layer with the contact workfunctions at the interfaces, the ionic charge redistributes too—it contributes significantly to the space-charge layers at the interface(s) in the same way as electronic charge; either by accumulating or depleting. This not only reduces the density of electronic charge at the interfaces when compared to a semiconductor with no mobile ionic charge, but also modifies the energetic landscape at the interfaces by locally increasing the charge density, reducing the space-charge layer thickness and, in turn, modifying the electric field in the space-charge region. In Chapter 4, the distribution of electric field and electrostatic potential of a single carrier device at equilibrium are shown in Figure 4.2. The simulated electric field and electrostatic potential profiles of devices at 75 V during a JV scan with frozen ions at different densities are shown in Figure 5.5 respectively. These show significant contribution of the ionic charge to the potential distribution and electric field distributions of the bulk and at the interface, even when the ions are spatially fixed during the simulated JV scan. The difference between a device with no mobile ionic charge and $10^{16}\ cm^{-3}$ ionic charge is negligible (the traces are essentially on-top of each other) at this voltage, only is the difference clear when the density is $10^{18}\ cm^{-3}$.

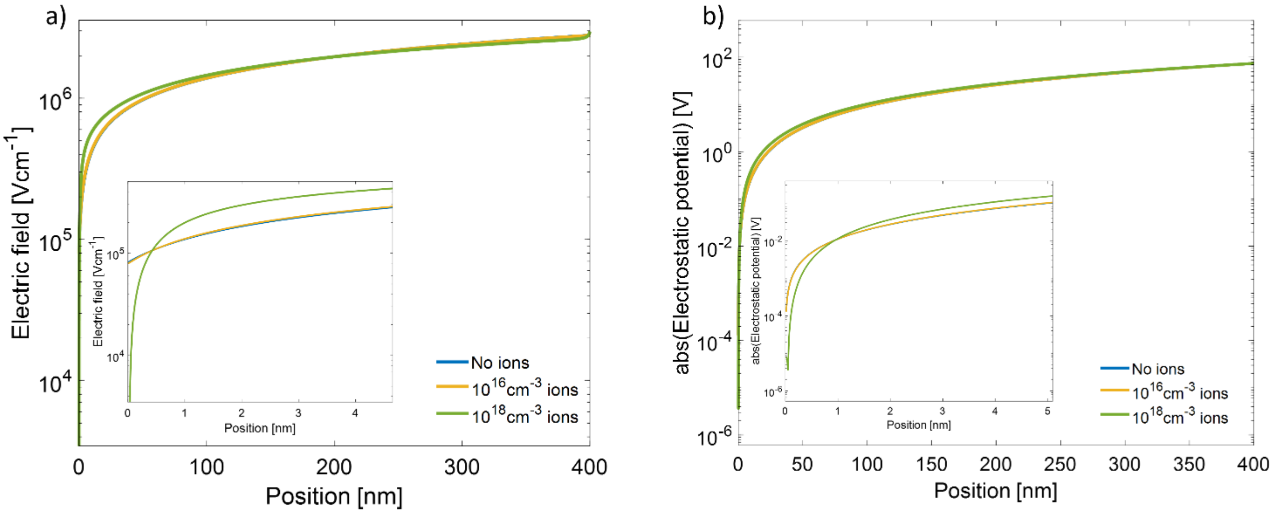

Figure 5.5 The electric field and electrostatic potential in a device at 75V during a JV scan with the ionic charge frozen in its equilibrium distribution. a) The electric field on a logarithmic scale. The insets of both figures show a “zoom in” on the region close to the left-hand interface. b) The magnitude of the electrostatic potential is shown, allowing for a logarithmic scale to be used. Electrostatic potential is negative for the whole device.

Figure 5.6a-c show experimental results for the case where ionic charge is nominally frozen during the JV scan using the pulsed voltage technique. These measurements were carried out on the same device as in Figure 5.2 and the data were obtained by a pulsed voltage method which is illustrated in the inset of panel Figure 5.6a and described in detail in sections 3.3.3 and 5.2.2.1 . The results from this pulsed voltage method are substantially different to those of the JV sweeps shown in Figure 5.2a-c: the ionic charge being ‘frozen’ has greatly reduced hysteresis (it may be that the small yet discernible hysteresis seen in Figure 5.6a is caused by the ionic charge not being entirely stationary for the short pulses and/or some experimental artefacts), yet we still see $g(V) > 2$. In fact, $g(V)$ extracted from the experimental data (as in Figure 5.6b) is somewhat erratic and never consistently ≈ 2. For simplicity, we calculate the mobility over the entire voltage range of 0.2-1.4 V, as shown in Figure 5.6c. The calculated estimates of hole mobility are $\sim 2 - 5 \times 10^{-4}\ \mathrm{cm}^2\mathrm{V}^{-1}\mathrm{s}^{-1}$, sitting orders of magnitudes lower than those reported in the literature, as with the mobilities determined from the JV sweeps (Figure 5.2). This suggests that despite the alternative measurement technique (using pulsed voltages) this does not really make MG analysis applicable or effective for this class of thin-film devices, since the calculated mobility is wrong by orders of magnitude. We present reasons for this in the following.

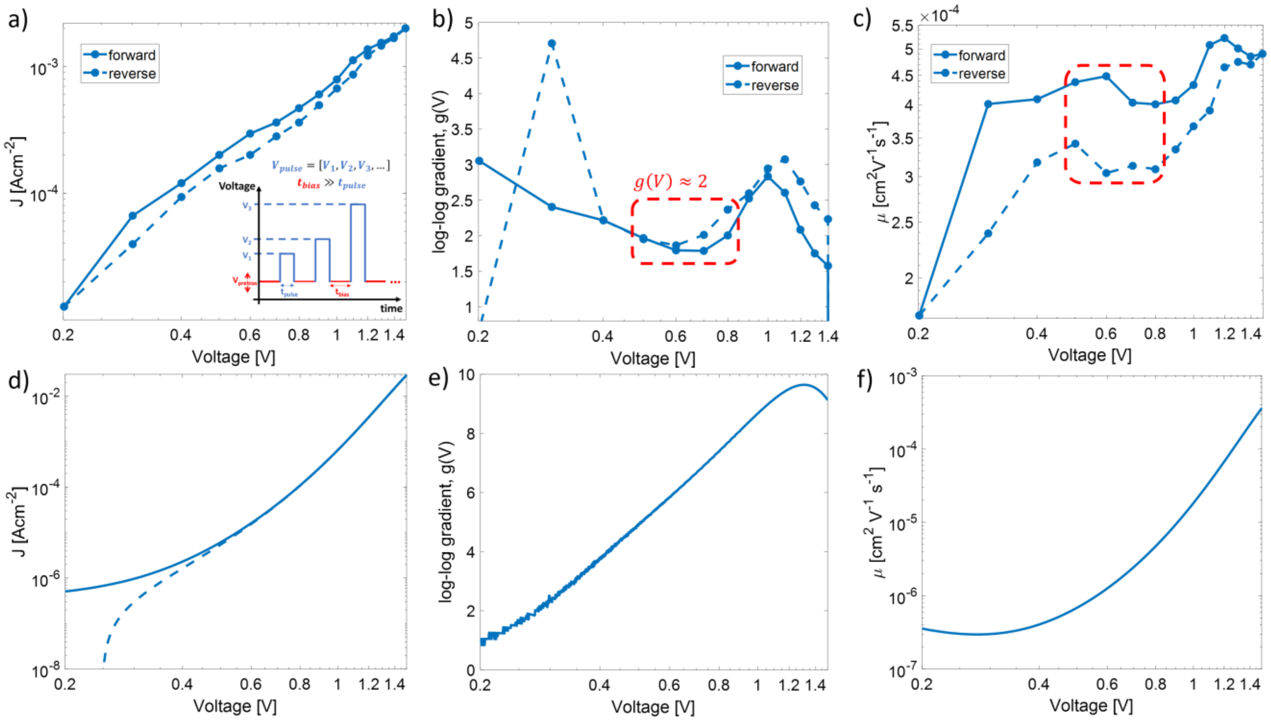

Figure 5.6 JV curves of a thin film device using the pulsed-voltage technique and simulations of them. (a) Experimental JV results of the same device represented in Figure 5.2a but using the pulsed voltage method depicted in the inset. Both forward (solid) and reverse (dashed) scans are shown. (b) *g(V)* of the curves in panel (a). (c) μ calculated using the MG law and values from the curves in panel (a). (d-f) are the simulation results of a device representative of the device investigated in panels (a-c) using the same analysis techniques with an input $\mu = 20\ cm^2\ V^{-1}\ s^{-1}$. The divergence between the forward and reverse scans at low voltages in panel (d) corresponds to capacitive charging/discharging with the frozen ions and is only visible at these very low total current densities. Corresponding simulation parameters are listed in Table D.1.

Figure 5.6d-f show simulations of the experimental case presented in Figure 5.6a-c. The disparity in current density between simulation and experiment that is present in Figure 5.2 is also seen here for the same reasons. Even though through most of the voltage range we see similar current densities, estimated mobilities and *g(V)* peak locations (1.1 - 1.2 V), the simulation shows a much higher *g(V)* at the peak (~9.5) than that of the experiments (~3), indicating that either the parameters of the simulation are not entirely representative of the real device or that the ionic charge is not completely frozen in the experiments, as it is in the simulations. The input mobility (20 cm^2 V^{-1} s^{-1}) and the mobilities (Figure 5.6f) derived from the JV curve (Figure 5.6d) are still orders of magnitude apart, showing that the MG law is ineffective at estimating the mobility of the majority charge carrier in this device and confirming the findings of the experimental results in Figure 5.6a-c.

In order to demonstrate that ionic charge, asymmetric contacts and the selective charge transport layers are still significantly affecting these results, we carry out the same sets of simulations as in Figure 5.6d-f while varying the ion density and then additionally remove the selective charge transport layers. The results are shown in Figure 5.7a-f. With this further investigation we find that in the full devices the ionic charge density in the perovskite layer changes the size and location of the peak of *g(V)*, which could be because of the effects of the built-in potential becoming significant at low ion densities. We also find that the ionic charge density reduces the current density and reduces the estimated mobility, even though the ionic charge is frozen during the JV scan. We also find that removing the selective transport layers only slightly increases the current density and estimated mobilities: the energetics of the metal contacts still matter and, therefore, the reasons for the non-ideal experimental results are indeed the combination of the ionic charge, the additional selective transport layers, and the asymmetric contacts. There is also a significant difference between the higher ion density scans in Figure 5.7a-c and Figure 5.7d-f, particularly in the low voltage region where the devices with selective transport layers (the green and light blue traces in Figure 5.7a) have much lower currents than the devices without selective transport layers (Figure 5.7d), one might suggest that the interfacial doping effect of Chapter 4 is supressed in Figure 5.7a due to the selective transport layers, changing the space-charge field distribution in the perovskite side of the interfacial region when compared to Figure 5.7d, this claim would need further evidence to substantiate it.

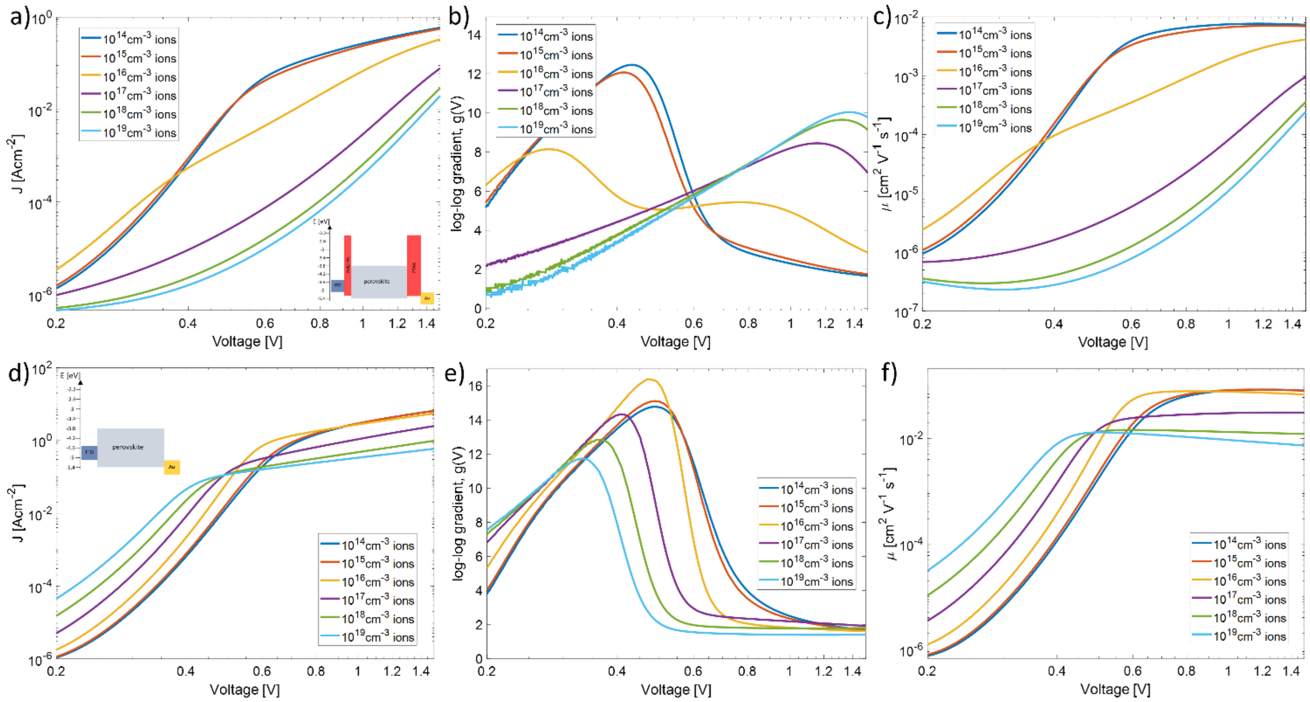

Figure 5.7 Simulations of the device used to produce the experimental results in this chapter (the same simulations as in Figure 5.6(d-f) with the parameters displayed in Table D.1 but varying ion density with the ionic charge frozen in their equilibrium position (a-c) and subsequently also removing the selective transport layers (d-f). (a) shows the JV curves for simulations of the full device, (b) shows the $g(V)$ values and (c) shows the mobilities calculated using the MG law. A heavy dependence of the results on ion density is seen. (d) shows the JV curves for simulations of the device without selective transport layers, (e) shows the $g(V)$ values and (f) shows the mobilities calculated using the MG law.

Altogether, the simulation and experimental results in Figure 5.6 further confirm that thin-film devices of this type are not suitable for analysis with the MG law and even though using the pulsed voltage measurement technique makes a significant difference to the JV curve, it is not sufficient for allowing the MG law to be applicable. We conclude that ionic charge, even when frozen in its initial position in an ideal device, still has a large impact on the JV measurement of the device and the utility of the application of the MG law to it: the simulations show that as mobile ion densities increase, the low voltage Ohmic current is increased (the interfacial doping effect) and the quadratic power law behaviour at high voltages is suppressed. We note that the effects of uniform, static doping on these devices, as described by Röhr and MacKenzie(138), show the same trends and are similar to, but not the same as, the effects due to ions seen here. If conventional doping is present in the perovskite(152) in addition to the mobile ionic defects considered here, both effects would simultaneously contribute to the conductance with the strongest of the two controlling the device behaviour. Our experimental results suggest that thin-film devices and/or other devices without ideal, symmetrical, ohmic contacts (and especially with additional selective transport layers) should not be characterised with the MG law, even if the ionic charge is static during the measurement by using the pulsed voltage method. We further propose that the original analyses derived from the MG law that use the same set of assumptions should not be used for analysing, for example, the so-called "trap-filled limit"(136), this will addressed explicitly in section 5.3.

While experimental results of the pulsed voltage method on a thin-film single-carrier device did not yield correct mobilities, the SCLC analysis of simulated JV curves for ideal devices with lower concentrations of 'frozen' mobile ions (Figure 5.4a-c) yielded mobilities close to what was expected (the input mobility). We will now investigate the validity region for SCLC measurements for which the application of the MG law could meaningfully be applied in the frozen ion regime.

5.2.4.4 Is there a region of validity for SCLC measurements of metal halide perovskites?

In order to determine a region of validity for using the MG law for analysing SCLC measurements, a parameter search is conducted: a series of simulations of the same ideal device shown previously where the contact workfunctions are varied symmetrically, i.e., the workfunctions of both contacts are always equal while ϕ_{offset} is increased, and the ionic density is varied. As before, JV measurements from 0 to 500 V with the ionic charge frozen in their equilibrium distribution are simulated. The maximum *g(V)* in the JV is found (depending on the simulated device this peak could occur anywhere in the range) and the voltage and current density at which this maximum occurs are used to calculate the mobility using the MG law. For our simulation results, this process selects for the calculated mobility in the JV curve closest to the set mobility (20 $\mathrm{cm}^2\ \mathrm{V}^{-1}\ \mathrm{s}^{-1}$). If a region of the JV curve does not fall within $J \propto V^{2\pm0.2}$, i.e., $1.8 < g(V) < 2.2$ (as depicted in Figure 5.8a)), then this is contained in the red shaded box depicting a region falling outside $J \propto V^2$ experimentally. The values of $g(V)$ for this set of simulations are given in Figure F.2. The results are presented as a heat-map in Figure 5.8a. Considering that these devices are ideal and should give close to perfect mobility values, these results show that a good estimate of the mobility can be obtained from the MG law for regions where $g(V) \approx 2$ for a device with no traps or interfacial states if the contacts are very close to perfectly Ohmic and where the ionic charge carrier density $\leq 10^{18}\ \mathrm{cm}^{-3}$. We also find that ideally the ion density should be $\ll\ 10^{18}\ \mathrm{cm}^{-3}$, otherwise the region where $1.8 < g(V) < 2.2$ is very small and the contacts must be perfectly Ohmic. There is a trade-off between how perfectly Ohmic the contacts must be (the amount of ϕ_{offset}) and the ion density: if the $\phi_{offset} > 0.08\ \mathrm{eV}$, the ion density must be $< 5 \times 10^{15}\ \mathrm{cm}^{-3}$ for MG analysis to remain valid. We note that the exact values of the above quantities depend on the assigned density of states and effective mass of electrons and/or holes (which are values commonly used in the literature) but the trends will still persist even if the density of states changes significantly. If the device falls outside of these given limits, the JV curve will not reach the SCLC regime since *g(V)* never reaches the range $1.8 < g(V) < 2.2$ (even if the ions are frozen) and these devices cannot be meaningfully analysed using the MG law or other related analytical frameworks.

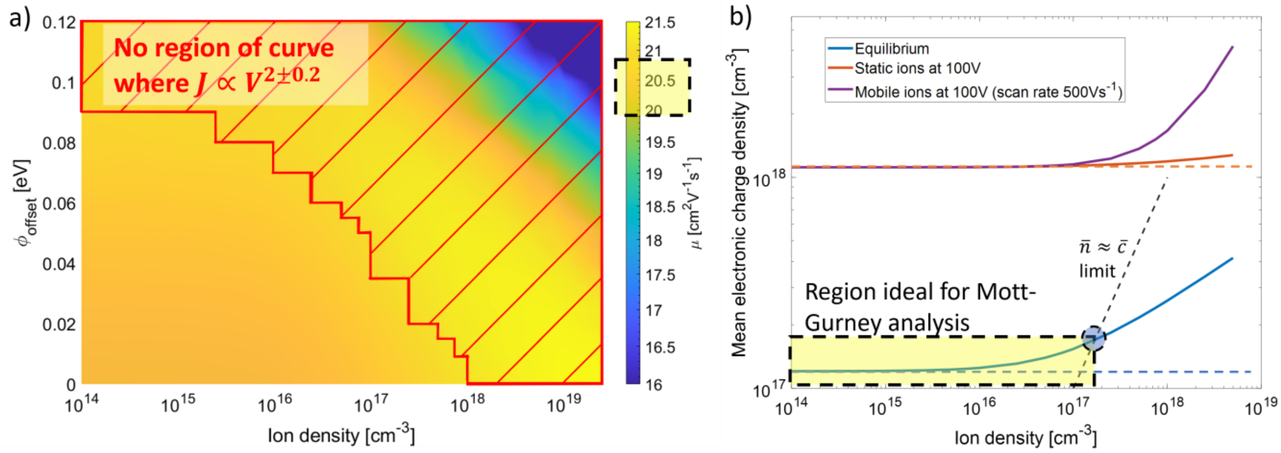

Figure 5.8 Analysis of drift-diffusion simulations showing the limits of the application of MG analysis to perovskite devices of 400 nm thickness. (a) A heat map representing the accuracy of the calculated mobility using the MG law for a set of contact energies (workfunction offset) and a set of ion densities. The set mobility is 20 cm^{2}V^{-1}s^{-1}. The region outside the colour map is represented in red shading. (b) Calculated mean electronic charge density for perovskite layers of different ion density at two points during a JV scan (0 V and 100 V). The black box with yellow shading represents a region where the current density and the internal electric field of the device is defined by electronic charge. This is true because the ion density does not have an appreciable effect on the electronic charge in the device at 0 V and 100 V. By examining the ion densities covered by the black box in (b) and noting the region of the same ion densities in figure (a) we can see an area of yellow/orange, indicating the value of mobility is the same as the input mobility (20 cm^2 V^{-1} s^{-1}). In this region of yellow/orange, we can see a set of parameters that gives the mobility calculated using the MG law that yields the correct result. This region is the part of the colour bar in yellow/orange highlighted by the black box. The boxes in panels a) and b) are showing cause and effect. This is a parameter set ideal for the application of the MG law. The blue circle in panel (b) shows the intersection of the calculated charge density at equilibrium with our suggested approximate limit for MG law analysis: $\bar{c} < \bar{n}$ (black dashed line). $\bar{c}$ and $\bar{n}$ are the cation density and majority charge carrier density averaged over the thickness of the device respectively.

We now present investigations into the dependence of the observations from Figure 5.8 on perovskite layer thickness. Figure 5.9 shows results from 1 μm thick devices undergoing JV scans up to 1500 V revealing that the constraints on ϕ_{offset} can be stretched by having a thicker device; the region of validity in Figure 5.9a is stretched in the y-axis when compared to Figure 5.8a. There appears to be no such change to the dependence of the validity region in the ion density axis. Figure 5.9b compares the electronic charge density averaged over the device thickness with the ion density. To demonstrate the universality of the limits described in the chapter, this graph is produced from a device without ohmic contacts, along the blue line from Figure 5.9a. We see that in regions where $1.8 < g(V) < 2.2$ (also represented by the yellow shaded dashed box) the electronic charge density is significantly greater than the ionic charge density suggesting further refinement to the limit $\bar{c} < \bar{n}$ is needed. Figure 5.9 is supplemented by Figure F.3a-c where a $100\ \mu m$ thick device with $\phi_{offset} = 0.3\ eV$, the JV curves show no region where $1.8 < g(V) < 2.2$ but the extracted mobilities at the maximum $g(V)$ yield very accurate results. This set of results is in the same region of calculated mobilities as the very bright yellow region in the red-shaded box of Figure 5.8a. We note that the application of the MG law would not be valid for the device in Figure F.3a-c due to the lack of SCLC, even though the mobility estimate is accurate.

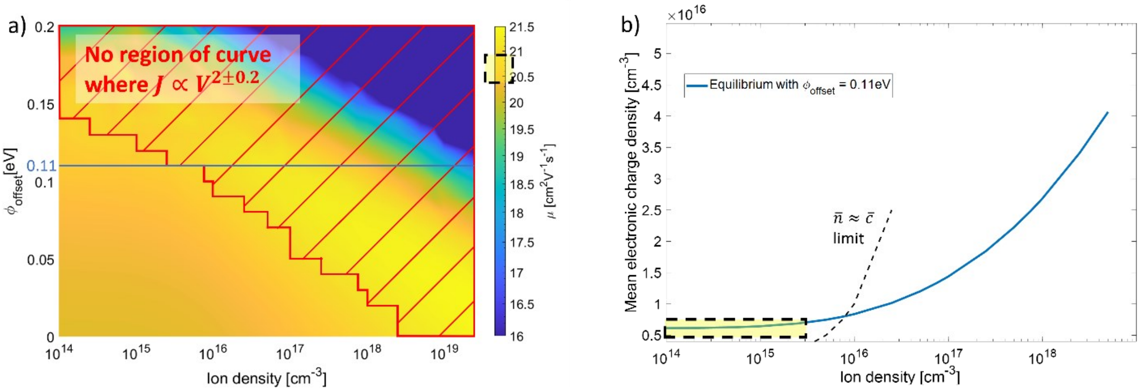

Figure 5.9 Analysis of a set of drift-diffusion simulations explaining the limits of the application of the MG law to perovskite devices of thickness $1\mu m$. (a) A heat map representing the accuracy of the calculated mobility using the MG law for a set of contact energies (workfunction offset) and a set of ion densities. The set mobility is 20 $\text{cm}^2\text{V}^{-1}\text{s}^{-1}$. The red shaded region represents the simulated JV curves where *g(V)* never entered the selection zone for MG analysis. (b) The calculated mean electronic charge density for perovskite layers of different ion density at equilibrium at 0.11eV ϕ_{offset}. The blue line on figure (a) is where the calculations to produce figure b are made. The region highlighted by a black-dashed box filled in yellow in (b) falls under the limit $5\bar{c} < \bar{n}$ and corresponds to the regions of the colour-map with mobilites withing the black-dashed box on the colour-scale in (a), this is where the MG law can be meaningfully applied.

To finalise the thickness dependent investigation, Figure 5.10 investigates devices of $\phi_{offset} = 0.2\ eV$ with varying thicknesses, confirming the observations from Figure 5.9 and Figure F.3 that larger offset can yield SCLC regions in thicker devices but with minimal changes to the validity region with respect to ion density (Figure 5.10b). Figure 5.10 also confirms the observation from Figure F.3c that, curiously, the MG law can yield accurate μ

estimates at $g(V)$ maxima (Figure 5.10a) without any clear sign of SCLC, the cause of this observation is yet to be understood. Figure 5.10c does, however, reveal that very thick devices ($> 10\mu m$) may not be realistically measurable due to the very high voltage required to reach the maximum value of $g(V)$ in the JV curves.

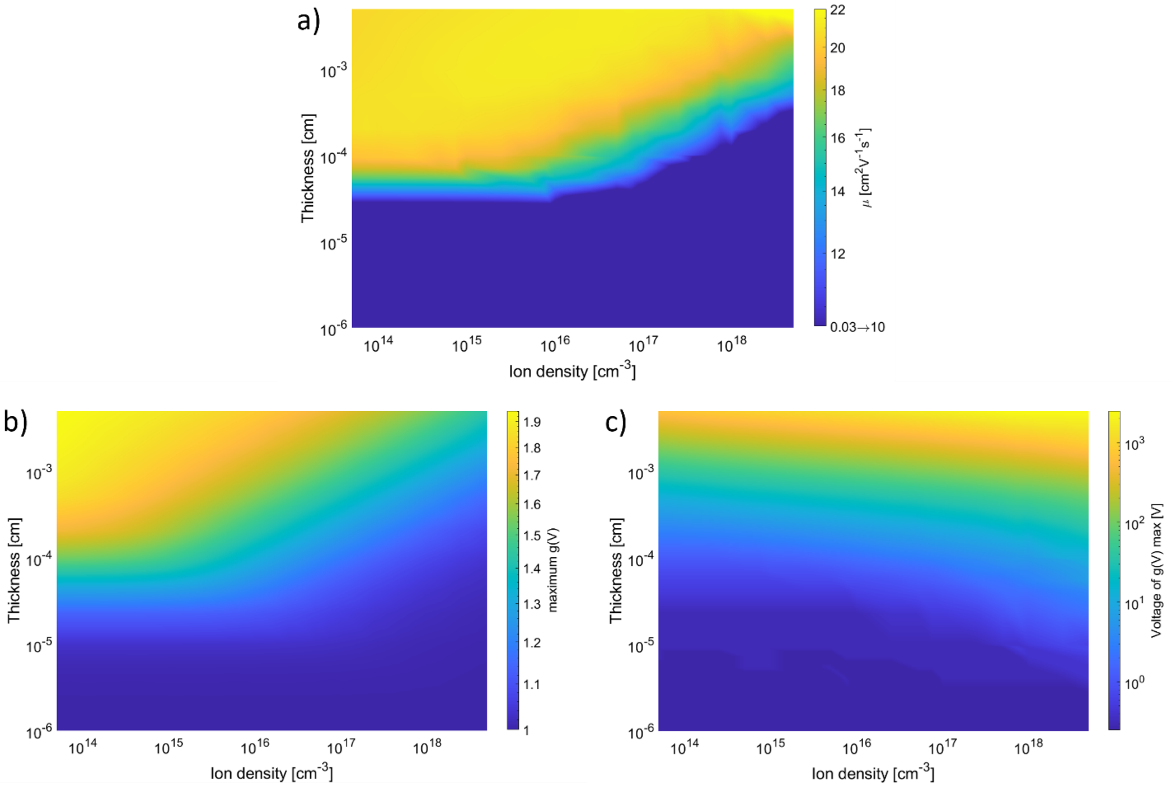

Figure 5.10 Heat maps of results from JV simulations to 2000 V with ionic charge frozen in their equilibrium distribution of a device with $\phi_{offset} = 0.2\ eV$ whilst varying the thickness of the active layer. (a) The mobility calculated using the MG law at the position of maximum g(V) in the JV curve. Note that the dark blue colour refers to a range of values from $\mu = 0.03 \rightarrow 10\ cm^2V^{-1}s^{-1}$, this was done such that the colour change is maximised near the mobility set in the simulations ($\mu = 20cm^2V^{-1}s^{-1}$). (b) the maximum value of $g(V)$ during the simulated JV curves, the values of $g(V) > 1.8$ indicate a SCLC regime has been reached. (c) the voltage at which the maximum value of $g(V)$ occurred during the JV scan.

Based on the observation that the region of validity for SCLC measurements depends on ϕ_{offset} and the ion density, and by noting that ϕ_{offset} is related to electronic charge carrier density (Equation 11), we conclude that the relative density of the ionic to electronic charge must be substantial. A refined limit of these relative densities is given below.

The explanation of the observation of ion density limiting $g(V)$ in a device even when it is static during the JV scan is shown in Figure 5.8b and Figure 5.9b. They present the average electronic charge carrier density ($\bar{n}/q$, where q is the electronic charge) in the perovskite layer of 400 nm and $1\ \mu m$ thickness respectively and is calculated using:

$$\bar{n} = \frac{q}{L}\int_0^L [n(x) + p(x)]\, dx$$

Equation 21

In Figure 5.8b, the results are for points at 0 V and 100 V (to represent an arbitrary point along the JV curve) during the same set of JV simulations (results at 20 V are given in Figure F.4a). First, we focus on the red and blue curves where the ion density is frozen. The subtraction of these curves is equal to the charge injected into the device during the JV scan (results showing the amount of injected charge explicitly are shown in Figure F.4 b and Figure F.4c). As the ion density increases in the perovskite, the electronic charge density at 0 V increases; the same happens to the electronic charge density at 100 V (and 20 V) until we reach the approximate limit where the ion density is comparable in size to the electronic charge carrier density at equilibrium ($\approx 10^{17}\ cm^{-3}$ for both at 0 V). This limit is depicted by the vertical, dashed black line in Figure 5.8b. At this limit the amount of injected charge starts to decrease as the high density of static ions at the interfaces limits charge injection: the subtraction of the red and blue traces decreases past this limit. This explains the apparent trade-off between workfunction offset and ion density in Figure 5.8a. This same limitation causes the trade-off seen in Figure 5.9a, but the charge densities are different because the device thicknesses are different. The electronic charge injection limitation by the ionic charge (Figure 4.2 and Figure 5.5 show the causes are the changes in electric field profile) begins at an even lower ion density for devices with higher ϕ_{offset} because there is less electronic charge in the device at equilibrium. Upon analysing the magnitude of injected charge (shown in figures Figure F.4a and Figure F.4c) we note that the influence of the ionic charge on the injected charge begins before $\bar{n} \approx \bar{c}$, this allows a more refined limit to be placed. We, therefore, propose a theoretical guide/limit for MG analysis: the electronic charge density initially (at 0 V) in the perovskite must be approximately 5 times higher than the ionic charge density for the analysis to be applicable in the frozen ion measurement regime ($5\bar{c} < \bar{n}$). This guide/limit is likely to be conservative, but it ensures that the limit is generally true and independent of the density of states for electrons/holes.

To demonstrate the implications of this claim, we can estimate an upper limit of the electron charge carrier density in a perovskite device with ideal Ohmic contacts at equilibrium and compare this to likely concentrations of ionic charge in perovskites. We take the density of free electrons expected when the Fermi level reaches the perovskite conduction band edge as this upper limit for the average concentration at equilibrium (n_0). Details of this estimation are shown in Chapter 8Appendix F, section Chapter 8F.2. We obtain an approximate upper limit of $n_0 \leq 2 \times 10^{18}\ cm^{-3}$ for $MAPbI_3$. We note that the effective mass of holes in these materials is similar to or higher than that of electrons ($0.29m_e$(153)) which would give a higher upper limit for the equivalent hole device (a factor of ~ 1.5 times higher). As stated above, ion densities must be approximately 5 times lower than the device's equilibrium electronic carrier concentration for the Mott-Gurney law to apply to an ideal device in the frozen ion regime, this gives an upper limit on ion density of $\bar{c} < 4 \times 10^{17}\ cm^{-3}$. The ion density would have to be significantly lower than this for devices without ideal Ohmic contacts, since the 0 V electronic charge carrier density would be lower. A further demonstration of the $5\bar{c} < \bar{n}$ limit is from Figure 5.9b shows that in cases of non-ideal Ohmic contacts, a thicker device and low ionic charge density, the electronic charge density is significantly higher than the ionic density where the MG law could be meaningfully applied.

The purple trace in Figure 5.8b shows the electronic charge density for a JV scan where the ions are mobile. The scan rate is selected such that hysteresis at 100 V for high ion density devices is very large and is very high but is necessary for demonstrating these effects when applying such high voltages, this also shows that very fast scan rates do not necessarily achieve the same results as the pulsed voltage technique (red trace). Similar discrepancies between the red and purple traces can be found at much lower voltages with much lower scan rates (see Figure 5.1a), this example demonstrates one of the ways in which the electronic charge density is greatly influenced by mobile ionic charge near the voltages analysed in Figure 5.8a and Figure 5.9a. In this example (the purple trace of Figure 5.8b) a very large amount of electronic charge injection is induced by the redistributing ionic charge. At other points in the JV scan (or at different scan rates) the magnitude of this influence changes and results in the hysteresis we see in Figure 5.1a. This result, further to the results from Figure 5.1, shows that the amount of injected electronic charge is very dependent on ion drift in devices with higher ion densities and that SCLC analysis should not be performed without frozen ions. Interestingly, in Figure 5.8b the purple trace also shows that if the ion density in the 400 nm perovskite layer is very low ($\leq 10^{15}\ cm^{-3}$ in this case) compared to the electronic charge density (by many orders of magnitude), there is little difference between a JV sweep and the pulsed voltage method, so a fast JV scan is an appropriate measurement technique.

We now comment on the constraints implied by our limit $5\bar{c} < \bar{n}$. Such Ohmic contacts would be very hard to find because of MAPbI$_3$'s $E_c \approx -3.8\ eV$ and $E_v \approx -5.4\ eV$. Examples of feasible metallic contacts for thin film devices are platinum and calcium. None of the metals commonly used for solar cell research are viable. As demonstrated earlier in the text, the constraints on ϕ_{offset} can be stretched by increasing device thickness and, therefore, gold and aluminium (giving $\phi_{offset} \approx 0.3\ eV$) may work for very thick devices. As described earlier, unfortunately, the thicker the device, the higher the voltage required to reach the MG regime (this is the example shown in Figure F.3 and evident in Figure 5.10c).

The density of mobile ionic charge in MHPs is quoted as high as $10^{18} - 10^{19}\ cm^{-3}$ in some theoretical models and experimental results (11,26,40,43–45,154,155) but in some other studies as low as $10^{16} - 10^{17} cm^{-3}$ (46–48) and sometimes even lower ($\approx 10^{13}\ cm^{-3}$)(49). A more detailed discussion of the mobile ionic vacancies in MHPs is given in section 2.4.3. Determining mobile ion densities accurately is still challenging (114). If this range of values is true, then it suggests that the validity of the MG law, which we have shown requires mobile ion density to be less than approximately 5 times equilibrium electronic density, may depend on layer morphology and perovskite composition. In many cases, though, it will not be known whether this mobile ion density limit is satisfied.

Finally, we note that the estimated mobilities in large portions of the red shaded box of a are reasonable and even though these device simulations produced no regions of the JV curve where $g(V) \approx 2$, the mobility determined from the peak of the JV is still very close to the value entered in the simulations (20 cm^2 V^{-1} s^{-1}). The only region where the determined mobility significantly deviates from the correct value is where $g(V)$ approaches 1.5 (which is broadly true for all the simulation results in this section). The observation that the MG law can extract reasonable mobility estimates with many different combinations of device parameters, even though the framework for its derivation is no longer valid, shows that there is more research to be done to fully understand the details of these results.

5.2.5 Conclusion and future work

We conclude that even measurement techniques that do not allow the ionic charge to move and that only probe electronic responses to applied voltage do not guarantee the applicability of analytical SCLC theory to the results. In its equilibrium position, increasing the mobile ionic charge increases the amount of electronic charge in the device but decreases the amount of injected charge which results in the MG regime not being reached and/or the wrong mobilities being calculated. The ionic charge accumulates at the interfaces as part of the space-charge regions that are normally formed at equilibrium, increasing the space-charge density and decreasing the width of the space-charge regions. This alters the local electric field in the space-charge regions. We have identified the controlling factor impacting the MG law's applicability as the relative densities of the ionic and electronic charge in the device; namely, the ionic charge density needs to be at least five times lower than the electronic charge density at equilibrium. If this condition is met by achieving sufficiently Ohmic contacts on a device with low ion densities (< 5 times electronic charge density), the ionic charge has little effect on any JV measurement so there is no need to modify the standard measurement procedure (with pulsed voltages, for example). The limits on contact energetics can be stretched by increasing perovskite layer thickness. Unfortunately, very thick devices ($>> 1\mu m$) require applied voltages with which it is experimentally inaccessible to reach the MG regime. Other features in real devices, including trap states and interfacial states, can affect SCLC measurements. The precise nature and origin of electronic trap states in metal halide perovskites are still unclear and varies significantly between perovskite compositions; thus, trap states are currently not well accounted for when modelling perovskite devices and analysing measurements of them. It is also challenging to find electrode materials that lead to ideal Ohmic contacts, and the density of ionic charge (particularly for polycrystalline thin films) is difficult to control and likely to be too high. We, therefore, suggest that it is difficult to make a single-carrier thin-film perovskite device that can be analysed using the MG law and its associated analyses. We demonstrated this through our own set of experimental results and recommend that metal halide perovskite devices should only be analysed with the MG law and associated techniques when the mobile ion density and contact energetics (workfunction offset) fit within the limits outlined by this work.

This work reveals the possibility of testing the validity window on several devices with purely ohmic contacts. If, say, a small $MAPbI_3$ single crystal could be fabricated with platinum electrical contacts, that may be suitable for coming close to the validity region.

5.3 Investigating the measurement of trap-filled-limits of metal halide perovskite JV curves

5.3.1 Abstract

A common analysis performed in conjunction with the application of the MG law to the JV curves of single carrier semiconducting devices is the V_{tfl} equation. This has been used to extract an estimate for the density of electronic charge traps in MHP devices. The interpretation of the JV curves of single carrier devices for the application of the MG law (addressed extensively in section 5.2) and the V_{tfl} equation has been of recent focus in the research community. Here, we provide commentary and analysis of the recent findings in the literature and carry out drift-diffusion simulations to analyse apparent voltage onsets in JV curves and the resulting extracted trap densities of MHP single carrier devices. We find that if the JV scan rate is slow, the mobile ionic charge in the MHP can create a “fake” V_{tfl} region. If this region is incorrectly used to extract a trap density, the obtained value is comparable to those previously reported in the literature.

5.3.2 Methods

Driftfusion simulations of JV sweeps were carried out using the methods described in section 3.4.1.2.

5.3.3 Introduction

In addition to applying the MG law for mobility extraction, it is common to also employ an analytical expression to extract the trap density of the device being measured. Identifying the trap density in a single-carrier device directly from the measured SCLC JV curve is, in principle, possible; however, one must ensure that the model being used accurately reflects the underlying physics of the device. One of the most used models for extracting trap densities from SCLC data obtained from perovskite single-carrier devices is Lampert’s trap-filled limit

(TFL) model, a highly simplistic model that assumes a single, discrete trap level and derives from the MG law. The effect of such a trap level manifests itself in the JV curve as a region of very steeply increasing current density with voltage (i.e. with $\mathrm{d}log(J)/\mathrm{d}log(V) \gg 2$). This region is referred to as the trap-filled-limit as traps are assumed mostly full at its onset (136). The model assumes that an Ohmic regime (with a reduced fraction of free charge-carrier density due to traps) is observed at low voltages, and that the transition voltage, V_{TFL}, from this Ohmic regime to a MG regime is observed once traps are filled,

$$V_{\mathrm{TFL}} = \frac{qn_{\mathrm{t}}L^2}{2\epsilon_0\epsilon_{\mathrm{r}}}$$

Equation 22

where n_{t} is the trap density. This expression can thus, in principle, be used to infer a trap density if V_{TFL} can be identified and if this voltage onset is indeed due to traps and not some other physical effects.

In section 2.4.3 I discussed defects, traps, and mobile ions in MHPs. From this discussion it is clear that the nature of electronic traps in this material class is not very well understood and is thought to be complicated by the atmospheric conditions, illumination and exact stoichiometry composition of the perovskite. As such, an estimation of the trap density in MHP layers/crystals would be valuable. In the previous section (section 5.2) I found that the measurement of JV curves of single carrier devices is easily affected by high densities of mobile ionic charge, and one must be careful to ensure that the ionic charge is not affecting the JV curve before analysing it. I also found that unless the mobile ionic defect density is low enough, SCLC measurements of MHPs cannot use the MG law to determine the charge carrier density. Since Equation 22 is derived from the MG law, this calls into question the validity of the technique. In the following we discuss the implications of using Equation 22 on a MHP device JV curve.

5.3.4 Literature, results, and discussion

Duijnstee *et al.* and Le Corre *et al.* (49,65,135) noted that for the trap-filled limit to be visible in a JV curve in typical perovskites a trap density of 10^{11} cm^{-3} needs a layer thickness of at least 100 μm and for a trap density of 10^{16} cm^{-3} the thickness can be 400 nm. Therefore, very high-quality single-crystal devices need to be very thick, and, because of this, any trap densities quoted outside these limits are partly due to other measurement/device artefacts. They also investigated the effect mobile ionic charge has on the measurement, noting that the scan rate needs to be sufficiently high to ensure that ions do not affect the measurement dynamically. To circumvent this, they used the pulsed voltage measurement technique used in section 5.2.4.3 and described in section 3.3.3. Even though this method gave a better estimate for trap density than that obtained from a traditional voltage sweep, the estimate for the trap density was off by 1 or 2 orders of magnitude. This was suggested to be due to the ionic charge "shielding" the electronic charge from the traps. In order to obtain a better result, the authors suggested fitting the experiment to a drift-diffusion simulation for more reliable results.

Fitting simulations in this manner must be done with caution, however, because multi-parameter fits for such complex models can present many different combinations of parameter values for solutions (local minima); so an approach similar to *Neukom et al*. (156) where simulations are used to reproduce measured results of several (nine in this case) different experimental techniques, thus parameter correlation is minimized due to the combination of various techniques, increasing the reliability of the parameter fits and is therefore preferable. Obviously, this is very labour intensive and is an impractical approach to take in most cases. We also note that the explanation of ionic charge "shielding" the electronic charge from the traps as the mechanism for this process is somewhat speculative. Another explanation we suggest is that the higher ion density in the device is increasing the electronic charge density in the device (the interfacial doping effect from Chapter 4) and as a result, the traps are being slowly filled at equilibrium or very low voltages. The increase in electronic charge due to the interfacial doping effect in the device is altering the trapping process such that the sudden increase in current at V_{tfl} is not observed. The V_{tfl} region of the JV curve is being removed by the existence of mobile ionic charge, but only by the increase in electronic charge density due to their presence in the device.

To demonstrate the point Le Corre *et al*. (49) have made about the influence of mobile ionic charge on the measurement and to suggest a broader application of their point, we analyse the causes for features observed in other JV curves presented in the literature which do not use the pulsed-voltage method. We show that this region can be seen without traps at all, only with ions and a slow JV sweep measurement. If this region is observed during an experiment, it could potentially be mis-interpreted as resulting from trapped charge. The effect ionic charge has on this method of analysis is more general than originally thought. We now present results from our own simulations.

Figure 5.11 shows current-voltage curves we simulated for a hole-only metal-semiconductor-metal perovskite device with ideal ohmic contacts. The perovskite layers contained: no traps and no mobile ionic charge, traps (10^{14} - 10^{15} cm^{-3}) and no mobile ionic charge, or no traps and one positively charged mobile ionic species (with an initial uniform density of 10^{18} cm^{-3}). The software package ASA was used to simulate the cases with traps and no ions, and the software package Driftfusion (88) was used to simulate the case with mobile ions and no traps, both software packages were used to simulate the case with no traps and no mobile ions and showed good agreement (the blue traces with pink and yellow markers in Figure 5.11a which overlap perfectly).

The JV curve for the device with ionic charge and no traps in Figure 5.11a (black trace) corresponds to a very low voltage scan rate (the system is in a quasi-steady state), so the mobile ions have reached a different equilibrium distribution for each voltage point. The presence of the ions results in significantly higher currents through the device via the interfacial doping effect described in Chapter 4 (consequently two current ranges have been used on the y-axes). Additionally, the presence of mobile ions results in a change in slope of the current-voltage curve ($\mathrm{d}log(J)/\mathrm{d}log(V)$) occurring at a voltage which could be misinterpreted as the trap filling limit voltage, V_{tfl}, yielding an apparent trap density in the material despite an absence of traps. This “fake” V_{tfl} regime is then treated as a real one: the current-density and voltage point at the onset of the steep region where $\mathrm{d}log(J)/\mathrm{d}log(V) > 2$ (this region can be easily seen in the slower JV scans in Figure 5.4b, which are identical simulations to this one) is extracted and used to determine a trap density. This trap density is then used in a simulation of an identical perovskite device but without mobile ionic charge (using ASA). The trap state is considered as a uniform trap density exactly in the middle of the perovskite bandgap. This result is the solid blue trace in Figure 5.11a. The device with no mobile ionic charge and a low density of deep traps is the assumed condition of MHPs characterised with the V_{tfl} equation in the literature and from our simulation results, this device does not have the same appearance as the original JV curve – the curve with only mobile ionic charge and no traps. An additional point to note from Figure 5.11a is the existence of the interfacial-doping effect at low voltages (seen by the higher current density of the black curve *vs* the blue curves) and that the change in current due to the interfacial doping effect is far greater than the change in current due to the introduction of traps (blue curve with yellow markers *vs* blue curve). As such, if this perovskite device contained a low density of traps, the change in current at low voltages would be undetectable due to the interfacial doping effect.

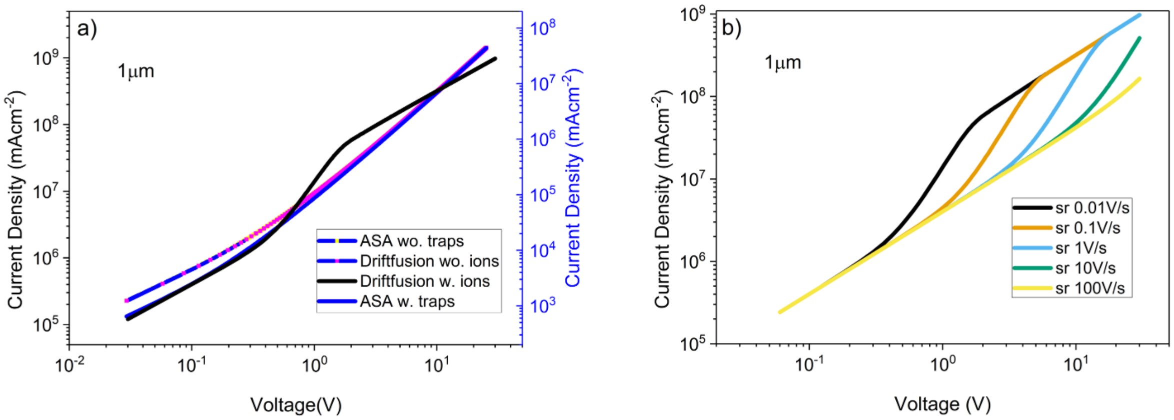

Figure 5.11 A set of simulated JV curves displaying the appearance of a “trap-filled limit” when no traps are present for a perovskite of 1um thickness. a) Includes an ion free Driftfusion simulation to show agreement between ASA and Driftfusion simulations. Panel b) demonstrates the effect of scan rate on the simulation. The ranges of the y-axes have been kept constant in all panels, so the gradient of each line is equivalent. The simulation parameters are identical to those listed in Table C.1, in the cases where ASA is used there is no ionic charge density, and the traps are set as a uniform level with $E_t = -4.6\ eV$.

Figure 5.11b shows the consequence of the mobile ions not reaching a steady state distribution whilst sweeping the voltage at higher scan rates. For a forward scan, the transition to a steep region of the JV curve shifts to higher voltages as the scan rate increases (this is seen again in Figure 5.4b). The opposite is the case if the scan is performed in the reverse direction. These observations indicate that if the mobile ionic charge were already displaced from a uniform distribution for another reason, such as screening a built-in potential or following an applied pre-bias voltage, the steep region of the JV curve could occur at an even lower voltage than the quasi-steady state case. This could be misinterpreted as resulting from an even lower trap-density.

Error! Reference source not found. Table 5.1 shows trap densities in perovskite layers previously inferred in the literature from estimates of V_{tfl} in the current-voltage characteristics of MHP devices. For comparison, Table 5.1 shows the trap densities which would be inferred from the voltage at which the change in the JV slope occurs in our simulations of perovskite layers containing mobile ionic charge, but with *no traps*. These values are comparable to or higher than those seen in the literature and decrease with increasing sample thickness. These observations cast doubt over whether the previous studies listed in Table 5.1 have correctly interpreted their data. They may have been observing an artefact due the consequences of mobile ions in the perovskite layer rather than the signature of traps.

In contrast, the simulation results from the layer with a low density of traps, but no mobile ions, show that the traps only reduce the current at low voltages, and do not result in a significant transition to steeper JV slopes. If the steeper region of the JV curve were used to infer V_{tfl}, and thus a trap density, the resulting value would be too low to satisfy the assumptions on which this analysis is based (136).

We therefore suggest that, depending on the measurement regime, the statements about V_{tfl} characterisation made by Le Corre *et al.* (49) can be generalised to situations where the ion density is much greater than the trap density. The ionic charge can be solely responsible for the increase of current when a JV sweep is performed. However, for the case where the ionic charge is effectively ‘frozen’ by measuring with the aforementioned pulsed measurement the regime of steeply rising current can, indeed, be caused by traps and subsequently obscured by the interfacial doping effect. If the interfacial doping effect is very small (due to a low ion density) and the trap density is high, the findings of Le Corre *et al.*(49) are applicable.

Material	**Thickness**	**V_{tfl} (V)**	**Inferred trap density (m^{-3})**	**Reference**
$MAPbI_3$, $MAPbBr_3$	n/a (size >100 mm^3)	24.2, 4.6	3.3×10^{10}, 5.8×10^9	(143)
$MAPbI_3$, $MAPbBr_3$	2.49mm, 2.32mm	n/a	1.4×10^{10}, 3×10^{10}	(144)
$MAPbI_3$ single crystal, thin film	3.3mm average, 1µm	10.7, n/a (<1 from fig S4)	3.6×10^{10}, 2×10^{15}	(146)
$MAPbCl_3$	~350µm	9.8	3.1×10^{10}	(147)
$FAPbBr_3$, $FAPbI_3$	1.2mm,1.2mm	2.9, 3	9.6×10^9, 1.13×10^{10}	(145)
$MAPbI_3$ simulations with no trap states	500nm, 1µm, 2µm	0.18, 0.27, 0.43	1.8×10^{15}, 6.9×10^{14}, 2.74×10^{14}	This work

Table 5.1 A table summarising results from the literature that use the V_{tfl} technique to infer a trap density from a measured JV curve. We include in the last column some results obtained from our own simulations demonstrating that trap densities can be inferred from a process that is purely arising from the mobile ionic charge in the device, not trapped charge.

5.4 Conclusion

In conclusion, we have shown using drift-diffusion simulations that the effects of a high density of mobile ionic charge in MHP devices can induce a “fake” trap-filled limit portion of a JV curve in symmetrical single carrier devices. If this region of a measured JV curve is, instead, interpreted as to be caused by electronic traps and is used to extract a trap density, values close to those previously reported in the literature can be found. As such, a warning is made to the research community that if the density of mobile ionic charge is much greater than the expected electronic trap density in the MHP layer being investigated, the V_{tfl} equation cannot be used on a conventional JV sweep to extract a trap density. In cases where the ionic charge is effectively “frozen” in its equilibrium position, either by a very fast scan rate or by using a pulsed-voltage technique, the findings of Le Corre *et al.*(49) are applicable but only if the ionic charge density is lower than the trap density. As mentioned in the conclusion to section 5.2 (section 5.2.5), it is difficult to control the ionic charge density in MHPs and it is likely to be too high. As a result, we suggest that this method is only used with great caution, ensuring that the measured device falls withing the constraints mentioned.

Chapter 6 – The Effects of Environmental Humidity on the Ionic Conductivity of Metal Halide Perovskites

6.1 Declaration of contributions

C.T. Lin[1] and T.J. Macdonald[2,3] performed the device fabrication for the devices measured in this chapter. The method described in section 3.2.2.

X. Shi[4] aided with the experiment method and set-up.

P. Barnes[4] designed the study.

[1]Department of Materials and Centre for Processable Electronics, Imperial College, London, W12 0BZ UK

[2]School of Engineering and Materials Science and Materials Research Institute, Queen Mary University of London, London, E1 4NS UK

[3]Department of Chemistry and Centre for Processable Electronics, Imperial College, London, W12 0BZ UK

[4]Department of Physics and Centre for Processable Electronics, Imperial College London, South Kensington Campus, London, SW7 2AZ, UK

6.2 Abstract

One of the prevailing challenges to commercializing MHP solar cells and other optoelectronic technologies is their degradation after exposure to oxygen, humidity, and light. Previous works have suggested that the degradation rates and mechanisms are dependent on the device structure and the precise composition of the perovskite layer. Furthermore, the dynamics of the ionic defect motion in perovskites is thought to play a role in some degradation pathways and to be dependent on the perovskite's stoichiometric composition and any hydrated phase formation. Using EIS measurements of devices under controlled humidity and temperature environments we show that the activation energy for ion transport in the perovskite decreases on exposure to water vapour and that this effect can be reduced by mixing a small amount of Cs^+ into the A cation cite of the ABX_3 structure. This result provides an explanation for the increased stability to water vapour from Cs doped $MAPbI_3$ that has been previously observed and it provides further evidence for the formation of monohydrate and intercalated water phases of perovskites. Our result provides experimental evidence to not only the suggestions of the reversible formation of

the monohydrated perovskite phase, but also the degradation mechanisms that subsequently occur. Our results also give an explanation as to why mixing of certain cations in metal halide perovskites increases stability.

6.3 Introduction

The stability of MHP devices to several environmental conditions is the most important aspect of device performance to improve if they are to become commercially viable (as mentioned in 2.4.4). Here, I focus on the instability due to exposure to water since it is the relevant form for this investigation. The instability of $MAPI_3$ due to water has been shown as partly due to the hydroscopic amine salts (157) and further, as presented by Wang *et al.* (7), one of the chemical processes that takes place in the degradation of MHPs (specifically $MAPbI_3$) is hydrolysis, where water acts as a catalyst. These hydrolysis reactions include the production and reaction of HI, which could be followed by further reactions induced by UV radiation and oxygen. A different mechanism for degradation in the presence of water was proposed by Frost *et al.* (158) where an acid-base reaction occurs producing similar degradation products to the reactions reported in Wang *et al.* (7) but with the additional formation of $\mathrm{PbI_2}$, an experimentally observed yellow solid. Further work by Yang *et al.*(159) has shown that the initiation of these perovskite-water reactions is at least partially due to the reversible formation of a hydrate, which does not produce any volatile by-products. Leguy *et al.*(160) further demonstrated that the formation of a dihydrate ($\mathrm{MA_4PbI_6 \cdot 2H_2O}$, the hydrate referred to by Yang *et al.*(159)) was preceded by the formation of a monohydrate ($\mathrm{MAPbI_3 \cdot H_2O}$), first suggested to exist by Poglitsch and Weber (161), which forms as insulating layers preferentially on grain boundaries. Ion migration was shown to be stronger at these grain boundaries in solar cells that were partially degraded by water (162), confirming that grain boundaries are an important part of this degradation process. Leguy *et al.*(160) also showed that solar-cell performance declined significantly when the hydrate was present but this completely recovered by an exposure to a dry N_2 atmosphere for > 5 hours. Further discussion of the degradation mechanism has shown that it is a fairly complicated process (163–165) with several possible mechanisms that could happen concurrently but suggestions of the involvement of vacancy migration (such as halide vacancy migration) could be important in the irreversible processes (166). Garcia-Fernandez *et al.* (167) have analysed some of changes in EIS spectra of $MAPbI_3$ after cyclically exposing films and single crystals to ambient conditions and drying them, finding an increase in electrical conductivity and “capacitance” by increasing the humidity. The applicability of the equivalent circuit used in the analysis of their experimental results seems limited and at the time of writing and I call into question the consequences of the temperature range used in their measurements.

The primary motivating study for the work presented in this chapter is from Jong *et al.* (168) where first principles calculations were used to investigate the properties of the monohydrated phase of MHPs ($\mathrm{MAPbX_3 \cdot H_2O}$ described earlier by the iodide version) and an intercalated phase ($\mathrm{MAPbX_3\_H_2O}$), the term intercalation refers to a phase of the perovskite structure that accommodates the water molecule without significant perturbation from the original structure. Since the interactions of water with the perovskite crystal lattice are via hydrogen bonding (169), the bond lengths with the relevant halide and cation were calculated, revealing that the halide hydrogen bond lengths change more than the hydrogen bond to methylammonium between the two investigated phases and between different perovskites containing different halides. They also found that the volume expansion of the crystal lattice is higher for the intercalated phase than the monohydrate and higher for perovskites with halides of lower atomic radius (lower atomic number). The results are presented in Table 6.1 to include values for the initial dry volume and the absolute expansion due to the formation of either the intercalated phase or the monohydrate. Interestingly, the absolute expansion of the bromide and chloride in the formation of the monohydrate shows a slight decrease.

Halide ($MAPbX_3$)	**Cubic lattice parameter (Å)**	**Initial dry volume ($Å^3$)**	**$MAPbX_3\_H_2O$ volume ($Å^3$)**	**Expansion percentage (r_0)**	**Absolute expansion ($Å^3$)**	**$MAPbX_3 \cdot H_2O$ volume ($Å^3$)**	**Expansion percentage (r_0)**	**Absolute expansion ($Å^3$)**
I	6.33	253.64	271.65	7.10	18.01	264.80	4.40	11.16
Br	5.90	205.38	226.29	10.18	20.91	224.69	9.40	19.31
Cl	5.68	183.25	207.79	13.39	24.54	201.96	10.21	18.71

Table 6.1: Values for the cubic lattice volume/size of the intercalated phase ($\mathrm{MAPbX_3\_H_2O}$) and the monohydrate phase ($\mathrm{MAPbX_3 \cdot H_2O}$) of the iodide, bromide, and chloride (X = I, Br, Cl) of $MAPbX_3$. The cubic lattice parameters are taken from Mosconi et al. (170) and the expansion percentages are taken from Jong et al. (168).

The formation energy and decomposition energy of these water-including states were then calculated, showing that perovskites with higher atomic number halides form these states with a more exothermic process and decompose with a more endothermic process. This calculation says nothing about the size of energy barriers to formation of the intercalated and hydrated states and for decomposition to initiate, which could be key parameters in the roles of these states in the perovskite degradation in humid environments. Finally, the activation energies for vacancy mediated migration of X^-, MA^+ and H_2O in the dry crystal, the intercalated and monohydrate phases were calculated. These values are important for the understanding of degradation rates of different perovskite compositions because, as mentioned earlier, the halide vacancies play an important role in an oxygen degradation pathway and may play a role in the degradation pathway including water. Their results are reproduced and shown in Table 6.2. They showed that all vacancy-mediated halide migration is made significantly easier in the intercalated phase (meaning the activation energies are much lower) and slightly easier in the monohydrate phase. This could suggest that MHPs degrade even faster than the individual degradation pathways show when exposed to water, light and oxygen simultaneously: the presence of water not only initiates a degradation pathway itself but facilitates an oxygen degradation pathway too, namely in the halide vacancy-mediated formation of a superoxide in the presence of light and oxygen (8). It is my opinion that this is consistent with the current observations in the literature. The activation energy for MA^+ and H_2O migration is shown to be faster only in the intercalated phase, suggesting that water molecules could spread through the bulk of the perovskite faster if the intercalated phase forms before/preferentially to the hydrated phase.

Perovskite Phase	X	X^- (eV)	MA^+ (eV)	H_2O (eV)
$MAPbX_3$	I	0.55	1.18	-
	Br	0.58	1.20	-
	Cl	0.62	1.24	-
$MAPbX_3\_H_2O$	I	0.22	0.38	0.28
	Br	0.29	0.54	0.31
	Cl	0.35	0.63	0.42
$MAPbX_3{\cdot}H_2O$	I	0.44	1.14	0.78
	Br	0.47	1.18	0.89
	Cl	0.49	1.23	1.08

Table 6.2. The calculated activation energies for ion transport in different perovskite phases: dry $MAPbX_3$, water intercalated $MAPbX_3\_H_2O$ and $MAPbX_3{\cdot}H_2O$. Data reproduced from Jong *et al*. (168).

Furthermore, the results shown in Jong *et al.* (168) and Table 6.1 show that for different perovskite halides the size of the initial unit cell is important; the smaller chloride perovskite must stretch more than its iodide counterpart to accommodate the water molecule. This structural feature causes the chloride to have shorter (and therefore stronger) hydrogen bonds with water molecules, making the ion migration for these halides harder (higher activation energy). If the cationic composition of the perovskite were changed, any structural variations should also be significant. However, the cubic lattice parameters for $MAPbI_3$, $FAPbI_3$ and $CsPbI_3$ are 6.279 Å, 6.346 Å (171) and 6.289 Å(172) respectively. I note that these cubic structures exist at different temperatures, but their comparison is relevant for the commonly used mixed-cation MHPs. If these values are used as indicators and are extrapolated to the mixed cation pseudo-cubic structures that reportedly have increased stability (see 2.4.4), the changes in lattice parameter are unlikely to be as large as the changes due to different halides (see Table 6.1) and are, therefore, unlikely the cause for the increased stability that has been noted in the literature. It is my opinion that these changes in observed stability by mixing the cationic species in MHPs could be due to changes in hydrogen bonding with water molecules and changes in lattice strain/twisting rather than changes in lattice parameters and the chemical reaction kinetics. The net effect of using mixed-cation MHPs on the interaction with H_2O could be very similar to the findings in Table 6.1 and Table 6.2, just via a slightly different mechanism.

From the analysis of the work of Jong *et al.* (168) and other work from the literature, it is clear that an understanding not only of the chemical reactions and structural changes during degradation but also the understanding of the mechanisms by which they initiate is important if the community is to significantly improve the lifetime of MHP devices. In addition to the above degradation mechanisms, $CsPbI_3$ undergoes a phase transformation in the presence of water which greatly diminishes their photovoltaic and light-emitting properties (173,174) and pure $FAPbI_3$ solar cells see no improved stability in high humidity environments, due to the hygroscopicity of the FA^+ cation (175). Any insights into the mechanism of mixed cation induced improvement in stability would be of great value. Could it be that all these detrimental processes can be avoided?

In this investigation I used EIS under different partial-pressures of atmospheric water at different temperatures combined with an equivalent circuit model to test the findings of Jong *et al.* (168): that there is a significant change in activation energy to ion migration due to the inclusion of water into the MHP structure via the formation of either a monohydrate or an intercalated phase in $MAPbI_3$. With this technique, the existence of pure forms of these phases, or some mix of them should be detectable. I compare these results to $Cs_xMA_{x-1}PbI_3$ and $FA_xMA_{x-1}PbI_3$ (x = 0.05 for both), to try to gain further insight into reasons for possible stability improvements due to cation mixing.

6.4 Method

6.4.1 Experiments

6.4.1.1 In situ humidity and temperature controlled electrochemical impedance spectroscopy

To control the environmental humidity and temperature of the solar cell whilst performing the EIS measurement described in section 3.3.4, gas was bubbled through various saturated salt solutions and then piped through a LINKAM DSCX600 temperature control stage at a low flow rate. The solar cell is connected to the Ivium CompactStat via the connections on the LINKAM DSCX600 and rests on the temperature stage in the centre of the measurement system. The method of using gas bubbled through saturated salt solutions has been previously shown as a method for controlling the humidity of the gas (176). In this experiment, I used Ar as it is chemically inert and will not induce any further degradation of the MHP. As such, the underlying assumption of this technique is that the humidity values determined in the literature (176) are independent of the gas used, provided there are no chemical reactions between the gas and the salt solution. The mechanism by which water vapor exists in equilibrium with another gas above liquid water is purely thermodynamic and is dependent on the phase diagram of water under the surrounding conditions, so this assumption seems to be reasonable.

The method for carrying out this study is represented by the flow chart in Figure 6.1. In reality, this experiment was carried out in two batches of experiments, one where a wide range of atmospheric humidity was investigated and the other where drying the solar cell between humidity conditions was investigated, hence the either/or box in Figure 6.1. Two separate method flow charts are given in Figure G.1 providing more detail for each measurement batch.

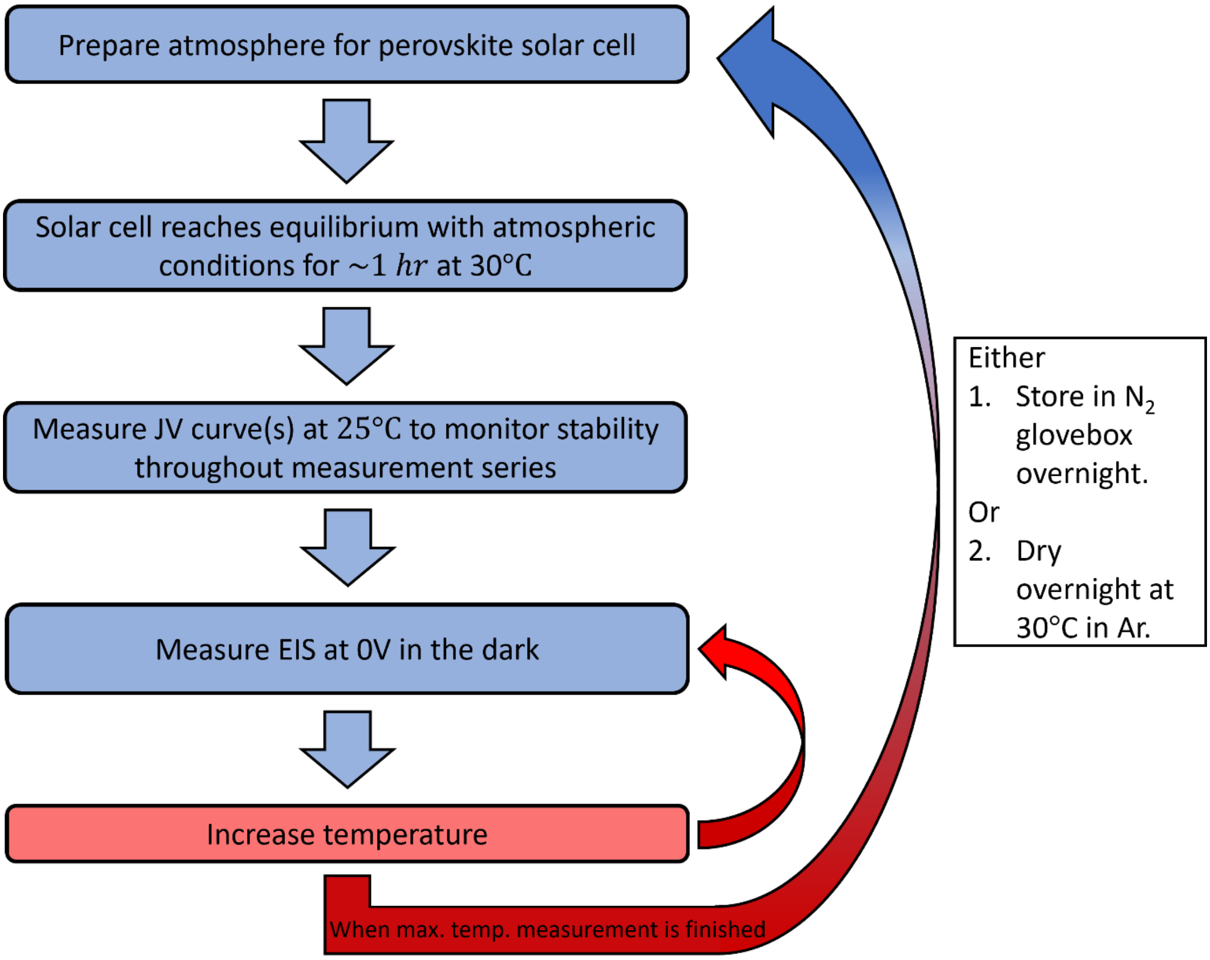

Figure 6.1 A flow chart depicting the workflow for the experimental method used to analyse the effect of environmental humidity on MHP solar cells.

The equilibrium time for the MHP solar cells with the humid environment and the subsequent drying procedure is based on the work by Leguy *et al.*(177) where perovskite single crystals and films were subject to environmental humidity and analysed using time-resolved XRD and ellipsometry to determine times for the formation of a monohydrate and to study the reversibility of the formation of this state (drying).

6.4.1.2 JV curves

The JV curves presented in this study were carried out in the way described in section 3.3.2 using a voltage series of 0 V→ 1.1 V → -0.3 V → 0 V at a scan rate of 50 mVs^{-1}. In measurement batch 1 the JVs were performed in the dark, in measurement batch 2 the JVs were performed under illumination. The illumination was provided by an LED ring of relatively constant illumination intensity. All JVs were proceeded by a 60 s equilibration at 0 V bias in the illumination condition of the JV. A solar simulator would have been used to capture the illuminated JV curves if it were not for laboratory restrictions at the time of making these measurements.

6.4.2 Equivalent Circuit Modelling (specifically the dark 0V approximation)

The equivalent circuit modelling technique was performed as described in section 3.4.2 using the equivalent circuit depicted in Figure 3.3 and Figure 6.2c. The impedance of this circuit (Equation 14) was fit to the experimental data by varying the parameters C_{ion}, C_g, R_{ion}, R_s, and J_{rec} until the difference between the modelled spectrum and the measurement was minimized. This was done using MATLAB's built-in function fmincon() which uses an 'interior-point' algorithm to perform a minimisation. Even with the fitting tolerances set un-reasonably low ($\sim 10^{-20}$) the fitting algorithm would still find solutions that were not physically reasonable or were obviously not "good" fits when the results were analysed graphically. As such, I took care to adjust the initial parameters many times over to ensure that the final solution was the "best" or "correct" solution, using the guides of the experimental data to provide good initial guesses for parameters; for example, $\lim_{\omega \to 0}(-(Z'')^{-1}\omega^{-1}) \approx C_{ion}/2$ and $\lim_{\omega \to \infty}(-(Z'')^{-1}\omega^{-1}) \approx C_g$.

In circumstances where errors are given for fitting parameters, they are estimated by performing small changes to that parameter for each fit and noting if the results deviated significantly from the data, rounding the error up to ensure no error underestimation is given. There is no method for extracting fitting errors from the minimization functions used in MATLAB in this analysis.

6.5 Results and discussion

To investigate the consequences of environmental humidity on the migration of mobile ionic charge in MHPs ($MAPbI_3$, $Cs_xMA_{x-1}PbI_3$ and $FA_xMA_{x-1}PbI_3, x = 0.05$) I present results from the analysis of EIS measurements described in 3.3.4 and 6.4.1 carried out at 0 V in the dark under different environmental humidities and at different temperatures as described in section 6.4.1.1. The measurement data is fit using the appropriate equivalent circuit, shown in Figure 6.2c and Figure 3.3. All the obtained parameters for the measurements under all conditions are given in Chapter 8Appendix G, section Chapter 8G.2 and section Chapter 8G.3. Figure 6.2a and Figure 6.2b show an example of the EIS measurement results in the form of a Nyquist plot and a Bode plot, where the perovskite and the conditions are

$Cs_{0.05}MA_{0.95}PbI_3$ at $25\ ^{\circ}\mathrm{C}$ under dry atmosphere (Argon). The fit to the data with the model is also plotted on the same graph and is represented by the solid line. Apart from the data points at the very lowest frequencies (one of which is highlighted by the red circle), the model agrees with this example of the data very well. The shape of the spectra is matched very closely and the ionic *RC* time constant, that is most easily seen as the "bump" in the phase angle spectrum at $\sim 100\ \mathrm{Hz}$, is also very closely matched. This quality of fit not only suggests that the parameter values are well optimized in the fitting routine, but also that the model is well suited to describing the measurement of this system. There were, however, some cases in which the fit to the data is not quite as close. Specifically, I note that if the value of R_{ion} is very low and/or the value of J_{rec} is very high, the model did not describe the data as well as the case presented in Figure 6.2a and Figure 6.2b. An example of a fit where R_{ion} is low ($990\ \Omega cm^2$) and where J_{rec} is high ($2.16 \times 10^{-5}\ Acm^{-2}$) is given in the Figure G.2.

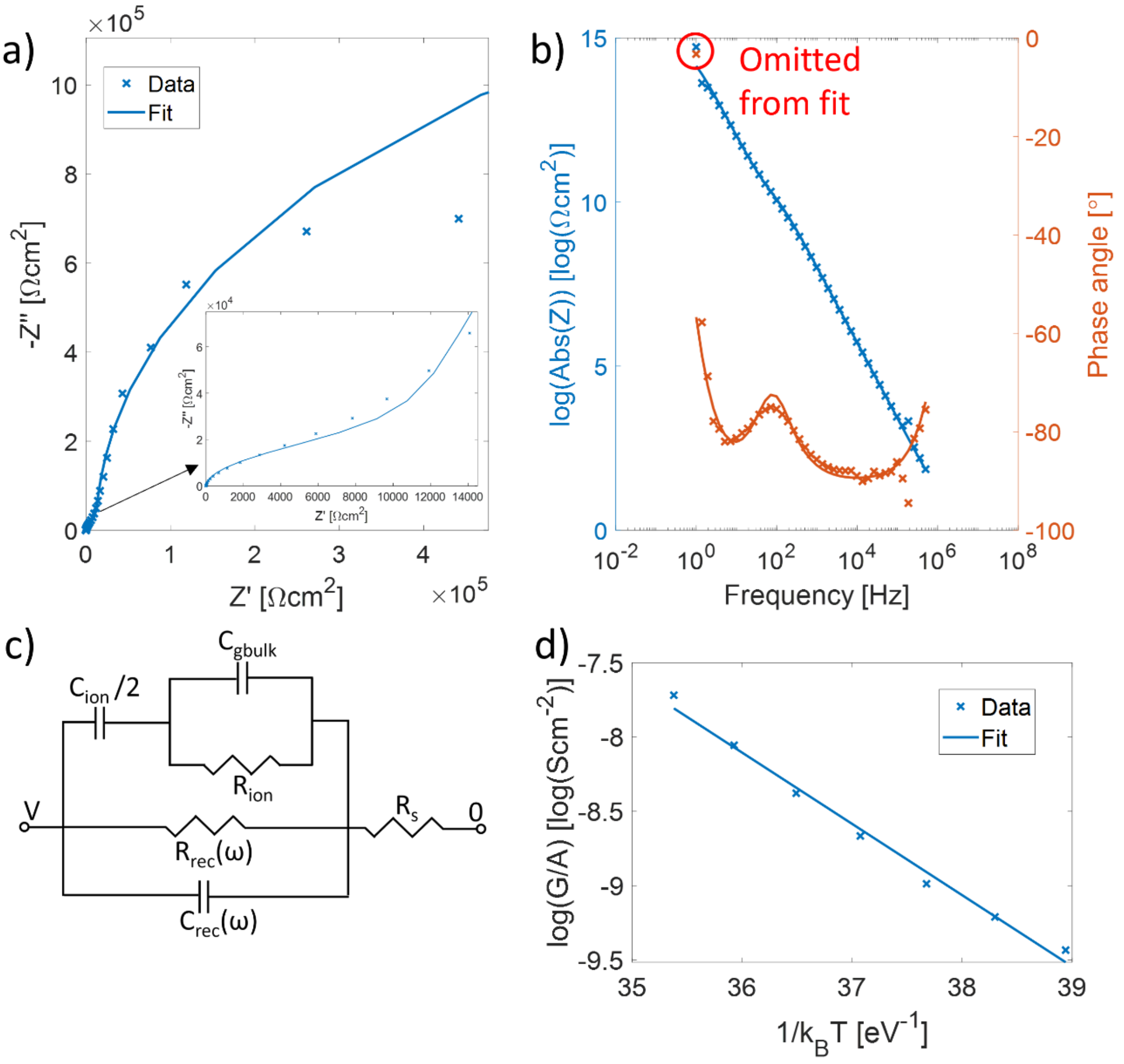

Figure 6.2 Experimental results from measuring the dark (measurement batch 2), EIS of a $Cs_{0.05}MA_{0.95}PbI_3$ solar cell at 0 V and fitting the data with our equivalent circuit model. a) the Nyquist plot of the EIS data (crosses) at 25°C with a zoom in of the high frequency region given in the inset with the fit shown by the line. b) The Bode plot of the same data in a), some values at the extreme low-frequency end of the spectrum are circled in red as they were omitted from the fitting procedure as they were anomalous, these points can't be seen on a) as they are outside of the range of the axes. c) the equivalent circuit used to model the measurements in a) and b). d) a straight line fit (line) to the values of R_{ion} converted to G/A(crosses) obtained by the process depicted in a), b) and c) for several temperatures and using the Arrhenius relationship to extract an activation energy.

For each perovskite solar cell in each atmospheric condition, the EIS is carried out at several temperatures between 25°C and 60°C. The value for R_{ion} at each temperature is then converted into conductance per unit area (G/A) by taking the reciprocal, $\log(G/A)$ values are then plotted against $1/k_BT$ for each temperature value. Considering the ion migration in the same way as Eames *et al*. (11), I assume the ion transport follows some Boltzmann-like barrier hopping process for diffusion (178) with an associated activation energy for hopping. An Arrhenius relationship can be used to extract an activation energy (E_a) for ion migration:

$$\frac{G}{A} = \frac{G_0}{A}\exp(-\frac{E_a}{k_B T})$$

Equation 23

where G_0/A is a constant, temperature independent conductance per unit area. An important feature of this Arrhenius relationship is that at higher temperatures, a change in E_a has less of an effect on G/A than at lower temperatures and so, the effects of activation energy will be more easily seen in the ionic conductivity at lower temperatures. Following on from Equation 23, the gradient of the $\log(G/A)\ vs\ 1/k_B T$ gives E_a. Figure 6.2d shows an example of a straight line fit to the determined R_{ion} values (which have been converted into G/A) in the form of the Arrhenius relationship shown in Equation 23. This example is for the $Cs_{0.05}MA_{0.95}PbI_3$ solar cell under dry atmosphere (Argon) at all investigated temperatures and, therefore, contains the example fit shown in Figure 6.2a and Figure 6.2b. The straight-line fit agrees with the data, indicating that the model is appropriate. An estimate for the errors in fitting R_{ion} is given in the discussion of Figure 6.5, unfortunately there is no systematic way to calculate a fitting error for this process. This is why there are no error bars displayed in Figure 6.2d.

In order to compare the activation energy for ion migration under different environmental humidities in these measurements, the humidity values are converted to the partial pressure of water vapour. A table showing the relationship between the salt used to create a saturated solution, the relative humidity of the gas in equilibrium with the solution and the partial pressure water vapour in that gas is given in Chapter 8Appendix G, section Chapter 8G.4. Using the values calculated from the literature humidities (176), the dependence of E_a on the partial pressure of water vapour is then plotted for each perovskite. The results are shown in Figure 6.3 and Figure 6.4, where the error bars come from the calculation of the fitting error from the Arrhenius relationship plot (see Figure 6.2d). The diagonal of a covariance matrix contains the values of the variance, the square root of the values on the diagonal is the standard deviation. The standard deviation is thusly calculated and is used here as representative of the fitting error: the larger the error, the larger the difference between the data and the linear fit (approximately).

Figure 6.3 shows the results from the first batch of measurements where the same solar cell for each perovskite type is measured throughout, but the pixel (precise area of top gold contact) is changed between measurements in order to avoid possible measurement-induced degradation. The results in Figure 6.3a show that the activation energy for ion migration in $MAPbI_3$ is reduced by increasing the partial pressure of water in the atmosphere that the perovskite is in equilibrium with. The results also suggest that at very high humidities, the activation energy is reduced further. Even though the value of E_a does not exactly reproduce the calculated values from Jong *et al*. (168) for the dry film (see Table 6.2Table 6.2), the reduction in E_a by $\approx 0.1\ eV$ in the formation of the monohydrate is potentially being shown by the values obtained for partial pressures > 0.2 kPa and < 1 kPa. The very highest partial pressure value (light blue data point) produces an activation energy similar to the calculated value for the intercalated phase. This contradicts the findings of Jong *et al*. (168) who suggest that the intercalated phase should form before the monohydrate and specifically on the surface of the film; if this phase dominated the ionic transport features of the film (and was, therefore, detectable with this method) it would appear in the region of the graph with low water partial pressure. Therefore, I suggest that under this very high partial pressure of water (light blue data point), some low level of recrystallisation (e.g., Ostwald ripening) and degradation could be occurring in the film which could cause the activation energy for ion migration to decrease. At the same time, the majority of the film is in the monohydrate phase.

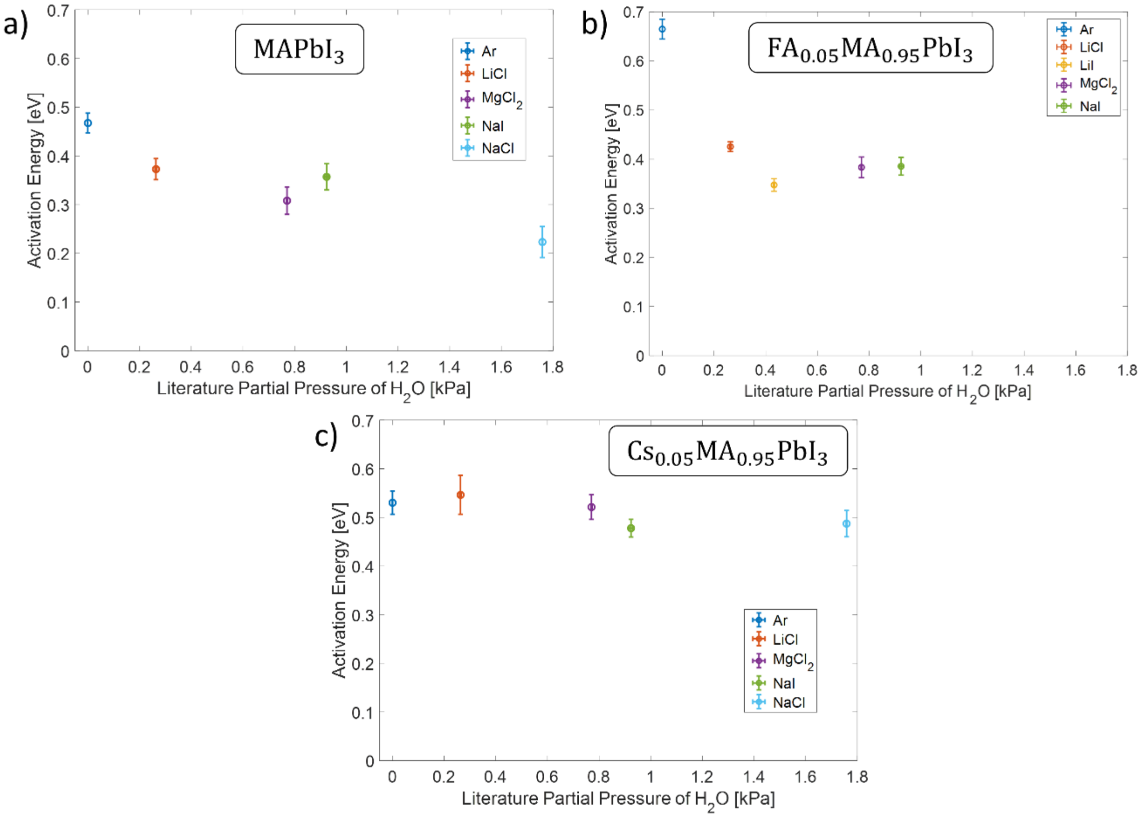

Figure 6.3 The calculated activation energies for ion migration of solar cells with different perovskite active layers under different atmospheric partial pressures of water vapor – batch 1. a) Results for $MAPbI_3$. b) Results for $FA_{0.05}MA_{0.95}PbI_3$. c) Results for $Cs_{0.05}MA_{0.95}PbI_3$. The error bars are obtained from the diagonal of the covariance matrix from the linear fit using the Arrhenius relationship (see Figure 6.2d).

My hypothesis for the mechanism of the interaction of water and this $MAPbI_3$ solar cell is that during the equilibration with a humid environment (or at equilibrium with a low partial pressure of water) the intercalated phase forms in an inhomogeneous way on the surface of the film, followed by the formation of the monohydrate phase in the bulk. An equilibrium is reached where most of the polycrystalline film is in the monohydrate phase, with some localized regions being the pure polycrystalline phase and some being the intercalated phase. In this equilibrium state, the ion migration activation energy is equivalent to the pure monohydrate phase since this phase makes up most of the film. The difference between the calculated activation energies from Jong *et al.* (168) and the values obtained in this work are probably due to the incompleteness of the model used in the calculations; the MHP thin films in this work are inhomogeneous and likely contain some lattice dislocations and distortions among other deviations from an ideal crystal. To detect the formation of each phase separately, some further spatially and temporally sensitive crystallography would need to be performed during the equilibration of the perovskite film with a humid environment, since I am assuming that the formation of these phases happens dynamically and simultaneously in different regions of the film.

The activation energies for ion migration in the $FA_{0.05}MA_{0.95}PbI_3$ solar cell are presented in Figure 6.3b and show similar trends to the $MAPbI_3$ solar cell results in Figure 6.3a except the dry film had a higher activation energy and the relative decrease in activation energy between dry, intermediate conditions and high partial pressure conditions was greater. This suggests that the $FA_{0.05}MA_{0.95}PbI_3$ film undergoes similar processes to the $MAPbI_3$ film but ion migration has higher activation energies in dry conditions, yet the film is slightly more susceptible to changes due to water. This is particularly seen in the result for the highest partial pressure data point (light blue) where the error bars are very high and the activation energy is very low, suggesting more substantial changes to the crystal structure and/or more degradation than the $MAPbI_3$ film.

Figure 6.3c shows the activation energies for ion migration in the $Cs_{0.05}MA_{0.95}PbI_3$ solar cell. The variation in activation energies due to the partial pressure of water is much smaller than for the other MHPs measured in this investigation. Most of the error bars overlap meaning there is no statistically significant difference between the determined activation energies, except for the data point measured with NaI saturated salt solution (green) which is lower than the dry (Ar, dark blue) data point. This device's activation energy is only slightly affected by environmental humidity. As such, my hypothesis is that adding a small amount of Cs to the $MAPbI_3$ crystal achieves one of two things: i) it greatly increases the energy of formation of the monohydrated and intercalated phases such that they take longer to form and/or they need higher atmospheric partial pressures of water to form; or ii) the monohydrate and intercalated phases form in the same way as in $MAPbI_3$ but the activation energy for ion migration is unaffected. In order to confirm the suggested explanations for the data presented in Figure 6.3b and Figure 6.3c, the calculations performed by Jong *et al.* (168) would need repeating for the mixed cation perovskites I investigated here.

To investigate the repeatability of the measurements shown in Figure 6.3 and to investigate the previously reported drying of MHPs (167,177), another measurement batch was conducted on a new set of solar cells that were fabricated using exactly the same method as the cells in the first measurement batch, except all of the measurements were performed on the same pixel (exact area of gold top contact) for each perovskite type. The results of this extra investigation are shown in Figure 6.4. Figure 6.4a displays the results for the $MAPbI_3$ solar cell and is, therefore, comparable to Figure 6.3a. Comparing the results for the $MAPbI_3$ solar cell in batch 1 (Figure 6.3a) and batch 2 (Figure 6.4a), it is apparent that the activation energy for ion migration changes between individual solar cells because the initial measurement under Ar gave $E_a = 0.47\ eV$ in batch 1 and $E_a = 0.57\ eV$ in batch 2. The introduction of atmospheric water has a very similar effect on the activation energy for ion migration in both sets of measurements for the $MAPbI_3$ solar cells; introducing a low partial pressure of water (between 0.2 and 0.5 kPa) reduces the activation energy by $\sim 0.1\ eV$ and slightly higher reductions in activation energy $\sim 0.15\ eV$ at moderate water partial pressures (~ 0.8 kPa) in Figure 6.4. Interestingly, the drying of the $MAPbI_3$ solar cell did not result in the recovery of the same activation energy. I suggest that this could be due to some recrystallisation of the film during the drying procedure (e.g., Ostwald ripening), as water has been shown to improve perovskite crystallization and surface coverage when added to precursor solutions (179).

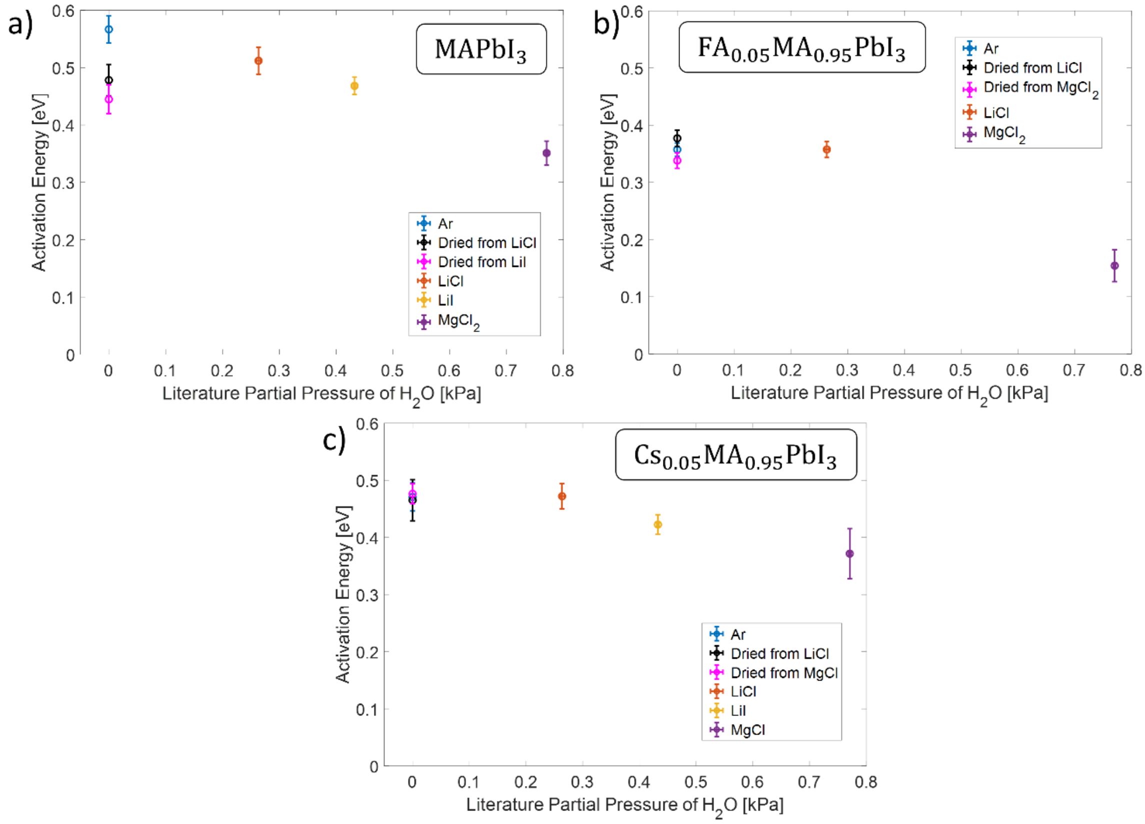

Figure 6.4 The calculated activation energies for ion migration of solar cells with different perovskite active layers under different atmospheric partial pressures of water vapor, including the analysis of the drying of the solar cell – batch 2. a) Results for MAPbI$_3$. b) Results for FA$_{0.05}$MA$_{0.95}$PbI$_3$. c) Results for Cs$_{0.05}$MA$_{0.95}$PbI$_3$. The error bars are obtained in the same way as in Figure 6.3. All “dried” measurements were performed under Ar.

No such reduction in activation energy for ion migration is observed in the drying procedure for the FA$_{0.05}$MA$_{0.95}$PbI$_3$ (Figure 6.4b) and Cs$_{0.05}$MA$_{0.95}$PbI$_3$ (Figure 6.4c) solar cells. This may be because the improvement in crystallization provided by the drying process for the MAPbI$_3$ device is already provided by the additional cationic species in the mixed cation perovskites. There are some inconsistencies in the FA$_{0.05}$MA$_{0.95}$PbI$_3$ (Figure 6.4b) results when compared to Figure 6.3b, the activation energy reduction at $\sim 0.8\ \mathrm{kPa}$ water (MgCl$_2$ induced atmosphere, purple) is much lower in the batch 2 (Figure 6.4b) measurements than in the batch 1 measurements (Figure 6.3b). I suggest that this is due to the device/pixel in Figure 6.4b being slightly degraded in some way, a discussion of degradation during the measurements is included below in the discussion of the JVs presented in Figure 6.6. The results from the Cs$_{0.05}$MA$_{0.95}$PbI$_3$ (Figure 6.4c) solar cell in this batch, generally agree with the results in Figure 6.3c where the reduction in activation energy for ion migration is much lower than in the other solar cells, although the reduction of between $0.05\ eV$ and $0.1\ eV$ is observed at slightly lower water partial pressures than in Figure 6.3c. These results further confirm that the mobile ionic charge in $Cs_{0.05}MA_{0.95}PbI_3$, reacts to the change in environmental humidity differently to $FA_{0.05}MA_{0.95}PbI_3$ and $MAPbI_3$ and matches the previous observations of improved MHP stability with the addition of Cs^+ (see section 2.4.4). The explanation for this is given in the discussion of Figure 6.3. If the migration of the high density of ionic charge is a significant factor in the degradation mechanism of MHPs, as discussed in the introduction to this chapter (section 6.3).

The results presented in Figure 6.3 and Figure 6.4 display the change in temperature dependence of R_{ion} (the bulk ionic resistance) due to the exposure of MHPs to water, this is essentially a check for any changes in the bulk transport for ions (the pre-factor G_0/A) in Equation 23. To further corroborate these findings, the changes in R_{ion} itself under exposure to different environmental humidities are now presented. A sample of the results is given in Figure 6.5, these results are representative of the changes in R_{ion} for all the measurements carried out in this investigation. Figure 6.5a shows results from the $Cs_{0.05}MA_{0.95}PbI_3$ solar cell data fitting in batch 2, where the cell was dried intermittently and are presented in the order the experiment was carried out. The results show R_{ion} decreases with humidity when the temperature is kept constant but also shows a decrease in R_{ion} after drying. If the perovskite returned to its original state after drying, the value of R_{ion} would be the same as the value after measuring under Ar after drying, so this is evidence of some change to the film during the drying process. Since the activation energies (which are represented here by the spread of R_{ion} for each condition across all measured temperatures) of the dried states for the $Cs_{0.05}MA_{0.95}PbI_3$ solar cell are identical (see Figure 6.4c), I suggest that this is further evidence of some recrystallisation effect, decreasing the density of grain boundaries in the film. The overall trend of a decrease in R_{ion} with environmental humidity could either be further confirmation of the results shown in Figure 6.3 and Figure 6.4 or be confounded by some moisture induced degradation that occurred during the measurement. I also note that the changes to R_{ion} are less significant at higher temperatures, as predicted in the description of Equation 23.

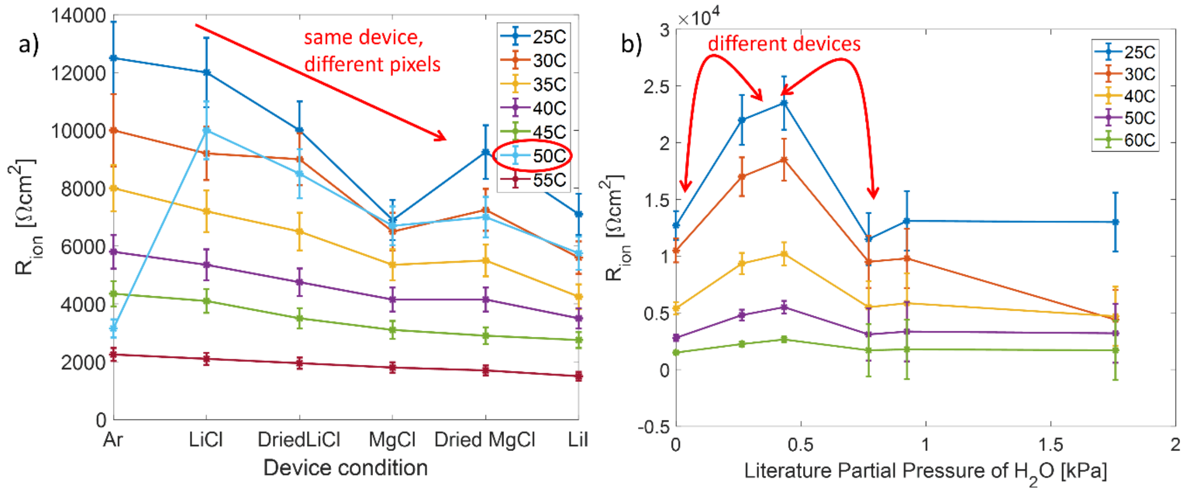

Figure 6.5 The change in R_{ion} for each measured temperature as environmental conditions. a) The results from $Cs_{0.05}MA_{0.95}PbI_3$ data fitting of batch 2 measurements. The data is presented in the same order as they were measured in. The $50°C$ data (light blue) was omitted from further analysis as represented by the red circle on the legend, I suspect the heating element failed and the device was at ambient temperature. b) The results from $MAPbI_3$ data fitting of batch 1 measurements. The data is presented in ascending partial pressure of water. The determination of the fitting error is given in section 6.4.2. The errors are $\sim \pm 0.1 \times R_{ion}$.

Figure 6.5b was measured by changing the pixel (exact region of gold contact and perovskite of the solar cell's thin film being measured) between each humidity condition and, therefore, reducing any measurement induced degradation. The results in Figure 6.5b are for the $MAPbI_3$ solar cell measured in batch 1. Interestingly, the changes in R_{ion} between pixels, which are likely due to changes in the grain-boundary structure of the MHP film under said pixel, outweigh any changes in R_{ion} between pixels due to water which appear as almost non-existent. This contrasts with the results presented in Figure 6.3 and Figure 6.4, where the activation energy changes significantly. Therefore, I suggest that the decrease in R_{ion} (bulk ionic transport properties) due to environmental humidity and the formation of the intercalated and monohydrate phases is mild when compared to the changes in the dynamics of hopping and is dependent on temperature, as described in Equation 23.

Therefore, I consider the conclusions drawn from the investigation of activation energy changes from exposure to environmental humidity to be valid and that any changes to ionic conduction are smaller than the variation across an entire device area. The pre-factor (G_0/A) in Equation 23 is much less dependent of environmental humidity than the activation energy because the ionic conductivity is not seen to decrease with humidity very much at higher temperatures ($55\ °\text{C}$ and $60\ °\text{C}$). The issue of degradation during this measurement process are not obviously significant from the results presented in Figure 6.5, the decrease in R_{ion} shown in Figure 6.5 is because of the changes in activation energy and bulk conductivity and are due to either some small change to the crystal morphology, the existence of the hydrated phases, or some measurement induced degradation. It is impossible to decouple the effects of degradation from the other effects in this set of results. Degradation effects are further discussed/presented in the following discussion of the JV curves presented in Figure 6.6.

The JV curves presented in Figure 6.6 are split into two columns (a, c, and e) and (d, e, and f) representing the 1st batch of measurements and the 2nd batch of measurements respectively. For further discussion of the JV measurement technique, see section 3.3.2. The order in which the curves appear in the legend are the order in which the measurements were performed. The JVs in the 1st batch were measured in the dark. The JVs in the 2nd batch of measurements were under illumination. Unfortunately, because of laboratory restrictions during 2021, the illuminated JV curves were not measured in a solar simulator but in a setup using a set of LED rings that had not been calibrated against the solar simulator (as a reference). As such, the illumination intensity is not known and is not constant throughout the JV curves presented. Therefore, attention is only paid to curves that are substantially different to the others in the same set - that are “misshapen” to the eye.

Figure 6.6a and Figure 6.6b show the JV curves for the $MAPbI_3$ solar cells and present no obvious signs of degradation; the gradient of the curves near 0 V (which is $\propto J_{rec}$) that does vary between curves is likely due to differences between pixels, since the curves in Figure 6.6a are not all on the same pixel. The change in J_{sc} in Figure 6.6b is only due to the change in illumination between scans, the V_{oc} and curvature of the curves are very comparable.

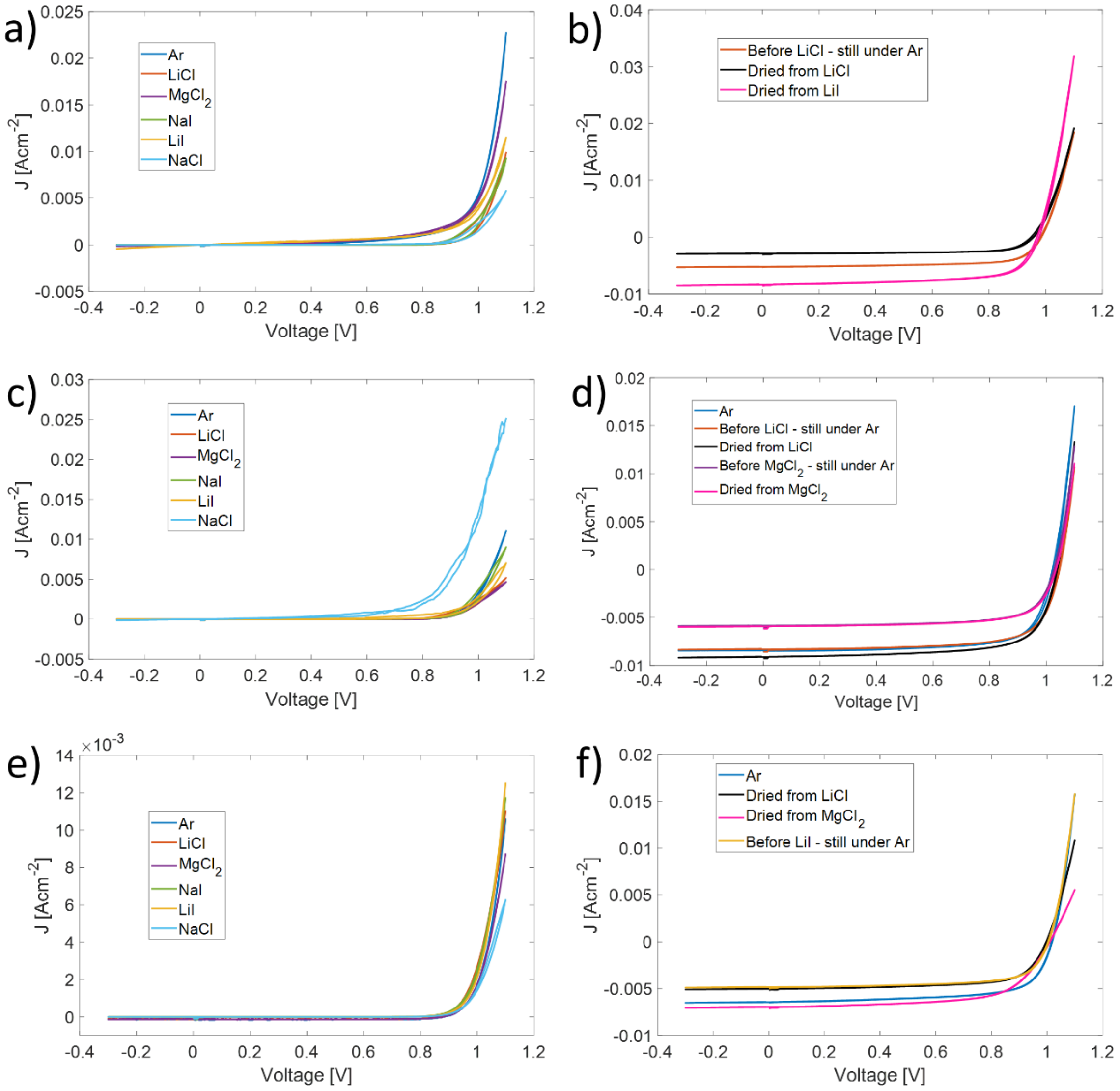

Figure 6.6 The JV curves in the dark or under illumination throughout the measurement sequence. a) $MAPbI_3$ solar cell in batch 1 in the dark. b) $MAPbI_3$ solar cell in batch 2 under illumination. c) $FA_{0.05}MA_{0.95}PbI_3$ solar cell in batch 1 in the dark. d) $FA_{0.05}MA_{0.95}PbI_3$ solar cell in batch 2 under illumination. e) $Cs_{0.05}MA_{0.95}PbI_3$ solar cell in batch 1 in the dark. f) $Cs_{0.05}MA_{0.95}PbI_3$ solar cell in batch 2 under illumination. All measurements were performed at a scan rate of $0.05\ Vs^{-1}$. The legend presents the scans in the order they were measured during the measurement procedure presented in Figure 6.1 and Figure G.1.

The only obvious sign of degradation in the JV curves of the $FA_{0.05}MA_{0.95}PbI_3$ solar cells in Figure 6.6c and Figure 6.6d is the light-blue trace of Figure 6.6c, where what would be the ideality-factor of the curve has changed substantially and the current density is no longer smoothly varying. This means that the result in Figure 6.3b for NaCl atmosphere (light blue) is invalid since the pixel/cell was no longer working. All other curves seem to show no obvious deviations from normal operation.

The JV curves of the $Cs_{0.05}MA_{0.95}PbI_3$ solar cells in Figure 6.3e and Figure 6.3f show no sign of degradation either. The sequence of JV curves in Figure 6.3f begins to suggest some change in device behaviour in the pink trace (measured after the second drying procedure) but the device then returns to producing a 'normal' JV curve in the subsequent measurement (yellow trace). I, therefore, cannot conclude that the device had undergone any changes that would invalidate the results presented earlier in this chapter.

Since our results seem to not be affected by degradation, our confidence in our drawn conclusions is relatively high. I note, however, that further measurements (microscopy and XRD, for example) of the MHP films would reveal structural changes from degradation due to water or the measurement procedure with more detail and would further bolster the evidence for the conclusions in this work.

6.6 Conclusion and future work

In summary, I have shown by using an in-situ temperature and humidity-controlled EIS experiment that environmental humidity reduces the activation energy for ion migration in $MAPbI_3$ by an amount similar to values previously calculated in the literature. I have found some evidence to show that the monohydrated phase of $MAPbI_3$ ($\mathrm{MAPbX_3 \cdot H_2O}$) forms when in equilibrium with relative humidities between $10\ \%$ and $40\ \%$. This phase could form in conjunction with some small amounts of the water intercalated phase ($\mathrm{MAPbX_3\_H_2O}$) and the pure polycrystalline phase, further crystallography measurements need to be done to determine if a phase-mixed system exists. I also found that at higher humidities, the activation energy reduces further, probably due to some other changes to the perovskite structure or some very minor degradation. I have also found that introducing a small ($\sim 5\ \%$ molar fraction) amount of FA has no effect on the activation energy for ion migration but adding the same amount of Cs greatly reduces the changes to the activation energy, possibly suggesting an increased stability to environmental humidity. I have also shown that the hydrated perovskite thin film can be dried to mostly restore the material's properties, although the activation energy to ion migration decreases slightly and the ionic conductivity increases slightly in the pure $MAPbI_3$ thin film after drying which I suggest comes from some re-crystallisation. The decrease in the absolute size of the ionic conductivity due to environmental humidity was found to be smaller than the variation between regions (pixels) of the thin film but more significant at lower temperatures, signifying that the changes induced by environmental humidity are indeed mostly to the hopping dynamics of the ionic charge (the activation energy) i.e., humidity does not greatly change the bulk ionic transport properties of the perovskite in ways other than the activation energy to hopping. This indicates that when the perovskite layer is in equilibrium with a humid environment, the involvement of vacancy migration in degradation pathways (discussed in section 2.4.4) would only increase with humidity at lower temperatures, where the changes in activation energy become significant. At higher temperatures ($> 50\ °C$), the ionic transport through the film is relatively unaffected by the environmental humidity but is faster only due to the higher temperature. By monitoring the JV curves of the solar cells throughout the measurement procedure, I confirmed that there was no significant degradation during the measurement apart from one data-point, validating the previously made conclusions.

This study has also validated the equivalent circuit model used to analyse the EIS data and has proven that this technique can be used to study the ion transport properties of MHPs, along with the other processes the model can also describe. It is an important step in finding a truly representative equivalent circuit model for these materials.

The conclusions of the work presented in this chapter leave some possibilities for future work to substantiate some of the claims. One investigation would be to confirm that thin films of $MAPbI_3$ and other MHPs do not form a pure film of the water intercalated phase ($\mathrm{MAPbI_3\_H_2O}$), more measurements of the type presented in this chapter would need to me carried out at lower relative humidities, unfortunately the saturated salt solution technique is rather limited for producing very low humidity environments. I have recently found a technique reported by Brandl and Forney (180) where glycerol and water are mixed and gas is bubbled through the liquid, much in the same way the gas is bubbled though the salt solution in this chapter, that could be used to investigate relative humidities < 10 %. Another future investigation would be for further *ab initio* calculations of the halide ion activation energies that include the cation mixing ratios of MHPs investigated in this chapter to be done. They would be useful for distinguishing between the conclusions of either increased stability to water by adding Cs to $MAPbI_3$ or the increase in ion migration activation energy in the monohydrate ($\mathrm{MAPbI_3 \cdot H_2O}$) by adding Cs to $MAPbI_3$.

Chapter 7 - Conclusions and Outlook

Prior to this work, the research community was beginning to account for the high density of mobile ionic charge in the analysis of some measurement techniques and in the modelling of metal halide perovskite devices. There was, however, still a need for further understanding of the mechanisms by which the ionic charge effected the electronic charge carriers in the measurement of devices under certain measurement conditions/protocol. This was partly seen by the extremely large variation in reported material parameters from both experiments and theoretical calculations (e.g. charge carrier mobility (181)). Additionally, there was (and still is) a need for experimental evidence of the mechanisms by which different metal halide perovskites degrade under different atmospheric conditions and how (or even if) the dynamics of the mobile ionic charge play a role in the degradation process.

This work presents a number of advances in the understanding of the interplay between the mobile ionic charge in perovskite devices and how this may affect measurements and device behaviour under certain conditions. This work also presents significant advances in the understanding of perovskite degradation due to water and the role of the mobile ionic charge in these conditions along with the use of an experimental technique and analysis that opens doors for further understanding of degradation and the mobile ions. Here I present a summary of the conclusions drawn from this work.

1. **Changing the workfunction of contacting materials, the thickness of the perovskite, the density of ionic charge and/or the bias history of the perovskite allows for the conductance of the whole device to be altered due to the mobile ions**

   One of the key findings of this work was the description of a new mechanism by which the mobile ionic charge effectively dopes the perovskite layer by reducing the space charge layer widths at the interfaces with contacting materials and reducing the electrostatic potential in the bulk of the device. In Chapter 4 I investigated the causes of this so-called “interfacial doping” effect by using drift-diffusion simulations, I further showed the device parameters that effect the magnitude of the doping and I described how applying a pre-bias to the device can induce this same effect. I further showed that this effect can be measured, and I demonstrated its existence using a pulsed-voltage experimental technique.

2. **Space-charge-limited current measurements and the application of the Mott-Gurney law are significantly affected by mobile ionic charge and the interfacial doping effect**

   Before this thesis there was debate in the community about the validity of the use of the Mott-Gurney law to find the charge carrier mobility in metal halide perovskites with there were suggestions that a pulsed-voltage technique can remove the contribution of the ions to the JV curve and allow for the use of the Mott-Gurney law (49,65). In Chapter 5, using drift-diffusion simulations and experiments, I investigated how the mobile ionic charge impacts the JV curves of single-carrier perovskite devices when a continuously varying applied voltage and a pulsed-voltage technique are used. I found that the pulsed-voltage technique removes the contribution to the JV curve of mobile ionic charge drifting during the measurement but, when the ionic charge density is higher than the electronic charge density, the equilibrium distribution of the ionic charge (as part of the interfacial doping effect) prevents the space-charge-limited current regime from being observed. I also found that if the ionic charge density is significantly lower than the electronic charge density, the use of the pulsed-voltage technique makes no difference to the JV curve. Using these results I presented a validity window for the application of the Mott-Gurney law to perovskites and suggested that any other electronic measurements of metal halide perovskites should consider similar limitations.

3. **The apparent trap-filled limit in perovskite single carrier devices can emerge entirely due to the existence of the mobile ionic charge**

   In Chapter 5 I followed the investigation of the space-charge-limited current measurements by commenting on the closely associated trap-filled limit analysis. I used drift-diffusion simulations to show that an apparent trap-filled limit can emerge in a JV curve purely from the mobile ionic charge drifting in response to the variation of applied potential during the measurement. I showed that this could very easily be the cause of some of the very low trap-densities reported in previous studies. I also pointed out that the interfacial doping effect could also mask the effect of low-density traps in the low voltage region of JV curves, which lead me to the conclusion that the trap-filled limit analysis is likely to be invalid in most cases for perovskite devices with significant concentrations of mobile ionic charge.

4. **The activation energy for ion migration in perovskites reduces after exposure to water and adding Cs to the perovskite reduces this change**
   In Chapter 6 I used electrochemical impedance spectroscopy and an equivalent circuit model to find that the activation energy for ion hopping dynamics is reduced upon the exposure to water vapour. This finding provides some important experimental evidence for the formation of the monohydrated perovskite phase and suggests that degradation pathways that involve the mobile ionic defects could be accelerated by the presence of water. I also showed that by adding a small amount of Cs^+ cation to the perovskite ($Cs_{0.05}MA_{0.95}PbI_3$) greatly reduces the observed reduction in activation energy to mobile ionic charge. This finding correlates with the observations in the literature of Cs^+ doped perovskites having greater stability and provides possible explanations for this observed behaviour.
5. **Perovskite solar cells can be very effectively modelled by equivalent circuit under the right conditions**
   In Chapter 6, I used an equivalent circuit model adapted from the work of Moia *et al.* (66) to fit electrochemical impedance spectroscopy (EIS) data and analyse the changes in the circuit elements due to changes in temperature and humidity. I showed that the ionic resistance can be extracted reliably from EIS data along with the other four fit parameters that all represent physical processes. This work provided a very important verification of this modelling technique and showed that other features of perovskites can be studied very effectively with this technique.

7.1 Outlook

In this thesis I presented significant advances in the understanding of the interaction between the mobile ionic charge in perovskites and the electronic charge at equilibrium and under applied bias. This new understanding presents design opportunities for new device applications of metal halide perovskites where the tuneable conductivity can be exploited. This understanding can also be used to re-analyse some of the previously observed experimental and simulation results, hopefully revealing new insights into perovskite device Physics.

I further presented a detailed analysis of SCLC measurements, the use of the MG law and the V_{tfl} equation with the new understanding of the interplay between mobile ions and electronic charge. This understanding can be further applied to other measurement techniques to validate their applicability and to ensure the use of the correct analysis. The description of this new mechanism and the consequences of it will hopefully further the research of metal halide perovskites for their application in optoelectronic devices.

The successful use of equivalent circuit modelling and EIS to analyse the change in ionic conduction under humid environments presents an exciting opportunity to further investigate other changes in device parameters during the exposure to other degradation-inducing environmental conditions. In my opinion, the stability of perovskites is by far the largest hurdle to overcome in the pursuit of commercial success for devices made with this material and not enough attention to detail is paid towards the thorough understanding of perovskite degradation. The results of this thesis and the successful demonstration of a powerful characterisation tool will hopefully provide an important step towards to improvement of perovskite device stability via an improved understanding of the mechanisms that control it.

Chapter 8 - Bibliography

1. Intergovernmental Panel on Climate Change (IPCC). IPCC: Climate Change 2021: The Physical Science Basis. Climate Chnage 2021: The Physical Science Basis. 2021.

2. U.S Energy Information Administration. International Energy Outlook 2021 [Internet]. International Energy Outlook 2021. 2021 [cited 2022 Mar 30]. Available from: https://www.eia.gov/outlooks/ieo/

3. Eurostat. Renewable energy statistics [Internet]. eurostat statistics explained. 2022 [cited 2022 Mar 30]. Available from: https://ec.europa.eu/eurostat/statistics-explained/index.php?title=Renewable_energy_statistics#Share_of_renewable_energy_more_than_doubled_between_2004_and_2020

4. IRENA. Renewable Energy Capacity Highlights. Int Renew Energy Agency. 2021;00(March 2021).

5. Snaith HJ. Present status and future prospects of perovskite photovoltaics. Vol. 17, Nature Materials. 2018.

6. Oxford PV [Internet]. 2018 [cited 2022 Mar 30]. Available from: https://www.oxfordpv.com/perovskite-silicon-tandem

7. Wang R, Mujahid M, Duan Y, Wang ZK, Xue J, Yang Y. A Review of Perovskites Solar Cell Stability. Vol. 29, Advanced Functional

Materials. 2019.

8. Aristidou N, Eames C, Sanchez-Molina I, Bu X, Kosco J, Saiful Islam M, et al. Fast oxygen diffusion and iodide defects mediate oxygen-induced degradation of perovskite solar cells. Nat Commun. 2017;8.

9. Nelson J. The Physics of Solar Cells. 1st ed. Imperial College Press; 2003.

10. Sze S., Ng KK. Physics of Semiconductor Devices. Third. Wiley; 2007.

11. Eames C, Frost JM, Barnes PRF, O’Regan BC, Walsh A, Islam MS. Ionic transport in hybrid lead iodide perovskite solar cells. Nat Commun. 2015;6(May):2–9.

12. Mott NF, Gurney RW. Electronic Processes in Ionic Crystals . 1st ed. Oxford University Press; 1940.

13. Geppert D V. Theoretical shape of metal-insulator-metal potential barriers. J Appl Phys. 1963;34(3).

14. Rohr JA. Measurements and Modelling of Space-Charge-Limited Current Transport in Organic Single-Carrier Devices. Imperial College London; 2018.

15. Senanayak SP, Yang B, Thomas TH, Giesbrecht N, Huang W, Gann E, et al. Understanding charge transport in lead iodide perovskite

thin-film field-effect transistors. Sci Adv. 2017;3(1):1–11.

16. Akihiro Kojima,† Kenjiro Teshima,‡ Yasuo Shirai and TM. Organometal Halide Perovskites as Visible- Light Sensitizers for Photovoltaic Cells. J Am Chem Soc. 2009;131(October):6050–1.

17. Kim HS, Lee CR, Im JH, Lee KB, Moehl T, Marchioro A, et al. Lead iodide perovskite sensitized all-solid-state submicron thin film mesoscopic solar cell with efficiency exceeding 9%. Sci Rep. 2012;2.

18. Green MA, Ho-Baillie A, Snaith HJ. The emergence of perovskite solar cells. Vol. 8, Nature Photonics. 2014.

19. Fu Y, Hautzinger MP, Luo Z, Wang F, Pan D, Aristov MM, et al. Incorporating Large A Cations into Lead Iodide Perovskite Cages: Relaxed Goldschmidt Tolerance Factor and Impact on Exciton-Phonon Interaction. ACS Cent Sci. 2019;5(8).

20. Xie LQ, Chen L, Nan ZA, Lin HX, Wang T, Zhan DP, et al. Understanding the Cubic Phase Stabilization and Crystallization Kinetics in Mixed Cations and Halides Perovskite Single Crystals. J Am Chem Soc. 2017;139(9).

21. Kang J, Wang LW. High Defect Tolerance in Lead Halide Perovskite CsPbBr3. J Phys Chem Lett. 2017;

22. Meggiolaro D, Motti SG, Mosconi E, Barker AJ, Ball J, Andrea Riccardo Perini C, et al. Iodine chemistry determines the defect

tolerance of lead-halide perovskites. Energy Environ Sci. 2018;

23. Yin WJ, Shi T, Yan Y. Unusual defect physics in CH3NH3PbI3 perovskite solar cell absorber. Appl Phys Lett. 2014;104(6).

24. Meggiolaro D, De Angelis F. First-Principles Modeling of Defects in Lead Halide Perovskites: Best Practices and Open Issues. ACS Energy Lett. 2018;

25. Steirer KX, Schulz P, Teeter G, Stevanovic V, Yang M, Zhu K, et al. Defect Tolerance in Methylammonium Lead Triiodide Perovskite. ACS Energy Lett. 2016;

26. Walsh A, Scanlon DO, Chen S, Gong XG, Wei SH. Self-regulation mechanism for charged point defects in hybrid halide perovskites. Angew Chemie - Int Ed. 2015;

27. Ball JM, Petrozza A. Defects in perovskite-halides and their effects in solar cells. Nat Energy. 2016;1(11).

28. Kim J, Lee SH, Lee JH, Hong KH. The role of intrinsic defects in methylammonium lead iodide perovskite. J Phys Chem Lett. 2014;

29. Stranks SD. Nonradiative Losses in Metal Halide Perovskites. ACS Energy Letters. 2017.

30. Luo D, Su R, Zhang W, Gong Q, Zhu R. Minimizing non-radiative recombination losses in perovskite solar cells. Nature Reviews

Materials. 2020.

31. Sherkar TS, Momblona C, Gil-Escrig L, Ávila J, Sessolo M, Bolink HJ, et al. Recombination in Perovskite Solar Cells: Significance of Grain Boundaries, Interface Traps, and Defect Ions. ACS Energy Lett. 2017;

32. Park JS, Calbo J, Jung YK, Whalley LD, Walsh A. Accumulation of Deep Traps at Grain Boundaries in Halide Perovskites. ACS Energy Lett. 2019;

33. Long R, Liu J, Prezhdo O V. Unravelling the Effects of Grain Boundary and Chemical Doping on Electron-Hole Recombination in CH3NH3PbI3 Perovskite by Time-Domain Atomistic Simulation. J Am Chem Soc. 2016;

34. Yun JS, Ho-Baillie A, Huang S, Woo SH, Heo Y, Seidel J, et al. Benefit of grain boundaries in organic-inorganic halide planar perovskite solar cells. J Phys Chem Lett. 2015;

35. Yang M, Zeng Y, Li Z, Kim DH, Jiang CS, Van De Lagemaat J, et al. Do grain boundaries dominate non-radiative recombination in CH3NH3PbI3 perovskite thin films? Phys Chem Chem Phys. 2017;

36. DeQuilettes DW, Zhang W, Burlakov VM, Graham DJ, Leijtens T, Osherov A, et al. Photo-induced halide redistribution in organic-inorganic perovskite films. Nat Commun. 2016;

37. Hoke ET, Slotcavage DJ, Dohner ER, Bowring AR, Karunadasa HI,

McGehee MD. Reversible photo-induced trap formation in mixed-halide hybrid perovskites for photovoltaics. Chem Sci. 2015;

38. Knight AJ, Patel JB, Snaith HJ, Johnston MB, Herz LM. Trap States, Electric Fields, and Phase Segregation in Mixed-Halide Perovskite Photovoltaic Devices. Adv Energy Mater. 2020;

39. Tian Y, Peter M, Unger E, Abdellah M, Zheng K, Pullerits T, et al. Mechanistic insights into perovskite photoluminescence enhancement: Light curing with oxygen can boost yield thousandfold. Phys Chem Chem Phys. 2015;

40. Sajedi Alvar M, Blom PWM, Wetzelaer GJAH. Device Model for Methylammonium Lead Iodide Perovskite With Experimentally Validated Ion Dynamics. Adv Electron Mater. 2020;

41. Calado P, Telford AM, Bryant D, Li X, Nelson J, O’Regan BC, et al. Evidence for ion migration in hybrid perovskite solar cells with minimal hysteresis. Nat Commun. 2016;7:1–10.

42. Richardson G, O’Kane SEJ, Niemann RG, Peltola TA, Foster JM, Cameron PJ, et al. Can slow-moving ions explain hysteresis in the current-voltage curves of perovskite solar cells? Energy Environ Sci. 2016;

43. Courtier NE, Richardson G, Foster JM. A fast and robust numerical scheme for solving models of charge carrier transport

and ion vacancy motion in perovskite solar cells. Appl Math Model. 2018;

44. Belisle RA, Nguyen WH, Bowring AR, Calado P, Li X, Irvine SJC, et al. Interpretation of inverted photocurrent transients in organic lead halide perovskite solar cells: Proof of the field screening by mobile ions and determination of the space charge layer widths. Energy Environ Sci. 2017;10(1).

45. Bertoluzzi L, Belisle RA, Bush KA, Cheacharoen R, McGehee MD, O’Regan BC. In Situ Measurement of Electric-Field Screening in Hysteresis-Free PTAA/FA0.83Cs0.17Pb(I0.83Br0.17)3/C60 Perovskite Solar Cells Gives an Ion Mobility of ∼3 × 10-7 cm2/(V s), 2 Orders of Magnitude Faster than Reported for Metal-Oxide-Contacted Perovskite Cells with Hysteresis. J Am Chem Soc. 2018;140(40).

46. Weber SAL, Hermes IM, Turren-Cruz SH, Gort C, Bergmann VW, Gilson L, et al. How the formation of interfacial charge causes hysteresis in perovskite solar cells. Energy Environ Sci. 2018;11(9).

47. Futscher MH, Lee JM, McGovern L, Muscarella LA, Wang T, Haider MI, et al. Quantification of ion migration in CH3NH3PbI3 perovskite solar cells by transient capacitance measurements. Mater Horizons. 2019;6(7).

48. Birkhold ST, Precht JT, Liu H, Giridharagopal R, Eperon GE, Schmidt-Mende L, et al. Interplay of Mobile Ions and Injected Carriers Creates Recombination Centers in Metal Halide Perovskites under Bias. ACS Energy Lett. 2018;3(6).

49. Le Corre VM, Duijnstee EA, El Tambouli O, Ball JM, Snaith HJ, Lim J, et al. Revealing Charge Carrier Mobility and Defect Densities in Metal Halide Perovskites via Space-Charge-Limited Current Measurements. ACS Energy Lett. 2021;6(3):1087–94.

50. Walsh A, Stranks SD. Taking Control of Ion Transport in Halide Perovskite Solar Cells. ACS Energy Lett. 2018;

51. Yang TY, Gregori G, Pellet N, Grätzel M, Maier J. The Significance of Ion Conduction in a Hybrid Organic-Inorganic Lead-Iodide-Based Perovskite Photosensitizer. Angew Chemie - Int Ed. 2015;54(27).

52. Ščajev P, Qin C, Aleksiejunas R, Baronas P, Miasojedovas S, Fujihara T, et al. Diffusion Enhancement in Highly Excited MAPbI3 Perovskite Layers with Additives. J Phys Chem Lett. 2018;9(12).

53. Lim J, Hörantner MT, Sakai N, Ball JM, Mahesh S, Noel NK, et al. Elucidating the long-range charge carrier mobility in metal halide perovskite thin films. Energy Environ Sci. 2019;

54. Snaith HJ, Abate A, Ball JM, Eperon GE, Leijtens T, Noel NK, et al.

Anomalous Hysteresis in Perovskite Solar Cells. J Phys Chem Lett. 2014;(5):1511–5.

55. Tress W, Marinova N, Moehl T, Zakeeruddin SM, Nazeeruddin MK, Grätzel M. Understanding the rate-dependent J-V hysteresis, slow time component, and aging in CH3NH3PbI3 perovskite solar cells: The role of a compensated electric field. Energy Environ Sci. 2015;8(3).

56. Unger EL, Hoke ET, Bailie CD, Nguyen WH, Bowring AR, Heumüller T, et al. Hysteresis and transient behavior in current-voltage measurements of hybrid-perovskite absorber solar cells. Energy Environ Sci. 2014;7(11).

57. Azpiroz JM, Mosconi E, Bisquert J, De Angelis F. Defect migration in methylammonium lead iodide and its role in perovskite solar cell operation. Energy Environ Sci. 2015;8(7).

58. Meloni S, Moehl T, Tress W, Franckeviius M, Saliba M, Lee YH, et al. Ionic polarization-induced current-voltage hysteresis in CH3NH3PbX3 perovskite solar cells. Nat Commun. 2016;7.

59. Game OS, Buchsbaum GJ, Zhou Y, Padture NP, Kingon AI. Ions Matter: Description of the Anomalous Electronic Behavior in Methylammonium Lead Halide Perovskite Devices. Adv Funct Mater. 2017;27(16).

60. Slotcavage DJ, Karunadasa HI, McGehee MD. Light-Induced

Phase Segregation in Halide-Perovskite Absorbers. Vol. 1, ACS Energy Letters. 2016.

61. Carrillo J, Guerrero A, Rahimnejad S, Almora O, Zarazua I, Mas-Marza E, et al. Ionic Reactivity at Contacts and Aging of Methylammonium Lead Triiodide Perovskite Solar Cells. Adv Energy Mater. 2016;6(9).
62. Kato Y, Ono LK, Lee M V., Wang S, Raga SR, Qi Y. Silver Iodide Formation in Methyl Ammonium Lead Iodide Perovskite Solar Cells with Silver Top Electrodes. Adv Mater Interfaces. 2015;2(13).
63. Shockley W, Prim RC. Space-charge limited emission in semiconductors. Phys Rev. 1953;90(5):753–8.
64. Bube RH. Trap Density Determination by Space-Charge-Limited Currents. J Appl Phys. 1962;33(5):1733–7.
65. Duijnstee EA, Ball JM, Le Corre VM, Koster LJA, Snaith HJ, Lim J. Toward Understanding Space-Charge Limited Current Measurements on Metal Halide Perovskites. ACS Energy Lett. 2020;(1):376–84.
66. Moia D, Gelmetti I, Calado P, Fisher W, Stringer M, Game OS, et al. Ionic-to-electronic current amplification in hybrid perovskite solar cells: ionically gated transistor-interface circuit model explains hysteresis and impedance of mixed conducting devices.

Energy Environ Sci. 2019;

67. Tang X, Brandl M, May B, Levchuk I, Hou Y, Richter M, et al. Photoinduced degradation of methylammonium lead triiodide perovskite semiconductors. J Mater Chem A. 2016;4(41).

68. Brennan MC, Draguta S, Kamat P V., Kuno M. Light-Induced Anion Phase Segregation in Mixed Halide Perovskites. ACS Energy Lett. 2018;3(1).

69. Nagabhushana GP, Shivaramaiah R, Navrotsky A. Direct calorimetric verification of thermodynamic instability of lead halide hybrid perovskites. Proc Natl Acad Sci U S A. 2016;113(28).

70. Huang HH, Tsai H, Raja R, Lin SL, Ghosh D, Hou CH, et al. Robust Unencapsulated Perovskite Solar Cells Protected by a Fluorinated Fullerene Electron Transporting Layer. ACS Energy Lett. 2021;6(9).

71. Lv Y, Zhang H, Liu R, Sun Y, Huang W. Composite Encapsulation Enabled Superior Comprehensive Stability of Perovskite Solar Cells. ACS Appl Mater Interfaces. 2020;12(24).

72. Bella F, Griffini G, Correa-Baena JP, Saracco G, Grätzel M, Hagfeldt A, et al. Improving efficiency and stability of perovskite solar cells with photocurable fluoropolymers. Science (80-). 2016;354(6309).

73. K. Rao M, Sangeetha DN, Selvakumar M, Sudhakar YN, Mahesha

MG. Review on persistent challenges of perovskite solar cells' stability. Vol. 218, Solar Energy. 2021.

74. Han G, Hadi HD, Bruno A, Kulkarni SA, Koh TM, Wong LH, et al. Additive Selection Strategy for High Performance Perovskite Photovoltaics. J Phys Chem C. 2018;122(25).

75. Yi C, Luo J, Meloni S, Boziki A, Ashari-Astani N, Grätzel C, et al. Entropic stabilization of mixed A-cation ABX3 metal halide perovskites for high performance perovskite solar cells. Energy Environ Sci. 2016;9(2).

76. Kulbak M, Gupta S, Kedem N, Levine I, Bendikov T, Hodes G, et al. Cesium Enhances Long-Term Stability of Lead Bromide Perovskite-Based Solar Cells. J Phys Chem Lett. 2016;7(1).

77. Choi H, Jeong J, Kim HB, Kim S, Walker B, Kim GH, et al. Cesium-doped methylammonium lead iodide perovskite light absorber for hybrid solar cells. Nano Energy. 2014;7.

78. Niu G, Li W, Li J, Liang X, Wang L. Enhancement of thermal stability for perovskite solar cells through cesium doping. RSC Adv. 2017;7(28).

79. Murugadoss G, Thangamuthu R, Vijayaraghavan S, Kanda H, Ito S. Caesium −Methyl Ammonium Mixed-Cation Lead Iodide Perovskite Crystals: Analysis and Application for Perovskite Solar Cells. Electrochim Acta. 2017;257.

80. Chen L, Tan YY, Chen ZX, Wang T, Hu S, Nan ZA, et al. Toward Long-Term Stability: Single-Crystal Alloys of Cesium-Containing Mixed Cation and Mixed Halide Perovskite. J Am Chem Soc. 2019;141(4).

81. Van Reenen S, Kemerink M, Snaith HJ. Modeling Anomalous Hysteresis in Perovskite Solar Cells. J Phys Chem Lett. 2015;

82. Foster JM, Snaith HJ, Leijtens T, Richardson G. A model for the operation of perovskite based hybrid solar cells: Formulation, analysis, and comparison to experiment. SIAM J Appl Math. 2014;

83. O'Kane SEJ, Richardson G, Pockett A, Niemann RG, Cave JM, Sakai N, et al. Measurement and modelling of dark current decay transients in perovskite solar cells. J Mater Chem C. 2017;

84. Neukom MT, Züfle S, Knapp E, Makha M, Hany R, Ruhstaller B. Why perovskite solar cells with high efficiency show small IV-curve hysteresis. Sol Energy Mater Sol Cells. 2017;

85. Courtier NE, Cave JM, Walker AB, Richardson G, Foster JM. IonMonger: a free and fast planar perovskite solar cell simulator with coupled ion vacancy and charge carrier dynamics. J Comput Electron. 2019;

86. Jacobs DA, Shen H, Pfeffer F, Peng J, White TP, Beck FJ, et al. The two faces of capacitance: New interpretations for electrical

impedance measurements of perovskite solar cells and their relation to hysteresis. J Appl Phys. 2018;

87. Mackenzie RCI. gpvdm. Available from: https://www.gpvdm.com/index.html

88. Calado P, Gelmetti I, Hilton B, Azzouzi M, Nelson J, Barnes PRF. Driftfusion: An open source code for simulating ordered semiconductor devices with mixed ionic-electronic conducting materials in one-dimension. arXiv. 2020.

89. Blakemore JS. Approximations for Fermi-Dirac integrals, especially the function F1 2(η) used to describe electron density in a semiconductor. Vol. 25, Solid State Electronics. 1982.

90. Farrell P, Patriarca M, Fuhrmann J, Koprucki T. Comparison of thermodynamically consistent charge carrier flux discretizations for Fermi–Dirac and Gauss–Fermi statistics. Opt Quantum Electron. 2018;50(2).

91. Lasia A. Electrochemical impedance spectroscopy and its applications. Vol. 9781461489337, Electrochemical Impedance Spectroscopy and its Applications. 2014.

92. Kanoun O. Impedance Spectroscopy: Advanced applications: Battery research, bioimpedance, system design. Impedance Spectroscopy: Advanced Applications: Battery Research, Bioimpedance, System Design. 2018.

93. Macdonald JR, Kenan WR. Interface effects in the electrical response of non-metallic conducting solids and liquids. IEEE Trans Electr Insul. 1981;EI-16(2).

94. Macdonald JR. Impedance Spectroscopy. Ann Biomed Eng. 1992;

95. Cole KS, Cole RH. Dispersion and absorption in dielectrics I. Alternating current characteristics. J Chem Phys. 1941;9(4).

96. Warburg E. Ueber das Verhalten sogenannter unpolarisirbarer Elektroden gegen Wechselstrom. Ann Phys. 1899;303(3).

97. Von Hauff E. Impedance Spectroscopy for Emerging Photovoltaics. J Phys Chem C. 2019;123(18).

98. Lin Q, Armin A, Nagiri RCR, Burn PL, Meredith P. Electro-optics of perovskite solar cells. Nat Photonics. 2015;9(2).

99. Juarez-Perez EJ, Sanchez RS, Badia L, Garcia-Belmonte G, Kang YS, Mora-Sero I, et al. Photoinduced giant dielectric constant in lead halide perovskite solar cells. J Phys Chem Lett. 2014;5(13):2390–4.

100. Almond DP, Bowen CR. An explanation of the photoinduced giant dielectric constant of lead halide perovskite solar cells. J Phys Chem Lett. 2015;6(9).

101. Guerrero A, Bisquert J, Garcia-Belmonte G. Impedance Spectroscopy of Metal Halide Perovskite Solar Cells from the

Perspective of Equivalent Circuits. Vol. 121, Chemical Reviews. 2021.

102. Guerrero A, Garcia-Belmonte G, Mora-Sero I, Bisquert J, Kang YS, Jacobsson TJ, et al. Properties of Contact and Bulk Impedances in Hybrid Lead Halide Perovskite Solar Cells Including Inductive Loop Elements. J Phys Chem C. 2016;120(15):8023–32.

103. Almora O, Cho KT, Aghazada S, Zimmermann I, Matt GJ, Brabec CJ, et al. Discerning recombination mechanisms and ideality factors through impedance analysis of high-efficiency perovskite solar cells. Nano Energy [Internet]. 2018;48(March):63–72. Available from: https://www.sciencedirect.com/science/article/pii/S2211285518301836

104. Pockett A, Eperon GE, Sakai N, Snaith HJ, Peter LM, Cameron PJ. Microseconds, milliseconds and seconds: Deconvoluting the dynamic behaviour of planar perovskite solar cells. Phys Chem Chem Phys. 2017;19(8).

105. Ghahremanirad E, Bou A, Olyaee S, Bisquert J. Inductive Loop in the Impedance Response of Perovskite Solar Cells Explained by Surface Polarization Model. J Phys Chem Lett. 2017;8(7):1402–6.

106. Kovalenko A, Pospisil J, Zmeskal O, Krajcovic J, Weiter M. Ionic origin of a negative capacitance in lead halide perovskites. Phys

Status Solidi - Rapid Res Lett. 2017;11(3).

107. Noel NK, Habisreutinger SN, Wenger B, Klug MT, Hörantner MT, Johnston MB, et al. A low viscosity, low boiling point, clean solvent system for the rapid crystallisation of highly specular perovskite films. Energy Environ Sci. 2017;10(1).

108. Barnes PRF, Miettunen K, Li X, Anderson AY, Bessho T, Gratzel M, et al. Interpretation of optoelectronic transient and charge extraction measurements in dye-sensitized solar cells. Adv Mater. 2013;25(13):1881–922.

109. Lee MM, Teuscher J, Miyasaka T, Murakami TN, Snaith HJ. Efficient hybrid solar cells based on meso-superstructured organometal halide perovskites. Science (80-). 2012;338(6107).

110. Dou L, Yang YM, You J, Hong Z, Chang WH, Li G, et al. Solution-processed hybrid perovskite photodetectors with high detectivity. Nat Commun. 2014;5.

111. Ling Y, Yuan Z, Tian Y, Wang X, Wang JC, Xin Y, et al. Bright Light-Emitting Diodes Based on Organometal Halide Perovskite Nanoplatelets. Adv Mater. 2016;28(2).

112. Xiao Z, Yuan Y, Shao Y, Wang Q, Dong Q, Bi C, et al. Giant switchable photovoltaic effect in organometal trihalide perovskite devices. Nat Mater [Internet]. 2014;14(2):193–8. Available from:

http://www.nature.com/doifinder/10.1038/nmat4150

113. Thiesbrummel J, Le Corre VM, Peña-Camargo F, Perdigón-Toro L, Lang F, Yang F, et al. Universal Current Losses in Perovskite Solar Cells Due to Mobile Ions. Adv Energy Mater. 2021;11(34).

114. Siekmann J, Ravishankar S, Kirchartz T. Apparent Defect Densities in Halide Perovskite Thin Films and Single Crystals. Vol. 6, ACS Energy Letters. 2021.

115. Fisher WR, Calado P, Röhr JA, Smith JA, Shi X, Game O, et al. The Validity Window of Space-Charge-Limited Current Measurements of Metal Halide Perovskite Devices. arXiv [Internet]. 2022 Apr 1; Available from: http://arxiv.org/abs/2204.00459

116. Wang Q, Shao Y, Xie H, Lyu L, Liu X, Gao Y, et al. Qualifying composition dependent p and n self-doping in CH3NH3PbI3. Appl Phys Lett. 2014;105(16).

117. Dänekamp B, Müller C, Sendner M, Boix PP, Sessolo M, Lovrincic R, et al. Perovskite-Perovskite Homojunctions via Compositional Doping. J Phys Chem Lett. 2018;9(11).

118. Cui P, Wei D, Ji J, Huang H, Jia E, Dou S, et al. Planar p–n homojunction perovskite solar cells with efficiency exceeding 21.3%. Nat Energy. 2019;4(2).

119. Zohar A, Levine I, Gupta S, Davidson O, Azulay D, Millo O, et al.

What is the Mechanism of MAPbI3 p-Doping by I2? Insights from Optoelectronic Properties. ACS Energy Lett. 2017;2(10).

120. Grishko AY, Eliseev AA, Goodilin EA, Tarasov AB. Measure is Treasure: Proper Iodine Vapor Treatment as a New Method of Morphology Improvement of Lead-Halide Perovskite Films. Chem Mater. 2020;

121. Eranna G, Joshi BC, Runthala DP, Gupta RP. Oxide materials for development of integrated gas sensors - A comprehensive review. Crit Rev Solid State Mater Sci. 2004;29(3–4).

122. Calado P, Barnes PRF. Ionic screening in perovskite p–n homojunctions. Vol. 6, Nature Energy. 2021.

123. Wang JTW, Wang Z, Pathak S, Zhang W, Dequilettes DW, Wisnivesky-Rocca-Rivarola F, et al. Efficient perovskite solar cells by metal ion doping. Energy Environ Sci. 2016;9(9).

124. Zhao W, Yao Z, Yu F, Yang D, Liu SF. Alkali Metal Doping for Improved CH3NH3PbI3 Perovskite Solar Cells. Adv Sci. 2018;5(2).

125. Muzammal uz Zaman M, Imran M, Saleem A, Kamboh AH, Arshad M, Khan NA, et al. Potassium doped methylammonium lead iodide (MAPbI3) thin films as a potential absorber for perovskite solar cells; structural, morphological, electronic and optoelectric properties. Phys B Condens Matter. 2017;522.

126. Chen C, Xu Y, Wu S, Zhang S, Yang Z, Zhang W, et al. CaI2: A more

effective passivator of perovskite films than PbI2 for high efficiency and long-term stability of perovskite solar cells. J Mater Chem A. 2018;6(17).

127. Klug MT, Osherov A, Haghighirad AA, Stranks SD, Brown PR, Bai S, et al. Tailoring metal halide perovskites through metal substitution: Influence on photovoltaic and material properties. Energy Environ Sci. 2017;10(1).

128. Phung N, Félix R, Meggiolaro D, Al-Ashouri A, Sousa E Silva G, Hartmann C, et al. The Doping Mechanism of Halide Perovskite Unveiled by Alkaline Earth Metals. J Am Chem Soc. 2020;142(5).

129. Yuen JD, Dhoot AS, Namdas EB, Coates NE, Heeney M, McCulloch I, et al. Electrochemical doping in electrolyte-gated polymer transistors. J Am Chem Soc. 2007;129(46).

130. Pei Q, Zuccarello G, Ahlskog M, Inganäs O. Electrochromic and highly stable poly(3,4-ethylenedioxythiophene) switches between opaque blue-black and transparent sky blue. Polymer (Guildf). 1994;35(7).

131. Giovannitti A, Nielsen CB, Sbircea DT, Inal S, Donahue M, Niazi MR, et al. N-type organic electrochemical transistors with stability in water. Nat Commun. 2016;7.

132. Maier J. Heterogeneous doping of silver bromide (AgBr:Al2O3). Mater Res Bull. 1985;20(4).

133. Maier J. Ionic conduction in space charge regions. Vol. 23, Progress in Solid State Chemistry. 1995.

134. Kim GY, Senocrate A, Moia D, Maier J. Ionically Generated Built-In Equilibrium Space Charge Zones—a Paradigm Change for Lead Halide Perovskite Interfaces. Adv Funct Mater. 2020;30(31):1–9.

135. Duijnstee EA, Le Corre VM, Johnston MB, Koster LJA, Lim J, Snaith HJ. Understanding Dark Current-Voltage Characteristics in Metal-Halide Perovskite Single Crystals. Phys Rev Appl. 2021;15(1).

136. Lampert MA. Simplified theory of space-charge-limited currents in an insulator with traps. Phys Rev. 1956;103(6):1648–56.

137. Rose A. Space-Charge-Limited Currents in Solids. 1955;1.

138. Röhr JA, Mackenzie RCI. Analytical description of mixed ohmic and space-charge-limited conduction in single-carrier devices. J Appl Phys. 2020;128(16).

139. Mark P, Helfrich W. Space-charge-limited currents in organic crystals. J Appl Phys. 1962;33(1):205–15.

140. Dacuña J, Salleo A. Modeling space-charge-limited currents in organic semiconductors: Extracting trap density and mobility. Phys Rev B - Condens Matter Mater Phys. 2011;84(19):1–9.

141. Röhr JA, Moia D, Haque SA, Kirchartz T, Nelson J. Exploring the

validity and limitations of the Mott–Gurney law for charge-carrier mobility determination of semiconducting thin-films. J Phys Condens Matter [Internet]. 2018;30(10):105901. Available from: http://stacks.iop.org/0953-8984/30/i=10/a=105901?key=crossref.ad888c5e6bfa28898a84fc9dc1e2ae08

142. Tress W, Marinova N, Moehl T, Zakeeruddin SM, Nazeeruddin MK, Grätzel M. Understanding the rate-dependent J-V hysteresis, slow time component, and aging in CH3NH3PbI3perovskite solar cells: The role of a compensated electric field. Energy Environ Sci. 2015;8(3):995–1004.

143. Shi D, Adinolfi V, Comin R, Yuan M, Alarousu E, Buin A, et al. Low trap-state density and long carrier diffusion in organolead trihalide perovskite single crystals. Science (80-). 2015;347(6221):519–22.

144. Saidaminov MI, Abdelhady AL, Murali B, Alarousu E, Burlakov VM, Peng W, et al. High-quality bulk hybrid perovskite single crystals within minutes by inverse temperature crystallization. Nat Commun [Internet]. 2015;6(May):1–6. Available from: http://dx.doi.org/10.1038/ncomms8586

145. Zhumekenov AA, Saidaminov MI, Haque MA, Alarousu E, Sarmah SP, Murali B, et al. Formamidinium Lead Halide Perovskite Crystals with Unprecedented Long Carrier Dynamics and

Diffusion Length. ACS Energy Lett. 2016;1(1):32–7.

146. Dong Q, Fang Y, Shao Y, Mulligan P, Qiu J, Cao L, et al. 5、Electron-hole diffusion lengths > 175 m m in solution-grown CH 3 NH 3 PbI 3 single crystals. Science (80-). 2015;347(6225):967–70.

147. Maculan G, Sheikh AD, Abdelhady AL, Saidaminov MI, Haque MA, Murali B, et al. CH3NH3PbCl3 Single Crystals: Inverse Temperature Crystallization and Visible-Blind UV-Photodetector. J Phys Chem Lett. 2015;6(19):3781–6.

148. Sajedi Alvar M, Blom PWM, Wetzelaer GJAH. Space-charge-limited electron and hole currents in hybrid organic-inorganic perovskites. Nat Commun. 2020;11(1).

149. Ponseca CS, Savenije TJ, Abdellah M, Zheng K, Yartsev A, Pascher T, et al. Organometal halide perovskite solar cell materials rationalized: Ultrafast charge generation, high and microsecond-long balanced mobilities, and slow recombination. J Am Chem Soc. 2014;136(14).

150. Gunawan O, Pae SR, Bishop DM, Virgus Y, Noh JH, Jeon NJ, et al. Carrier-resolved photo-Hall effect. Nature. 2019;575(7781).

151. Xia CQ, Peng J, Poncé S, Patel JB, Wright AD, Crothers TW, et al. Limits to Electrical Mobility in Lead-Halide Perovskite Semiconductors. J Phys Chem Lett. 2021;12(14).

152. Euvrard J, Yan Y, Mitzi DB. Electrical doping in halide perovskites. Vol. 6, Nature Reviews Materials. 2021.

153. Giorgi G, Fujisawa JI, Segawa H, Yamashita K. Small photocarrier effective masses featuring ambipolar transport in methylammonium lead iodide perovskite: A density functional analysis. J Phys Chem Lett. 2013;4(24).

154. Calado P, Telford AM, Bryant D, Li X, Nelson J, O'Regan BC, et al. Evidence for ion migration in hybrid perovskite solar cells with minimal hysteresis. Nat Commun. 2016;

155. Richardson G, O'Kane SEJ, Niemann RG, Peltola TA, Foster JM, Cameron PJ, et al. Can slow-moving ions explain hysteresis in the current-voltage curves of perovskite solar cells? Energy Environ Sci. 2016;9(4):1476–85.

156. Neukom M, Züfle S, Jenatsch S, Ruhstaller B. Opto-electronic characterization of third-generation solar cells. Sci Technol Adv Mater [Internet]. 2018;19(1):291–316. Available from: http://doi.org/10.1080/14686996.2018.1442091

157. Cheng Z, Lin J. Layered organic-inorganic hybrid perovskites: Structure, optical properties, film preparation, patterning and templating engineering. CrystEngComm. 2010;12(10).

158. Frost JM, Butler KT, Brivio F, Hendon CH, Van Schilfgaarde M, Walsh A. Atomistic origins of high-performance in hybrid halide

perovskite solar cells. Nano Lett. 2014;14(5).

159. Yang J, Siempelkamp BD, Liu D, Kelly TL. Investigation of CH3NH3PbI3degradation rates and mechanisms in controlled humidity environments using in situ techniques. ACS Nano. 2015;9(2).

160. Leguy MA, Hu Y, Campoy-quiles M, Alonso MI, Weber OJ, Azarhoosh P, et al. Reversible Hydration of CH 3 NH 3 PbI 3 in Films, Single Crystals, and Solar Cells. 2015;

161. Poglitsch A, Weber D. Dynamic disorder in methylammoniumtrihalogenoplumbates (II) observed by millimeter-wave spectroscopy. J Chem Phys. 1987;87(11).

162. Yun JS, Kim J, Young T, Patterson RJ, Kim D, Seidel J, et al. Humidity-Induced Degradation via Grain Boundaries of HC(NH2)2PbI3 Planar Perovskite Solar Cells. Adv Funct Mater. 2018;28(11).

163. Shirayama M, Kato M, Miyadera T, Sugita T, Fujiseki T, Hara S, et al. Degradation mechanism of CH3NH3PbI3 perovskite materials upon exposure to humid air. J Appl Phys. 2016;119(11).

164. Xiao Z, Wang D, Dong Q, Wang Q, Wei W, Dai J, et al. Unraveling the hidden function of a stabilizer in a precursor in improving hybrid perovskite film morphology for high efficiency solar cells. Energy Environ Sci. 2016;9(3).

165. Zheng C, Rubel O. Unraveling the Water Degradation Mechanism of CH3NH3PbI3. J Phys Chem C. 2019;123(32).

166. Kye YH, Yu CJ, Jong UG, Chen Y, Walsh A. Critical Role of Water in Defect Aggregation and Chemical Degradation of Perovskite Solar Cells. J Phys Chem Lett. 2018;9(9).

167. García-Fernández A, Moradi Z, Bermúdez-García JM, Sánchez-Andújar M, Gimeno VA, Castro-García S, et al. Effect of Environmental Humidity on the Electrical Properties of Lead Halide Perovskites. J Phys Chem C. 2019;123(4):2011–8.

168. Jong UG, Yu CJ, Ri GC, McMahon AP, Harrison NM, Barnes PRF, et al. Influence of water intercalation and hydration on chemical decomposition and ion transport in methylammonium lead halide perovskites. J Mater Chem A. 2018;6(3).

169. Grancini G, D'Innocenzo V, Dohner ER, Martino N, Srimath Kandada AR, Mosconi E, et al. CH3NH3PbI3 perovskite single crystals: Surface photophysics and their interaction with the environment. Chem Sci. 2015;6(12).

170. Mosconi E, Amat A, Nazeeruddin MK, Grätzel M, De Angelis F. First-principles modeling of mixed halide organometal perovskites for photovoltaic applications. J Phys Chem C. 2013;117(27).

171. Senno M, Tinte S. Mixed formamidinium-methylammonium lead

iodide perovskite from first-principles: hydrogen-bonding impact on the electronic properties. Phys Chem Chem Phys. 2021;23(12).

172. Trots DM, Myagkota S V. High-temperature structural evolution of caesium and rubidium triiodoplumbates. J Phys Chem Solids. 2008;69(10).

173. Thomas CJ, Zhang Y, Guillaussier A, Bdeir K, Aly OF, Kim HG, et al. Thermal Stability of the Black Perovskite Phase in Cesium Lead Iodide Nanocrystals under Humid Conditions. Chem Mater. 2019;31(23).

174. Lin Z, Zhang Y, Gao M, Steele JA, Louisia S, Yu S, et al. Kinetics of moisture-induced phase transformation in inorganic halide perovskite. Matter. 2021;4(7).

175. Eperon GE, Stranks SD, Menelaou C, Johnston MB, Herz LM, Snaith HJ. Formamidinium lead trihalide: A broadly tunable perovskite for efficient planar heterojunction solar cells. Energy Environ Sci. 2014;7(3).

176. Greenspan L. HUMIDITY FIXED POINTS OF BINARY SATURATED AQUEOUS SOLUTIONS. J Res Natl Bur Stand Sect A Phys Chem. 1977;81 A(1).

177. Leguy AMA, Hu Y, Campoy-Quiles M, Alonso MI, Weber OJ, Azarhoosh P, et al. Reversible hydration of CH3NH3PbI3 in films,

single crystals, and solar cells. Chem Mater. 2015;

178. Fang TT, Chen MI, Hsu WD. Insight into understanding the jump frequency of diffusion in solids. AIP Adv. 2020;10(6).
179. Gong X, Li M, Shi XB, Ma H, Wang ZK, Liao LS. Controllable Perovskite Crystallization by Water Additive for High-Performance Solar Cells. Adv Funct Mater. 2015;25(42).
180. Forney CF, Brandl DG. Control of Humidity in Small Controlled-environment Chambers using Glycerol-Water Solutions. Horttechnology. 2018;2(1).
181. Herz LM. Charge-Carrier Mobilities in Metal Halide Perovskites: Fundamental Mechanisms and Limits. ACS Energy Lett. 2017;2(7):1539–48.
182. McDougall J (University of L, Stoner EC (University of L. The Computation of Fermi-Dirac Functions. Philos Trans R Soc London [Internet]. 1938;237(773):67–104. Available from: https://royalsocietypublishing.org/doi/abs/10.1098/rsta.1938.0004
183. NIST. H2O - Antoine equation parameters [Internet]. NIST Chemistry WebBook, SRD 69. [cited 2021 Feb 10]. Available from: https://webbook.nist.gov/cgi/cbook.cgi?ID=C7732185&Mask=4&Type=ANTOINE&Plot=on

Appendix A - Simulation parameters

A.1 Simulation parameter set for parameter investigation in Chapter Chapter 4

VARIABLE	MAPI	UNIT
Thickness	4×10^{-5}	cm
Electron affinity	-3.8	eV
Ionization potential	-5.4	eV
Equilibrium Fermi energy	-4.6	eV
eDOS conduction band	1×10^{19}	cm^{-3}
eDOS valence band	1×10^{19}	cm^{-3}
Cation density	Variable	cm^{-3}
Anion density	Variable	cm^{-3}
Electron mobility	20	$cm^2\,V^{-1}\,s^{-1}$
Hole mobility	20	$cm^2\,V^{-1}\,s^{-1}$
Cation mobility	1×10^{-10}	$cm^2\,V^{-1}\,s^{-1}$
Anion mobility	0	$cm^2\,V^{-1}\,s^{-1}$
Relative dielectric constant	23	-
Device Boundaries		
Left hand boundary electron extraction coefficient	1×10^{10}	$cm\,s^{-1}$
Right hand boundary electron extraction coefficient	1×10^{10}	$cm\,s^{-1}$
Left hand boundary hole extraction coefficient	1×10^{10}	$cm\,s^{-1}$
Right hand boundary hole extraction coefficient	1×10^{10}	$cm\,s^{-1}$
$\phi_{\mathrm{m,left}}$	Variable	eV
$\phi_{\mathrm{m,right}}$	Variable	eV

Table A.1 Key parameters for metal/perovskite/metal device simulation results for all non-thickness dependent investigations apart from figure 5 in the main text.

Appendix B - Simulation parameters

B.1 Simulation parameter set for simulating experimental results in Chapter Chapter 4

Variable	MAPI	PolyTPD	PTAA	Unit
Thickness	$4\mathrm{x}10^{-5}$	$6\mathrm{x}10^{-7}$	$2\mathrm{x}10^{-6}$	cm
Electron affinity	-3.8	-2.3	-2.3	eV
Ionization potential	-5.4	-5.2	-5.3	eV
Equilibrium Fermi energy	-4.6	-5	-5.1	eV
eDOS conduction band	$1\mathrm{x}10^{19}$	$1\mathrm{x}10^{19}$	$1\mathrm{x}10^{19}$	cm^{-3}
eDOS valence band	$1\mathrm{x}10^{19}$	$1\mathrm{x}10^{19}$	$1\mathrm{x}10^{19}$	cm^{-3}
Cation density	$1\mathrm{x}10^{18}$	-	-	cm^{-3}
Anion density	$1\mathrm{x}10^{18}$	-	-	cm^{-3}
Electron mobility	20	$7.5\mathrm{x}10^{-3}$	$7.5\mathrm{x}10^{-3}$	$\mathrm{cm}^{2}\ \mathrm{V}^{-1}\ \mathrm{s}^{-1}$
Hole mobility	20	$7.5\mathrm{x}10^{-3}$	$7.5\mathrm{x}10^{-3}$	$\mathrm{cm}^{2}\ \mathrm{V}^{-1}\ \mathrm{s}^{-1}$
Cation mobility	$1\mathrm{x}10^{-10}$	-	-	$\mathrm{cm}^{2}\ \mathrm{V}^{-1}\ \mathrm{s}^{-1}$
Anion mobility	0	-	-	$\mathrm{cm}^{2}\ \mathrm{V}^{-1}\ \mathrm{s}^{-1}$
Relative dielectric constant	23	3	3	-
Device Boundaries				
Left hand boundary electron extraction coefficient	-	-	$1\mathrm{x}10^{10}$	$\mathrm{cm\ s}^{-1}$
Right hand boundary electron extraction coefficient	-	$1\mathrm{x}10^{10}$	-	$\mathrm{cm\ s}^{-1}$
Left hand boundary hole extraction coefficient	-	-	$1\mathrm{x}10^{10}$	$\mathrm{cm\ s}^{-1}$
Right hand boundary hole extraction coefficient	-	$1\mathrm{x}10^{10}$	-	$\mathrm{cm\ s}^{-1}$
$\phi_{m,left}$	-5.1			eV
$\phi_{m,right}$	-4.6			eV

Table B.1 Key parameters for Au/PTAA/perovskite/PolyTPD/ITO simulation of the experimental results presented in figures 5 of the main text.

Appendix C - Simulation parameters

C.1 Simulation parameter set for simulation investigation results in Chapter

Chapter 5

VARIABLE	MAPI	UNIT
Thickness	$4\text{x}10^{-5}$	cm
Electron affinity	-3.8	eV
Ionization potential	-5.4	eV
Equilibrium Fermi energy	-4.6	eV
eDOS conduction band	$1\text{x}10^{19}$	cm^{-3}
eDOS valence band	$1\text{x}10^{19}$	cm^{-3}
Cation density	$1\text{x}10^{18}$	cm^{-3}
Anion density	$1\text{x}10^{18}$	cm^{-3}
Electron mobility	20	$\text{cm}^2\,\text{V}^{-1}\,\text{s}^{-1}$
Hole mobility	20	$\text{cm}^2\,\text{V}^{-1}\,\text{s}^{-1}$
Cation mobility	$1\text{x}10^{-10}$	$\text{cm}^2\,\text{V}^{-1}\,\text{s}^{-1}$
Anion mobility	0	$\text{cm}^2\,\text{V}^{-1}\,\text{s}^{-1}$
Relative dielectric constant	23	-
Device Boundaries		
Left hand boundary electron extraction coefficient	$1\text{x}10^{10}$	cm s^{-1}
Right hand boundary electron extraction coefficient	$1\text{x}10^{10}$	cm s^{-1}
Left hand boundary hole extraction coefficient	$1\text{x}10^{10}$	cm s^{-1}
Right hand boundary hole extraction coefficient	$1\text{x}10^{10}$	cm s^{-1}
$\phi_{\text{m,left}}$	-5.4	eV
$\phi_{\text{m,right}}$	-5.4	eV

Table C.1 Key parameters for metal/perovskite/metal device simulation results presented in figures 1 and 3 in the main text.

Appendix D - Simulation parameters

D.1 Simulation parameter set for simulating experimental results in Chapter Chapter 5

Variable	MAPI	PolyTPD	PTAA	Unit
Thickness	$4\text{x}10^{-5}$	$6\text{x}10^{-7}$	$2\text{x}10^{-6}$	cm
Electron affinity	-3.8	-2.3	-2.3	eV
Ionization potential	-5.4	-5.2	-5.3	eV
Equilibrium Fermi energy	-4.6	-5	-5.1	eV
eDOS conduction band	$1\text{x}10^{19}$	$1\text{x}10^{19}$	$1\text{x}10^{19}$	cm^{-3}
eDOS valence band	$1\text{x}10^{19}$	$1\text{x}10^{19}$	$1\text{x}10^{19}$	cm^{-3}
Cation density	$1\text{x}10^{18}$	-	-	cm^{-3}
Anion density	$1\text{x}10^{18}$	-	-	cm^{-3}
Electron mobility	20	$7.5\text{x}10^{-3}$	$7.5\text{x}10^{-3}$	$\text{cm}^2\,\text{V}^{-1}\,\text{s}^{-1}$
Hole mobility	20	$7.5\text{x}10^{-3}$	$7.5\text{x}10^{-3}$	$\text{cm}^2\,\text{V}^{-1}\,\text{s}^{-1}$
Cation mobility	$1\text{x}10^{-10}$	-	-	$\text{cm}^2\,\text{V}^{-1}\,\text{s}^{-1}$
Anion mobility	0	-	-	$\text{cm}^2\,\text{V}^{-1}\,\text{s}^{-1}$
Relative dielectric constant	23	3	3	-
Device Boundaries				
Left hand boundary electron extraction coefficient	-	-	$1\text{x}10^{10}$	cm s^{-1}
Right hand boundary electron extraction coefficient	-	$1\text{x}10^{10}$	-	cm s^{-1}
Left hand boundary hole extraction coefficient	-	-	$1\text{x}10^{10}$	cm s^{-1}
Right hand boundary hole extraction coefficient	-	$1\text{x}10^{10}$	-	cm s^{-1}
$\phi_{m,left}$	-5.1			eV
$\phi_{m,right}$	-4.5			eV

Table D.1 Key parameters for Au/PTAA/perovskite/PolyTPD/ITO simulations presented in figures 2 and 4 in the main text.

Appendix E - Supplementary figures

E.1 Supplementary figures for Chapter 4

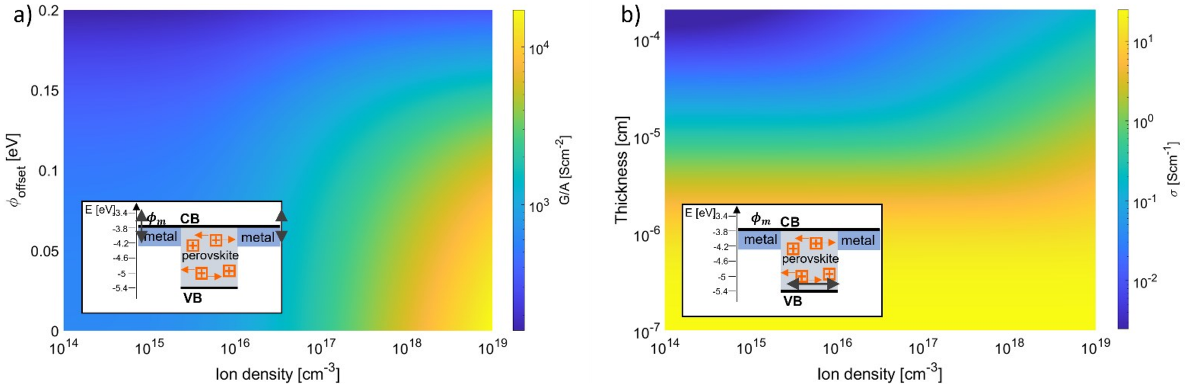

Figure E.1 Colour maps replicating the parameter variation in Figure 4.3 but for electron devices, this causes the ionic charge to be depleted at the interface rather than accumulated. (a) The contact energetics are varied by modifying ϕ_{offset} for devices with different ion densities. The interfacial doping effect (enhanced G/A with higher ion densities) exists for $\phi_{offset} \leq 0.15\ eV$ and ion density $\geq 5 \times 10^{16}\ cm^{-3}$. The highest G/A value is not as high as the highest value in Figure 4.3a and Figure 4.3b. (b) The variation of σ with device thickness and ion density. The interfacial doping effect is stronger in thicker devices and does not exist in devices with thickness $\leq 10^{-6}\ cm$. This result is very similar to Figure 4.3c.

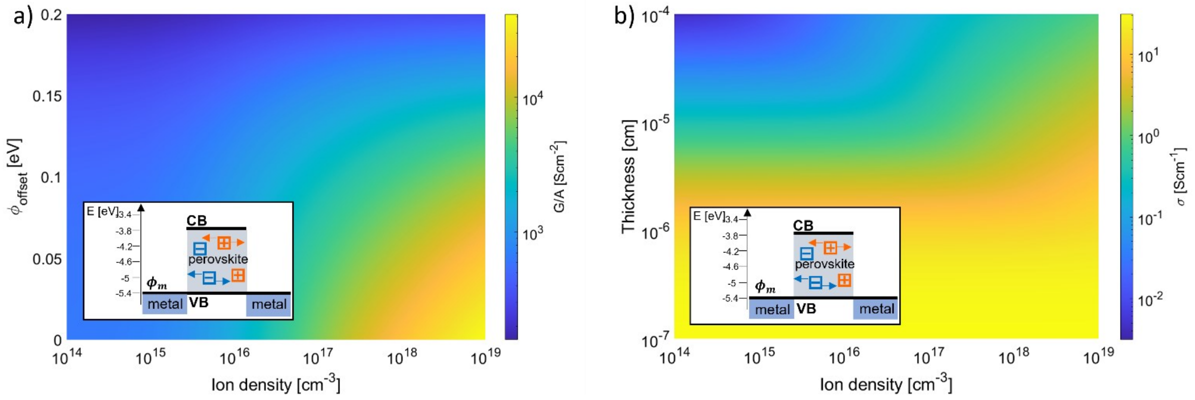

Figure E.2 Colour maps replicating the parameter variation in Figure 4.3 for hole devices but with two equivalent ionic species of opposite charge. (a) The contact energetics are varied by modifying ϕ_{offset} for devices with different ion densities. The interfacial doping effect (enhanced G/A with higher ion densities) exists for $\phi_{offset} \leq 0.15\ eV$ and ion density $\geq 5 \times 10^{16}\ cm^{-3}$. The highest value of G/A is higher than the highest values in Figure 4.3a and Figure 4.3b due to the combined space-charge contribution of two ion species being greater than the contribution of one. (b) The variation of σ with device thickness and ion density. The interfacial doping effect is stronger in thicker devices and does not exist in devices with thickness $\leq 10^{-6}\ cm$. This result is very similar to Figure 4.3c.

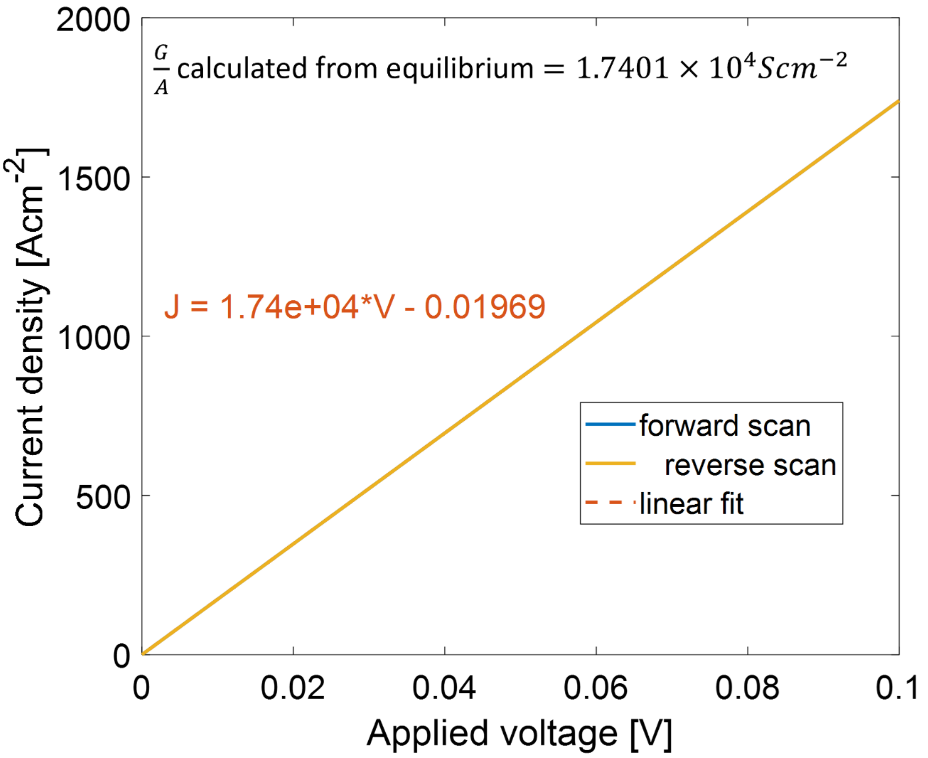

Figure E.3 A demonstration that a linear fit of the JV curve gives a G/A value equal to the value calculated using the equilibrium charge densities. A JV simulation of a hole device with mobile ionic charge frozen in its equilibrium position from 0 V to 0.1 V and back is shown. The forward and reverse scans are equal and overlap on this graph. The linear fit, which is obscured by the reverse scan, is performed on the JV curve and the equation of the resulting straight line is given on the graph. The coefficient of the voltage in this equation is equal to G/A.

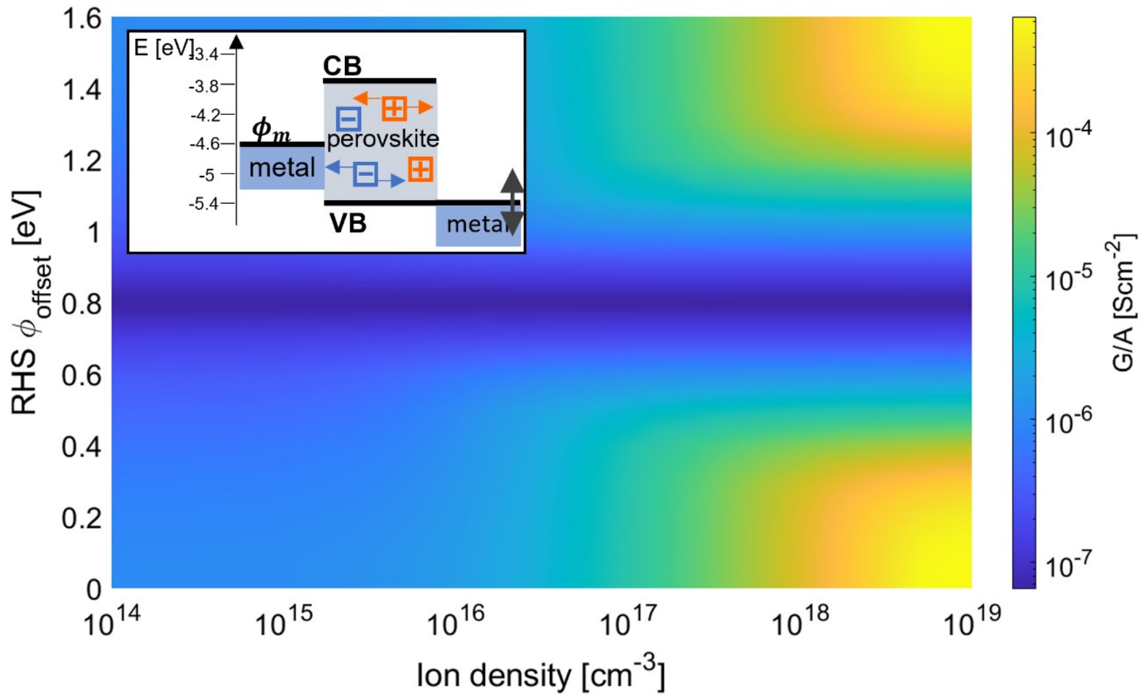

Figure E.4 A colour map depicting the variation in calculated G/A with ion density and $LHS\ \phi_{offset}$ for a 400 nm thick device with two equivalent ionic species of opposite charge and fixed mid band-gap left-hand contact workfunction ($RHS\ \phi_{offset} = 0.8\ eV$). The fact that there is always an ionic species of the same sign as the majority charge carrier means that the interfacial doping effect can occur when $RHS\ \phi_{offset} = E_{CB}$ and E_{VB}. E_{CB} is the conduction band edge and E_{VB} is the valance band edge.

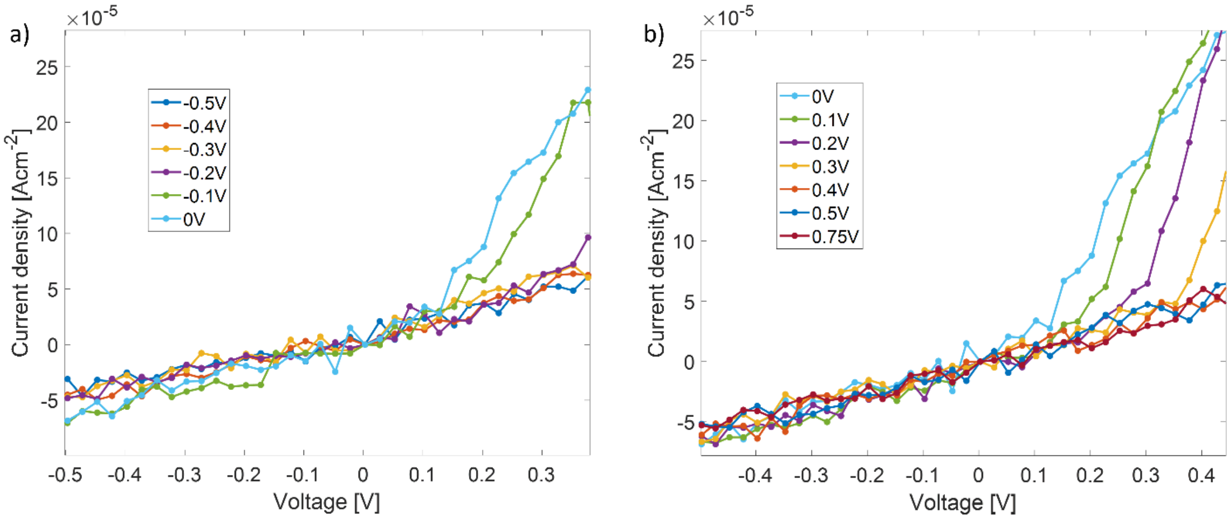

Figure E.5 The experimentally determined pulsed voltage JV curves used to measure the conductance per unit area of the device after different $V_{pre\text{-}bias}$. a) All $V_{pre\text{-}bias}$ are positive as shown in the legend. b) All $V_{pre\text{-}bias}$ are negative as shown in the legend. The $V_{pre-bias} = 0\ V$ curve is shown in both panels for ease of comparison.

Appendix F - Supplementary figures

F.1 Supplementary figures for Chapter Chapter 5

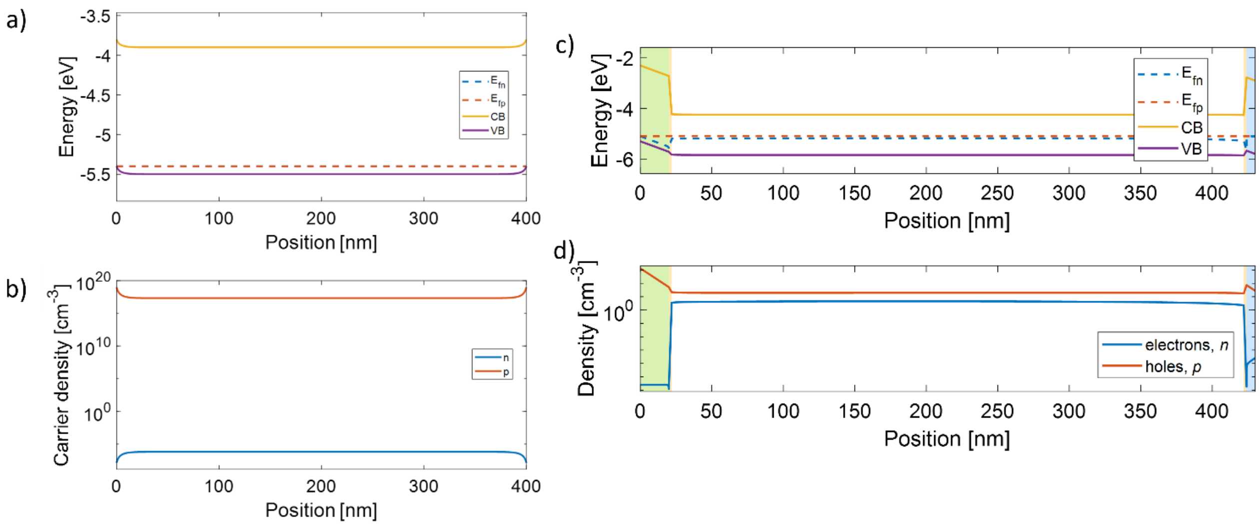

Figure F.1 Simulation results for the equilibrium solution of devices investigated in Chapter Chapter 5. a-b) Simulation results for the equilibrium solution of a device with symmetrical contacts with no workfunction offset at the valence-band (at -5.4eV) showing a) the energy levels and quasi-Fermi levels of the device and b) the charge carrier densities. c-d) Simulation results for the equilibrium solution of the device investigated experimentally in this work c) the energy levels and quasi-Fermi levels of the device and d) the charge carrier densities.

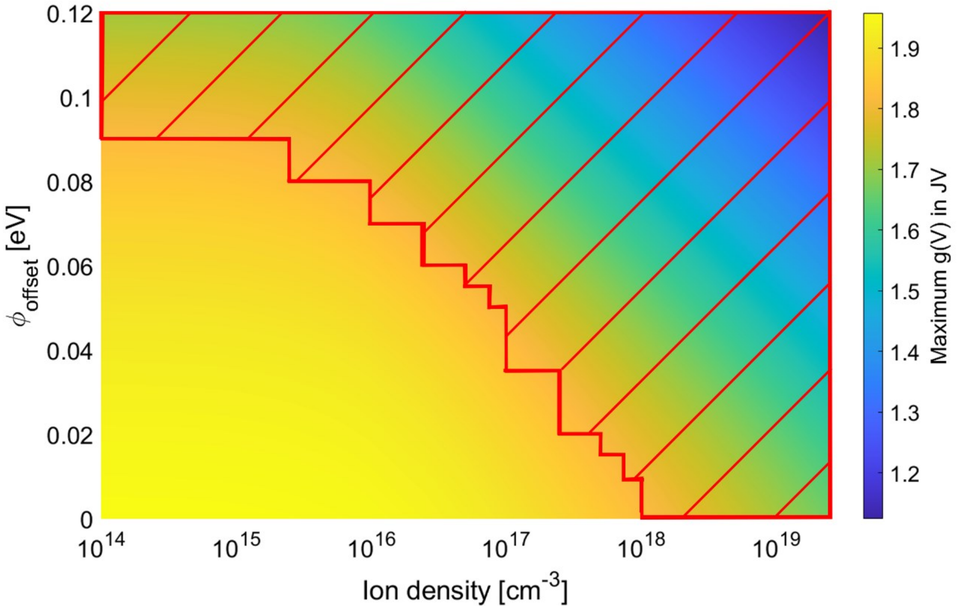

Figure F.2 Analysis of a set of drift-diffusion simulations explaining the limits of the application of MG analysis to perovskite devices of thickness 400 nm showing the highest value of *g(V)* for each simulated JV curve for this set of devices. The red shaded box shows the region where $g(V) < 1.8$.

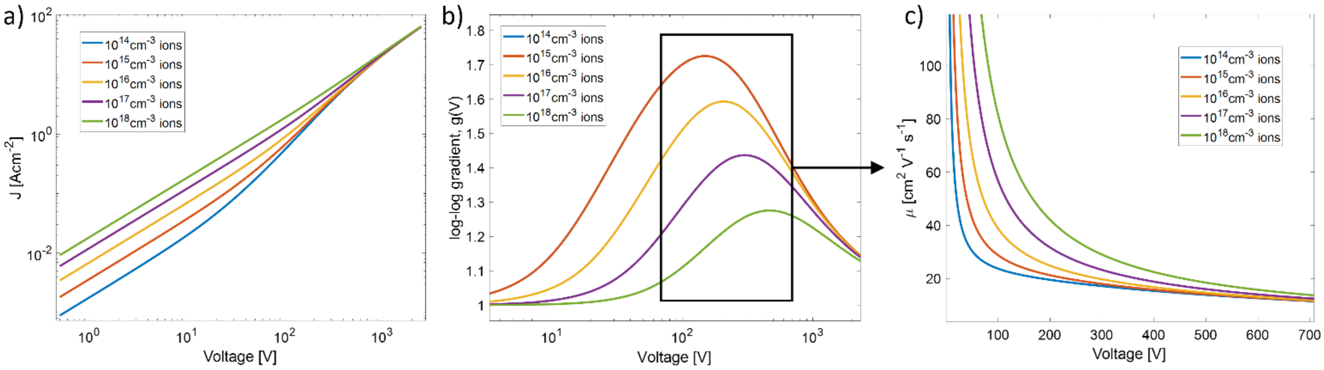

Figure F.3 Investigating the JV curves of a device with $\phi_{offset} = 0.3\ eV$ and thickness $100\mu m$. (a) JV simulations where ion density is varied. (b) the *g(V)* values calculated from the JV curves in (a) – note that the blue curve is very close to the red curve and is obscured. (c) the mobility values calculated from the region in the black box of (b): the region where the peaks in *g(V)* occur.

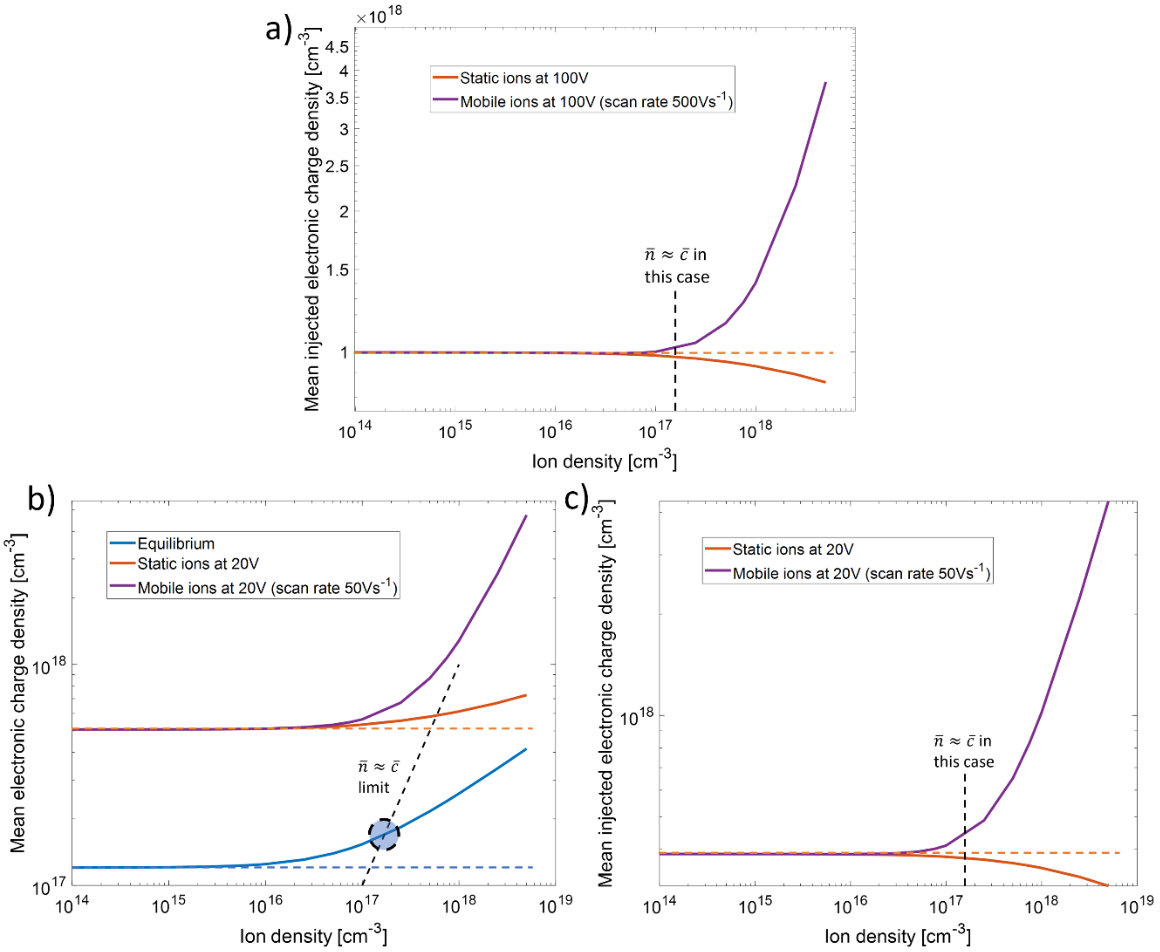

Figure F.4 Total calculated charge densities and injected charge densities at different voltages of JV curves under different measurement regimes. (a) the injected electronic charge averaged across the device thickness at 100V during JV scans *vs* ion density. The specific limit for MG analysis of this device is shown by the black dashed line. (b) the mean total electronic charge density at equilibrium and at 20V during JV scans, the blue circle represents the intersection of our suggested limit (black dashed line) and the charge density at equilibrium, for ion densities lower than at the blue circle, MG analysis will be valid. (c) the injected electronic charge averaged across the device thickness at 100 V during JV scans *vs* ion density. The specific limit for MG analysis of this device is shown by the black dashed line.

F.2 Calculation for the estimation of the upper limit of charge carrier densities in single carrier perovskite devices

Derivations of this form are very common in many semiconductor textbooks and lecture series, the derivation used here is some arbitrary combination of many of them. In a device with ideal ohmic contacts the work function energies of the contacts are aligned with the conduction band (electron affinity) or valence band (ionization potential) energies of the semiconductor. Under these circumstances the maximum density of electrons or holes in the semiconductor can be estimated by finding the density when the Fermi level (*E_F*) is at the conduction or valence band edge. The electron density in a semiconducting material can be calculated from the integral:

$$n_0 = \int_{E_c}^{\infty} g(E)F(E)dE$$

Equation 24

where E_c is the energy of the conduction band edge, *g(E)* is the density of states and *F(E)* is the occupancy factor as a function of energy *E*. The equation for approximating the density of states near the conduction band edge of a semiconductor is also well known if the system is 3 dimensional and the dispersion relation is assumed to be parabolic:

$$g(E) = \frac{(m^*)^{\frac{3}{2}}\sqrt{2(E - E_c)}}{\pi^2\hbar^3}$$

Equation 25

where m^* is the effective mass of the electron and $\hbar$ is the reduced Planck's constant. The occupancy factor is given by the Fermi-Dirac distribution (since Boltzmann statistics do not apply for $(E - E_F) \leq k_BT$),

$$F(E) = \frac{1}{1 + e^{\frac{(E-E_F)}{k_BT}}}$$

Equation 26

where k_BT is the thermal energy. Equation 25 and Equation 26 are substituted into Equation 24 assuming $E_F = E_C$ and rearranged to obtain an integral known as the Fermi-Dirac integral of order ½ (here $F_{1/2}(\eta_F)$) giving,

$$n_0 = \frac{\sqrt{2}(m^*k_BT)^{\frac{3}{2}}}{\pi^2\hbar^3}\int_0^{\infty}\frac{\eta^{\frac{1}{2}}}{1 + \exp(\eta - \eta_F)}d\eta$$

Equation 27

where the substitutions $\eta = (E - E_c)/k_BT$ and $\eta_F = (E_F - E_c)/k_BT$ have been made. For a device with ideal and symmetrical Ohmic contacts the equilibrium position of the Fermi level in the perovskite is at the conduction band edge meaning $\eta_F = 0$ and $F_{1/2}(0)$. Values for the general function $F_{1/2}(x)$ have been evaluated in (182) giving $F_{1/2}(0)$ = 0.678 (only quoted to 3dp here). Then taking $m^* \approx 0.23 m_e$ in a perovskite conduction band (assumed as $MAPbI_3$ here) (153) where m_e is the rest mass of an electron. We obtain an upper limit of $n_0 \leq 2 \times 10^{18} cm^{-3}$.

Appendix G - Supplementary figures

G.1 Supplementary figures for Chapter 6

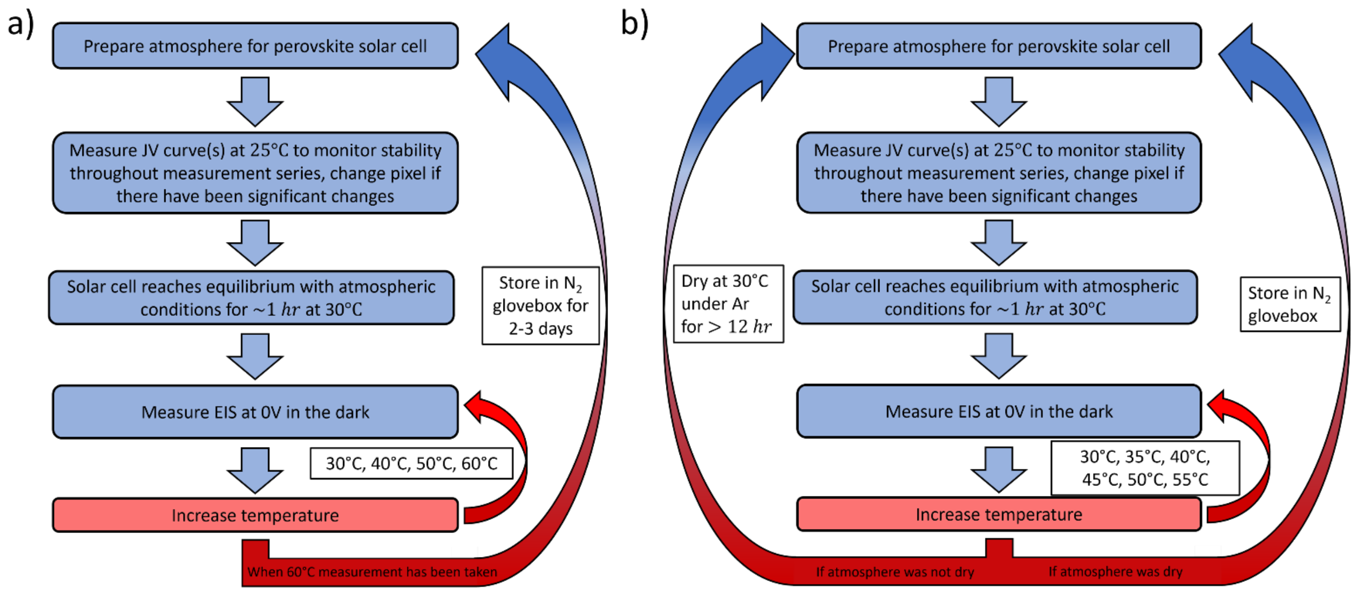

Figure G.1 Measurement batch specific workflow diagrams. (a) A workflow diagram representing the technique used to collect all data from the 1st batch of measurements. b) A workflow diagram representing the technique used to collect all data from the 2nd batch of measurements where the device is either dried or stored in an inert atmosphere after measuring.

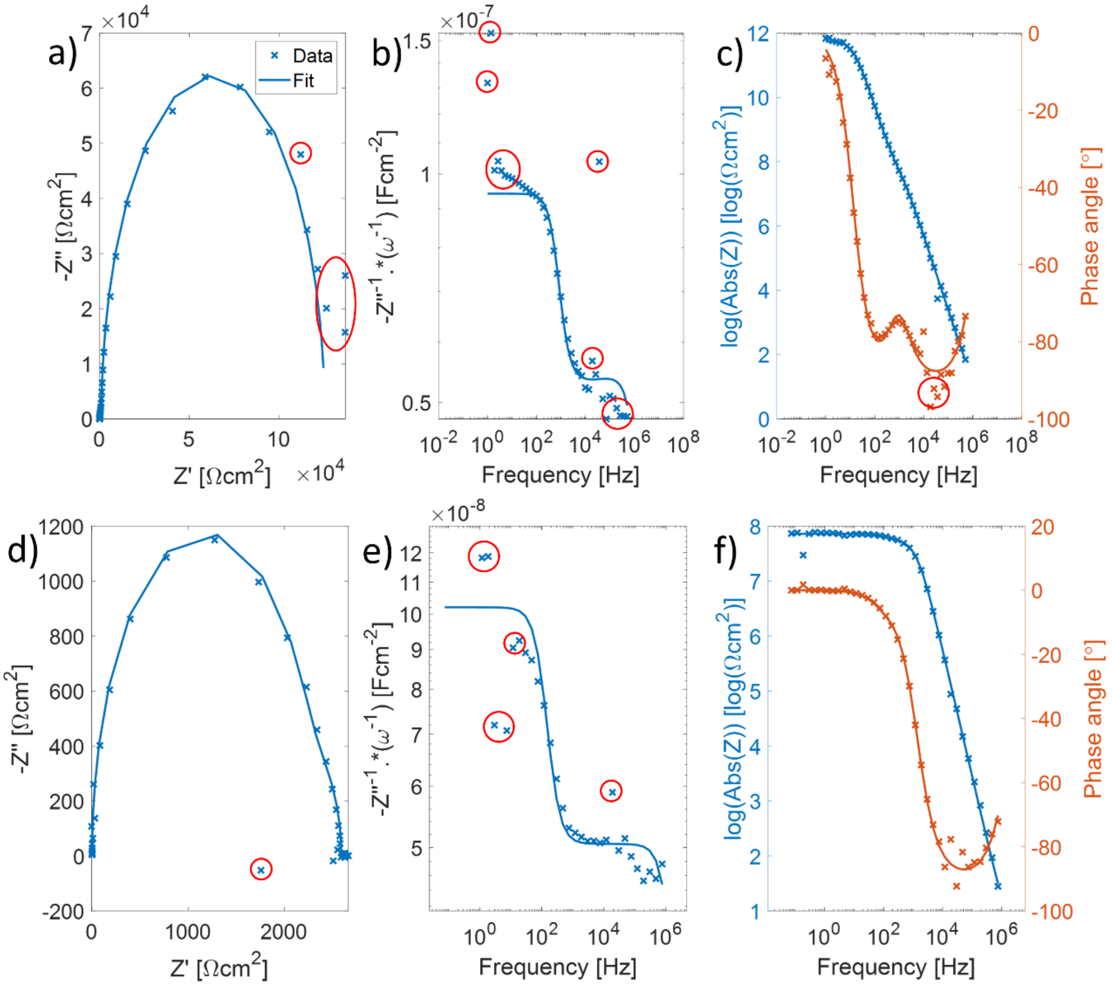

Figure G.2 Further examples of EIS data and the fits to them. (a-c) EIS data from the $FA_{0.05}MA_{0.95}PbI_3$ device in batch 2 at $40°C$ under a LiCl atmosphere in the form of a Nyquist plot, a "capacitance" *vs* frequency plot and a Bode plot respectively. In this example, R_{ion} is low. This is one example of where the fit to the data is less ideal than the example in Figure 6.2. (d-f) EIS data from the $MAPbI_3$ device in batch 1 at $50°C$ under a $MgCl_2$ atmosphere in the form of a Nyquist plot, a "capacitance" *vs* frequency plot and a Bode plot respectively. In this example, R_{ion} is low and J_{rec} is very high, so high that the *RC* time constant "bump" in phase angle is not visible. This is one example of where the fit to the data is much less ideal than the example in Figure 6.2.

G.2 Parameter values obtained from fitting data from measurement batch 1.

MAPbI$_3$						
Salt used	Parameter	Temperature (°C)				
		25	**30**	**40**	**50**	**60**
Ar	**Cion**	1.40E-07	1.43E-07	1.48E-07	1.58E-07	1.59E-07
	Cg	5.29E-08	5.29E-08	5.30E-08	5.15E-08	5.11E-08
	Rion	1.60E+04	1.25E+04	7.00E+03	4.50E+03	2.25E+03
	Rs	1.50E+00	1.50E+00	1.50E+00	1.50E+00	1.50E+00
	Jrec	1.10E-06	1.32E-06	1.76E-08	1.98E-06	3.72E-06
LiCl	**Cion**	1.65E-07	1.68E-07	1.68E-07	1.70E-07	1.70E-07
	Cg	4.64E-08	4.66E-08	4.66E-08	4.65E-08	4.68E-08
	Rion	2.50E+03	2.00E+03	1.35E+03	9.00E+02	5.10E+02
	Rs	1.50E+00	1.50E+00	1.50E+00	1.50E+00	1.50E+00
	Jrec	1.50E-09	1.10E-09	1.20E-09	1.60E-09	2.30E-09
MgCl$_2$	**Cion**	1.13E-07	1.16E-07	1.17E-07	1.13E-07	1.41E-07
	Cg	5.26E-08	5.21E-08	5.12E-08	5.08E-08	5.03E-08
	Rion	5.00E+03	4.20E+03	3.40E+03	2.10E+03	1.40E+03
	Rs	1.50E+00	1.50E+00	1.50E+00	1.50E+00	1.50E+00
	Jrec	7.95E-06	7.05E-06	9.33E-06	2.16E-05	1.11E-05
NaI	**Cion**	1.63E-07	1.63E-07	1.61E-07	1.63E-07	1.62E-07
	Cg	4.70E-08	4.67E-08	4.66E-08	4.65E-08	4.59E-08
	Rion	1.60E+03	1.35E+03	9.50E+02	6.00E+02	3.55E+02
	Rs	1.70E+00	1.60E+00	1.50E+00	1.50E+00	1.50E+00
	Jrec	9.00E-10	9.50E-10	1.20E-09	1.75E-09	2.45E-09
NaCl	**Cion**	1.50E-07	1.55E-07	1.54E-07	1.57E-07	-
	Cg	4.86E-08	4.92E-08	4.77E-08	4.74E-08	-
	Rion	7.50E+02	7.50E+02	5.30E+02	4.00E+02	-
	Rs	6.00E+00	6.00E+00	6.00E+00	6.00E+00	-
	Jrec	2.50E-06	2.16E-06	2.65E-06	3.07E-06	-

FA$_{0.05}$MA$_{0.95}$PbI$_3$						
Salt used	Parameter	Temperature (°C)				
		25	**30**	**40**	**50**	**60**
Ar	**Cion**	1.70E-07	1.75E-07	-	1.77E-07	1.84E-07
	Cg	5.03E-08	5.05E-08	-	4.83E-08	4.69E-08
	Rion	3.20E+04	2.30E+04	-	4.80E+03	2.50E+03
	Rs	1.50E+00	1.50E+00	-	1.50E+00	2.00E+00
	Jrec	3.50E-09	5.55E-09	-	1.26E-08	1.64E-08
LiCl	**Cion**	1.61E-07	1.63E-07	1.66E-07	1.68E-07	1.71E-07
	Cg	4.79E-08	4.81E-08	4.81E-08	4.82E-08	4.78E-08
	Rion	3.70E+03	2.90E+03	1.70E+03	1.00E+03	6.80E+02

	Rs	1.80E+00	1.80E+00	1.50E+00	1.50E+00	1.50E+00
	Jrec	4.40E-08	4.20E-08	3.27E-08	2.75E-08	2.90E-08
$MgCl_2$	**Cion**	1.64E-07	1.64E-07	1.64E-07	1.65E-07	1.68E-07
	Cg	4.74E-08	4.72E-08	4.72E-08	4.71E-08	4.66E-08
	Rion	1.90E+03	1.60E+03	1.00E+03	5.60E+02	4.25E+02
	Rs	1.50E+00	1.50E+00	1.50E+00	1.50E+00	1.50E+00
	Jrec	3.15E-08	4.90E-08	3.00E-08	3.47E-08	4.38E-08
NaI	**Cion**	1.45E-07	1.45E-07	1.43E-07	1.43E-07	1.47E-07
	Cg	4.77E-08	4.77E-08	4.69E-08	4.65E-08	4.65E-08
	Rion	4.20E+03	3.50E+03	2.00E+03	1.10E+03	9.00E+02
	Rs	1.20E+00	1.20E+00	1.20E+00	1.20E+00	1.20E+00
	Jrec	7.00E-07	8.35E-07	1.11E-06	1.73E-06	3.27E-06
NaCl	**Cion**	1.35E-07	1.14E-07	1.14E-07	1.18E-07	1.28E-07
	Cg	4.48E-08	4.41E-08	4.30E-08	4.31E-08	4.33E-08
	Rion	4.20E+02	3.80E+02	3.30E+02	2.72E+02	2.35E+02
	Rs	1.50E+00	1.50E+00	1.50E+00	1.50E+00	1.50E+00
	Jrec	7.55E-06	3.32E-05	3.80E-05	3.82E-05	2.40E-05
$Cs_{0.05}MA_{0.95}PbI_3$						
Salt used	Parameter	Temperature ($^\circ C$)				
		25	**30**	**40**	**50**	**60**
Ar	**Cion**	1.78E-07	1.80E-07	1.78E-07	1.76E-07	1.81E-07
	Cg	5.23E-08	5.22E-08	5.13E-08	5.08E-08	5.05E-08
	Rion	1.27E+04	1.05E+04	5.40E+03	2.80E+03	1.50E+03
	Rs	1.00E+00	1.00E+00	1.50E+00	1.50E+00	1.50E+00
	Jrec	3.00E-10	3.00E-10	3.50E-10	4.50E-10	6.00E-10
LiCl	**Cion**	1.82E-07	1.82E-07	1.85E-07	1.82E-07	1.84E-07
	Cg	5.29E-08	5.24E-08	5.18E-08	5.11E-08	4.99E-08
	Rion	2.20E+04	1.70E+04	9.35E+03	4.80E+03	2.25E+03
	Rs	2.00E+00	2.00E+00	2.00E+00	2.00E+00	2.00E+00
	Jrec	6.20E-10	6.00E-10	1.00E-09	1.50E-09	2.00E-09
$MgCl_2$	**Cion**	1.90E-07	1.90E-07	1.86E-07	1.85E-07	1.86E-07
	Cg	5.33E-08	5.25E-08	5.19E-08	5.14E-08	4.98E-08
	Rion	2.35E+04	1.85E+04	1.02E+04	5.50E+03	2.65E+03
	Rs	1.80E+00	1.75E+00	1.80E+00	1.80E+00	1.80E+00
	Jrec	1.75E-09	2.25E-09	4.60E-09	7.50E-09	9.90E-09
NaI	**Cion**	1.84E-07	1.86E-07	1.84E-07	1.85E-07	1.85E-07
	Cg	5.38E-08	5.32E-08	5.24E-08	5.19E-08	5.08E-08
	Rion	1.31E+04	9.80E+03	5.85E+03	3.35E+03	1.78E+03
	Rs	1.50E+00	2.25E+00	2.00E+00	2.00E+00	2.00E+00
	Jrec	2.50E-09	1.90E-09	2.90E-09	1.00E-09	2.00E-09
NaCl	**Cion**	1.84E-07	1.54E-07	1.55E-07	1.58E-07	1.58E-07
	Cg	5.38E-08	4.47E-08	4.43E-08	4.40E-08	4.35E-08
	Rion	1.30E+04	4.40E+03	4.70E+03	3.20E+03	1.70E+03

	Rs	2.10E+00	1.50E+00	1.50E+00	1.50E+00	1.50E+00
	Jrec	2.50E-09	2.30E-09	2.50E-09	5.25E-09	4.25E-09

Table G.1 Parameter values obtained from fitting data from measurement batch 1

G.3 Parameter values obtained from fitting data from measurement batch 2.

MAPbI$_3$								
Salt used	Parameter	Temperature ($^{\circ}C$)						
		25	**30**	**35**	**40**	**45**	**50**	**55**
Ar	Cion	1.45E-07	1.45E-07	1.43E-07	1.45E-07	1.47E-07	1.50E-07	-
	Cg	4.60E-08	4.58E-08	4.59E-08	4.58E-08	4.58E-08	4.53E-08	-
	Rion	3.50E+04	2.50E+04	1.60E+04	1.10E+04	9.00E+03	6.50E+03	-
	Rs	2.00E+00	2.00E+00	2.00E+00	2.00E+00	2.00E+00	2.00E+00	-
	Jrec	1.70E-07	1.80E-07	2.10E-07	2.10E-07	2.10E-07	2.10E-07	-
Dried LiCl	Cion	1.52E-07	1.55E-07	1.58E-07	1.57E-07	1.58E-07	1.58E-07	1.58E-07
	Cg	4.55E-08	4.50E-08	4.45E-08	4.42E-08	4.40E-08	4.37E-08	4.32E-08
	Rion	2.15E+04	1.40E+04	1.00E+04	9.00E+03	6.75E+03	4.75E+03	3.50E+03
	Rs	1.00E+00	7.50E-01	7.50E-01	7.50E-01	7.50E-01	7.50E-01	7.50E-01
	Jrec	3.85E-08	4.25E-08	3.45E-08	4.40E-08	3.50E-08	2.90E-08	2.80E-08
Dried LiI	Cion	1.39E-07	1.40E-07	1.47E-07	1.53E-07	1.52E-07	1.53E-07	5.15E-07
	Cg	4.49E-08	4.46E-08	4.46E-08	4.44E-08	4.38E-08	4.33E-08	5.37E-08
	Rion	1.50E+04	1.02E+04	8.25E+03	7.10E+03	5.25E+03	3.85E+03	2.75E+03
	Rs	7.50E-01	7.50E-01	7.50E-01	1.75E+00	1.75E+00	1.75E+00	1.75E+00
	Jrec	2.35E-07	2.45E-07	7.40E-08	6.10E-08	6.25E-08	6.50E-08	7.60E-08
LiCl	Cion	1.52E-07	1.53E-07	1.56E-07	1.56E-07	1.58E-07	1.58E-07	1.58E-07
	Cg	4.58E-08	4.59E-08	4.58E-08	4.56E-08	4.55E-08	4.45E-08	4.40E-08
	Rion	2.70E+04	2.15E+04	1.65E+04	1.15E+04	8.50E+03	6.00E+03	4.20E+03
	Rs	2.00E+00	1.75E+00	1.75E+00	1.75E+00	1.75E+00	1.75E+00	2.00E+00
	Jrec	4.25E-08	5.51E-08	5.65E-08	6.00E-08	7.75E-08	9.50E-08	6.00E-08
LiI	Cion	1.55E-07	1.55E-07	1.55E-07	1.54E-07	1.55E-07	1.55E-07	1.55E-07
	Cg	4.48E-08	4.43E-08	4.42E-08	4.37E-08	4.35E-08	4.33E-08	4.27E-08
	Rion	1.60E+04	1.15E+04	9.25E+03	7.00E+03	5.20E+03	4.00E+03	2.75E+03
	Rs	7.50E-01	7.50E-01	7.50E-01	7.50E-01	7.50E-01	7.50E-01	7.50E-01
	Jrec	1.40E-08	4.00E-08	3.75E-08	5.45E-08	4.50E-08	6.00E-08	4.75E-08
MgCl$_2$	Cion	1.48E-07	1.48E-07	1.48E-07	1.48E-07	1.48E-07	1.50E-07	1.50E-07
	Cg	4.39E-08	4.39E-08	4.34E-08	4.34E-08	4.33E-08	4.31E-08	4.26E-08
	Rion	4.20E+03	6.50E+03	5.60E+03	4.70E+03	3.75E+03	2.90E+03	2.30E+03
	Rs	2.50E+00	2.50E+00	2.00E+00	2.00E+00	1.75E+00	1.75E+00	1.75E+00
	Jrec	2.20E-08	2.30E-08	2.75E-08	2.35E-08	3.45E-08	3.75E-08	7.60E-08
FA$_{0.05}$MA$_{0.95}$PbI$_3$								
Salt used	Parameter	Temperature ($^{\circ}C$)						
		25	**30**	**35**	**40**	**45**	**50**	**55**
Ar	Cion	1.86E-07	1.83E-07	1.83E-07	1.85E-07	1.86E-07	1.88E-07	1.88E-07

	Cg	5.52E-08	5.42E-08	5.39E-08	5.39E-08	5.32E-08	5.18E-08	5.15E-08
	Rion	2.00E+03	1.60E+03	1.30E+03	1.05E+03	7.75E+02	6.75E+02	5.85E+02
	Rs	1.25E+00	1.50E+00	1.60E+00	1.60E+00	1.60E+00	1.60E+00	1.60E+00
	Jrec	2.47E-07	2.90E-07	3.30E-07	3.70E-07	4.15E-07	4.70E-07	5.75E-07
Dried LiCl	Cion	1.84E-07	1.84E-07	1.84E-07	1.85E-07	1.86E-07	1.86E-07	1.87E-07
	Cg	5.45E-08	5.43E-08	5.39E-08	5.32E-08	5.28E-08	5.27E-08	5.26E-08
	Rion	1.85E+03	1.55E+03	1.20E+03	9.50E+02	7.00E+02	5.95E+02	5.20E+02
	Rs	1.60E+00	1.60E+00	1.75E+00	1.75E+00	1.75E+00	1.75E+00	1.75E+00
	Jrec	4.10E-07	3.90E-07	2.39E-07	3.60E-07	3.10E-07	4.10E-07	4.25E-07
Dried $MgCl_2$	Cion	1.85E-07	1.86E-07	1.88E-07	1.90E-07	1.88E-07	1.91E-07	1.93E-07
	Cg	5.41E-08	5.37E-08	5.35E-08	5.30E-08	5.23E-08	5.15E-08	5.06E-08
	Rion	1.18E+03	9.75E+02	8.10E+02	6.60E+02	4.85E+02	4.20E+02	3.75E+02
	Rs	1.75E+00	1.75E+00	1.75E+00	1.75E+00	1.75E+00	1.75E+00	1.75E+00
	Jrec	1.00E-07	2.80E-08	3.00E-08	2.35E-08	3.20E-08	1.90E-08	3.00E-08
LiCl	Cion	1.87E-07	1.87E-07	1.87E-07	1.87E-07	1.87E-07	1.87E-07	1.87E-07
	Cg	5.51E-08	5.48E-08	5.45E-08	5.40E-08	5.35E-08	1.87E-07	5.25E-08
	Rion	1.80E+03	1.50E+03	1.22E+03	9.90E+02	7.20E+02	6.15E+02	5.30E+02
	Rs	1.75E+00	1.75E+00	1.75E+00	1.75E+00	1.75E+00	1.75E+00	1.75E+00
	Jrec	2.54E-07	3.12E-07	3.50E-07	4.30E-07	4.50E-07	5.40E-07	6.20E-07
$MgCl_2$	Cion	1.85E-07	1.88E-07	1.90E-07	1.90E-07	1.92E-07	1.92E-07	1.94E-07
	Cg	5.34E-08	5.31E-08	5.27E-08	5.17E-08	5.13E-08	5.08E-08	5.04E-08
	Rion	1.50E+02	2.00E+02	3.55E+02	4.40E+02	3.85E+02	3.50E+02	3.40E+02
	Rs	1.75E+00	1.75E+00	1.75E+00	1.75E+00	1.75E+00	1.75E+00	1.75E+00
	Jrec	9.50E-08	2.50E-08	6.80E-08	7.10E-08	7.10E-08	8.20E-08	9.70E-08
$Cs_{0.05}MA_{0.95}PbI_3$								
Salt used	Parameter	Temperature ($°C$)						
		25	**30**	**35**	**40**	**45**	**50**	**55**
Ar	Cion	1.90E-07	1.90E-07	1.95E-07	1.90E-07	1.95E-07	1.90E-07	1.90E-07
	Cg	5.25E-08	5.25E-08	5.20E-08	5.14E-08	5.12E-08	5.06E-08	1.49E-07
	Rion	1.25E+04	1.00E+04	8.00E+03	5.80E+03	4.35E+03	3.15E+03	2.25E+03
	Rs	1.75E+00	1.75E+00	1.00E+00	1.20E+00	7.50E-01	7.50E-01	1.00E+00
	Jrec	2.00E-08	2.00E-08	3.00E-08	2.50E-08	2.80E-08	3.90E-08	2.25E-08
Dried LiCl	Cion	1.90E-07	1.95E-07	1.90E-07	1.92E-07	1.92E-07	1.90E-07	1.92E-07
	Cg	5.17E-08	5.20E-08	5.14E-08	5.05E-08	5.02E-08	5.06E-08	4.97E-08
	Rion	1.00E+04	9.00E+03	6.50E+03	4.75E+03	3.50E+03	8.50E+03	2.00E+03
	Rs	5.00E+00	5.00E+00	5.00E+00	5.00E+00	5.00E+00	5.00E+00	5.00E+00
	Jrec	8.00E-09	9.00E-09	1.00E-08	9.00E-09	8.50E-09	8.50E-09	1.50E-08
Dried $MgCl_2$	Cion	1.85E-07	1.87E-07	1.87E-07	1.89E-07	1.87E-07	1.87E-07	1.87E-07
	Cg	5.13E-08	5.09E-08	5.04E-08	5.05E-08	5.01E-08	5.09E-08	4.96E-08
	Rion	9.25E+03	7.25E+03	5.50E+03	4.15E+03	2.90E+03	7.00E+03	1.70E+03
	Rs	1.00E+01	3.00E+00	3.50E+00	3.50E+00	3.50E+00	3.00E+00	3.00E+00

	Jrec	8.00E-09	8.00E-09	9.50E-09	1.10E-08	1.10E-08	9.50E-09	1.50E-08
LiCl	Cion	1.90E-07	1.92E-07	1.95E-07	1.95E-07	1.95E-07	1.95E-07	1.98E-07
	Cg	5.27E-08	5.24E-08	5.22E-08	5.16E-08	5.15E-08	5.20E-08	5.02E-08
	Rion	1.20E+04	9.20E+03	7.20E+03	5.35E+03	4.10E+03	1.00E+04	2.10E+03
	Rs	1.75E+00	1.75E+00	1.75E+00	1.75E+00	2.00E+00	1.50E+00	1.50E+00
	Jrec	7.75E-09	7.00E-09	8.50E-09	8.50E-09	1.00E-08	7.00E-09	1.50E-08
LiI	Cion	1.83E-07	1.83E-07	1.83E-07	1.86E-07	1.88E-07	1.85E-07	1.85E-07
	Cg	5.17E-08	5.17E-08	5.12E-08	5.06E-08	5.02E-08	5.16E-08	4.93E-08
	Rion	7.10E+03	5.60E+03	4.25E+03	3.50E+03	2.75E+03	5.75E+03	1.50E+03
	Rs	1.00E+00	1.00E+00	1.00E+00	1.00E+00	8.00E-01	1.00E+00	7.50E-01
	Jrec	3.40E-08	7.50E-08	1.05E-07	1.00E-07	7.75E-08	7.90E-08	1.05E-07
$MgCl_2$	Cion	1.92E-07	1.92E-07	1.92E-07	1.91E-07	1.92E-07	1.93E-07	1.92E-07
	Cg	5.18E-08	5.18E-08	5.13E-08	5.10E-08	5.02E-08	5.14E-08	4.91E-08
	Rion	6.90E+03	6.50E+03	5.35E+03	4.15E+03	3.10E+03	6.70E+03	1.80E+03
	Rs	1.50E+00	1.50E+00	1.50E+00	1.75E+00	1.75E+00	1.75E+00	1.75E+00
	Jrec	6.00E-09	6.00E-09	3.00E-09	8.00E-09	9.00E-09	9.00E-09	5.00E-09

Table G.2 Parameter values obtained from fitting data from measurement batch 2

G.4 Relationship between the salt used in saturated solution, the relative humidity, and the partial pressure.

Salt	Relative Humidity (%)	Equilibrium vapour pressure (kPa)	Partial pressure (kPa)
LiCl	11.31	2.33	0.26
LiI	18.56	2.33	0.43
$MgCl_2$	33.07	2.33	0.77
NaI	39.65	2.33	0.92
NaCl	75.45	2.33	1.76

Table G.3 The conversion between relative humidity and partial pressure for each saturated salt solution used. The relative humidity values are taken from Greenspan (176) and the equilibrium vapor pressure is calculated using the Antoine equation with parameters from the *NIST* database (183).

Appendix H - Impedance derivations

Following the method set out by Moia *et al.*(66), we note that at 0 V dc bias and in the dark, the electronic current flowing through the device is controlled by a diode-like expression:

$$J_{rec} = J_{s1} \exp\left(\frac{qV_1}{k_B T}\right)$$

where *V₁* is the electrostatic potential at interface 1 and will vary relative to the equilibrium position of the device as the ionic charge redistributes in response to an applied potential. In the full circuit model, *V₁* controls the voltage at the base of the bipolar transistors that represent a modulated interfacial current. In this circumstance (at 0 V dc bias and in the dark) this is presented by drawing the updated equivalent circuit as follows:

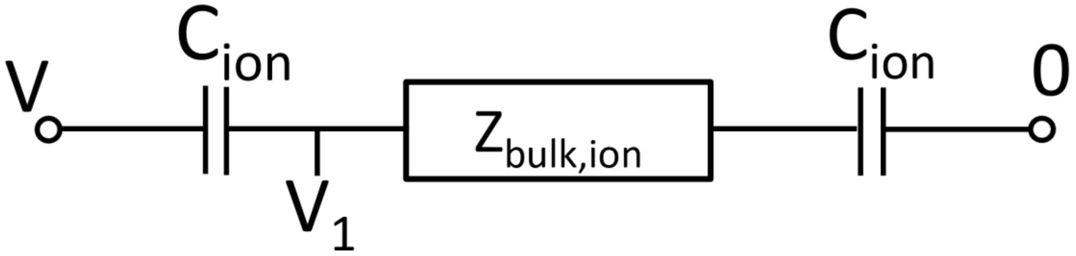

Figure H.1 The ionic branch of the dark, 0V equivalent circuit approximation. $Z_{bulk,ion}$ is the impedance of the parallel combination of the ionic resistance, R_{ion}, and the bulk geometric capacitive element C_{gbulk}. It is represented in this way for easy comparison to the original work/derivation.

When a voltage $V = \bar{V} + v(\omega)$ is applied, the voltage will drop across each element in the circuit of Figure H.1 so that $V_1 = V - V_{C_{ion}}$. At steady state there is no ionic current, so the voltage that drops across R_{ion} (and therefore $Z_{bulk,ion}$) is also zero. As such $\bar{V_1} = \bar{V}/2$ and so far, the derivation has identical results to the work of Moia *et al.* In the frequency domain, the small perturbation component to the voltage, *V*, is

$$v(\omega) = \frac{2J_{ion}}{i\omega C_{ion}} + J_{ion} Z_{bulk,ion}$$

where the contribution of the ionic capacitors of each interface are assumed equal and their terms have been summed. Substituting this into $v_1 = v - J_{ion}/i\omega C_{ion}$ gives,

$$V_1 = \frac{\overline{V}}{2} + \frac{v}{2}\left(2 - \frac{1}{1 + \frac{i\omega Z_{bulk,ion} C_{ion}}{2}}\right).$$

Following Moia *et al.*, the reciprocal of the recombination impedance is the differential of J_{rec} with respect to the applied voltage, V. The small perturbation limit gives the equation of this differential $\left(\frac{dj_{rec}}{dv}\right)$:

$$\frac{1}{Z_{rec}} = \frac{1}{R_{rec}} + i\omega C_{rec} = \left(1 - \frac{1}{2 + i\omega Z_{bulk,ion} C_{ion}}\right)\frac{qJ_{rec}}{k_B T}.$$

By substituting $Z_{bulk,ion} = \left(\frac{1}{R} + i\omega C_{gbulk}\right)^{-1}$ into the above expression and separating the real and imaginary components, the expressions for R_{rec} and C_{rec} shown in section 3.4.2 can be found.

The expression for Z (Equation 14) is found by finding the impedance of the ionic branch Z_{ion}, combining it in parallel with C_{rec} and R_{rec} before adding the series resistance:

$$Z = R_s + \left(\frac{1}{\frac{1}{i\omega C_{rec}}} + \frac{1}{R_{rec}} + \frac{1}{Z_{ion}}\right)^{-1}$$

where

$$Z_{ion} = \frac{2}{i\omega C_{ion}} + Z_{bulk,ion}.$$